TRANSVERSE COLLECTIVE FLOW AND EMISSION ORDER OF MID-RAPIDITY FRAGMENTS IN FERMI ENERGY HEAVY ION COLLISIONS

A Dissertation

by

ZACHARY WAYNE KOHLEY

Submitted to the Office of Graduate Studies of
Texas A&M University
in partial fulfillment of the requirements for the degree of

DOCTOR OF PHILOSOPHY

August 2010

Major Subject: Chemistry

TRANSVERSE COLLECTIVE FLOW AND EMISSION ORDER OF MID-RAPIDITY FRAGMENTS IN FERMI ENERGY HEAVY ION COLLISIONS

A Dissertation

by

ZACHARY WAYNE KOHLEY

Submitted to the Office of Graduate Studies of
Texas A&M University
in partial fulfillment of the requirements for the degree of

DOCTOR OF PHILOSOPHY

Approved by:

Chair of Committee,	Sherry J. Yennello
Committee Members,	Joseph B. Natowitz
	Rand L. Watson
	Che-Ming Ko
Head of Department,	David H. Russell

August 2010

Major Subject: Chemistry

ABSTRACT

Transverse Collective Flow and Emission Order of Mid-Rapidity Fragments in Fermi Energy Heavy Ion Collisions. (August 2010)

Zachary Wayne Kohley, B.S., Hillsdale College

Chair of Advisory Committee: Dr. Sherry J. Yennello

The Equation of State (EoS) of asymmetric nuclear matter has been explored through the study of mid-rapidity fragment dynamics from the 35 MeV/u ^{70}Zn+^{70}Zn, ^{64}Zn+^{64}Zn, and ^{64}Ni+^{64}Ni systems. The experimental data was collected at the Texas A&M Cyclotron Institute using the 4π NIMROD-ISiS array, which provided both event characterization and excellent isotopic resolution of charged particles.

The transverse collective flow was extracted for proton, deuteron, triton, ^{3}He, alpha, and ^{6}He particles. Isotopic and isobaric effects were observed in the transverse flow of the fragments. In both cases, the transverse flow was shown to decrease with an increasing neutron content in the fragments. The $(N/Z)_{sys}$ dependence of the transverse flow and the difference betwen the triton and ^{3}He flow were shown to be sensitive to the density dependence of the symmetry energy using the stochastic mean-field model. A stiff parameterization of $E_{sym}(\rho)$ was found to provide better agreement with the experimental data.

The transverse flow for intermediate mass fragments (IMFs) was investigated, providing a new probe to study the nuclear EoS. A transition from the IMF flow strongly depending on the mass of the system, in the most violent collisions, to a dependence on the charge of the system, for the peripheral reactions, was observed. Theoretical simulations were used to show that the relative differences in the IMF flow are sensitive to the density dependence of the symmetry energy. The best agreement between the experiment and theory was achieved with a stiff $E_{sym}(\rho)$.

A new method was developed in which correlations between the projectile-like and mid-rapidity fragments were examined using a scaled flow. Theoretical simulations were used to show that the scaled flow of the particles was connected to their average order of emission. The experimental results suggest that the mid-rapidity region is preferentially populated with neutron-rich light charged particles and the Z=3-4 IMFs at a relatively early stage in the collision.

This work presents additional constraints on the nuclear EoS and insight into the mid-rapidity dynamics observed in Fermi energy heavy-ion collisions.

To Melanie and Briella

ACKNOWLEDGMENTS

I would like to thank the staff of Texas A&M University Cyclotron Institute for their continuous help before, during, and after my dissertation experiment. This work would not have been possible without them. Thanks to Dr. Massimo di Toro, Dr. Maria Colonna, and Dr. Malgorzata Pfabe for help running and interperting the results of the SMF model. Similarly, thanks are due to Dr. Roy Wada and Dr. Akira Ono for support in using the AMD-DS model. I would like to thank Dr. George Souliotis and Dr. Aldo Bonasera for help with the CoMD model. Additionally, I would like to thank Dr. Aldo Bonasera for all of his ideas and the enlightening discussions we had both in and out of group meeting. I would like to thank my committee members, Dr. Joseph Natowitz, Dr. Che-Ming Ko, and Dr. Rand Watson. I would also like to thank Dr. Kris Hagel for a seemingly endless amount of help in setting up my experiment, calibrating the NIMROD-ISiS array, and properly using the ROOT package throughout my analysis. I need to thank all the undergrads, grad students, and post-docs that I have had the pleasure of working with for not only helping me but also for making grad school a lot of fun. Thanks to all my friends and family for their support and encouragement. Specifically, I need to thank my amazing wife, Melanie, for always being there for me through out the ups and downs of graduate student life (and for point picking). Lastly, a huge thank you is due to my advisor Dr. Sherry Yennello for all of her guidance and advice in both research and life. I doubt I will ever be able to thank her enough for everything that she has taught me.

TABLE OF CONTENTS

CHAPTER Page

CHAPTER Page

LIST OF TABLES

LIST OF FIGURES

FIGURE Page

FIGURE Page

FIGURE Page

FIGURE Page

FIGURE Page

FIGURE Page

FIGURE Page

FIGURE Page

FIGURE Page

FIGURE Page

FIGURE Page

FIGURE Page

FIGURE Page

FIGURE Page

FIGURE Page

FIGURE Page

FIGURE Page

FIGURE Page

FIGURE Page

CHAPTER I

INTRODUCTION

Improving our understanding of the nuclear Equation of State (EoS) is an important goal for the field of nuclear science. In particular, the form of the EoS for asymmetric nuclear matter is not well-known and therefore, requires additional experimental constraints. Heavy-ion collisions (HICs) provide a unique opportunity to examine nuclear matter at temperatures, densities, and neutron-to-proton (N/Z) ratios away from that of ground state nuclei.

A. Nuclear Equation of State

Ground state nuclei allow for the examination of nuclear matter at a temperature T=0 MeV and density $\rho_\circ$=0.16 nucleons/fm^3 (saturation density). The nuclear binding energy of ground state nuclei can be described relatively well through the liquid drop model, originally derived by Weizsäcker in 1935 [1]. The form of the Weizsäcker, or semi-empirical, mass formula is commonly shown as,

$$BE(MeV) = a_v A - a_s A^{2/3} - a_{Coul}\frac{Z^2}{A^{1/3}} - a_{sym}\frac{(N-Z)^2}{A} \pm \delta \qquad (1.1)$$

where the binding energy, BE, is calculated from a variety of terms that are dependent on the mass (A), charge (Z), and neutron content (N) of the nuclei [1, 2]. The positive binding energy is due to the volume term (a_v) while the surface (a_s), Coulomb (a_{Coul}) and symmetry (a_{sym}) terms decrease the binding energy. The last term (δ) accounts for the change in the binding energy due to the pairing of nucleons. Therefore, the binding energy is increased for even-even nuclei and decreased for odd-odd nuclei. The

---

The journal model is Physical Review C.

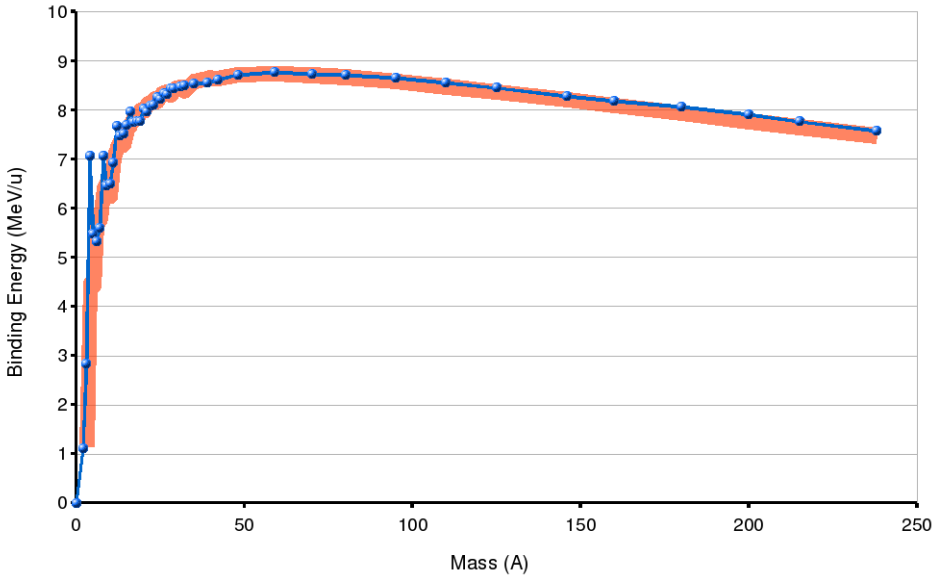

FIG. 1. Binding energy per nucleon is plotted as a function of the mass for the most stable isotopes. The blue circles represent experimentally determined masses taken from Ref. [3]. The red fill area is the binding energy per nucleon calculated from the Weizsäcker, or semi-empirical, mass formula without the pairing term (Eq. 1.1).

parameters of the mass formula can be fit such that the calculated binding energies are within a few percent of the experimentally determined values [1, 2]. In Figure 1 the experimental and calculated binding energy values are compared. The semi-empirical mass formula was used with the coefficient values from Ref. [1] and the pairing term was not included. The results demonstrate that the liquid drop model provides a reasonable description for ground state nuclei, which represents cold nuclear matter at the saturation density.

Understanding nuclear properties away from ground state nuclei presents a challenging task. The nuclear EoS describes the basic properties of infinite nuclear matter at temperatures, densities, and neutron-to-proton ratios (N/Z) away from that of ground state nuclear matter. The EoS for nuclear matter is often represented in a

parabolic form,

$$E(\rho, I) = E(\rho, 0) + E_{sym}(\rho)I^2 \tag{1.2a}$$

$$I = \frac{\rho_n - \rho_p}{\rho_{total}} \approx \frac{N - Z}{A} \tag{1.2b}$$

where the binding energy, E(ρ,I), is a function of both the density (ρ) and isospin concentration (I) of the infinite nuclear matter [4]. The isospin concentration, I, is the percent difference in the neutron (ρ_n) and proton (ρ_p) densities of the nuclear matter. The first term of the EoS, E(ρ,0), is not dependent on I and therefore represents the binding energy for symmetric (N=Z) nuclear matter as a function of density. The second term is referred to as the symmetry energy, $E_{sym}(\rho)$, and becomes increasingly important in describing asymmetric (N≠Z) nuclear matter since it has an I^2 dependence. The symmetry energy represents the energy required to change every proton in symmetric nuclear matter into a neutron. Thus, the symmetry energy is equal to the difference between the binding energy of pure neutron matter, E(ρ,1), and symmetric nuclear matter, E(ρ,0).

The nuclear EoS for I=0.0, 0.5, and 1.0 nuclear matter was calculated from two different interactions (Gogny and Gogny-AS [5]) and is presented in Figure 2. Both interactions have been used in heavy-ion collisions simulations and provide the same EoS for symmetric nuclear matter, E(ρ,0). As the asymmetry of the nuclear matter is varied from I=0.0 to I=1.0 the difference in the interactions is obvious. The EoS of pure neutron matter (I=1.0) is drastically different for the two interactions. Therefore, the differences observed between the Gogny and Gogny-AS interactions for pure neutron matter can be represented by the density dependence of the symmetry energy since it is equal to the difference between I=0.0 and I=1.0 nuclear matter. The density dependence of the symmetry energy, calculated from the two interactions, is

shown on the right of Figure 2. The Gogny-AS interaction produces a "stiff" density dependence with the symmetry energy increasing beyond $\rho/\rho_\circ$=1.0, whereas a "soft" $E_{sym}(\rho)$ is shown for the Gogny interaction.

The binding energy of symmetric nuclear matter is well defined at the saturation density, $\rho_\circ \approx 0.16$ fm^{-3}, with E($\rho_\circ$,0) $\approx$ -16 MeV because the binding energies of ground state nuclei are well known [6]. The EoS for symmetric nuclear matter, E(ρ,0), is also thought to be relatively constrained from HIC transverse flow measurements [7, 8, 9, 10, 11] and giant monopole resonances [12]. The form of the EoS of symmetric nuclear matter is often described by the compressibility (K),

$$K = 9\rho_\circ^2 \frac{d^2(E/A)}{d\rho^2}|_{\rho_\circ} \tag{1.3}$$

which represents the curvature of the EoS around the saturation density [6, 12]. Current constraints imply a relatively soft EoS for symmetric nuclear matter with a compressibility of K=220-260 MeV [12]. For reference, the EoS for the symmetric nuclear matter (I=0.0), shown in Figure 2, calculated from the Gogny and Gogny-AS interactions has a K=228 MeV.

Current theoretical models exhibit good agreement for the symmetry energy of the nuclear EoS near the saturation point of nuclear matter but can diverge drastically in the high and low density regions [6, 13, 14, 15, 16, 4]. Understanding the form of the symmetry energy can provide information on nuclear properties, astrophysical processes, and the fundamental nucleon-nucleon interaction [17, 15, 18, 19, 20, 21, 22, 23, 24]. In particular, the density dependence of the symmetry energy can greatly affect predictions of neutron star properties, such as the density profile, proton fraction, the mass to radius ratio, and the cooling processes [19, 21, 22, 25, 26]. For example, Li has calculated the proton fraction as a function of density for a neutron star in β equilibrium using two interactions which produce a stiff and soft density dependence

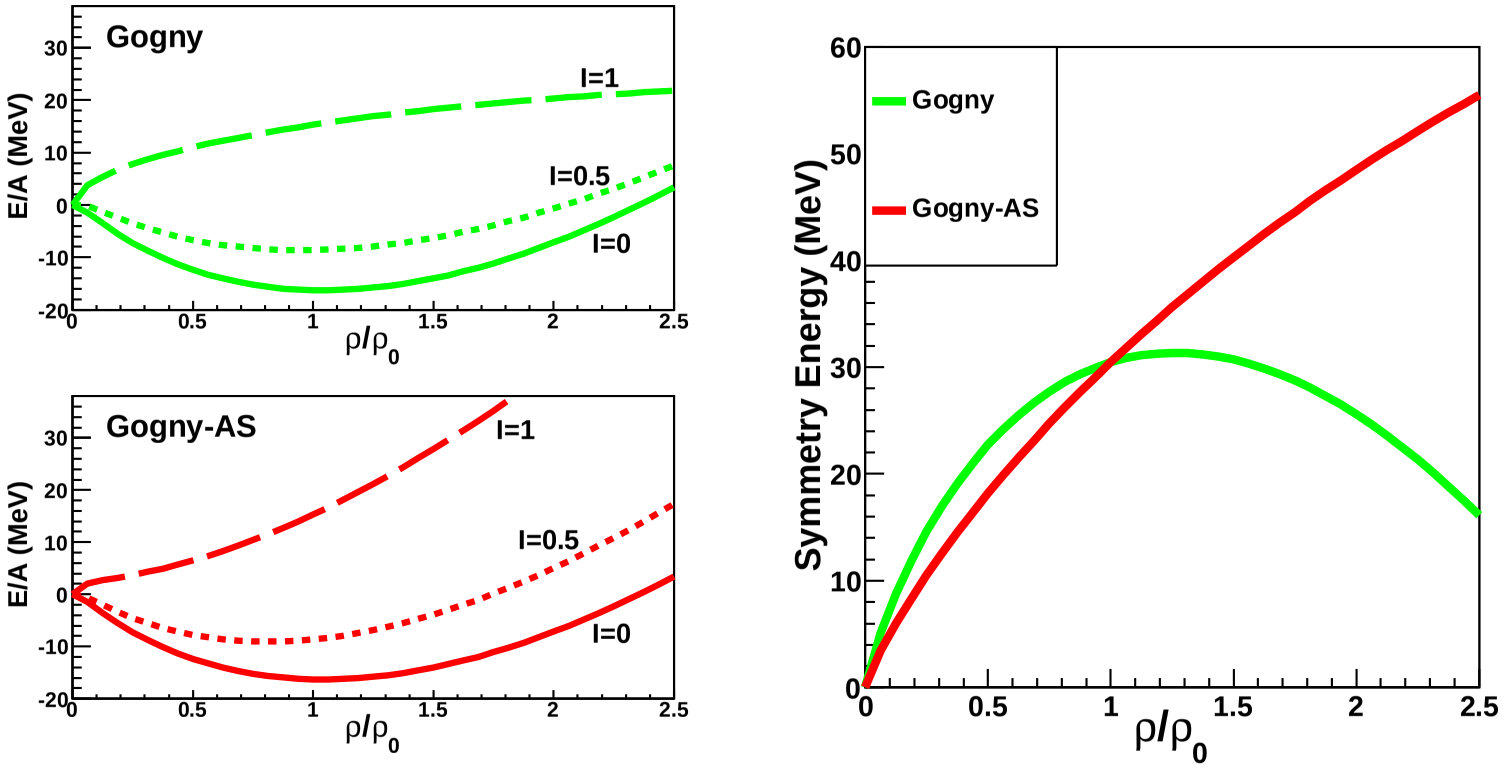

FIG. 2. Binding energy per nucleon (E/A) of infinite nuclear matter as a function density calculated using the Gogny (top-left) and Gogny-AS (bottom-left) interactions. The EoS of I=0.0, 0.5, and 1.0 nuclear matter is provided. The resulting density dependence of the symmetry energy is shown on the right for the two different equations of state.

of the symmetry energy [26, 27]. The results showed that the stiff $E_{sym}(\rho)$ would produce a higher proton fraction in the neutron star enabling it to enter the direct URCA process,

$$n + e^+ \rightarrow p + \bar{\nu}_e \tag{1.4a}$$

$$p + e^- \rightarrow n + \nu_e \tag{1.4b}$$

which allows the star to cool faster relative to the standard URCA process

$$p + (n,p) + e^- \rightarrow n + (n,p) + \nu_e \tag{1.5a}$$

$$n + (n,p) + e^+ \rightarrow p + (n,p) + \bar{\nu_e} \tag{1.5b}$$

that requires three nucleons to participate in order to conserve momentum [19]. Thus, the neutron star will cool slower with a soft $E_{sym}(\rho)$ since it cannot enter the direct URCA process. Therefore, it is vital that the form of the density dependence of the symmetry energy be constrained in order produce accurate predictions of asymmetric nuclear matter at high, or low, densities and temperatures.

Heavy-ion collisions provide the ability to examine the EoS of asymmetric nuclear matter away from $\rho_\circ \approx 0.16$ fm^{-3} and T=0 MeV. Recent experimental results are being used to apply constraints to the asymmetric part of the EoS, or density dependence of the symmetry energy ($E_{sym}(\rho)$) [28, 13, 18, 15]. Free neutron-proton ratios [29], isobar ratios [30], isoscaling [18, 31, 32], and isospin diffusion [33] measurements from heavy-ion collisions have provided evidence suggesting a stiff density dependence of the symmetry energy [28]. Theoretical predictions have suggested that insight into the nuclear EoS, specifically the density dependence of the symmetry energy, could also be gained through examination of collective flow [34, 35, 13] and neck emission/dynamics [36, 37, 38, 39] which will be introduced in Sections B and

C, respectively.

B. Transverse Collective Flow

Transverse collective flow in heavy-ion collisions can be described as an enhancement of particle emission in the reaction plane. The first experimental measurements of transverse flow were achieved at the Bevalac in Berkeley, CA in the 1980s [40, 41]. The 800 MeV/u Ar+Pb and 400 MeV/u Ca+Ca and Nb+Nb reactions provided evidence of a "bounce-off" of the projectile and a "sidewards flow" or "side-splash" of fragments being produced with velocities between that of the projectile and target. This demonstated a flow of energy or nuclear matter in the reactions. Since the pioneering research at the Bevalac, collective flow measurements have been extracted from heavy-ion collisions over a large range of energies (10 MeV/u to 200 GeV/u) [9, 10].

A simple depiction of a mid-peripheral heavy-ion collision is shown in Figure 3 in order to illustrate the concept of transverse flow. The initial interaction of the projectile and target is shown on the left-side of Figure 3. By convention, the z-axis corresponds to the beam axis and together with the x-axis they represent the reaction plane. The impact parameter vector is shown as the blue arrow pointing in the direction of the projectile. After the projectile and target separate, forming a quasi-projectile (QP) and quasi-target (QT), a formation of particles can be found in between the QP and QT (right-side of Figure 3). The movement of these mid-velocity fragments in the reaction plane, following the QP and QT, defines the transverse flow. Thus, a larger transverse flow is observed with an increased in-plane momentum of the particles.

Experimentally the transverse flow is often quantified as the slope of the average

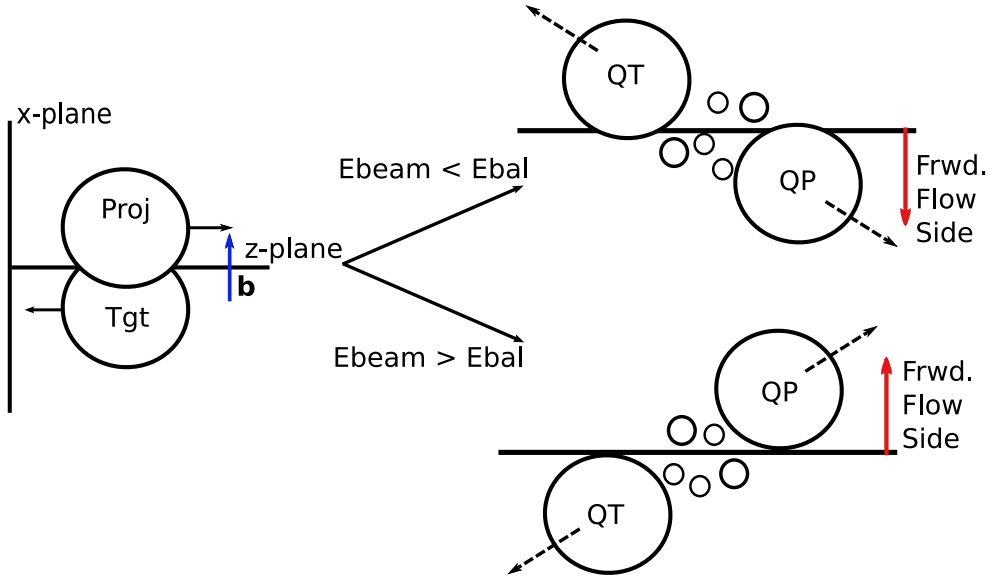

FIG. 3. Illustration of a mid-peripheral heavy-ion collision. The left-side shows the initial overlap of the projectile and target. The resulting trajectory of the QP, QT, and mid-velocity fragments, relative to the initial configuration, is presented for both a beam energy (E_{beam}) greater than and less than the balance energy (E_{bal}) of the system, which represents the energy at which the transverse flow vanishes. The impact parameter vector, or reaction plane angle, is shown as the blue arrow and the forward flow side of the reaction plane is represented by the red arrows.

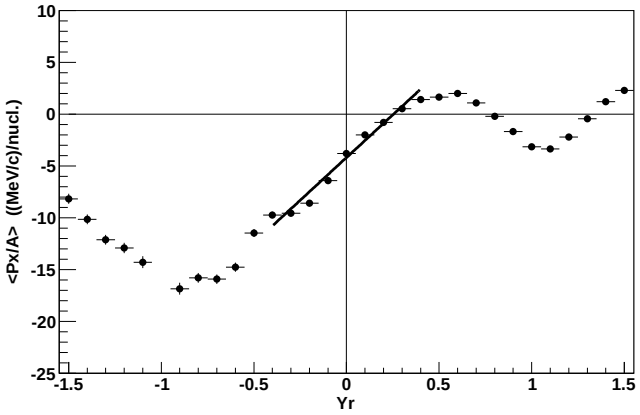

FIG. 4. Typical flow plot showing the average in-plane momentum per nucleon, $\langle p_x \rangle$, as a function of the reduced rapidity Y_r for protons. The solid black line shows a linear fit over the mid-rapidity region where the slope represents the flow parameter.

in-plane momentum, $\langle p_x \rangle$, over the mid-rapidity region. The flow parameter (F) is then defined as,

$$F = \frac{\partial \langle p_x \rangle}{\partial Y_r}|_{Y_r=0.5} \tag{1.6}$$

where Y_r represents the reduced rapidity, which is equal to the center-of-mass rapidity of the fragment scaled by the center-of-mass rapidity of the projectile (Y_r=$Y_{cm,frag}$/$Y_{cm,proj}$). In the Fermi Energy regime the rapidity, Y, is nearly equivalent to the parallel, or beam direction, velocity (v_z). A typical flow plot is shown in Figure 4 demonstrating a linear fit over the mid-rapidity region from which the flow parameter can be extracted.

The beam energy of the reaction has an important affect on the observed transverse flow as shown in Figure 3. If the energy of the projectile, E_{beam}, is less than the balance energy, E_{bal}, of the system (defined in the following paragraph), then the projectile and target rotate around each other, as shown in the top-right of Figure 3.

The forward flow side of the reaction plane, shown as a red arrow, is defined by the QP position. Thus, below E_{bal} the forward flow side of the reaction plane is 180° from the original reaction plane angle defined by the impact parameter vector (blue arrow). If $E_{beam} > E_{bal}$ then the projectile and target "bounce-off" each other and the forward flow side and impact parameter vector are aligned, as shown in the bottom-right of Figure 3. It is important to note that, in general, only the forward flow side of the reaction plane can be determined, not the impact parameter vector, from the experimental data. Therefore, it is often not possible to differentiate whether the projectile rotates or bounces off the target. Thus, the flow parameter will always be positive since it is extracted with respect to the forward flow side. If the true reaction plane angle could be determined, then below E_{bal} the flow parameter would be negative. Tsang *et al.* observed the negative flow below E_{bal} by measuring circular polarized γ-rays from the residual target in coincidence with light charged particles [42].

The transition from the rotation to bounce-off mechanism of the projectile and target became a large focus for many heavy-ion experiments. The beam energy at which the transverse flow disappears, representing the change from the rotation to bounce-off mechanisms, is referred to as the balance energy [43, 44, 45, 46]. In 1989, Krofcheck *et al.* examined the flow from La+La reactions at different energies and found that the transverse flow disappeared around 50 MeV/u [47]. This presented a scenario in which the attractive mean-field is the dominant component in the transverse flow at low energies and at higher energies the repulsive nucleon-nucleon (NN) collisions becomes dominant [48]. At low energies, below E_{bal}, the attractive mean-field is responsible for the the rotation of the projectile and target around each other while the "bounce-off" above E_{bal} can be attributed to the repulsive NN-collisions, as shown in Figure 3. Therefore, at an intermediate energy a balance between the attractive mean-field and NN-collisions is reached such that the transverse flow dis-

appears. Westfall *et al.* examined the system mass dependence of the balance energy and found that it followed an $A^{-1/3}$ power law which represents a balance between the attractive mean-field potential which scales with the surface, $A^{2/3}$, and the repulsive nucleon-nucleon collisions which should scale with the interaction volume, A [48, 16].

The experimental E_{bal} results provided an excellent opportunity to study both the nuclear potential and nucleon-nucleon cross-sections. Microscopic transport calculations, for example the Boltzmann-Uehling-Uhlenbeck (BUU) model, were used to simulate the heavy-ion collisions through solving the Boltzmann Langevin Equation defined as,

$$\frac{\partial}{\partial t} f - \{h[f], f\} = I_{coll}[f] \tag{1.7}$$

where the left-side of the equation represents the propagation of the one-body distribution, $f(\mathbf{r}, \mathbf{p}, t)$, in a self-consistent mean-field and I_{coll} takes into account the NN-collisions, as well as Pauli-blocking [49, 16, 50]. Both the form of the mean-field and the nucleon-nucleon cross-sections could be modified in order to fit the experimental data. In general, the results indicated that the E_{bal} was weakly sensitive to the mean-field and very sensitive to the nucleon-nucleon cross-section [45, 51, 43, 52]. The transport calculations, through comparison with the experiment mass-dependence of the E_{bal}, demonstrated the need for a reduced, or in-medium, nucleon-nucleon cross-section [48]. While, the E_{bal} results were very useful in understanding the need for a reduced cross-section, information about the compressibility (K) of symmetric nuclear matter was also examined and results indicated a preference for a soft compressibility [11]. Danielewicz *et al.* was able to provide additional constraints on the compressibility, also demonstrating a preference for a soft EoS, through examining the transverse flow over a large range of energies (0.1-10 GeV/u) [7]. These results demonstrate how vital the study of the collective flow in heavy-ion collisions has been

in improving our understanding of the nuclear properties.

While transverse flow measurements have been very important in helping elucidate the EoS for symmetric nuclear matter, it has been consistently discussed as a probe to examine the density dependence of the symmetry energy [16, 35, 13, 15]. Pak *et al.* demonstrated that both the the transverse collective flow for Z=1-3 particles and the balance energy increased with an increasing neutron to proton ratio of the system, $(N/Z)_{sys}$ [53, 54]. This was the first evidence that the collective flow was sensitive to the isospin concentration of the colliding system. The isospin dependence of the transverse flow and balance energy were attributed to the isospin dependence of the mean-field and in-medium isospin-dependent nucleon-nucleon cross sections through comparisons with a BUU and quantum molecular dynamics (QMD) model [55, 56]. Scalone *et al.* used a Boltzmann-Nordheim-Vlasov (BNV) simulation to demonstrate that the isospin dependence observed by Pak *et al.* was also sensitive to the density dependence of the symmetry energy [34].

Differences between the free neutron and free proton transverse collective flows have been predicted to be strongly sensitive to $E_{sym}(\rho)$ [57, 58, 27]. However, obtaining accurate energy and angular measurements of free neutrons, along with charged particles, is a difficult task. Currently, experimental data from the FOPI/LAND detectors are being used to extract preliminary neutron and proton collective flows in order examine the sensitivity to the density dependence of the symmetry energy [59, 60]. The results will be used to plan a dedicated experiment in an attempt to apply high density constraints to the symmetry energy.

Scalone *et al.*, using a BNV microscopic transport simulation, have shown that a comparison of the flow parameter from ^{3}H and ^{3}He light clusters would exhibit a similar dependence on $E_{sym}(\rho)$ as the neutron and proton flows [34]. The simulations showed that for a stiff symmetry energy parameterization the ^{3}He clusters should

have an estimated 20% larger flow than the ^{3}H clusters in a 55 MeV/u, ^{58}Fe+^{58}Fe reaction [34]. In the case of a soft parameterization, the difference in the flow parameter between the ^{3}H and ^{3}He would disappear [35, 34]. Thus, by measuring the flow parameter of the ^{3}H and ^{3}He clusters one should be able to gain insight into the density dependence of the symmetry energy. Recently, Yong *et al.*, using a BUU calculation, have demonstrated that the ^{3}H and ^{3}He flow, from a 400 MeV/u reaction, could be used to probe the density dependence of the symmetry energy at supra-saturation densities [61].

The theoretical simulations suggest that examining the transverse flow of isotopically resolved fragments could provide insight into the nuclear EoS. However, there is little experimental data in which the transverse flow of fragments has been investigated in reference to their isospin content. Thus, a brief overview of the dependence of the transverse flow on the mass and charge of fragments is provided in the following. For Au+Au reactions at 150-800 MeV/u, it has been shown that the flow parameter per nucleon increases as a function of the charge of the fragment up to Z$\sim$4 and then becomes relatively constant for heavier fragments [62, 9]. Similar results were also observed in 200 MeV/u ^{84}Kr+^{197}Au reactions, which showed an increased transverse flow with increased fragment mass [63]. Partlan *et al.* also observed an increased flow with increased particle mass in comparing protons, deuterons, tritons, ^{3}He, and alpha particles in Au+Au reactions at 0.25-1.15 GeV/u [64]. All of these results are from reactions above the balance energy. The increased flow with increased particle mass trend was interperted as the fragment flow being comprised of both a thermal and collective component. The thermal component, which diminishes the collective motion, was thought to be independent of the fragment mass while the collective component should scale with the mass of the fragment. Therefore, the heavier fragments would exhibit an increased flow per nucleon due to a larger collective component relative to

the thermal component.

Below the balance energy, the results of Pak *et al.* demonstrated that the flow parameter increased from Z = 1 fragments to Z = 3 fragments [53]. If one assumes an average mass for the Z=2 fragments to be A=4 and the Z=3 fragments to be A=7 then it appears that the flow *per nucleon* actually decreases with increasing charge. However, theoretical QMD calculations suggested that the flow per nucleon increases with increasing mass for 25 MeV/u Ca+Ca collisions [65]. Therefore, there is a discrepancy below the balance energy. Furthermore, results from the INDRA collaboration show the evolution of the flow parameter per nucleon as function of energy, both above and below the balance energy, for isotopically resolved fragments of A = 1 to A = 4 [44]. However, the flow of the fragments was not compared directly and it is difficult to discern a distinct trend. Most recently, the INDRA and ALADiN collaborations have investigated the directed flow of isotopically resolved particles ranging from protons to ^{7}Li, for ^{124}Xe + ^{112}Sn and ^{129}Xe + ^{124}Sn systems at 100 MeV/u, which is above balance energy [66]. The results did not show any obvious isotopic or isobaric trends.

It is clear that additional experimental research is needed to explore the transverse flow of fragments, specifically with isotopic identification, below the balance energy where the mean-field is dominant as this could provide new insight into the nuclear EoS. Thus, new measurements have been made to examine the flow of isotopically identified fragments below the balance energy and are presented in this dissertation.

C. Mid-Rapidity/Neck Emission

Understanding the mechanisms responsible for particle production in the Fermi energy domain is an important task that could provide additional insights into the behavior and properties of nuclear matter. In the examination of peripheral and semi-peripheral intermediate energy heavy-ion collisions, a large source of particle production has been found to originate from a mid-rapidity (also termed mid-velocity or neck) region in between that of the quasi-projectile, QP, and quasi-target, QT [36, 67, 68, 69, 70, 71]. This can be visualized in Figure 3 by the light charged particles in between the QP and QT. Exploring the dynamics/mechanisms responsible for the formation of this neck-like source could provide information on the nucleon-nucleon interaction and nuclear equation of state (EoS).

Experimental results from both dissipative mid-peripheral reactions and ternary fission showed a production of light charged particles and/or intermediate mass fragments in between the projectile and target like fragments (or fission fragments) [72, 68, 73, 74, 75]. The mid-rapidity production mechanism suggested an important non-equilibrium dynamical component of fragment formation which could not be explained by a statistical break-up of the QP and QT [36]. Experimental and theoretical studies have suggested that the mid-rapidity region is composed of a combination of particles from both dynamical (neck-fragmentation) and statistical processes. In particular, a 3-Body Coulomb trajectory calculation was used to demonstrate that the production of mid-rapidity IMFs (intermediate mass fragments) could be connected to both a fast emission from the neck region and a later emission from the surface of the QP or QT [76]. Furthermore, studies by Hudan *et al.* and McIntosh *et al.* suggested that the QP is likely deformed after the collisions producing an asymmetric emission pattern focused towards the mid-rapidity region [77, 78]. Gingras *et al.* used a molecular

dynamics simulation to show that the formation of the mid-rapidity particles could be attributed to both a prompt emission, due to nucleon-nucleon collisions, and a later emission from the tails of the QP and QT [79]. Therefore, the mid-rapidity particles are likely formed from a combination of mechanisms, ranging from prompt emission to statistical decay, occurring during the heavy-ion collision.

Experimental results have demonstrated an increased neutron to proton ratio (N/Z) of the mid-rapidity region in comparison to the quasi-projectile (QP) source through the examination of isotopically resolved fragments as well as the detection of free neutrons [70, 71, 80, 81, 82, 83, 84, 85, 86]. For example, Lukasik *et al.* showed that 65-70% of the total triton production can be attributed to the mid-rapidity region [70]. Furthermore, it has been suggested that the neck-like structure represents a low-density region of nuclear matter between the higher density QP and QT [87, 88]. Thus, the neck region can provide an opportunity to examine dilute neutron-rich nuclear matter. The study of this low-density asymmetric nuclear matter should provide observables sensitive to the nuclear EoS. Theoretical models have shown that the isospin content and production of intermediate mass fragments (IMFs) in the neck region could be used to probe the nuclear equation of state [36, 37, 38, 39].

Since these mid-rapidity products are likely being produced by different mechanisms or sources, it is of interest to explore the time-scale and order of their emission. Particle-particle correlations [89], velocity correlations [90, 91, 92, 93], fission fragment angular distributions [94], and Coulomb proximity effects [95, 96, 97, 77, 78] have all been used in attempts to extract information on the emission time of fragments from various sources. For example, Ghetti *et al.* used particle-particle correlations functions to study the emission time of light charged particles in semi-peripheral collisions from both the PLF (projectile-like fragment) and intermediate velocity, or neck, sources. The results suggested that protons had the largest average emission

time from the PLF followed by alphas and then tritons [98]. In comparing protons, deuterons, and tritons from the intermediate velocity source it was found that the longest average emission time was observed for tritons followed by protons and then deuterons [99]. In addition to the particle-particle correlations, the affect of the proximity of the PLF and TLF on the mid-rapidity light charged particles (LCPs) can be exploited to provide information on their emission time since particles emitted at early stages in the reaction will feel an increased Coulomb potential due to the proximity of the PLF or TLF. In particular, the angular distribution of LCPs in the PLF-frame has been related to the emission time from the PLF-source [96, 97, 78]. The results of McIntosh *et al.* suggest that the emission of the IMFs can occur over a range from 90 fm/c to 450 fm/c [78].

In general, understanding the time and order of emission of LCPs and IMFs is important for improving our understanding of both the dynamical and statistical components of the fragmentation process. Additionally, it is of interest to explore how the order of emission may change with the isospin concentration of the fragments. The average time of emission of LCPs has even been predicted to be sensitive to the nuclear EoS [100, 101]. In this work a new method has been developed to explore the average order of emission of isotopically identified mid-rapidity fragments.

D. Outline

In this dissertation, new experimental results are presented from the 35 MeV/u ^{70}Zn+^{70}Zn, ^{64}Zn+^{64}Zn, ^{64}Ni+^{64}Ni reaction systems. In Chapter II the experimental details, particle identification method, and energy calibrations are discussed. A brief overview of the different theoretical models used in this work is provided in Chapter III. The transverse flow results from the light charged particles and interme-

diate mass fragments, for systems below the balance energy, are presented from both experiment and theory in Chapter IV. The order of emission of LCPs and IMFs in the mid-rapidity region extracted from the experimental data is discussed in Chapter V. Lastly, in Chapter VI a summary of the work is presented.

CHAPTER II

EXPERIMENTAL

The reactions of ^{70}Zn+^{70}Zn, ^{64}Zn+^{64}Zn, and ^{64}Ni+^{64}Ni at 35 MeV/u were studied at the Texas A&M Cyclotron Institute. The NIMROD-ISiS (Neutron-Ion Multidetector for Reaction Oriented Dynamics and Indiana Silicon Sphere) array [102] was used for the collection of the experimental data. The NIMROD-ISiS array provides near 4π angular coverage which is essential for the study of collective flow. Furthermore, the reaction systems were chosen to be mass symmetric, which is advantageous in studying the transverse flow and neck emission from the heavy-ion collisions because the center-of-mass and nucleon-nucleon frames are equivalent.

In this chapter the experimental details are described in Section A and the configuration of the NIMROD-ISiS array, including electronics set-up and data acquisition, are discussed in Section B. The particle identification procedure and energy calibrations for the array are described in Sections C and D, respectively. Lastly, the production and structure of the final physics tapes is discussed in Section E.

A. Experiment

The K500 Superconducting Cyclotron at the Texas A&M University Cyclotron Institute was used to produce beams of ^{70}Zn, ^{64}Zn, and ^{64}Ni at 35 MeV/u which were collided with ^{70}Zn, ^{64}Zn, and ^{64}Ni self-supporting targets, respectively. The ^{64}Zn, and ^{64}Ni targets were purchased from MicroMatter [103]. The ^{70}Zn target was fabricated by the Argonne National Laboratory Target Lab [104] with materials purchased from Trace Sciences [105]. Information about each reaction system, including the projectile energy, projectile charge state, system N/Z, target thickness, target purity, number of raw events, and number of physics events, are presented in Table I. The beam in-

TABLE I. Projectile energy, projectile charge state, system N/Z, target thickness, target purity, number of raw events, and number of physics events are for each reaction system.

Reaction	^{70}Zn+^{70}Zn	^{64}Zn+^{64}Zn	^{64}Ni+^{64}Ni
Projectile Energy (MeV/u)	35	35	35
Proj. Charge State	22+	21+	21+
System N/Z	1.33	1.13	1.28
Target Thickness	0.985mg/cm^2	1.0mg/cm^2	1.14mg/cm^2
Target Purity	95%	99.85%	97.92%
# of Raw Events	$12.2{\cdot}10^7$	$9.3{\cdot}10^7$	$9.5{\cdot}10^7$
# of Physics Events	$11.6{\cdot}10^7$	$8.5{\cdot}10^7$	$9.1{\cdot}10^7$

tensity for each reaction was chosen such that the dead time was kept below 50% and the silicon detectors of the NIMROD-ISiS array would not be damaged. On average, the beam intensity ranged from 200-350 electrical pA which corresponded to 170-240 raw events per second recorded by the data acquisition. A Faraday-cup was placed at the end of the beam line, beyond the NIMROD-ISiS array, to record the total charge deposited by the beam.

In addition to the three reaction systems discussed above, the K500 superconducting cyclotron was used to produce four additional calibration beams. Details about the calibration beams are presented in Table II. These beam-target combinations were chosen with the specific intent to produce well known calibration points in the detectors of the NIMROD-ISiS array. For further details about the choice and use of the calibration beams please refer to Section D.

TABLE II. The beam-target combinations for the calibration systems along with the energy of the calibration beam.

Calibration Beam	$^{1}H_2$	^{20}Ne	^{4}He	^{1}H-^{2}D
Beam Energy (MeV/u)	55	35	25	30
Targets	^{nat}Th,^{28}Si	^{nat}Th	^{nat}Th	^{nat}Th,^{28}Si

B. NIMROD-ISiS Array

The NIMROD array [106, 107] was recently upgraded with additional forward angle silicon detectors and the replacement of the backward angle detectors with the forward hemisphere of the ISiS array [108]. The upgraded array, named NIMROD-ISiS, consists of both a 4π charged particle array and a neutron calorimeter, originally the TAMU Neutron Ball [109]. The upgraded NIMROD-ISiS array [102] provides increased isotopic resolution for fragments with Z$\geq$3 and improved angular granularity in the backward direction. The NIMROD-ISiS array was chosen for the collection of the experimental data because of the combination of 4π angular coverage and excellent isotopic resolution. This provides the ability to examine global variables which will allow for event characterization and reaction plane analysis, while simultaneously examining the isospin degree of freedom obtained from the isotopic resolution of fragments ranging from Z=1 to Z=18.

1. Charged Particle Array Configuration

The NIMROD-ISiS charged particle array consists of 14 concentric rings ranging from 3.6^o to 167.0^o in lab. As shown in Figure 5, the rings are numbered from ring 2 to ring 15, with ring 2 being at the most forward angle. The entire charged particle array is housed inside the Texas A&M Neutron Ball [109], which provides an average

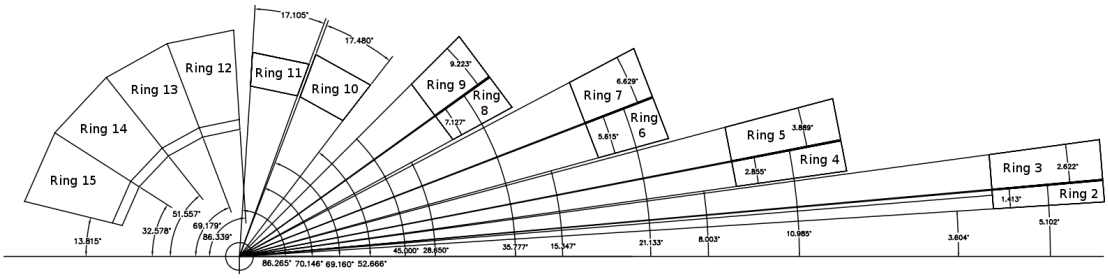

FIG. 5. Side view of the charged particle detectors of the NIMROD-ISiS array. Each ring is labeled with the corresponding lab angle.

neutron multiplicity for each event. Figure 6 shows the combination of the charged particle array and neutron ball.

Rings 2-9 of the NIMROD-ISiS array came from the original NIMROD array and were designed with the same geometry as the INDRA array [110]. The forward hemisphere of the ISiS array covers the backward angles of the NIMROD-ISiS array representing rings 12-15. Rings 10-11 were designed from the ISiS geometry and used as the mating section between the NIMROD and ISiS contributions to the array. Three turbo molecular pumps were used to keep the entire charged particle array at a pressure of 1.4 x 10^{-5} torr throughout the experiment.

The charged particle detectors in each ring were designed with a modular set-up, as shown Figure 7. Each detector module can consist of an ionization chamber, two silicon detectors and a thallium doped cesium-iodide, CsI(Tl), crystal with a photo-multiplier (PMT) or photodiode (PD) attached. However, for this experiment the ionization chambers were not employed. Two different detector module configurations were used in the array. The single telescope configuration consisted of a 150μm, 300μm, or 500μm, silicon placed in front of the CsI(Tl)-PMT detector. The super-telescope configuration had two silicon detectors, 150μm and 500μm, placed in front of a CsI(Tl)-PMT detector. In both cases, the module provided a ΔE-E detector

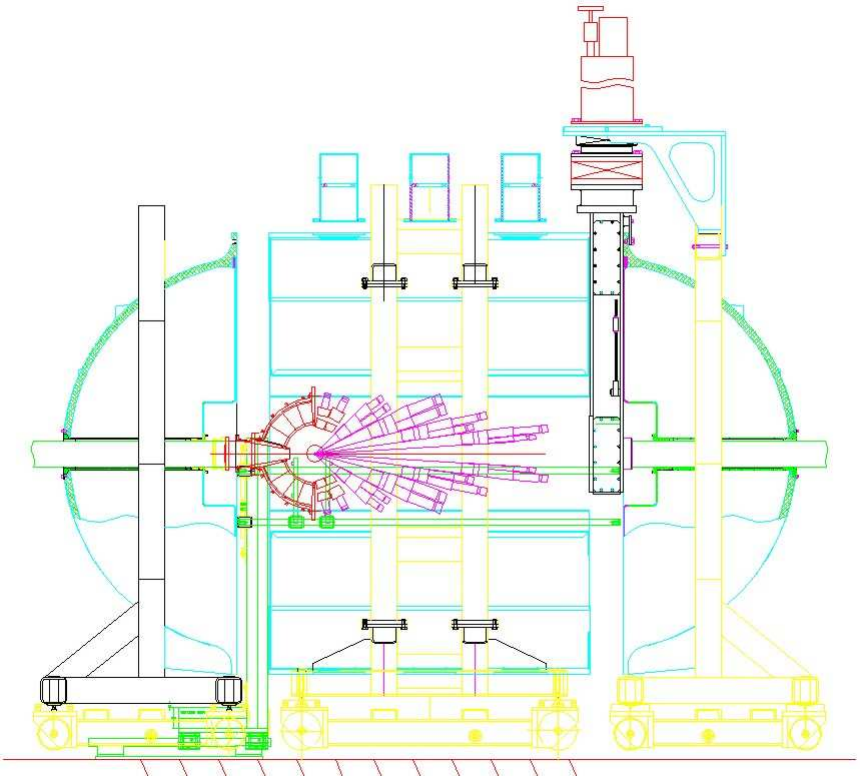

FIG. 6. Schematic of the NIMROD-ISiS array, showing the charged particle array housed inside the neutron ball. (color online)

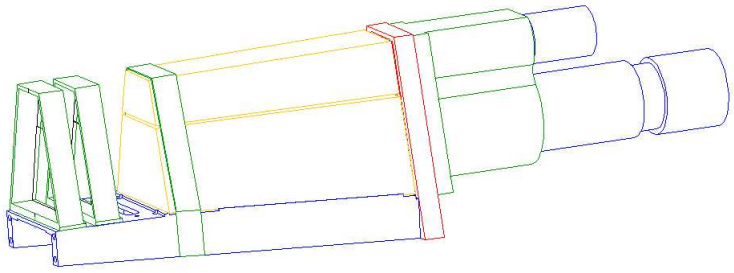

FIG. 7. Detector module from the NIMROD-ISiS array consiting of two silicon detectors and a CsI(Tl) crystal with a PMT attached. This detector module provides coverage for two rings of the array. (color online)

set-up. In the single telescope configuration, the single silicon detector provided the energy loss, ΔE, as a particle passed through and the CsI(Tl)-PMT detector recorded the residual energy, E. In the case of the super-telescope there are two ΔE-E detectors. In the first ΔE-E detector, the 150μm silicon acted as the ΔE and the 500μm silicon as the E. The second ΔE-E detector is the same as that of the single telescope, with the 500μm silicon and CsI(Tl)-PMT acting as the ΔE and E detectors, respectively. Details on the use of the detector module configurations in particle identification can be found in Section C.

An important aspect of the modular detector configurations is the segmentation of the front-plane of the silicon wafers used in the NIMROD-ISiS array for rings 2-9. In Figure 7 two CsI(Tl) detectors are stacked on top of each other, showing that this single detector module covers two different lab angles or represents two different rings. Therefore, the silicon(s) detector is segmented in order to match the angular coverage of the CsI(Tl). On the right side of Figure 8 an example of the segmented front-plane of a silicon detector used in ring 4-5 is shown. The wafer consists of four pads such that it can provide increased granularity for both the theta and phi angles. In the single telescope modules, the signal for the two adjacent pads, in the same ring,

were combined outside the chamber due to a constraint on the number of available ADC channels. For the super-telescope modules all four pads were kept separate, thus creating four super-telescopes.

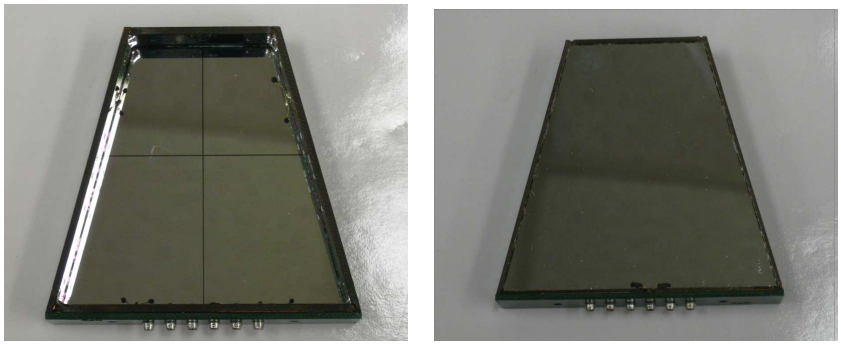

FIG. 8. Picture of the segmented front-plane (Right) and the unsegmented back-plane (Left) of a ring 4-5 silicon wafer. (color online)

The silicon detectors from rings 2-9 allowed for charge collection from both the p+, front, segmented side and the unsegmented n+ back-plane, as shown on the left side of Figure 8. A negative charge (electrons) was collected on the front-plane and a postive charge (holes) was collected on the back-plane. The back of the silicon wafer covers two rings since it is not segmented. So, even though the back-plane of the silicon did not provide any additional angular coverage, it could be set with a lower gain then the front-plane. Thus, a higher gain was used on the front-plane silicon signal in order to maximize the isotopic resolution and the gain was set lower on the back-plane of the silicon in order to provide elemental detection up to the charge of the beam. The back-plane signal was only available for collection in rings 2-7 for this experiment.

The configuration of the detector module set-up varied from ring to ring in the NIMROD-ISiS array. Table III presents a variety of information about each ring. As shown, rings 3-9 each had four super-telescopes (ring 2 had two super-telescopes)

while the rest of the ring consisted of single telescopes. Beyond ring 9, only single telescope modules were used. It is important to notice that full silicon coverage is achieved through-out the array. As previously mentioned, each CsI(Tl) crystal has a PMT or PD attached in order to convert the light output from the crystal into a electronic signal. Table III shows that for rings 2-11 a PMT was attached to the CsI crystals while a PD was used in rings 12-15. The lengths of the CsI crystals, listed in Table III, were chosen such that complete collection of the highest energy protons, in the Fermi Energy range, is achieved [102]. A more detailed schematic representation of each ring is presented in Appendix A, which shows the exact placement of each single and super-telescope within the ring.

In an attempt to maximize the resolution of the silicon detectors by suppressing the amount of noise created from free electrons, a positive bias was applied to the target ladder and aluminized mylar foils were placed in front of rings 2-9. The free electrons can cause increased noise in the silicon detectors, which will decrease the detector resolution. A positive 15 KeV bias was applied to the target ladder in the NIMROD-ISiS array in order to try and caputre the electrons. Also, to try and decrease the number of electrons reaching the detectors a 365 μg/cm^2 thick sheet of aluminzed mylar was placed in front of rings 2-9. For each ring, the sheet of aluminzed mylar was attached to the frame of the ionization chamber, ensuring full coverage of the silicon detectors.

2. TAMU Neutron Ball

As shown in Figure 6, the charged particle array of NIMROD-ISiS is housed inside of a neutron calorimeter, referred to as the TAMU Neutron Ball (NBL). The TAMU Neutron Ball was originally designed with a small reaction chamber at the center of the calorimeter and used to examine neutron multiplicities associated with reactions

TABLE III. The theta range, ΔPhi, number and thickness of single telescopes, number of super-telescopes, PMT or PD attached to CsI, and CsI length for each ring of the NIMROD-ISiS array.

Ring	Theta Range	ΔPhi of CsI	# of Single Telescopes and thickness	# of Super-Telescopes	PMT or PD attached to CsI	CsI(Tl) Length (cm)
2	3.6^o-5.0^o	30^o	10 (300μm)	2	PMT	10.0
3	5.0^o-7.6^o	30^o	10 (300μm)	4	PMT	10.0
4	8.0^o-10.8^o	30^o	10 (300μm)	4	PMT	10.0
5	10.8^o-14.7^o	30^o	10 (300μm)	4	PMT	10.0
6	15.3^o-20.9^o	30^o	5 (300μm) 5 (150μm)	4	PMT	6.5
7	20.9^o-27.6^o	15^o	10 (300μm) 10 (150μm)	4	PMT	6.5
8	28.6^o-35.8^o	30^o	6 (300μm) 4 (150μm)	4	PMT	6.0
9	35.8^o-45.0^o	15^o	12 (300μm) 8 (150μm)	4	PMT	6.0
10	52.7^o-69.2^o	20^o	18 (300μm)	0	PMT	4.0
11	70.1^o-86.3^o	20^o	18 (300μm)	0	PMT	3.0
12	93.5^o-110.8^o	20^o	18 (500μm)	0	PD	2.8
13	110.8^o-128.4^o	20^o	18 (500μm)	0	PD	2.8
14	128.4^o-147.4^o	20^o	18 (500μm)	0	PD	2.8
15	147.4^o-167.0^o	20^o	18 (500μm)	0	PD	2.8

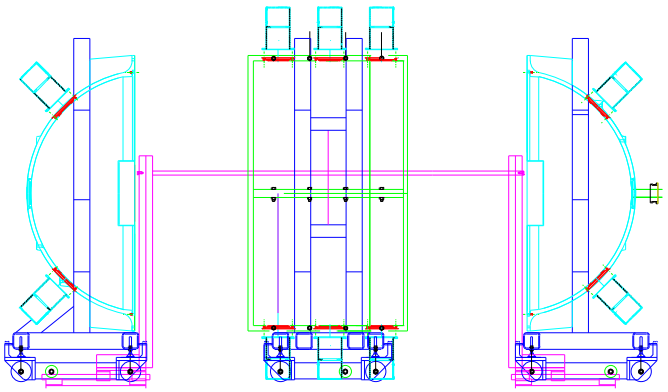

FIG. 9. Side-view depiction of the TAMU Neutron Ball (without charged particle array). The three sections, consisting of two hemispheres and the center cylinder, are shown separated, demonstrating the ability to move each section of the neutron ball independently.(color online)

at intermediate energies [109]. The original neutron ball was expanded in order to create space for the NIMROD charged particle array. A four quadrant cylinder was placed in between the original two hemispheres of the neutron ball, as shown in Figure 9. The hemispheres and center cylinder are individually set on tracks, such that each section of the neutron ball can be moved independently allowing access to the charged particle array.

The neutron ball is filled with 0.3% wt. gallodium (Gd) doped pseudocumene liquid scintillator. In a nuclear collision in the Fermi energy range, the neutron ball will record two distinct set of signals. The first will be the gamma flash, occurring at the time of the nuclear reaction. This produces a very large and distinct signal in the neutron ball. After the immediate production of gamma rays, signals will also be produced in the scintillator fluid from the collection of free neutrons. These free neutrons are thermalized in the liquid scintillator through neutron-proton collisions. After thermalization, the neutrons will drift through the detector for a period of

microseconds and will either diffuse out or undergo a capture reaction with the Gd, which has a high neutron capture cross-section [109]. This process produces, on average, three gamma rays with a total energy of 8 MeV [109, 106]. The gamma ray energy is dissipated in the scintilator and the resulting flash of light is detected by the photomultiplier tubes mounted on the neutron ball. The NBL PMTs are coupled to fish eye lense, which helps to improve the detection efficiency [102]. A total of twenty PMTs are attached to the neutron ball, four PMTs per hemisphere and three PMTs per quadrant of the center cylinder. Due to the relatively long time period required for the neutrons to thermalize and be captured by the Gd, a gate of 50-100 μs is required to count the number of delayed flashes, each representing a neutron [109]. Additional information on how the neutron multiplicity was recorded is provided in the following section.

3. Electronics

The electronics set-up for the NIMROD-ISiS array allows for the conversion of the analog signals produced from the silicon, cesium-iodide, and neutron ball detectors to digital signals which are then collected by the data acquisition software (DAQ). The electronics for the silicon detectors, CsI(Tl)-PMT, CsI(Tl)-PD, neutron ball PMTs, and trigger logic are shown in Figures 10-15. In this experiment, the events were triggered by signals from either the CsI or back-plane of the silicons from rings 2-7. In Table IV, abbreviations and short descriptions of the electronic modules used in the experiment are provided.

The silicon detector electronics can be divided into three groups: the front-plane of the silicons in rings 2-9, the back-plane of silicons in rings 2-7, and the silicons in rings 10-15. The electronics diagrams for the front-plane and back-plane signals are shown in Figure 10. In rings 2-9, custom designed microcontroller boards

TABLE IV. Short description, abbreviations and examples of the electronic modules used in the experiment. Additional information about the electronics modules can be found in Refs. [111, 112]

Module Name	Abv.	Function	Example Modules
Leading Edge Discriminator	LED	Determines if a signal is above a threshold.	LeCroy 623B, Pico Sys. Shaper Disc.
Constant Fraction Discriminator	CFD	Determines if the signal is above a threshold based on a constant fraction of peak amplitude, which provides a consistent triggering time.	LeCroy 3420, Tennelec 454
Peak Sensing Analog to Digital Converter	ADC	Converts analog peak height to digital signal.	Phillips 7164
Peak Integrating Analog to Digital Converter	QDC	Converts peak integral to digital signal.	LeCroy 1885F, Phillips 7166
Fast Amplifier	FA	Amplifies the signal without changing its shape.	LeCroy 612A
Shaping Amplifier	-	Amplifies, integrates, and differentiates the signal producing a uni- or bipolar signal.	Pico Systems Shaper and Shaper Discriminator

TABLE IV. Continued

Module Name	Abv.	Function	Example Modules
Charge-Sensitive Pre-Amplifier	Pre-Amp	Integrates the charge from the detector and provides initial amplification.	Zepto Systems Pre-Amplifier
Logic Fan in Fan out	FI/FO	Creates a single logic signal if any input fired.	LeCroy 429A, PS 757,756
Linear Fan in Fan out	FI/FO	Creates a linear sum of the input signals. with both OR and SUM signals available.	LeCroy 428F
Overlap	-	Produces a logic signal when the selected signal(s) overlap with a gate.	LeCroy 356AL
Bit Register	-	Marks a bit assigned to each fired CsI-PMT when event is triggered.	LeCroy 4448, 2341A
Gate Generator	-	Creates an adjustable width logic signal.	LeCroy 222, PS 794, GG 8000,8010
Scaler	-	Counts signals received.	LeCroy 4434

were connected directly to the outside of the chamber to collect both the front- and back-plane silicon signals. These boards were used to hold Zepto System pre-amplifiers [113], supply the pre-amps with +/-12 volts, and supply the bias voltage for the silicon detectors. Due to the geometrical space constraints of rings 10-15, Zepto system designed micrcontroller boards [113] were used, instead of the custom microcontroller boards, and were mounted with the Zepto System pre-amps.

In all cases, the silicon bias voltage was supplied from a Tennelec High Voltage Supply Module and the +/-12 volts for the pre-amps was supplied by Topward Dual-Channel DC Voltage Supplies. After amplification by the pre-amps, the gain and shape of the silicon signal was adjusted by the shaping amplifier. In rings 2-9, CAMAC Pico Systems [114] Shaping Amplifers were used for the front-plane signals and CAMAC Pico Systems Shaper Discriminators were used for the back-plane signals of rings 2-7. The Shaper Discriminators, as shown in Figure 10, allow for the back-plane signals to be processed before going to the ADCs and act as a leading-edge discriminator which provides OR and SUM signals for triggering.

After the shaping amplifiers, the analog silicon signals from rings 2-9 were converted to digital signals using CAMAC Philips peak sensing ADCs. In rings 10-11, CAMAC Pico System Shaping Amplifiers were used along with VME peak sensing ADCs and in rings 12-15 the modified ISiS shaping amplifiers were used in conjunction with VME peak sensing ADCs. The original ISiS modules [108] contained both a pre-amp and shaping amplifier. The modules were modified to bypass the pre-amplifier component and the Zepto system pre-amplifiers (discussed above) were used for the ISiS Si signals. If a good event was triggered, then a 20μs gate was produced and the digital signals from the ADCs were recorded by the DAQ software.

The electronics for the CsI detectors are best described in two parts: the CsI-PMT detectors of rings 2-11 and the CsI-PD detectors of rings 12-15. The CsI-PMT

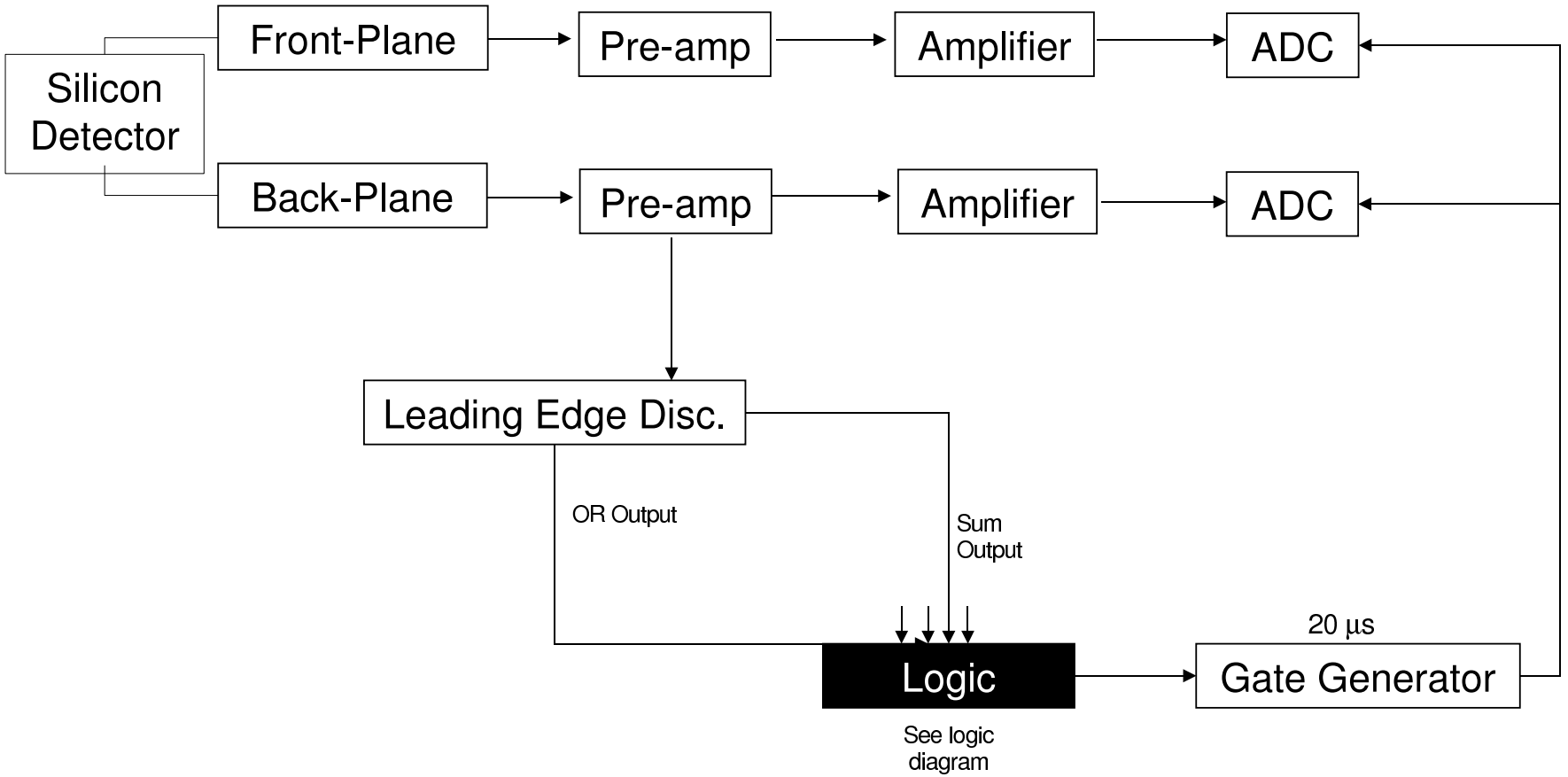

FIG. 10. Electronics diagram for the front-plane and back-plane silicon signals which were collected in Rings 2-15 and Rings 2-7, respectively.

signals are used for both pulse-shape analysis and event triggering. In the pulse-shape analysis the signal is split into a fast and slow component, which when plotted against each other provides isotopic identification for Z=1-3 fragments. A LeCroy 1440 High Voltage supply was used to supply voltage to custom resistor-chain boards, which provided the correct voltage to each dynode of the photomultiplier tube.

The CsI-PMT electronics diagram, Figure 11, shows the PMT signal being split for both event triggering and collection by the dynamic-range QDCs. The copy of the signal sent through the the fast amplifier is then sent into a constant fraction discriminator which will produce a SUM and OR signal that is used by the logic module for triggering an event. The CsI CFD signals were also sent to a bit register used to keep track of the number of times each CsI fired. Another copy of the signal is sent into a custom built splitter/attenuator that produces two more copies of the original signal that can each individually be attenuated. These two attenuated signals are then used for the fast and slow components of the signal.

If an event is triggered, the logic module sends a trigger for a 400ns gate to be created. The 400ns gate is then sent to a QDC to record the fast portion of the CsI signal (see Figure 12). The CsI signal is delayed (300ns) such that the 400ns gate begins at the peak of the signal. A 1μs gate is produced 1μs later to record the slow portion of the CsI signal, as shown in Figure 12. The placement of the 400ns (fast) and 1μs (slow) gates relative to the signal shape where chosen in order to maximize the resolution of the isotopic identification from the pulse-shape analysis [102]. The dynamic-range QDCs also helped in maximizing the isotopic resolution since they allow for the large signals to be collected with a low gain and the smaller signals to be collected with a higher gain.

The CsI crystals of rings 12-15 were coupled to photodiodes for collection of light output. The electronics for the CsI-PD were different than those used for the CsI-

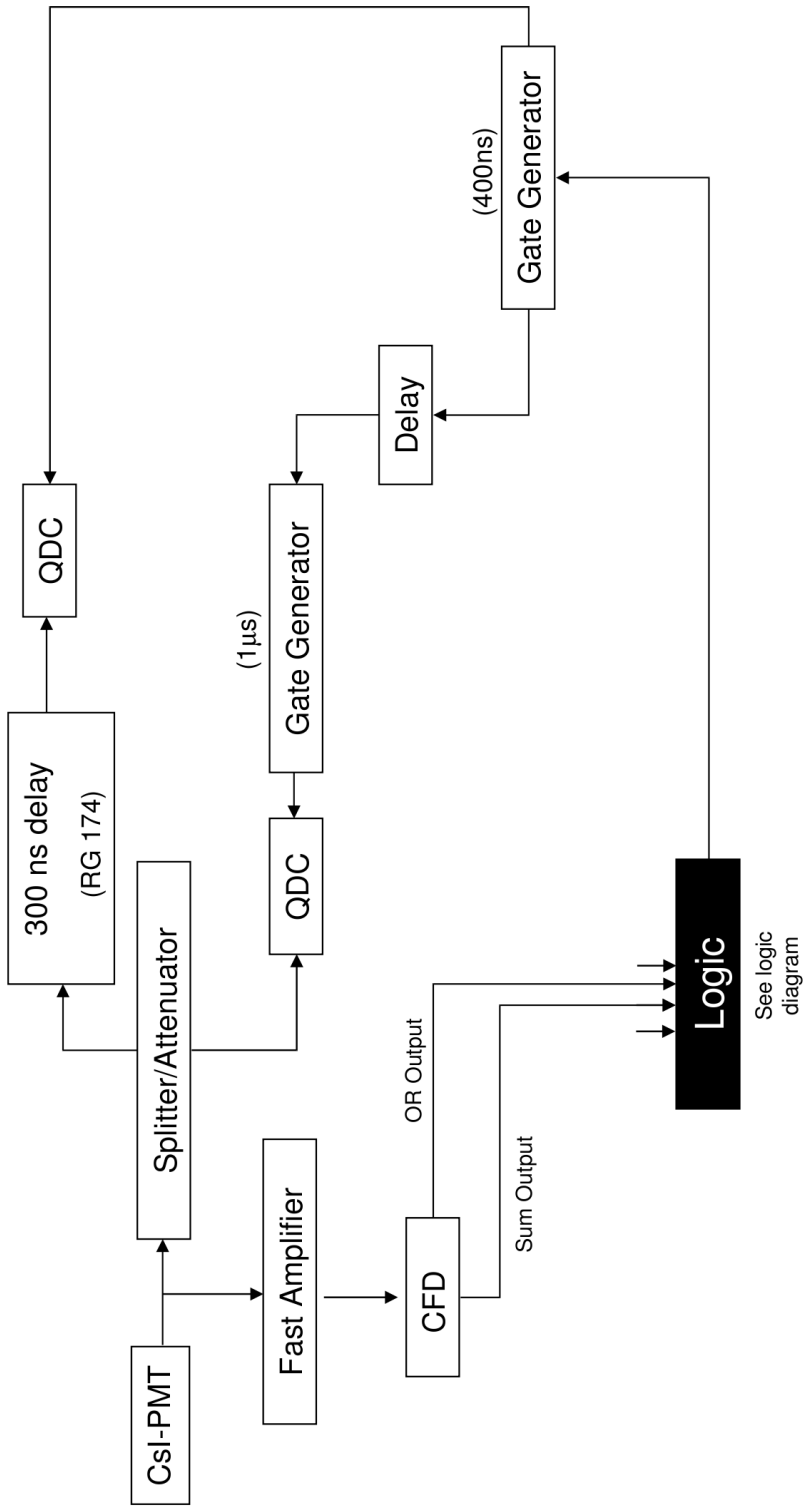

FIG. 11. Electronics diagram for the CsI-PMT signals of rings 2-11.

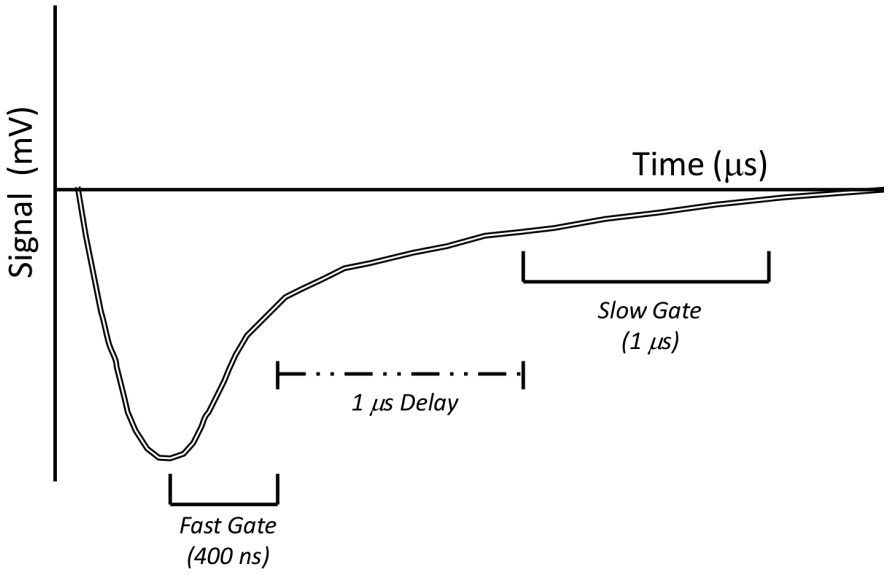

FIG. 12. Illustration of the signal resulting from the CsI-PMT detector. Both the fast and slow signal gates are shown along with the 1μs delay.

PMTs, since the signals were not used for pulse-shape analysis or event triggering. The set-up for the CsI-PD electronics (Figure 13) is identical to that of the ring 12-15 silicon signals. The only differences are the amplification and shaping times for the signals. The photodiodes are connected to Zepto System [113] microcontroller boards with Zepto System pre-amplifiers. Again, the microcontroller board delivers the photodiode bias and +/-12 volts for the pre-amps. The amplified signal was then processed by the modified ISiS shaping amplifiers [108] and digitized using VME ADCs. The digital signal was then recorded by the DAQ software if an event was triggered.

The electronics set-up for the neutron ball were designed such that both a background and an event neutron multiplicity was collected. Therefore, a "true" neutron multiplicity could be recovered from analyzing the event and background multiplicities. As Figure 14 shows, the signal from each PMT on the neutron ball was fed into

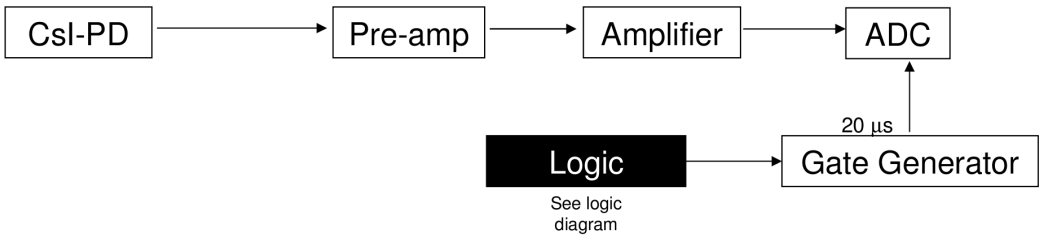

FIG. 13. Electronics diagram for the CsI-PD signals of rings 12-15.

a fast amplifier and then a constant fraction discrimantor, CFD. The CFD thresholds were set such that efficiency of the neutron ball for the emission of neutrons from a ^{252}Cf fission would match the simulated GEANT-3/GCALOR efficiency for the NIMROD-ISiS array of ∼70% [102, 107].

When a NBL PMT signal was above the CFD threshold a logic signal was sent from the CFD to the logic Fan In Fan Out (FI/FO) module. From the FI/FO module, the OR signal was passed to two different overlap modules, which accept any signal that are within the supplied gate. An OR signal is used because it provides 1 logic ouput for each neutron regardless of how may PMTs fire. Therefore, if three PMTs fire at one time a single OR signal will be recorded, representing one neutron. The first overlap module passes the signals, that fall within the 100μs gate, to a scaler. This scaler should provide a count of the number of neutrons that are thermalized and captured in the neutron ball from the reaction. However, the neutron ball has a background signal that needs to be taken into account. Therefore, a second 100μs gate is generated immediately after the initial 100μs gate. As shown in Figure 14, the OR signals from the FI/FO module are also sent to the second overlap module which is receiving the delayed gate. The signals that fall within the delayed gate represent the background signal because 100μs have passed since the triggered event.

It is also important to note that there is an initial 5ns delay of the trigger from the logic module. This 5ns delay ensures that the large gamma flash signal in the neutron ball, which occurs at the time of the reaction, does not overlap with the initial 100μs gate.

In each electronics diagram, Figures 10-14, a common feature shown is the requirement of a trigger signal from the logic module which allows for the detector signals to be recorded. The electronics set-up for the trigger logic module is shown in Figure 15. As previously mentioned, the triggering of events for this experiment came from both the CsI-PMT signals of rings 2-11 and the silicon back-plane signals from rings 2-7. Leading edge discriminators were used to produce SUM and OR outputs for the silicon back-plane signals that were above the threshold. The SUM and OR signals for the CsI-PMTs were produced using CFD modules.

The OR(SUM) signals for the silicon back-plane and CsI were combined using Logic(Linear) FI/FO modules. In the experiment three different event types were collected: minimum bias, high multiplicity, and pulser events. A minimum bias trigger means that all events are accepted regardless of the multiplicity and the distribution of events should represent a triangular impact parameter distribution. For the min bias trigger, the OR signals from the CsI and silicon back-plane were combined in a Logic FI/FO. Logic FI/FO modules are used for the min bias events because no matter how many CsI and silicon detectors fire, a single signal is produced for the event. For the high mult trigger, the Linear FI/FO modules are used to add the SUM signals from the CsI and back-plane silicon detectors. The SUM from the Linear FI/FO module is then passed to a CFD, which has a threshold representing the minimum number of silicon back-plane and CsI signals that must have fired for the event to be considered high mult. For this experiment, the high mult CFD threshold required a SUM signal of three detectors. Lastly, a pulser is used to randomly trigger events. These pulser

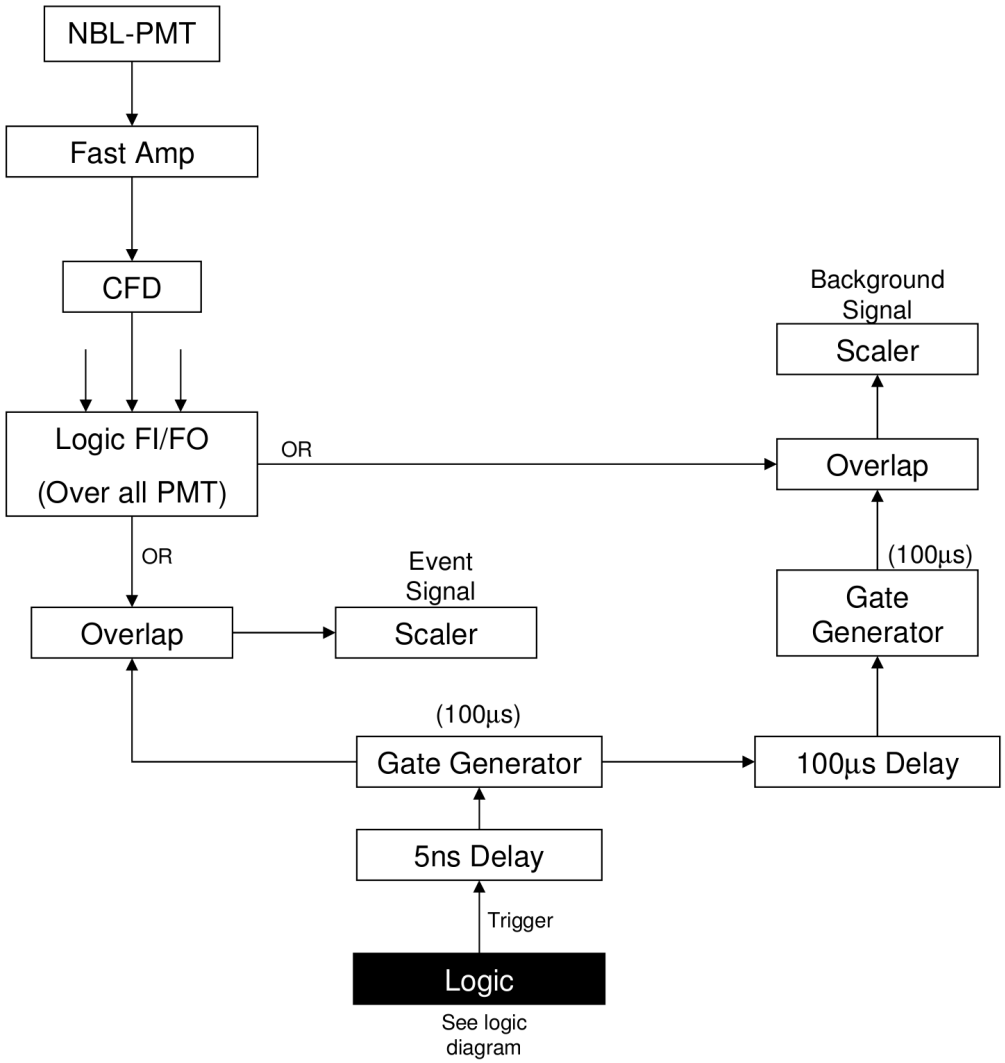

FIG. 14. Electronics diagram for the PMT signals of the Neutron Ball.

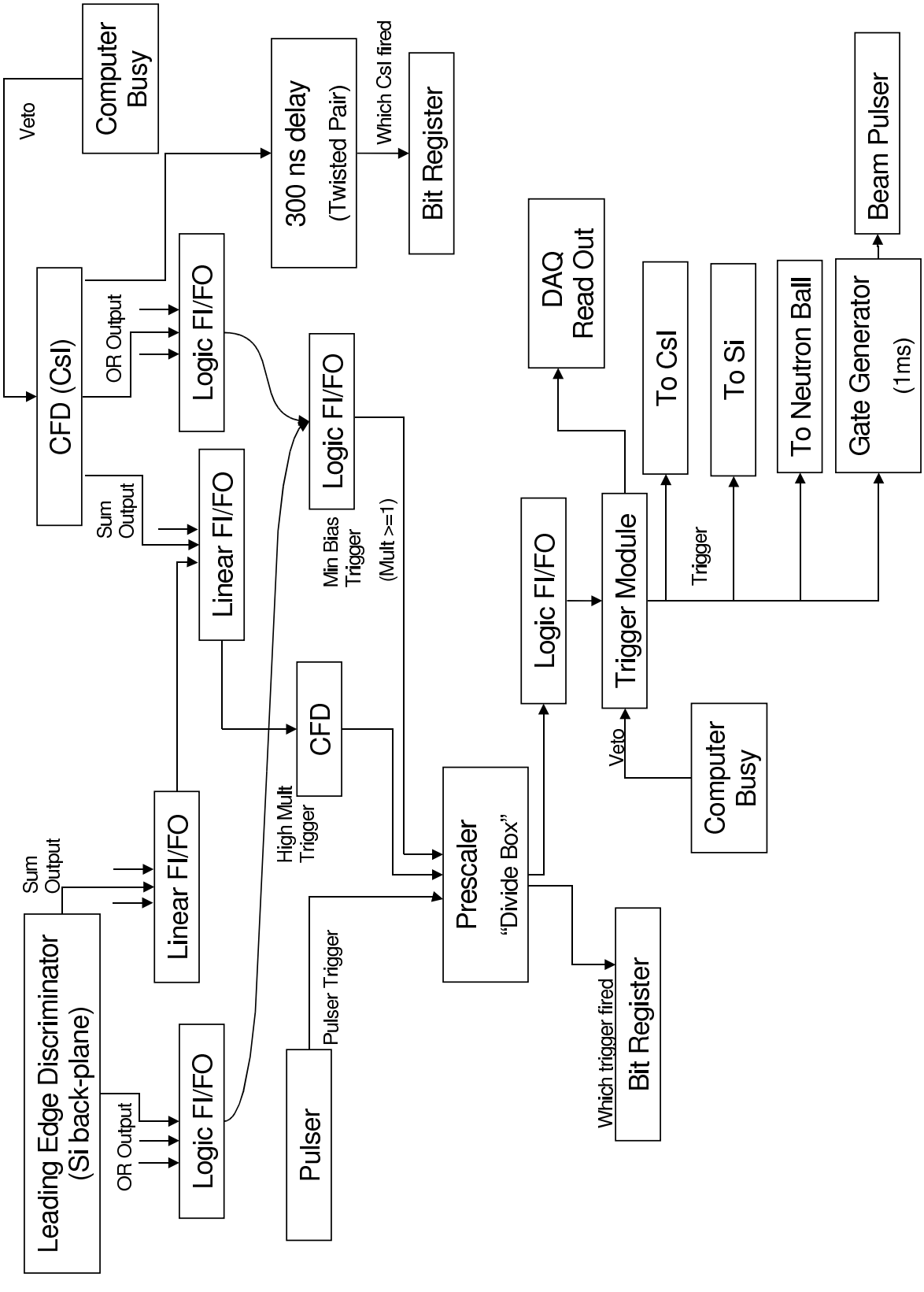

FIG. 15. Electronics diagram for the trigger logic.

triggered events can then be used to examine background noise in the neutron ball since it is not associated with a reaction occurring.

Whenever an event is triggered, no matter the type, the signal is sent into the Prescaler module. This module allows one to downscale specific event types. For example, in this experiment the min bias and pulser events had a downscale of ten. This means that the Prescaler module would only accept one min. bias event for every ten that were delivered to the module. The high mult events did not have a downscale, therefore all the high mult events were passed through the Prescaler. The Prescaler module provides a signal to a bit register and another Logic FI/FO module. The bit register keeps track of what type of event was passed through the Prescaler. The Logic FI/FO module sends a signal to the trigger module which sends a trigger signal out if the DAQ is not busy.

If the computer, or DAQ, is unable to read another event then a veto signal can be sent which blocks the trigger signal from being generated and the CsI CFD from firing. It is important to stop the CsI CFD because it only remains dead for 250ns after firing and therefore, could trigger multiple times on the long CsI signal decay ($\sim 5\mu$s). Thus, events are only triggered when the computer is not busy reading in the data. The dead time for the read out of the DAQ is on the order of 3ms and, as mentioned, the number of events vetoed from the computer was kept around 50% by adjusting the beam current.

The trigger signal prompts the CsI, silicon, and neutron ball electronics, as shown in Figures 10-14, to generate gates for recording the QDC, ADC, and scaler signals. The trigger signal is also sent to the Data Acquisition (DAQ) computer to signal the read out of all the QDCs, ADC, and scaler modules. Lastly, the trigger signal is passed to a gate generator which is used to trigger the beam pulser. Upon receiving the gate signal, the beam pulser stops the beam from the cyclotron in order to minimize

background in the neutron ball. However, even though the beam coming out of the cyclotron is stopped there still remains $\sim$25μs of beam in the beamline between the cyclotron and NIMROD-ISiS array.

C. Particle Identification

The NIMROD-ISiS array offers three forms of particle identification (PID): Si vs. Si, Si vs. CsI, and CsI Fast vs. Slow plots. The placement of each of these detector combinations or modules within the NIMROD-ISiS array has been discussed in Section B. The combination of these different PID methods allows for isotopic resolution of a wide range of particles, from Z=1 to Z=18, and elemental resolution of fragments up to the beam. The PID procedure is accomplished using a linearization method to linearize the 2-D plots and project them onto a 1-D axis. Gaussian functions are fit to each isotope in the 1-D projection, which provides a quantitative method for the isotopic identification.

1. CsI Fast Versus Slow (FastSlow)

As discussed in Section B.3, both a fast and slow component from the CsI(Tl)-PMT signal are collected for pulse-shape discrimination. In general, most scinitllators do not exhibit a two-component decay but rather a single fast component is observed due to interaction with radiation [112]. However, certain inorganic scintillators, such as CsI, have both a fast and slow decaying component [112, 111]. The two different components arise from the excitations of different types of excited states, radiative and metastable, in the CsI crystal. A high ionization density favors the production of radiative states, while a low ionization density produces more metastable states [112]. The ionization density will depend on the dE/dx profile of the radiation [111].

For example, a heavy ion will produce a high ionization density in the CsI crystal, therefore producing a larger fraction of radiative states than metastable states. A proton will travel farther into the crystal and have a lower ionization density producing more metastable states in comparison to the heavy ion. The result is that in comparing the fast component (radiative states) against the slow component (metastable states) different types of radiation or particles can be identified.

It should be noted that the reason for the thallium doping of the cesium-iodide crystal is to add energy levels in the forbidden energy gap of the semiconductor, which provides a path for the excited electron to decay back into the valence band. This modification also causes a shift in the wavelength of the emitted light since the excited electron is moving from a state within the forbidden gap, rather than the conduction band, to the valence level. The light is shifted into a region in which the sensitivity of the PMT response is much larger [111]. The thallium impurities are often referred to as activators.

In Figure 16 the slow component is shown as a function of the fast component of the CsI-PMT signal. The pulse-shape discrimination provides isotopic particle identification for Z=1-3. In the Z=1 band, protons, deuterons, and tritons can be clearly identified. For Z=2, ^{3}He, ^{4}He, ^{6}He, and ^{8}He can be differentiated. However, it is important to realize that the ^{8}He line is a combination of both ^{8}He and 2α double hits, further discussion can be found in Section C.6. As discussed, the Z=1 particles are shown having a large slow component in comparison to the heavier Z=2 and Z=3 fragments. Above Z=3 the differences in the ionization density are not large enough to provide isotopic or elemental resolution.

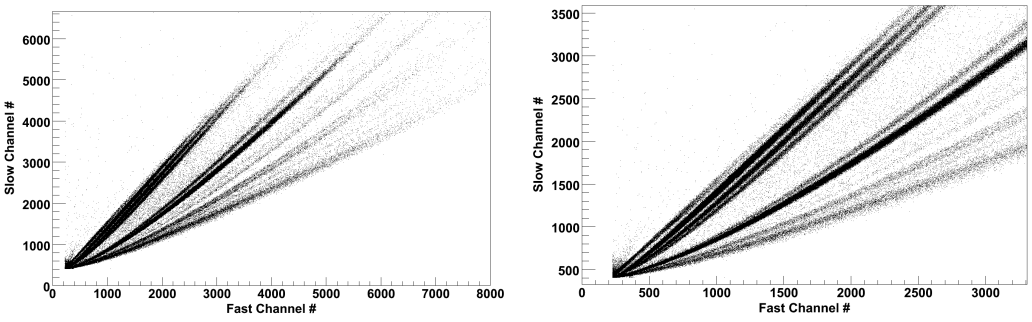

FIG. 16. Full(left) and zoomed-in(right) CsI Fast versus Slow plot.

2. Silicon Versus CsI (SiCsI)

The main method for particle identification of fragments with Z≥3, in the NIMROD-ISiS array, is to plot the energy lost in the silicon detector against the residual energy left in the CsI crystal. As discussed in Section B, the entire charged particle array is outfitted with Si-CsI modules in order to maximize the detection of heavy fragments. In rings 2-7 there are two opportunities for isotopic identification through Si-CsI plots because of the back-plane and front-plane signals from the silicon. In Figure 17 both the front-plane and back-plane signals are plotted against the CsI signal. The main advantage of using the back-plane is that the shaper/amplifier gain on the signal can be set very low. Therefore, high elemental identification can be achieved. The back-plane vs. CsI plot in Figure 17 shows the beam spot from the Z=30 projectiles. Meanwhile, the gain on the front-plane of the silicon can be kept at a higher value, allowing for better isotopic resolution to be achieved. For example, in the front-plane vs. CsI plot of Figure 17 isotopic resolution is visible up to Z=17.

The energy loss, dE/dx, of charged particles through a material, such as silicon, can be described by

$$-\frac{dE}{dx} \propto \frac{Z^2}{\nu^2} \propto \frac{Z^2 \cdot A}{KE} \tag{2.1}$$

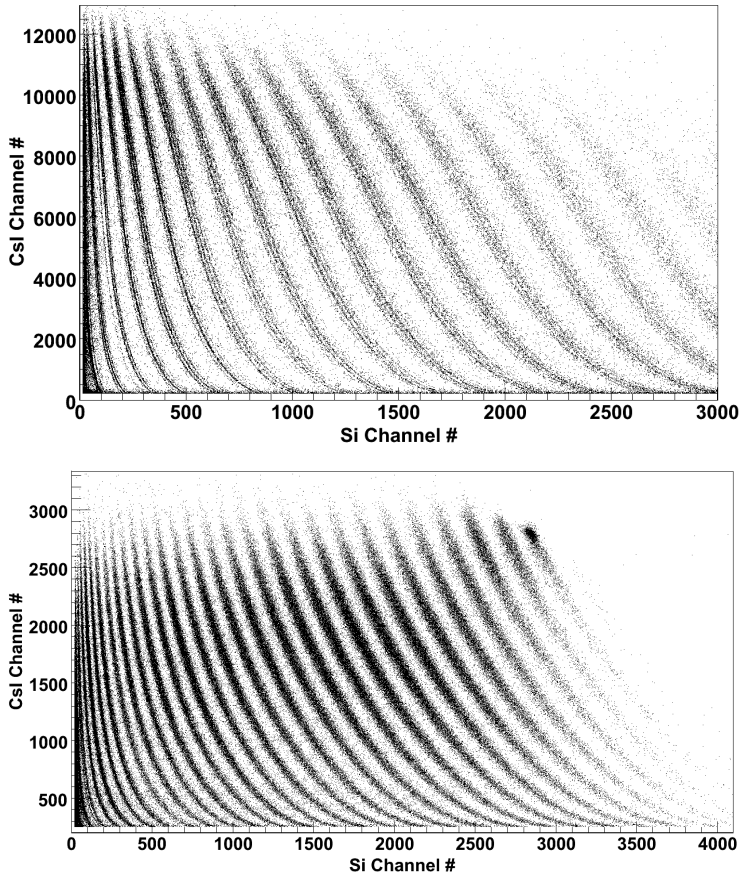

FIG. 17. Silicon front-plane signal versus CsI signal, top, and silicon back-plane signal versus CsI signal, bottom.

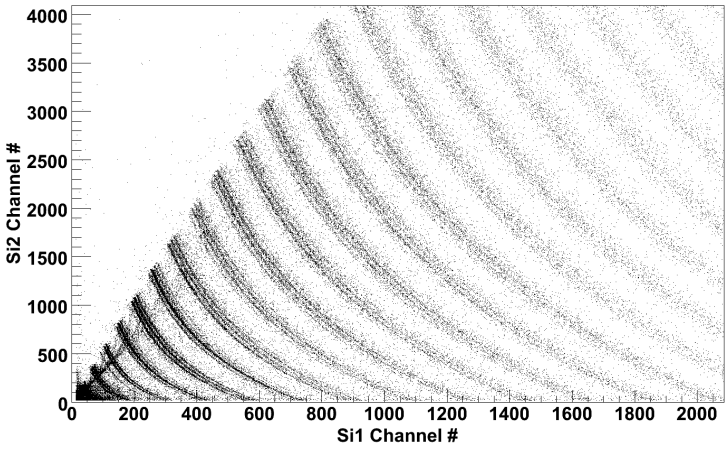

FIG. 18. Silicon-1(150μm) versus Silicon-2(500μm) signals.

where KE is the kinetic energy of the particle with a charge Z and mass A [111]. Equation 2.1 is a simplified form of the *Bethe-Bloch formula* [112]. It is clear that the energy loss in the silicon detector will depend strongly on both the Z and A of the charged particle. Therefore, both elemental and isotopic separation can be achieved in the Si-CsI, or ΔE-E, plots.

3. Silicon Versus Silicon (SiSi)

The super-telescopes in the NIMROD-ISiS array offer particle identification through both the Si-Si and Si-CsI plots. The Si-Si detector consists of a 150μm silicon placed in front of a 500μm silicon. The particle identification is accomplished by plotting silicon-1 (150μm) signal against the silicon-2 (500μm) signal, as shown in Figure 18. The super-telescope configuration is advantageous because it offers a lower threshold, due to the 150μm silicon, and generally provides better isotopic identification due to the increased resolution of using silicon for both the ΔE and E detectors.

4. Linearization Method

A linearization method was implemented to convert the 2-D plots, shown in Figures 16-18, into 1-D projections of the data. The 1-D projections of the data were then used to define the Z and A of each particle (refer to Section C.5). The first step of the linearization procedure was to hand-pick lines that followed the curvature and form of each elemental line. A spline fit was used to generate 100 evenly spaced points, shown as the blue circles in Figure 19a, from the user picked points. Using the spline fit points, the experimental data was linearized producing the 2-D plot shown in Figure 19b.

The linearization procedure consists of calculating the relative distance between the two closest lines for each experimental data point. For example, if an experimental point was exactly half the distance in between the Z=3 and Z=4 lines then it would be assigned a linearization value, LinZ, of 3.5. The linearization values were calculated using Equations 2.2-2.4, where Line1(Line2) is the Z of the line and dist1(dist2) is the distance of the data point to the respective line. Equation 2.2 is used if the data points are to the left of the first line, Equation 2.3 is for data points that are in between two lines, and Equation 2.4 is for data points that are to the right of the last line.

$$LinZ = \frac{dist2}{|dist2 - dist1|} Line1 - \frac{dist1}{|dist2 - dist1|} Line2 \tag{2.2}$$

$$LinZ = \frac{dist1}{|dist1 + dist2|} Line2 + \frac{dist2}{|dist1 + dist2|} Line1 \tag{2.3}$$

$$LinZ = \frac{dist1}{|dist1 - dist2|} Line2 - \frac{dist2}{|dist1 - dist2|} Line1 \tag{2.4}$$

In order to calculate the distance from the data point to the nearest lines, the 100 spline fit points were treated as 99 line segments. Then, the distance from the data

point to each line segment was determined and the minimum distance was used in Equations 2.2-2.3. After calculating the linearization value, LinZ, for each data point, a 2-D linearization plot was produced, as shown in Figure 19b, where the y-axis from the original 2-D plot, Figure 19a, is plotted against the linearization value (LinZ) of the experimental data. For additional information on the linearization procedure please refer to Refs. [115, 116].

Limits were set on the 2-D linearized plot, Figure 19b, before the data was projected onto the x-axis producing Figure 19c. The limits served the purpose of both defining the atomic number (Z) and removing any noise for each elemental band of data. In Figure 19b the blue and green vertical lines represent the left and right limits, respectively, for a given element. The horizontal red lines show the threshold value chosen such that the noise was removed from the accepted data. The 1-D projection of data, shown in Figure 19c, consists of all the data points that where within the limits placed on the 2-D linearization. For each element in the 1-D projection the different isotope peaks can be clearly identified. This now provides the opportunity to correlate each of these peaks with the correct isotopic identification. The process of defining the Z and A of each peak is described in in the following (Section C.5).

5. Gaussian Fitting for PID

The 1-D linearized projections of the experimental data, produced using the linearization method, were fit with Gaussian functions in order to define the Z and A of each peak. Examples of the fitted 1-D projections for a linearized CsI Fast-Slow and Si-CsI plot are shown in Figures 20 and 21, respectively. As shown, each Gaussian represents one isotope of a given element. The Gaussian function was defined as

$$G(x) = C \cdot e^{-0.5 \cdot \left(\frac{x-\mu}{\sigma}\right)^2} \tag{2.5}$$

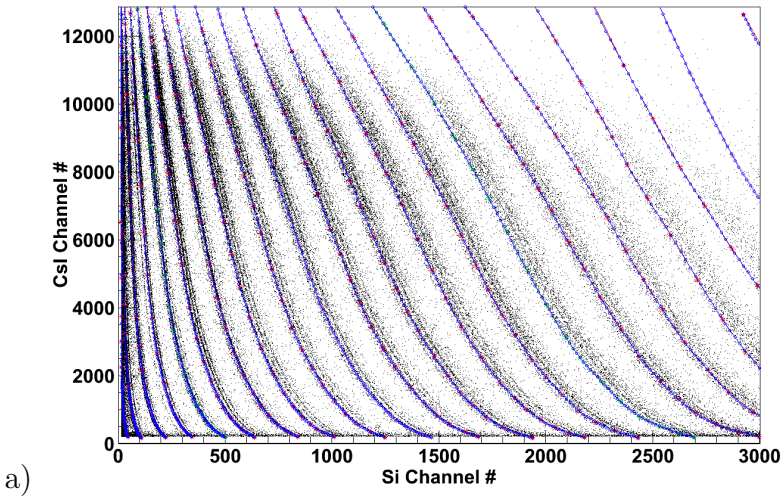

a)

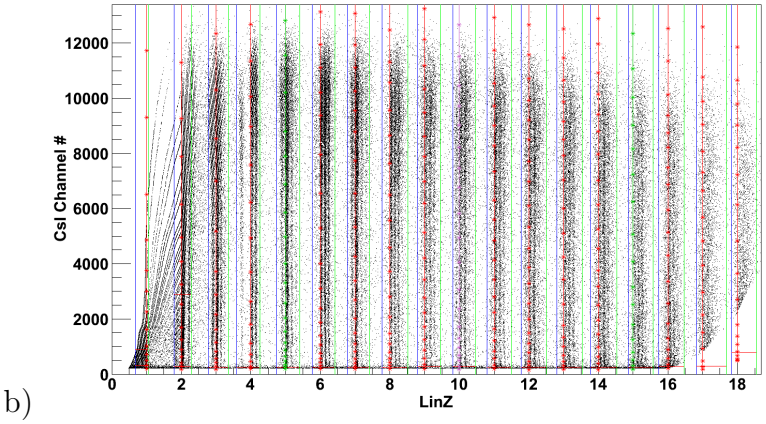

b)

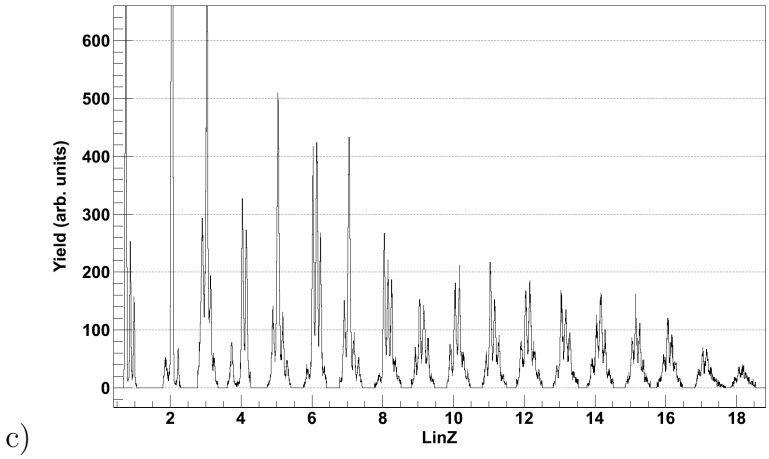

c)

FIG. 19. The linearization process is presented showing a 2-D Si-CsI plot (Panel a), the linearized 2-D plot (Panel b), and the 1-D projection (Panel c) of the linearization.

where C is the height, μ is the center, and σ defines the width of the Gaussian. The parameters for each individual Gaussian were determined by minimizing the total error between the sum of the Gaussians and the experimental data for each element. One of the main advantages of fitting the 1-D projections with Gaussian functions, rather than setting hard limits to define each isotope, is that the amount of contamination in the identified particles can be calculated. The percent contamination for the LinZ value calculated for each particle was defined as

$$\%Contam = \frac{\left(\sum_{i=0}^{N_{Gauss}} G_i(LinZ)\right) - G_{Max}(LinZ)}{G_{Max}(LinZ)} \tag{2.6}$$

with N_{Gauss} equaling the number of Gaussian functions for the given element, G_i(LinZ) representing the value of the i^{th} Gaussian at the point LinZ, and G_{max}(LinZ) representing the maximum G_i(LinZ) for all the Gaussians. The Gaussian that provided the maximum value, G_{max}(LinZ), was used to define the A for the particle. At this point, the Z and A for each particle has been determined. Along with the percent contamination, the fraction of sigma was also calculated for each particle as

$$FracSigma = \frac{|LinZ - \mu|}{\sigma} \tag{2.7}$$

where μ and σ are Gaussian parameters from Equation 2.5 for G_{max}(LinZ). The fraction of sigma provides a measure of how far away the data point is away from the center of the Gaussian. Combined, the percent contamination and fraction of sigma can provide a measure of accuracy for the isotopic determination of each particle. The procedure and requirements for accepting the isotopic identification of a particle are discussed in Section C.6.

The A of each Gaussian was assigned, for the lighter fragments, by comparing the observed experimental yields for the different peaks to the natural abundances for the

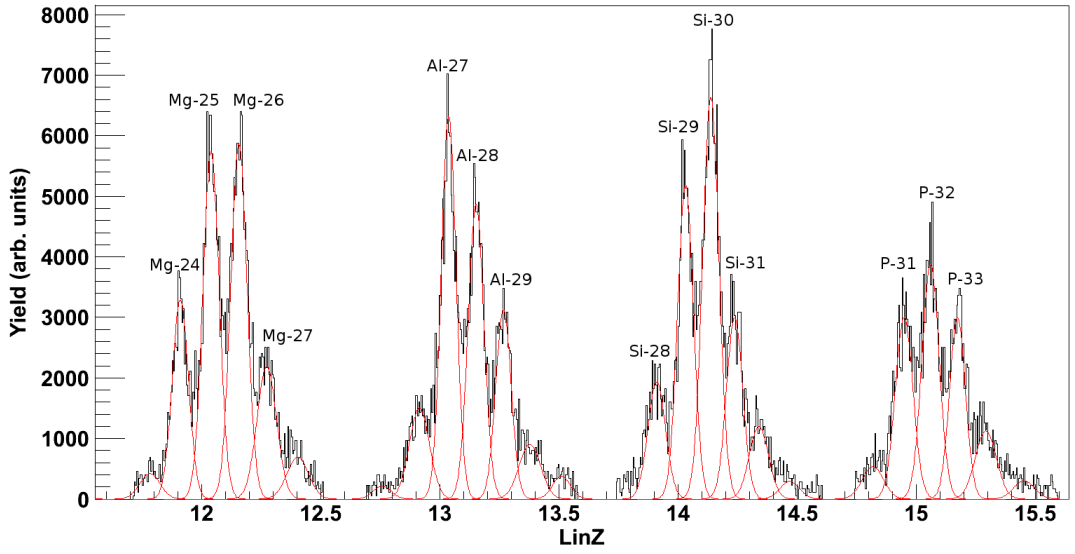

FIG. 20. 1-D projection of Si-CsI plot showing the Gaussian fits to the Z=12-15 isotopes.

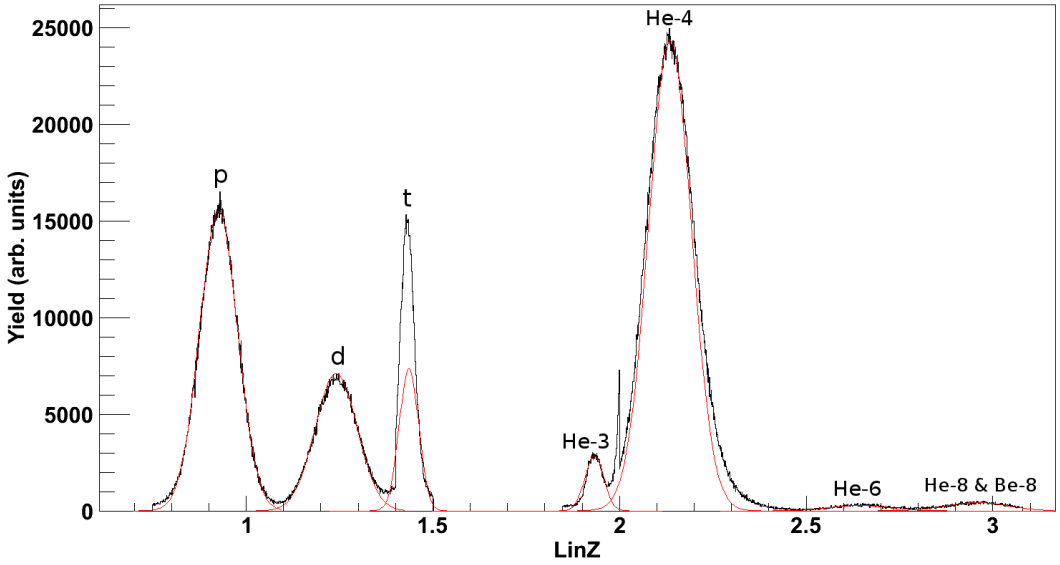

FIG. 21. 1-D projection of CsI Fast-Slow plot showing the Gaussian fits to the Z=1 (proton, deuteron, and triton) and Z=2 isotopes. The He-8 peak includes both He-8 production and the 2 alpha break-up of Be-8.

given element. In most cases one or two isotopes had significantly large yields, such as ^{12}C and ^{13}C, that would allow for trivial identification of the other peaks, or isotopes. For the higher Z elements, the Gaussians were assigned by comparing the yields of the peaks to the yields from experimental data collected using MARS [117], as well as a previous NIMROD-ISiS experiment[118]. In the cases where isotopic identification was not achieved a single Gaussian function was fit over each element and the particles were assigned an A=0. These particles would later receive a "GuessA" which was taken as the most probable A inferred from the detectors with good isotopic resolution or the yields from the MARS data [117].

This process of determining the Z and A of the particle was carried out for each type of detector in the NIMROD-ISiS array. Therefore, a particle could potentially have a Z and A assigned from the CsI Fast-Slow, SiFront-CsI, SiBack-CsI, and/or Si-Si plot. The process of determining the correct Z and A identification is discussed in the following (Section C.6).

6. Finalizing PID

After the linearization process and Gaussian fitting was completed, the last step of the particle identification was to check for cases in which the particle was incorrectly identified. This is important because the NIMROD-ISiS array, as mentioned, allows for a single particle to be identified in multiple types of detectors. The first cut placed on the experimental data required that the FracSigma value for any good identification be less than 3.0. This removes particles at the edges of each elemental distribution that are near the level of the noise. The 3.0 FragSigma cut removed $\sim$0.2% of the total number of particles.

Since each particle can possibly recieve multiple Z and A identifications, a labeling system was used in describing the origin of the idenfiticaiton and is presented in

TABLE V. Particle identification labels and descriptions.

Label	Description
CsIZ	Z identification obtained from CsI Fast vs. Slow
CsIA	A identification obtained from CsI Fast vs. Slow
SiFrontZ	Z identification obtained from front-plane silicon vs. CsI
SiFrontA	A identification obtained from front-plane silicon vs. CsI
SiBackZ	Z identification obtained from back-plane silicon vs. CsI
SiBackA	A identification obtained from back-plane silicon vs. CsI
SiCsIZ	Z identification obtained from either front- or back-plane vs. CsI
SiCsIA	A identification obtained from either front- or back-plane vs. CsI
SiSiZ	Z identification obtained from super-telescope (Si1 vs. Si2)
SiSiA	A identification obtained from super-telescope (Si1 vs. Si2)

Table V.. These labels are used in the flow charts shown below depicting the PID procedures used in this work. Also, it is appropriate to remind the reader that in the super-telescope modules particle identification is available through both Si-CsI and Si-Si linearizations. Therefore, the following general discussion about the Si-CsI PID also pertians to the Si2 silicon from the supertelescope modules, since this is used for Si-CsI identification.

The flow chart shown in Figure 22 illustrates the process for checking the particle identification. The process starts in the green box, asking if the particle received a Z identification from the CsI Fast-Slow (CsIZ) linearization. Only Z=1-3 particles were identified in the CsI Fast-Slow. If the particle was identified in the CsI then the Z identification in the front-plane silicon vs. CsI (SiFrontZ) linearization was checked. If the particle was identified in the front-plane vs. CsI linearization, then the

SiFrontZ and CsIZ were compared. If the SiFrontZ=CsIZ the particle was accepted. If the SiFrontZ was not equal to CsIZ, then the particle was checked for having been assigned CsIZ=2 and CsIA=8. If the particle was assigned a CsIZ=2 and CsIA=8, it was accepted despite CsIZ≠SiFrontZ because it likely represents a double alpha hit, possibly the break-up of ^{8}Be. Therefore, special attention was paid to seperate 2α and ^{8}He detection, which is discussed in further detail below. Similarly, particles that received a CsIZ=1 and a SiFrontZ=2 were accepted because they likely represent a double proton hit. Particles that had a different SiFrontZ and CsIZ, and were not associated with the 2α or 2p hit, were cut from the data. The particles removed due to this cut represented about ∼0.8% of the total particles, as shown in the middle red box of Figure 22.

Particles that did not receive a SiFrontZ, but were identified in the CsI, were then checked for identification from the back-plane silicon vs. CsI linearization (SiBackZ), as shown in the right portion of Figure 22. If the particle received neither a SiFrontZ or a SiBackZ, it was accepted with only identification in the CsI. If the particle did have both a valid CsIZ and SiBackZ then the same process discussed above, and shown in Figure 22, was completed for comparing the CsIZ and SiBackZ particle identifications. Again, particles that were likely originating from a 2α or 2p hit on a detector were kept. If the SiBackZ and CsIZ were different the particle was cut which removed ∼0.5% of the total particles.

If the particle was not identified in the CsI (all particles with Z>3) then the SiFrontZ and SiBackZ identification were examined, as shown on the left portion of the flow chart of Figure 22. If the particle was only identified in the silicon front- or back-plane linearizations then it was accepted. If the particle was identified in both the front- and back-plane then the SiFrontZ and SiBackZ were compared. If the SiFrontZ and SiBackZ were not equal then the particle was cut, which accounted for

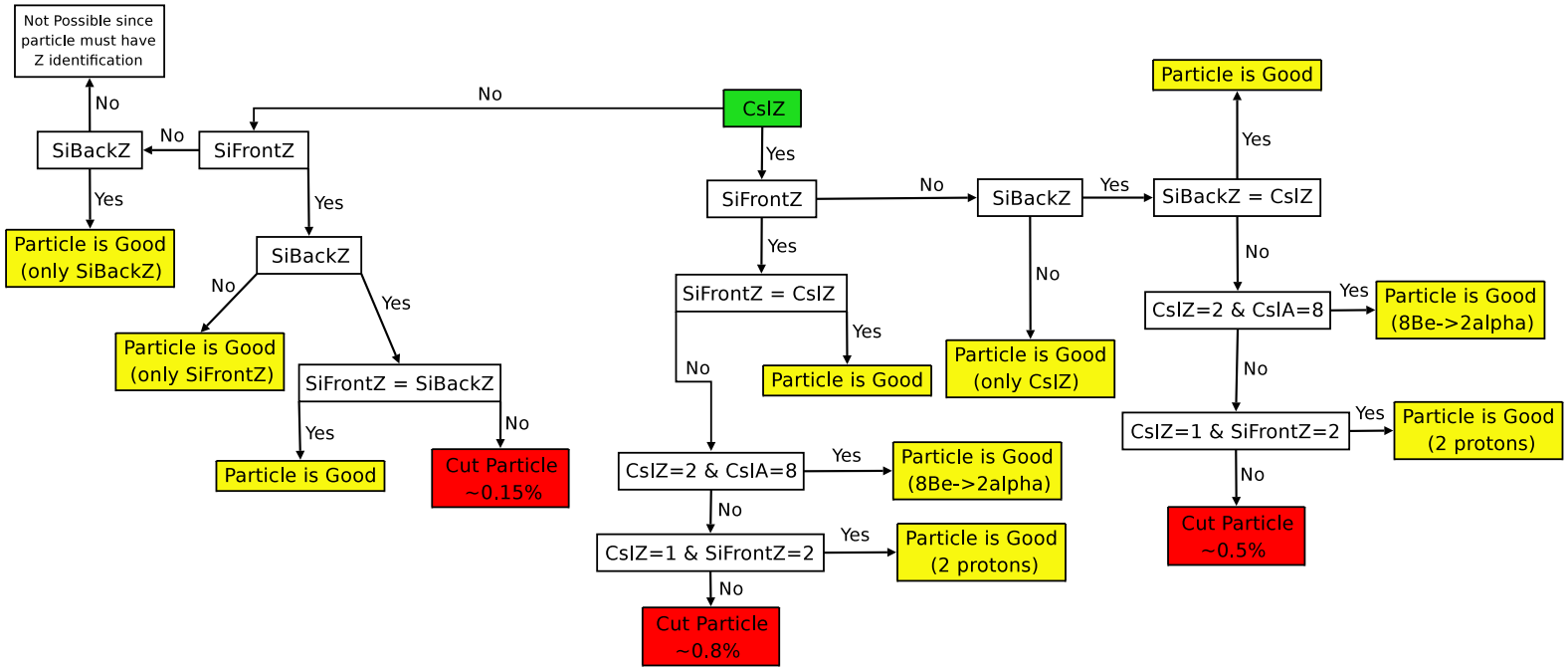

FIG. 22. Flow chart depicting the process for checking and comparing the particle identifications in different detector types.

$\sim$0.15% of the total particles. If the SiFrontZ was equal to the SiBackZ the particle was kept.

As mentioned above, the 2α and 2p double hit was accepted despite having differing SiFrontZ and CsIZ identification. The reason that the double hits cause different SiFrontZ and CsIZ is due to the Fast-Slow signal produced in the CsI. With a double alpha hit, the SiFrontZ will be larger than Z=2 since a total charge of Z=4 is passing through the silicon. Similarly, a 2p hit will have a total charge of Z=2 passing through the silicon. However, even though the total charge is Z=4 or Z=2 for the double hits, it has been shown in Ref. [107] that in a CsI Fast-Slow plot the double hit will be identified as a Z=2 or Z=1, respectively. The 2α hit will, specifically, be identified in the ^{8}He band. Therefore, any particles that were identified as CsIZ=2 and CsIA=8 needed to defined as either a ^{8}He or 2α. This was accomplished by comparing the SiCsI linearization value (LinZ) for the particle, even if it was not identified in the SiCsI, with the Z=2 and Z=3 limits. If the SiCsI linearization value was near or beyond the Z=3 limits then it was a 2α hit and if it was near or in the Z=2 limits then it represented a ^{8}He. In the case of the 2α hit, the particle was assigned a Z=4 and GuessA=8. As discussed, if the isotope identification is not determined the particle is assigned a GuessA. Therefore, the 2α is given a GuessA=8 because it was not actually a ^{8}Be reaching the detector but rather a double alpha signal, which is likely due to the break-up of ^{8}Be but could also simply be two correlated alpha particles. Similarly, in the detection of a 2p hit, the particle was assigned a Z=2 and GuessA=2 depicting a double proton hit.

After examining the identification of each particle individually, as shown in Figure 22, it was compared to every other particle in the event. This allowed for determining if two particles were identified in a single detector module. Specifically, this could occur in detector modules in which a single silicon detector is placed in front

of two or three CsI or where two silicon detectors are in front a single CsI. Figure 23 shows a flow chart illustrating the process of comparing the particle of interest (PoI) against the other particles (Pj) of the event for the case of 1 silicon in front of 2 or 3 CsI. As shown, the SiCsI identification (SiCsIZ) is checked for both particles. If either particle was not identified in the SiCsI plot then the PoI is accepted. If both particles were identified in the SiCsI, then the silicon detector numbers (SiId) of both particles are compared. Again, if the detector numbers are different the PoI is accepted. If the detector numbers are the same then that means that the SiCsIZ identification for both particles should not be trusted since two particles went through the same silicon. However, if the particle was identified independently in the CsI then the CsI identification is accepted since that is unaffected by two particles passing through the silicon detector. The process depicted in Figure 23 applies for both the front- and back-plane of any silicon detector that is in front of 2 or 3 CsI crystals. It was found that 0.08% and 0.1% of the total particles were cut due to double hits on the SiFront and SiBack silicon detectors, respectively.

Figure 24 shows the flow chart for testing if two particles were identified in a module with two silicons placed in front of a single CsI. This case only occurs in supertelescopes where the two segmented front-plane silicon pads are placed in front of 1 CsI. Therefore, the first step of the flow chart was to check if the PoI and Pj were identified in a supertelescope module. If both particles did hit a supertelescope module, then the number of CsI behind the supertelescope of the PoI was examined. If 2 CsI were behind the 2 silicon detectors then PoI was accepted since the CsI did not have a double hit. Next, the SiSiZ of both the PoI and Pj were checked. If either the PoI or Pj were identified in the Si1 vs. Si2 linearization then there was not a double hit in the CsI. Lastly, if neither particle had a SiSiZ identification, the silicon detector numbers were tested to determine if the particles hit adjacent silicons, which

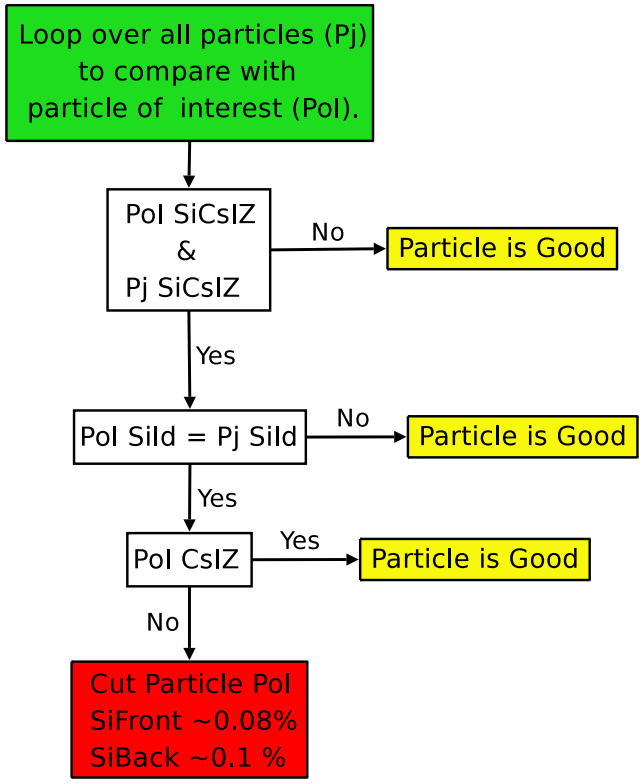

FIG. 23. Flow chart depicting the process in which particles were compared in order to make sure that two particles were not identified in a detector module in which one silicon detector was placed in front of 2 CsI.

would have a single CsI. If both the PoI and Pj were identified in the adjacent silicon detectors then the CsI had a double hit of two particles with each particle passing through separate silicon detectors. This type of identification was relatively rare, only removing 0.025% of the total particles.

After verifying that the identification of each particle was accurate, following the flow charts of Figures 22-23, the final Z, A, GuessA, %Contam, and FracSigma was determined and kept in the final Physics Tapes (see Section E). The final Z and A of each particle was determined by comparing the different %Contam calculated from the different linearizations (CsI, SiBackCsI, SiFrontCsI,and SiSi). The identification with the lowest %Contam was accepted. If isotopic identification for a given element was not achieved, the particles were given A=0 and assigned a GuessA. Even if a particle was given A identification, the mass was only used in the analysis if the %Contam<20% and the FracSigma<2.5.

D. Energy Calibration

Along with the collection of the experimental data, calibration beams (Table II) were used to scatter particles at pre-determined energies into the detectors of the NIMROD-ISiS array producing calibration points. The calibration particles from the different reactions are presented in Table VI. A two-body kinematics code [119] was used to calculate the scattering energy of each particle into the different rings of the array. The results are presented only for rings 2-11 since the backward angle scattering did not have a large enough cross-section for producing calibration points.

As shown in Table VI, some calibration beams were collided on both ^{nat}Th and ^{28}Si targets. The ^{nat}Th was chosen because it has a large charge (Z=90) and therefore would maximize the cross-section for scattering particles in the higher angle rings.

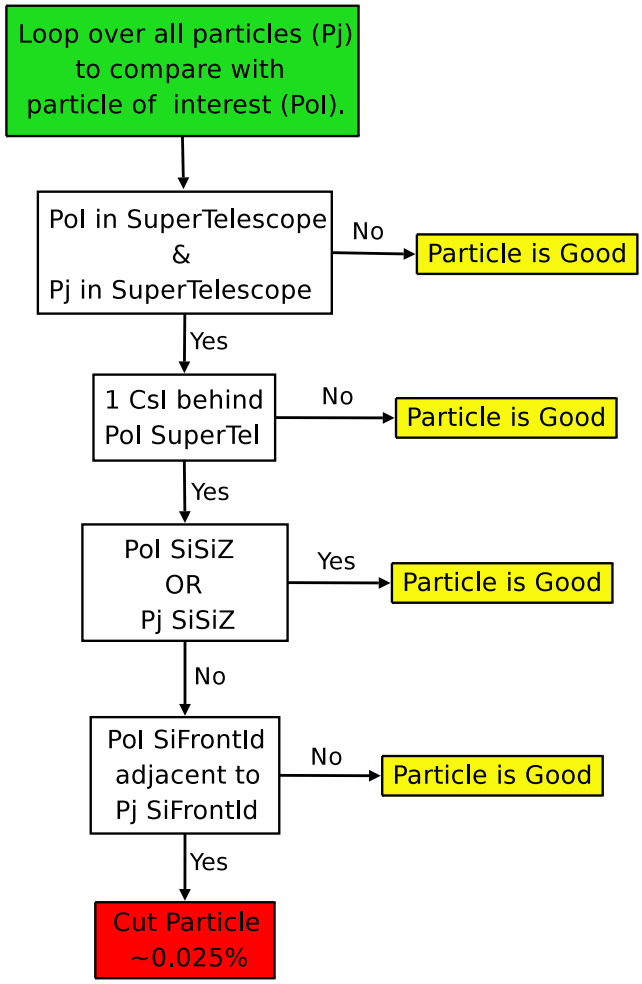

FIG. 24. Flow chart depicting the process in which particles were compared in order to make sure that two particles were not identified in a supertelescope in which two silicon detectors were placed in front of 1 CsI.

The ^{28}Si target was used to try and identify different excited state scatterings of the particles in order to produce multiple calibration points for the CsI [120, 121]. However, the CsI resolution did not allow for the ground state and excited state scatterings to be separated. Therefore, the energies shown in Table VI with the ^{28}Si target are calculated as the average of the ground state and 1^{st} excited state scattering energy. These calibration points, a ^{228}Th source, and the punch-through points on the silicon detectors were used to calibrate the NIMROD-ISiS array.

The silicon detectors were calibrated using the punch-through points and ^{228}Th source. In the forward rings the gains were set relatively low and the ^{228}Th source peaks were not visible. Therefore, the forward ring silicon detectors were calibrated using the punch-through points and the calibration was checked against the 500 MeV ^{20}Ne calibration beam. The punch-through point is defined as the point on the 2-D Si-CsI or Si-Si plot that represents the energy at which a given isotope can pass through the silicon detector. For the Si-CsI plots, the punch-through energy is taken as the lowest silicon signal that is accompanied with a valid CsI signal, thus representing the particle having just enough energy to reach the CsI. In the case of the Si-Si plots two punch-through points can be observed. One point represents the energy at which the isotope is able to pass through the 150μm silicon and the other representing the punch-through of the 500μm silicon. The Si-Si plots, as shown in Figure 18, provide clear punch-through points for the 500μm silicons, in comparison to the Si-CsI plots where the punch-through points can be obscured due to detector noise. After picking the punch through points, the energy needed for a given isotope to punch-through the silicon was calculated using an energy loss table [122]. The silicon detectors in rings 10-15 had gains set such that the ^{228}Th source, which provides 8 peaks on the energy spectra due to the alpha-chain decay, was visible and could be used in addition to the punch-through points for the calibration.

TABLE VI. The calibration particles and scatter energies produced in rings 2-11 of the NIMROD-ISiS array from the different calibration reaction systems.

Reaction	55 MeV/u $^{1}H_2$+^{nat}Th	55 MeV/u $^{1}H_2$+^{28}Si	25 MeV/u ^{20}Ne+^{nat}Th	25 MeV/u α+^{nat}Th	30 MeV/u ^{1}H-^{2}D+^{nat}Th		30 MeV/u ^{1}H-^{2}D+^{28}Si	
Calibration Particles	55 MeV proton	55 MeV proton	500 MeV ^{20}Ne	100 MeV alpha	30MeV proton	60MeV deuteron	30MeV proton	60MeV deuteron
Ring 2	55.0 MeV	54.1 MeV	499.7 MeV	99.5 MeV	30.0 MeV	60.0 MeV	29.1 MeV	59.1 MeV
Ring 3	55.0 MeV	54.1 MeV	499.5 MeV	99.5 MeV	30.0 MeV	60.0 MeV	29.1 MeV	59.1 MeV
Ring 4	55.0 MeV	54.1 MeV	498.7 MeV	99.4 MeV	30.0 MeV	60.0 MeV	29.1 MeV	59 MeV
Ring 5	55.0 MeV	54.0 MeV	497.7 MeV	99.4 MeV	30.0 MeV	60.0 MeV	29.1 MeV	58.9 MeV
Ring 6	55.0 MeV	53.9 MeV	495.7 MeV	99.3 MeV	30.0 MeV	60.0 MeV	29 MeV	58.7 MeV
Ring 7	54.9 MeV	53.7 MeV	492.5 MeV	99.2 MeV	30.0 MeV	59.9 MeV	28.9 MeV	58.4 MeV
Ring 8	54.9 MeV	53.5 MeV	487.0 MeV	99 MeV	30.0 MeV	59.8 MeV	28.8 MeV	57.8 MeV
Ring 9	54.9 MeV	53.2 MeV	480.0 MeV	98.7 MeV	30.0 MeV	59.7 MeV	28.6 MeV	57.1 MeV
Ring 10	54.7 MeV	51.7 MeV	457.0 MeV	97.7 MeV	29.9 MeV	59.5 MeV	28.0 MeV	54.8 MeV
Ring 11	54.6 MeV	50.9 MeV	435.0 MeV	96.8 MeV	29.8 MeV	59.2 MeV	27.4 MeV	52.6 MeV

The calibration between the particle energy and silicon signal was assumed to have a linear relationship [112]

$$Energy = SiChannel \cdot m + b \tag{2.8}$$

where m and b represent the slope and intercept, respectively, of the calibration. Figure 25 shows a silicon calibration where the blue circles represent the punch-through points determined from a Si-Si plot. The punch-through points are fit to Equation 2.8, therefore producing the energy calibration. The green squares in Figure 25 represent the 100 MeV α and 500 MeV ^{20}Ne calibration beams. The results show that the punch-through point calibration is in excellent agreement with the calibration points. The back-plane of the silicon detectors were calibrated from the calibration of the front-plane, since each particle would have produced a signal in both planes of the detector. Figure 26 shows the calibration in the red dashed line, which was fit to a plot of the energy calculated from the front-plane versus the back-plane channel number (open circles). The results again show a linear dependence between the energy and silicon signal.

The energy calibration of the CsI-PMT signal was determined from the calibration points and comparison with previously calibrated energy spectra for a ^{64}Zn+^{58}Ni reaction system at 35 MeV/u taken on the NIMROD array [107]. The energy calibration was completed using the CsI-PMT slow signal because the fast signal became saturated at high energies for a variety of detectors. Unlike the silicon calibration, the relationship between the particle energy and CsI signal is non-linear and depends on the charge and mass of the particle. The relationship between the light output, or CsI signal, and particle energy was taken from Ref. [123], which is based on the Birks formula [111, 112]. The 3 parameter equation relating the light output, h, from the

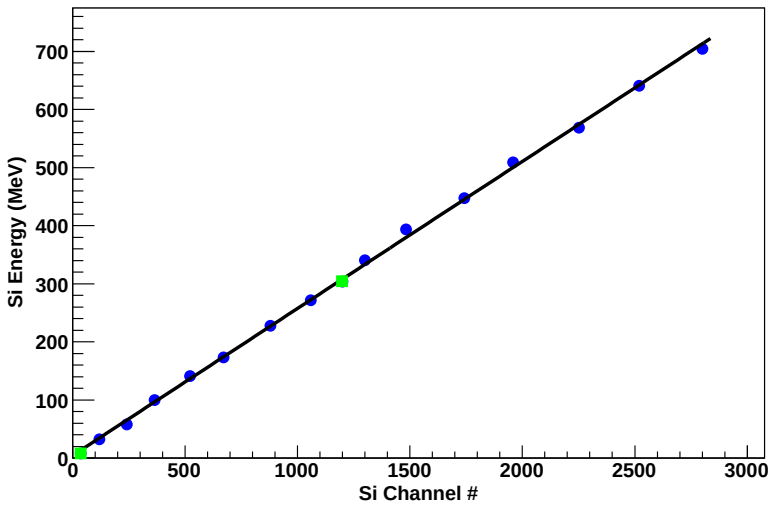

FIG. 25. Example of a silicon calibration. The silicon energy from the punch-through points is plotted as a function of the silicon signal channel number (blue circles). The fitted energy calibration, Equation 2.8, is shown as the black line. The calibration points from the 100 MeV α and 500 MeV ^{20}Ne beams are shown as the green squares.

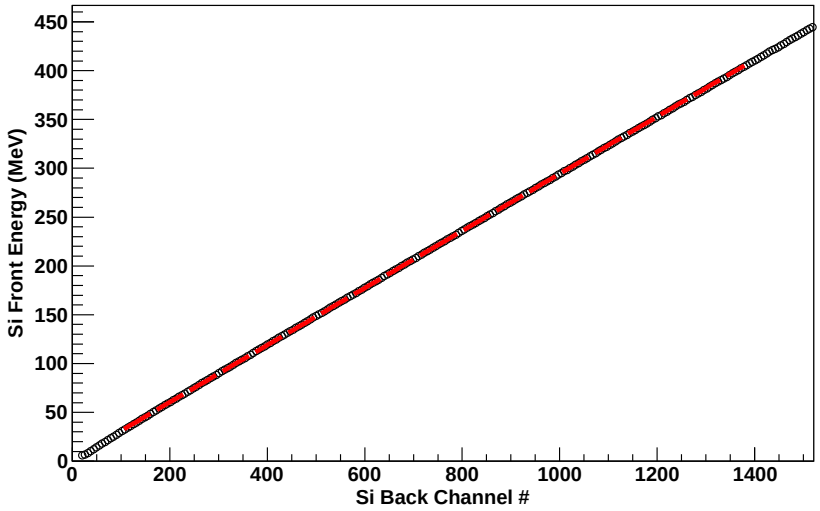

FIG. 26. The energy determined from the front-plane silicon calibration is shown as a function of the silicon back-plane channel number (open circles). The calibration was determined by fitting Equation 2.8 (red dashed line) to the data.

CsI and energy, E, of the particle is

$$E = \sqrt{h^2 + 2\rho h\left(1 + ln\left(1 + \frac{h}{\rho}\right)\right)} \tag{2.9}$$

$$\rho = \eta Z^2 A \tag{2.10}$$

$$h = \frac{chan - ped}{scal} \tag{2.11}$$

where *chan* is the CsI-PMT slow signal channel number, *ped* represents the size of the pedestal for the detector, η and *scal* are fitting parameters, Z is the charge of the particle, and A is the mass of the particle. The calibration points, shown in Table VI, were used to constrain the parameters for the CsI energy calibration. Figure 27 shows a CsI calibration in which the parameters of Equation 2.11 have been determined through minimizing the error between the calibration, shown as the solid colored lines, and the calibration points, shown as black circles. The resulting

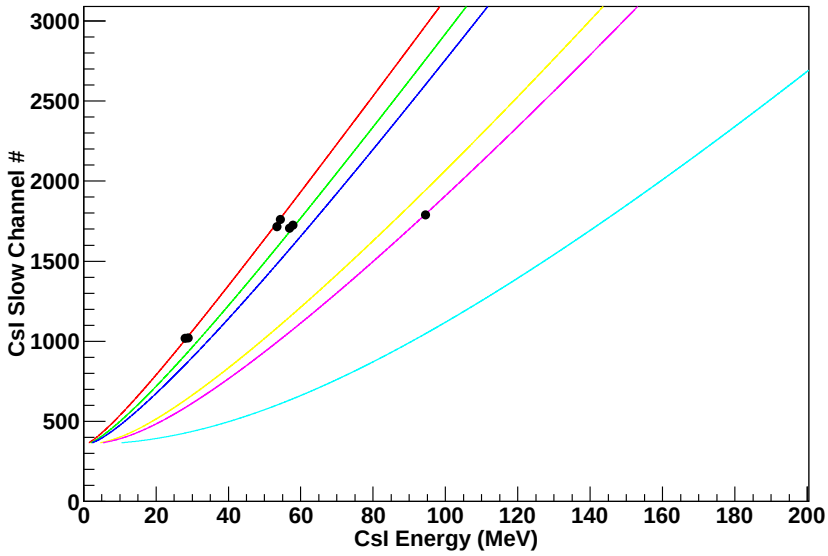

FIG. 27. Example of CsI calibration showing the CsI slow signal channel versus the energy. The calibration points (black circles) were used to constrain the parameters of Equation 2.11. The energy calibration for protons (red line), deuterons (green line), tritons (blue line), ^{3}He (yellow line), α (pink line), and ^{7}Li (light blue line) are shown.

fit shows good agreement with all the different calibration points.

After completing the calibration of both the silicon and CsI detectors, the total energy for each particle was determined. The energy for all particles with Z$\geq$4 was calculated by taking the calibrated energy loss in the silicon detector and using a energy loss table [122] to determine residual energy left in the CsI. In rings 2-11, the residual energy left in the CsI for Z=1 and Z=2 particles was calculated using the CsI calibration. The energy loss table was then used to determine the energy loss in the silicon from the residual CsI energy, thus providing the total energy. The silicon calibration could not be used to calculate the energy for the Z=1 and Z=2 particles because the gains were set such that the silicon signals were compressed at the bottom of the spectrum. For this reason the Z=3 particle energy was calculated

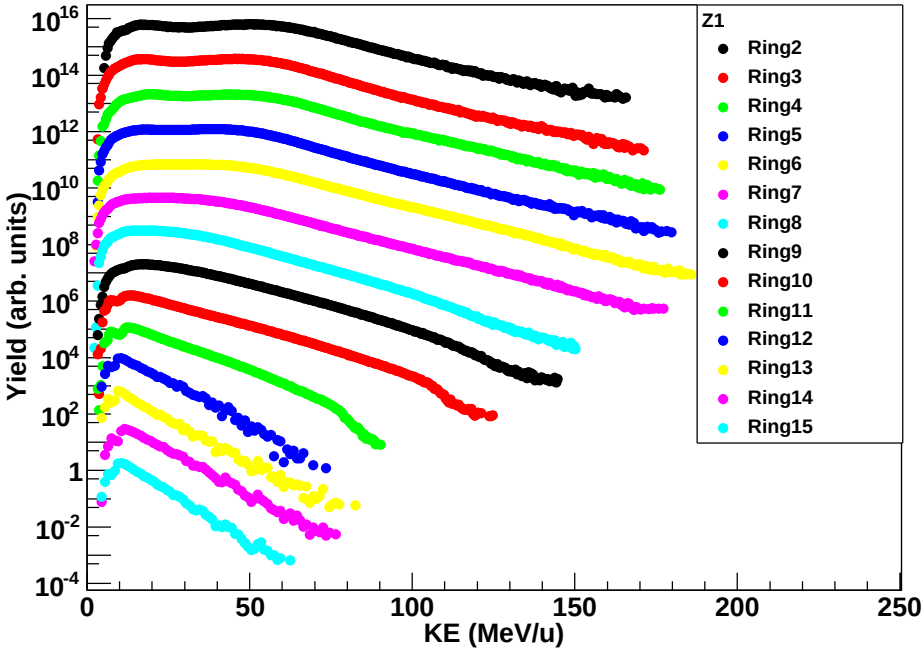

FIG. 28. Energy spectra of the Z=1 fragments for each ring of the NIMROD-ISiS array for the 35 MeV/u ^{64}Ni+^{64}Ni system.

using the CsI calibration in ring 2 and the silicon calibration in rings 3-11. In rings 12-15, a higher silicon gain was set, in comparison to the forward rings, and silicon energy calibrations were used for all particles. The resulting Z=1 energy spectra for the 35 MeV/u ^{64}Ni+^{64}Ni system is shown in Figure 28 for rings 2-15. The energy spectra for all particles in each ring are presented in Appendix B.

E. Production of Tapes

As the particle identification and energy calibration processes each reached completion different sets of tapes were produced containing the experimental data. Each set of tapes differed in the information contained in the event and particle C++ objects. Three different sets of data tapes were produced throughout the analysis of

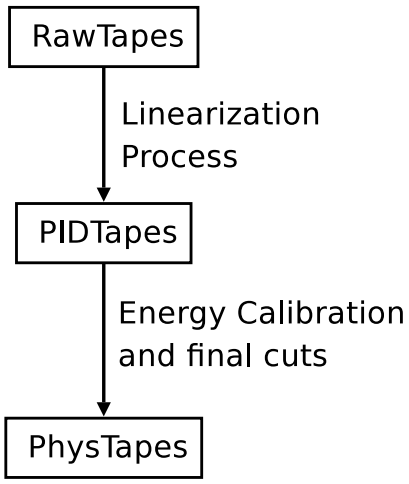

FIG. 29. Flow chart depicting the different tapes produced in the PID and calibration of the experimental data.

the raw experimental data, as shown in Figure 29. The RawTapes represented the raw data collected during the experiment and have the event structure from the C++ T070208Event object. The RawTapes have event-by-event information on the signals recorded from each ADC or QDC channel. The ADC or QDC channel numbers are then converted to detector numbers based on the detector map.

The raw signals are then used in the linearization process, as discussed in Section C, to determine the charge and mass of the particles produced in the reactions. In the PID tapes, information on each fragment is contained in an event-by-event format. The PID tapes are based on the PIDEvent and PIDParticle objects. The PIDEvent contains information such as the multiplicity of the event and the type of trigger the event was collected from (MinBias, Pulser, or HighMult). Each PIDParticle holds the charge, mass, linearization value, percent contamination, fraction of sigma, and raw detectors signals for each fragment. It is important to note that the charge and mass identification for each detector type (SiCsI, CsI Fast-Slow, SiBackCsI, and/or SiSi) is retained, in order to later evaluate the correct identification.

The final tapes produced, referred to as PhysTapes or Physics Tapes, are used for all the subsequent analysis discussed in this dissertation. The PhysTapes are produced from applying the different PID cuts and energy calibrations discussed in Sections C.6 and D, respectively. The PhysTapes contain only fragments that have a correct particle identification and energy calibration. The PhysEvent (PhysEvent.h) object contains data members such as the charged particle multiplicity, the neutron multiplicity, the background neutron multiplicity, and the event trigger.

The PhysParticle (PhysParticle.h) object contains a collection of information from the preceding RawTapes and PIDTapes. The theta and phi angles of each particle are determined from the detector number that the particle was identified in. The PhysParticle has both the detector theta and phi, as well as a theta and phi value determined from a Monte-Carlo calculation over the surface of the detector. The final charge and mass identification of the particle is kept along with the percent contamination and the fraction of sigma. If the particle was not mass identified (only an elemental Gaussian was fit) then a GuessA value was set based on the most probable mass value for that element in the reaction. Therefore, a specific cut on the FracSigma or %Contam was not placed on the particles before being placed in the PhysTapes. This allows for the constraints on the accepted isotopic identification to be easily varied for different analysis. As mentioned, in this work the criteria of %Contam$<$20% and the FracSigma$<$2.5 was required for the isotopic identification to be used in the analysis.

The energy of the particle, as well as the source of the energy calibration (CsI, SiFront, or SiBack) is stored in the PhysParticle object as well. An energy flag is stored for each particle designating the energy as good, acceptable, or bad. This energy flag was determined through comparing the energy spectra for all the detectors in a given ring. The detectors which had well behaved energy spectra where assigned

a flag of good, if the energy spectra had a high energy threshold or a small deviation in comparison to the good spectra then the flag was set as acceptable, and if the spectra did not exhibit the expected behavior it was assigned a bad flag. Therefore, in carrying out an analysis all particles would still be available for examining global variables or event characterization, yet when examining very specific signatures only the particles with well trusted energy spectra would be used. Lastly, from the energy and angle of the particles the momentum and velocity vectors, in both the lab and center-of-mass frames, where calculated and stored in the PhysParticle object. Thus, the PhysTapes contain all the necessary event-by-event and particle information needed to complete a study from the 35 MeV/u ^{70}Zn+^{70}Zn, ^{64}Zn+^{64}Zn, and ^{64}Ni+^{64}Ni reaction systems.

A C++ module (TestModule.cxx, TestModule.h) has been created in the directory /home/sjygroup/zkohley/070208/src which provides an example of how to access the 35 MeV/u ^{70}Zn+^{70}Zn, ^{64}Zn+^{64}Zn, and ^{64}Ni+^{64}Ni experimental data. The Config file (ConfigTestModule.C) used to run the TestModule object is available in /home-/sjygroup/zkohley/070208/dTestModule/ConfigTestModule.C. These codes are also presented (with comments) in Appendix C. In examining the calibrated experimental data it is important to know what run numbers correspond to the different reaction systems since the final Physics Tapes are labeled by run number. Table VII presents the corresponding run numbers for each reaction system.

TABLE VII. Physics tape run numbers corresponding to each of the experimental reaction systems are presented.

Reaction System	Physics Tape Run Numbers
35 MeV/u ^{64}Zn+^{64}Zn	13 - 91
35 MeV/u ^{70}Zn+^{70}Zn	94 - 201
35 MeV/u ^{64}Ni+^{64}Ni	234 - 297

CHAPTER III

SIMULATIONS

A variety of different theoretical models were used in comparison to the experimental data. In the following, a brief description of each model is provided.

A. Dynamical Simulations

Dynamical simulations are used to model the interaction, or collision, of the heavy-ions over a given time-interval.

1. Classical Molecular Dynamics (CMD)

In the classical molecular dynamics (CMD) model [124, 125, 126, 127] the nucleons are treated classically and therefore are represented by point-particles. The nucleons are propagated by the classical Hamiltonian equation of motion with two body nucleon-nucleon potentials. The neutron-proton potential (V_{np}(r)) was attractive at large distances, r, and repulsive at short distances. The proton-proton and neutron-neutron potential (V_{nn}(r)=V_{pp}(r)) was repulsive at all distances. Therefore, the V_{nn}(r) and V_{pp}(r) potentials prohibit the formation of a bound state of identical nucleons, such as a di-neutron. This imitates the Pauli principle in the sense that two neutron, or two protons, would be unable to occupy the same phase-space. The nucleon-nucleon interaction used in the CMD model provides an compressibility for symmetric nuclear matter of K=250 MeV [125].

In Chapter V, the CMD model was used to examine the effect of the Coulomb potential on the dynamics of light charged particles in peripheral collisions. The heavy-ion collisions were propagated to 400 fm/c. The Coulomb potential (V_C) is

defined as

$$V_C = \frac{kZ_1Z_2}{r}(MeV) \tag{3.1}$$

with k being a constant, Z representing the charge of the particle, and r equaling the distance between the particles. The constant k is defined as 1.44 MeV·fm. The constant k was varied as k=0, k=1.44, and k=2.88 allowing for the examination of the simulation with no Coulomb, normal Coulomb, and twice the normal Coulomb potential, respectively.

2. Constrained Molecular Dynamics (CoMD)

The constrained molecular dynamics model [128, 129] represents each nucleon through a Gaussian wave-function. Therefore, the distribution function can be described as,

$$f_i(\mathbf{r}, p) = \frac{1}{(2\pi\sigma_r\sigma_p)^3} \cdot exp\left[-\frac{(\mathbf{r} - \langle\mathbf{r_i}\rangle)^2}{2\sigma_r^2} - \frac{(\mathbf{p} - \langle\mathbf{p_i}\rangle)^2}{2\sigma_p^2}\right] \tag{3.2}$$

where $\langle\mathbf{r_i}\rangle$ and $\langle\mathbf{p_i}\rangle$ represent the centers of position and momentum of the i_{th} nucleon. The widths of the position and momentum (σ_r and σ_p) were used as variable parameters to reproduce basic properties of ground state nuclei. The time-dependent variational principle was used to derive the equation of motion. A momentum-independent Skyrme interaction was used in the calculation which produces an EoS with a compressibility of K=200 MeV. The symmetry term of the Skyrme interaction could be changed such that the compressibility remained constant and, thus, the form of the density dependence of the symmetry energy could be investigated.

An important aspect of the CoMD model is the treatment of the Pauli Principle. In a general quantum molecular dynamics (QMD) model a Pauli potential is used in which prevents nucleons of the same isospin and spin state from occupying the same phase-space. However, this Pauli potentail adds a repulsive force that does not exist

in the nucleus. In the CoMD model, the occupation density ($\overline{f_i}$) of each nucleon is calculated every 1 fm/c during the simulation. An occupation density greater than 1 represents a violation of the Pauli principle. This is corrected in the CoMD model by randomly changing the momentum of the neighboring particles. It should be noted that special consideration is taken to ensure that both the total momentum and total kinetic energy is conserved. After the change if $\overline{f_i} < 1$ then the configuration is accepted. Thus, the Fermionic nature of the system is reproduced without the need for an additional potential or force. Furthermore, the occupation density requirement is used to accept or reject nucleon-nucleon collisions based on whether the final state has a $\overline{f_i} \geq 1$. In Ref. [128] the CoMD model was compared with a QMD model to demonstrate the importance of the treatment of the Pauli principle. The results showed that the occupation density constraint in the CoMD model had a drastic effect on the number of collisions during the reaction and the production of intermediate mass fragments. Further improvements in the model are presented in Ref. [129], such as conservation of the total angular momentum throughout the reaction. The conservation of angular momentum was shown to have important consequences on Ca+Ca fusion cross-sections and should be important in describing the heavy-ion collision reaction dynamics.

One advantage of the CoMD model is that the treatment of the Pauli principle allows for the computation time to scale as N^2 (N is the number of nucleons). In comparison the antisymmetrized molecular dynamics model, discussed below, scales as N^3 since the wave-functions are antisymmetrized. Thus, the CoMD model allows for the reaction to be propagated on a longer time scale with a reasonable amount of computational requirements. For comparison with the experimental data, the heavy-ion collisions were propagated to 3000 fm/c in order to allow the system to evolve dynamically. At 3000 fm/c any existing hot fragments were de-excited using the

Gemini code (discussed below).

The filtered minimum bias charge and mass distributions from the CoMD simulation, in comparison to the experimental data, is presented in Figure 30. The distributions are shown from CoMD after 3000 fm/c with and without the Gemini de-excitation. The results demonstrate that the system has, in general, reached a final state by 3000 fm/c. The only observed difference upon applying the Gemini code is the increased yield of the light charged particles (Z=1-2) from the decay of the remaining hot fragments. For comparison, the CoMD results are also shown with the Gemini code applied after 600 fm/c. The results demonstrate the final fragment yields at 3000 fm/c are relatively well reproduced by the Gemini decay of the 600 fm/c hot fragments. The 600 fm/c CoMD-Gemini results do increase the yield of the Z=3-7 intermediate mass fragments, producing better agreement with the experimental data.

In general, the CoMD results are able to reproduce both the charge and mass distributions. The largest discrepancy is observed in the yield of the projectile-like fragments, which is overproduced in the CoMD simulation. In order to better match the experimental distribution, the CoMD simulation would need an increased break-up, or fission, of the heavy fragments, thus producing more IMFs. The comparison also confirms a previous observation demonstrating the over-production of the protons from the model [128].

3. Antisymmetrized Molecular Dynamics (AMD)

In the antisymmetrized molecular dynamics (AMD) model [130] the wavefunction for a reaction with A nucleons is represetned by a Slater determinant of Gaussian wave

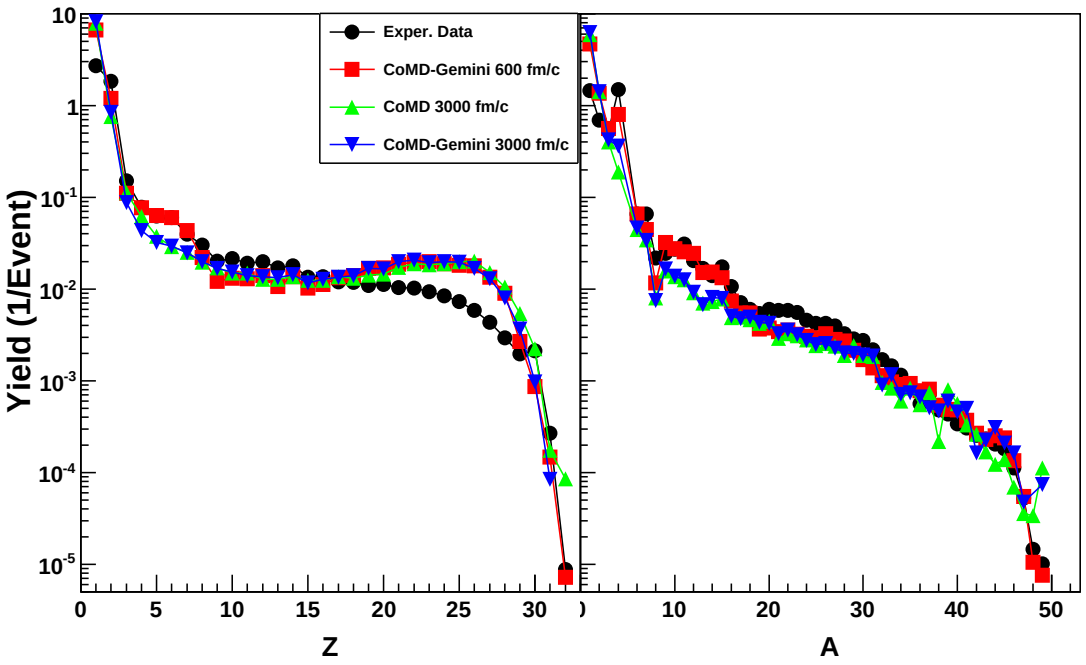

FIG. 30. The minimum bias charge (Z) and mass (A) distribution from the ^{70}Zn+^{70}Zn system are shown for the filtered CoMD simulation in comparison to the experimental data. The results were normalized by the total number of events.

packets,

$$\Phi(Z) = det\left[exp\left\{-\nu\left(\mathbf{r}_j - \frac{\mathbf{Z}_i}{\sqrt{\nu}}\right)^2 + \frac{1}{2}\mathbf{Z}_i^2\right\}\chi_{\alpha i}(j)\right] \tag{3.3}$$

where Z$\equiv \{\mathbf{Z}_i\}_{i]=1,....,A}$ is a set of complex variables. The complex variable $\mathbf{Z}$ is defined as,

$$\mathbf{Z} = \sqrt{(}\nu)\mathbf{D}_i + \frac{i}{2\hbar\sqrt{\nu}}\mathbf{K}_i \tag{3.4}$$

where $\mathbf{D}_i$ and $\mathbf{K}_i$ represent the centroid of the position and momentum, if the anti-symmetrization is ignored, for the ith nucleon. For example, in dilute nuclear matter, where the antisymmetrization effect is small, $\mathbf{D}_i$ and $\mathbf{K}_i$ have a physical meaning [107]. The width parameter, ν, of Eq. 3.3 is a constant at 0.16 fm^{-2} and $\chi_{\alpha i}$ represents the spin-isospin states of p↑, p↓, n↑, or n↓. The equation of motion for the centroids, $\mathbf{D}_i$ and $\mathbf{K}_i$, are determined from the time-dependent variational method.

Since the total wavefunction is antisymmetrized the Pauli principle, or the Fermionic nature of the nucleus, is respected at all times. Furthermore, the Pauli blocking of nucleon-nucleon collisions can be treated accurately by the examining the Slater determinant before and after the collision. In order to simulate the two-body nucleon-nucleon collisions a physical set of coordinates, $\mathbf{W}$, are calculated from the $\mathbf{Z}$ coordinate system. This is necessary in AMD since two wave-packets may be very close in phase-space, yet the actual nucleon positions may be far apart in order to respect the Pauli principle. Therefore, the NN-collision can be calculated in the physical space, $\mathbf{W}$, and after the collision a transformation back to the $\mathbf{Z}$ coordinates is performed. If the transformation is not allowed, representing a violation of the Pauli principle, the collision is blocked.

An important aspect of any heavy-ion collision simulation is the incorporation of a stochastic term which will allow a single initial state to produce a variety of final states. This is often achieved through the stochastic nucleon-nucleon collisions.

However, the AMD model was extended to allow for quantum branching of the initial state into a distribution of final states through effects beyond that of nucleon-nucleon collisions. This is achieved by allowing the Gaussian wave packets to be propagated following the Vlasov equation, which represents the single-particle motion in a mean-field. At some time, τ, it is assumed that decoherence takes place and the single-particle wave functions are separated into an ensemble of Gaussian wave-packets producing a stochastic branching. In the one-body mean-field propagation the single-particle wave-function is allowed to diffuse and at the decoherence time it is localized producing the many-body correlations. This quantum branching, through the one-body mean-field propagation, improved the ability of AMD to treat reactions with a large amount of channels, such as multi-fragmentation. This extension to AMD was referred to as AMD-V (for Vlasov) and more recently as AMD-D (for diffusion) [131]. A further extension allowed for the single-particle wavefunctions to shrink as well as diffuse and has been referred to as AMD-DS (for shrinking) [132]. The wave-function shrinking allowed in AMD-DS causes a slower expansion after the collision, in comparison to AMD-D, and therefore produces heavier fragments more abundantly, which improved agreement with experimental results.

The results from the AMD-DS model are presented in this work for comparison to the experimental data. Due to the exact description of the antisymmetrization of the wavefunction the simulation is computationally demanding and therefore, the simulations were stopped at 300 fm/c. The statistical decay code Gemini was used to de-excite the hot fragments. In Figure 31 the filtered minimum bias charge and mass distributions from the AMD simulation are compared to the experimental data. The results are shown for the fragment yield both before (at 300 fm/c) and after the Gemini de-excitation. As shown, the distribution at 300 fm/c has an increased amount of heavy projectile-like fragments in comparison to the data. However, after

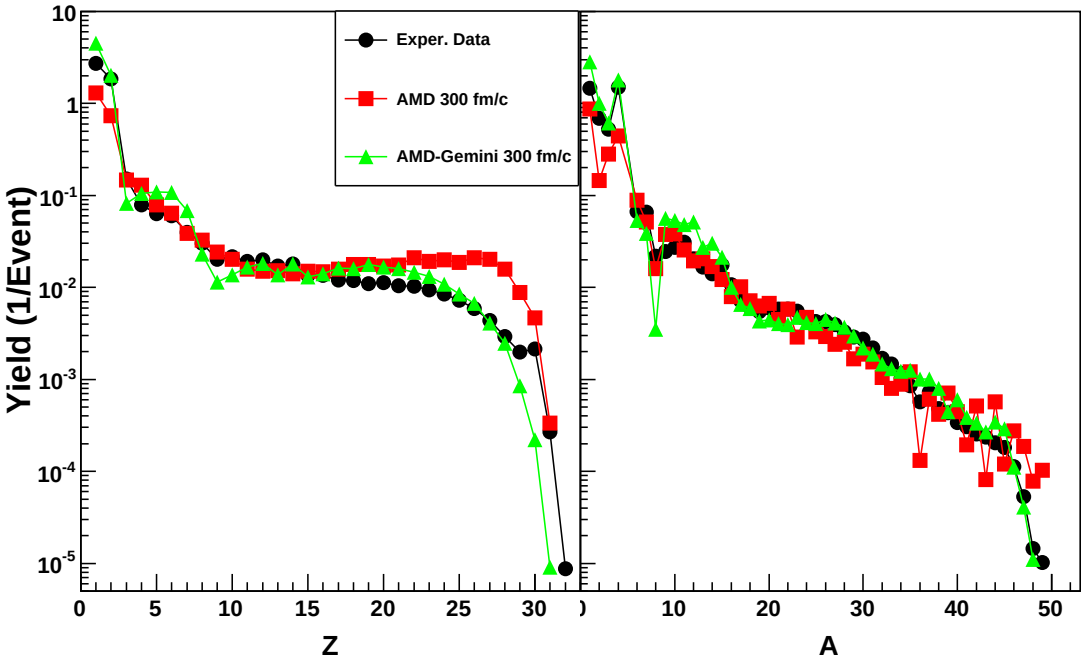

FIG. 31. The minimum bias charge (Z) and mass (A) distribution from the ^{70}Zn+^{70}Zn system are shown for the filtered AMD simulation in comparison to the experimental data. The results were normalized by the total number of events.

the heavy fragments decay, through the Gemini code, the filtered charge and mass distributions (Figure 31) are in good agreement with the experimental results.

The momentum-dependent Gogny and Gogny-AS interactions were used in the AMD simulations [5, 130]. As shown in Figure 2 (in Chapter I), the EoS calculated from the Gogny and Gogny-AS interaction has a compressibility of K=228 MeV. A soft density dependence of the symmetry energy is produced from the Gogny interaction and a stiff dependence is calculated with the Gogny-AS interaction. Thus, in the simulations the symmetric part of the EoS was kept constant and the density dependence of the symmetry energy could be investigated, specifically in comparison to the experimental data.

4. Stochastic Mean-Field Model (SMF)

The stochastic mean-field (SMF) model [15, 133, 134] describes the time evolution of the system using the Boltzmann-Langevin transport equation (BLE) [135, 49]. The BLE can be written as,

$$\frac{df}{dt} = \frac{\partial}{\partial t} f - \{H[f], f\} = I_{coll}[f] + \delta I[f] \tag{3.5}$$

where H is the one-body Hamiltonian ($H[f] = p^2/2m + U[f]$) and $f(\mathbf{r}, \mathbf{p}, t)$ represents the one-body distribution function. The left-side of the equation represents the propagation of $f(\mathbf{r}, \mathbf{p}, t)$ through a self-consistent mean-field, $U[f]$. The average two-body collisions are represented by the average collision term, I_{coll}, which includes the appropriate Pauli blocking factor (often referred to as the Uehling-Uhlenbeck collision term). The stochastic nature of the collision term is incorporated from the Langevin term, $\delta I[f]$.

The test particle method [135, 49] was used to numerically solve the BLE and consists of representing each nucleon by a set of N_{test} test particles. Each test particle is associated with a triangular wave-function of width 0.85 fm [136]. A suitable number of test particles can then provide an accurate calculation of the one-body distribution function with good phase-space coverage. In the limit of $\mathrm{N}_{test} \to \infty$ the numerical solution should approach the exact solution. To account for the increased number of particles, the nucleon-nucleon collision cross-section has to be reduced by a factor of N_{test}.

In the SMF model the stochastic nature of the collision ($\delta I[f]$) is included through agitation in the spatial density of the system [15, 136, 37, 137]. After the system reaches thermal equilibrium, the coordinate space is divided into cells, in which the local density and temperature is calculated. From the local temperature, the density

fluctuation amplitude, σ_ρ, can be determined. Then, the density fluctuation for each cell, $\delta\rho$, is randomly selected from a Gaussian distribution, $exp\left(-\delta\rho^2/2\sigma_\rho^2\right)$ [137, 136]. Thus, the number of test particle in each cell is stochastically changed producing density fluctuations. Special attention is taken to ensure conservation of N_{test}, energy, and momentum after the fluctuation process has been completed [136]. As mentioned above, these stochastic fluctuations are an important aspect in reproducing many of the phenomena observed in heavy-ion collisions.

The effective interaction or mean-field potential used in the SMF model was derived from the original EoS of Bombaci [138] and the parameterization of the interaction proposed by Gale, Bertsch, and Das Gupta [139]. This interaction is therefore referred to as the BGBD interaction and produces a compressibility of K=210 MeV for symmetric nuclear matter [133, 134]. The momentum dependence of the GBD interaction was modified to include an isospin-dependent term. A momentum dependent mean-field implies an effective nucleon mass defined as,

$$\frac{m_\tau^*}{m} = \left\{1 + \frac{m}{\hbar^2 k}\frac{dU_\tau}{dk}\right\}^{-1}_{k=k_F^{[\tau]}} \tag{3.6}$$

where τ stands for either neutrons or protons, U_τ is the mean field potential, and k_F is the Fermi momentum. Thus, the isospin-dependent part of the momentum dependence, which is included in U_τ, can cause the neutron and proton effective masses (m_n^* and m_p^*) to be different, often referred to as effective mass splitting. The parameters of the BGBD interaction have been chosen in order to allow for both the density dependence of the symmetry energy and the effective mass splitting to be independently varied [133, 134].

The SMF model was used to simulate the reactions studied in this work. The reaction was simulated until 120 fm/c, at which point the quasi-projectile and quasi-target separated in the mid-peripheral reactions. Since the simulation is carried out

in a defined box it must be stopped relatively early in order to minimize the pile-up of particles at the edges. One hundred test particles per nucleon were used to sample the one-body distribution functions. A phase-space coalescence code [140] was applied to the test particle distribution to determine the fragment identities. Due to the difficulty in calculating the excitation energy of the fragments, a secondary decay was not applied. Thus, the results represent the phase-space distribution of the hot fragments at an early time stage. Both the density dependence of the symmetry energy and the effective mass splitting was varied to explore their sensitivity to the collective flow observables.

B. Statistical Simulations

The statistical models are based on the assumption that at some point after the collision thermal equilibrium is reached and the break-up, or de-excitation, of the hot fragments can be described statistically.

1. Gemini

The original GEMINI code [141] has been recently updated to improve the calculation of the width of the charge and mass distributions from fission of heavy fragments. The new code was written in C++ and was therefore named GEMINI++ [142], however in the following work it will still be referred to as GEMINI. In this thesis, the GEMINI code was used to de-excite the hot fragments produced by the AMD and CoMD simulations.

The GEMINI code is a statistical decay code in which the excitation energy, angular momentum, charge, and mass of the hot fragment is used to calculate the decay path. A Monte Carlo method is used to calculate a series of sequential binary

decay paths from the initial hot fragment. The Hauser-Feshbach formalism is used to calculate the decay widths of the light charged particles (n, p, d, t, ^{3}He, α, ^{6}He, and $^{6-8}$Li fragments). The fission channel is calculated from the Bohr-Wheeler formalism. In addition to the charged particle emission and fission channels, the decay-width for gamma-ray emission is determined. This is important when the excitation energy is low, since gamma-ray and particle decay widths can be similar.

It is important to note that in using the GEMINI code as an afterburner to the dynamical AMD or CoMD simulations that some assumptions are applied. The GEMINI code calculates the decay of the hot nucleus assuming it is spherical and at normal nuclear density ($\rho_\circ$=0.16 fm^{-3}). However, when the dynamical simulation is stopped the fragments are likely deformed and at a density below $\rho_\circ$, which would likely affect the decay process. Also, after the decay by GEMINI the final trajectories of the fragments are defined and no further nuclear or Coulomb forces are considered. While certain important assumptions are necessary in using GEMINI to cool the hot fragments, AMD-GEMINI results have produced reasonable agreement with a variety of experimental observables [107, 130].

2. Statistical Multi-Fragmentation Model (SMM)

The statistical multi-fragmentation (SMM) model [143, 144, 145] describes the statistical break-up of a hot nucleus. The excitation energy, angular momentum, charge, and mass are the required inputs for the hot source. SMM differs from the GEMINI code in that all break-up channels are explored, from compound nucleus to vaporization, and the initial fragmentation occurs simultaneously (rather than a binary decay process). The hot nucleus is assumed to be at low density and therefore, the fragmentation occurs at a freeze-out volume [145]. The calculations presented in this work are shown with a freeze-out volume of 6 times that of the normal volume, which

corresponds to a density of $\frac{1}{6}\rho_\circ$. A Markov chain generation method is used, along with the Metropolis algorithm, to examine the possible partitions [146]. This method allows for the whole partition space to be examined without having to calculate every possible partition, which would be extremely computationally intensive.

The statistical weight of each partition is calculated as the exponential of the entropy ($W_i \propto e^{S_i}$), which is calculated from the free energy of the partition. The free energy of each fragment (F_{AZ}) is calculated as,

$$F_{AZ} = F_{AZ}^{Vol} + F_{AZ}^{Surf} + F_{AZ}^{Coul} + F_{AZ}^{Sym} + F_{AZ}^{trans} \tag{3.7}$$

which is the summation of the volume (F_{AZ}^{Vol}), surface (F_{AZ}^{Surf}), Coulomb (F_{AZ}^{Coul}), symmetry (F_{AZ}^{Sym}), and translational (F_{AZ}^{trans}) energy terms [144]. Light fragments with A$\leq$4 and Z$\leq$2 are considered as stable nuclei and only the translational energy contributes to the total free energy of the partition. Fragments with A$>$4 are considered hot nuclear liquid drops and there individual free energy is calculated according to Eq. 3.7. It is important to note that the resulting partitions do assume that the fragments are isolated and formed at normal nuclear density in the expanded volume [143, 145, 147]. Following the initial partition, the fragments are propagated along their Coulomb trajectories and no further nuclear interactions are considered. Some of the fragments from the initial, or primary, partition may still be hot and therefore, are able to undergo particle evaporation, fission, or Fermi break-up during the propagation, which produces a final cold distribution [143, 144].

In peripheral collisions, the fragmentation of the quasi-projectile (QP) is occurring within the vicinity of the quasi-target (QT). The SMM model has been modified [148, 149] such that the Coulomb field produced by the nearby QT is accounted for in the fragmentation of the hot QP. The particle distribution and Coulomb acceleration of the fragments are modified by the Coulomb energy of the two body (PLF

and TLF) system, as described in Refs. [148] and [149]. This produces an asymmetry in the QP, where the neutrons are preferentially distributed toward the QT. Thus, more neutron-rich fragments, as well as IMFs, are produced between the PLF and TLF due to the mutual Coulomb field produced by the two-body system. The effect of the Coulomb field in the production of mid-rapidity fragmentation was investigated in Chapter V.

CHAPTER IV

TRANSVERSE FLOW ANALYSIS

The transverse flow has been investigated for isotopically identified light charged particles (LCPs) and intermidiate-mass fragments (IMFs) for the 35 MeV/u ^{70}Zn+^{70}Zn, ^{64}Zn+^{64}Zn, and ^{64}Ni+^{64}Ni systems. In order to determine the transverse flow from the experimental data an estimation of both the impact parameter and reaction plane was required on an event-by-event basis. In Section A the method used for the impact parameter determination is discussed. A comparison of different reaction plane determination techniques is presented and discussed in Section B. The experimental LCP results are shown in Section C along with theoretical comparisons. A new method was developed to examine the IMF transverse flow and is discussed in Section D along with the experimental and theoretical results.

A. Estimation of Impact Parameter

The ability to sort the experimental events based on the impact parameter is essential for flow analysis since the transverse flow is known to change as a function of the centrality of the collision [150, 151, 54, 53, 9, 152, 153]. An extensive list of variables and methods have been previously used to estimate the impact parameter as discussed in Refs. [153, 154, 155, 156, 157, 158, 159] and references therein. However, it is important that the application of any method be evaluated on a separate basis for each experiment, since different detector configurations will have different biases. Thus, the best method for impact parameter determination may vary from experiment to experiment.

The filtered AMD-Gemini and CoMD simulations were used to examine a wide-range of global variables to determine their correlation with the impact parameter.

These variables included the charge particle multiplicity, raw neutron multiplicity, Z=1-2 multiplicity, IMF multiplicity, total transverse momentum, Z=1-2 transverse momentum, total transverse energy, Z=1-2 transverse energy, largest fragment, total detected charge, mid-rapidity charge, total energy, total parallel momentum, and the different moments of the charge distribution. Since the impact parameter is known for each simulated event, the relationship between the filtered observable and the impact parameter can be formed. The results presented in this Section represent data taken with a minimum bias trigger. The events collected under the minimum bias trigger should have a triangular impact parameter distribution, since the probability for an event at a given impact parameter, b, is related to the cross-section, $\sigma=\pi b^2$.

The touching spheres radius for the A_{sys}=140 (A_{sys}=128) system can be approximated as 9.9 fm (9.6 fm) assuming the radius of the projectile to be $R = r_0 A^{1/3}$, with $r_0 = 1.2$ fm. Therefore, the AMD and CoMD calculations were completed for impact parameters ranging from 0-10 fm. The triangular impact parameter distribution for each simulation before and after the events have been filtered is shown in Figure 32. The results show that the triangular impact parameter distribution is maintained after the NIMROD-ISiS software filter was applied. The AMD-Gemini results show that above $\sim$8 fm the NIMROD-ISiS array has a decreasing efficiency for detecting the very peripheral events. These un-detected events correspond to reactions in which the projectile-like fragment (PLF) has a small deflection angle and does not hit the detector array.

Since the triangular impact parameter distribution is maintained through the NIMROD-ISiS array, one should be able to correlate the distribution of a global variable with the impact parameter distribution. As mentioned above, a variety of global variables were investigated, using AMD-Gemini and CoMD, to determine the strength of their correlation with the impact parameter. In Figure 33 the total

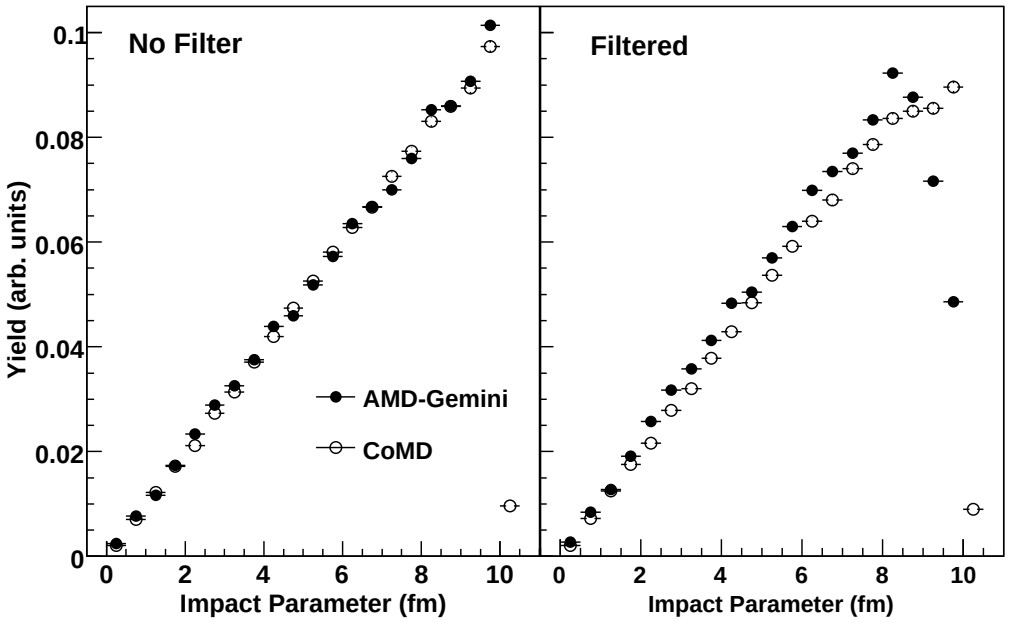

FIG. 32. Impact parameter distributions for the AMD-Gemini (closed circles) and CoMD (open circles) simulations for the ^{70}Zn system. The results are shown with (Right) and without (Left) the NIMROD-ISiS software filter being applied to the data.

detected charge (ztot) is shown to have a poor correlation with the impact parameter. The results show that the total detected charge will likely be ztot≅23, regardless of the impact parameter of the collision.

Examples of observables that showed a "good" correlation with the impact parameter are presented in Figure 34. The average value of the variables is plotted versus a reduced impact parameter, which is defined as b_{red}=b/b_{max} with b_{max} = 10 fm. The large differences observed in Figure 34 between AMD-Gemini and CoMD can be attributed to the over-production of neutrons and Z=1 particles in CoMD, as discussed in Chapter III. Overall, the variables shown in Figure 34 demonstrate a nearly linear relationship with b_{red} from the peripheral to mid-peripheral reactions. In comparison the total detected charge (ztot), shown in Figure 33, exhibited a linear relationship only for the most peripheral collisions. The results presented in Figure 34 demonstrate that even the "good" global variables do not allow one to clearly differentiate the most central events. These results are in agreement with previous studies [107, 155] that have shown the difficulty in separating the central collisions in the Fermi energy domain.

The global variables that have shown a good correlation with the impact parameter were then used to create impact parameter selections. This is accomplished by assuming a linear relationship between the impact parameter distribution and the given variable distribution. For example, in Figure 35 a charged particle distribution has been binned such that each bin should correspond to a range of 0.25 b_{red}. This is accomplished by determing what percent of the events should have a b_{red} between 1.0 and 0.75 assuming a triangular distribution, which is about 44%, and then selecting the bottom 44% of the events from the charge particle multiplicity distribution, thus producing Bin 0. This procedure is then carried out for the next bin corresponding to a b_{red} range of 0.75 to 0.5. The final result, shown in Figure 35, is four bins each

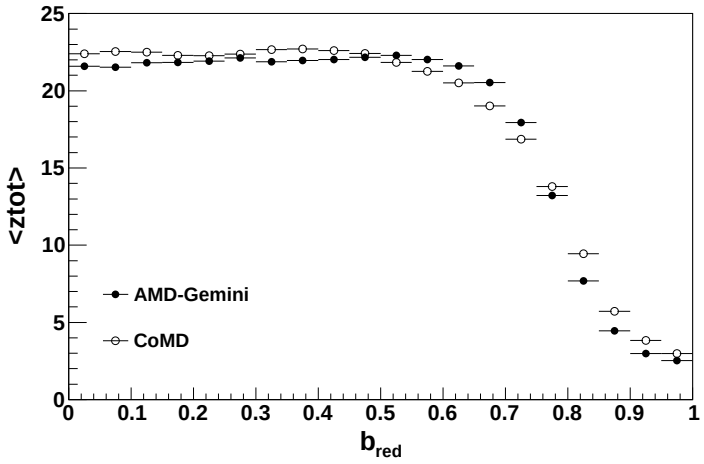

FIG. 33. Average total detected charge, ztot, as a function of the reduced impact parameter for the AMD-Gemini (closed circles) and CoMD (open circles) simulations. Results shown are for the 35 MeV/u ^{70}Zn system.

representing the same range in b_{red}.

Previous studies have used theoretical simulations to show that increasing the number of variables used in the impact parameter selection can help improve the accuracy of the method [159, 157, 156, 106]. Specifically studies, using the NIMROD array, have used 2-D plots to perform the impact parameter selection [106, 107, 160]. In performing cuts on a 2-D plot it is important to choose variables that do not have strong autocorrelations which may bias the selections [106]. Therefore, a good choice to use is the neutron multiplicity along with another variable, such as the charge particle multiplicity, since it has been shown that the neutron multiplicity generally has minimal autocorrelations with other observables [106, 127].

Figure 36 shows the experimental 2-D distribution of the raw neutron multiplicity (NMult) versus the charged particle multiplicity (CPMult). By adding together NMult and CPMult for each event a 1-D distribution can be created of the total multiplicity and the same procedure discussed above can be carried out to create impact

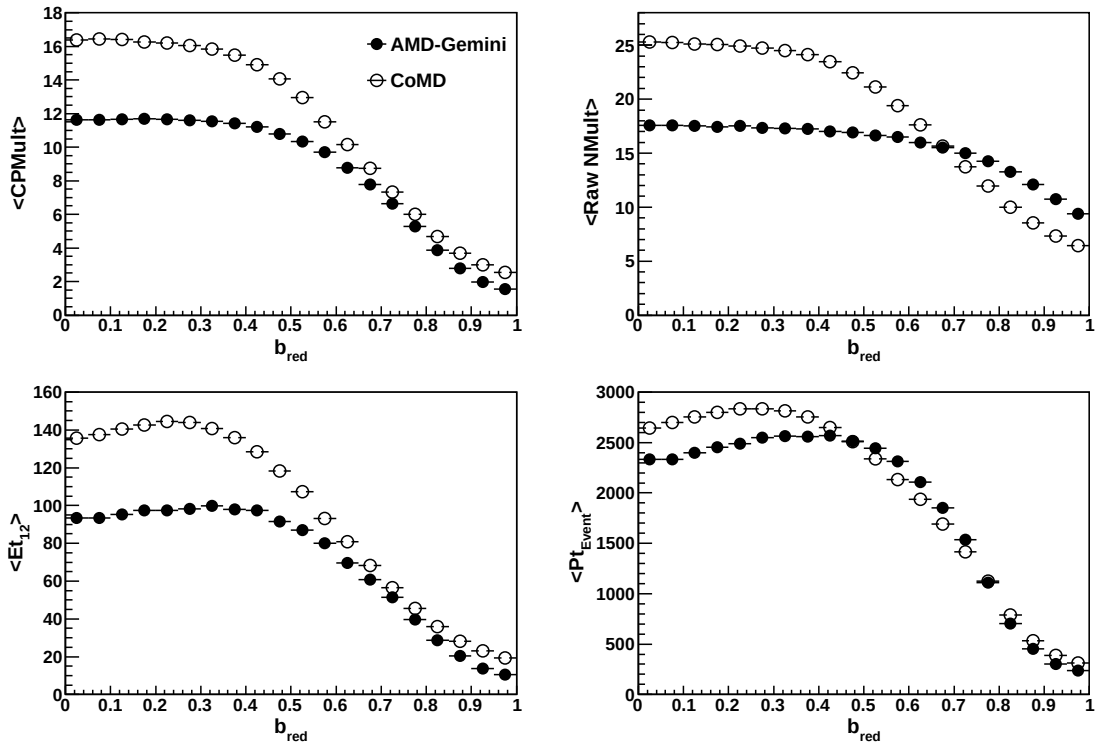

FIG. 34. Average charged particle multiplicity (Top Left), average raw neutron multiplicity (Top Right), average transverse energy for Z=1-2 particles (Bottom Left), and average total transverse momentum (Bottom Right) as function of the reduced impact parameter for the AMD-Gemini (closed circles) and CoMD (open circles) simulations. Results shown are for the 35 MeV/u ^{70}Zn system.

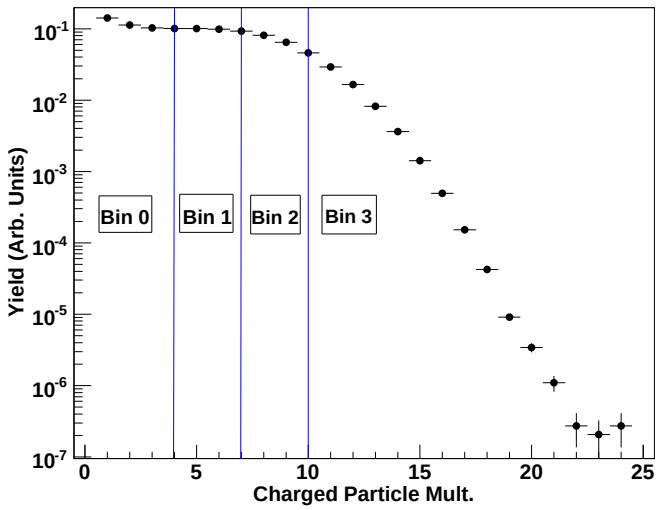

FIG. 35. Charged particle multiplicity distribution for the experimental 35 MeV/u ^{70}Zn system. The blue vertical lines separate the different impact parameter selections, labeled as Bins 0-3. See text for details about how the bin width was determined.

parameter selection bins. However, if the 2-D distribution does not have a slope=1 then the two variables will not equally contribute to the impact parameter selection.

In order to ensure an equal contribution from both the NMult and CPMult the maxima of the 2-D distribution were fit with a linear function and the slope was extracted, as in Figure 36. The linear fit is represented by the solid black line which had a slope of 0.83. After extracting the slope, a 1-D distribution can be produced from the modified total multiplicity, modTotMult, as defined in Equation 4.1.

$$modTotMult = slope \cdot CPMult + NMult \tag{4.1}$$

Using Equation 4.1 ensures that the CPMult and NMult have equal contributions to the impact parameter selection. In Figure 37 the modified total multiplicity distribution, constructed from the 2-D plot of Figure 36, is shown. The same binning procedure as described above has been used to create four bins of equal b_{red} spacing, as depicted by the blue vertical lines of Figure 37. The same bins shown in Figure 37 can also be viewed from a 2-D representation as shown in Figure 38. Each bin represents a different region of the 2-D raw neutron multiplicity versus modified charged particle multiplicity distribution.

The ability of the different methods (1 variable vs. 2 variables) and the choice of what global variables to be used in the impact parameter selection can be examined through the use of the theoretical models. The total number of bins used for the selection was varied between 3-5 Bins and the procedures discussed above were used on the filtered theoretical data. Table VIII shows the b_{red} range that each bin should represent depending on the total number of bins used. As shown, if one uses an increased number of total bins then the b_{red} range decreases for each bin, which will in turn decrease the available statistics per bin. Therefore, the choice in the total number of bins will depend on the statistics and impact parameter definition required

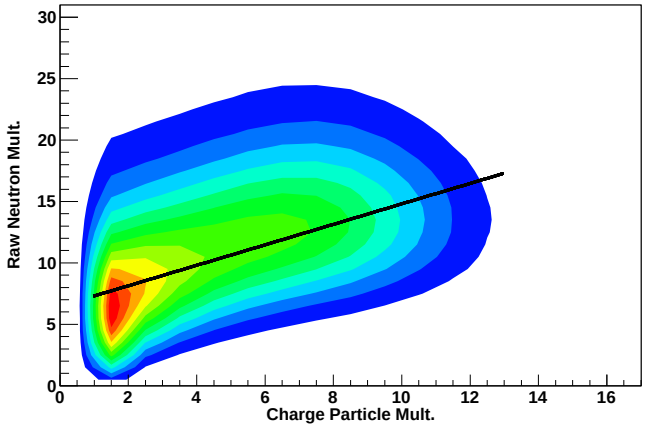

FIG. 36. Neutron multiplicity plotted against the charged particle multiplicity for the experimental 35 MeV/u ^{64}Ni system. The solid black line represents a linear fit through the maxima of the 2-D distribution.

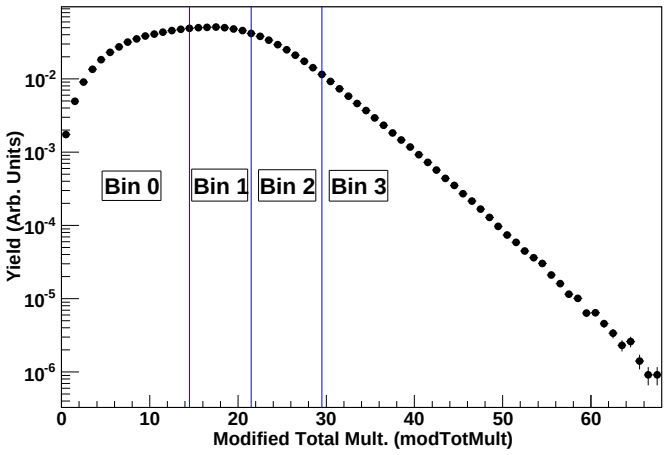

FIG. 37. Modified total multiplicity distribution, as defined by Equation 4.1, for the experimental 35 MeV/u ^{64}Ni system. The solid blue vertical lines represent the different impact parameter bins as described in the text.

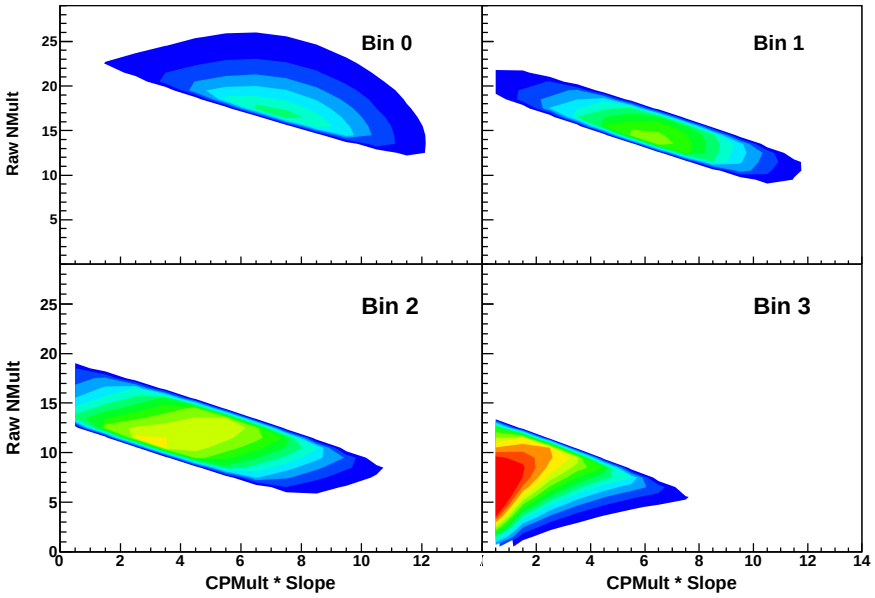

FIG. 38. Raw neutron multiplicity is plotted against the charged particle multiplicity multiplied by the slope from Equation 4.1 for the experimental 35 MeV/u ^{64}Ni system. The four impact parameter selection bins, as shown in Figure 37, are labeled in the top right corner of each panel.

TABLE VIII. The b_{red} range that each impact parameter selection bin should correspond to is presented based on the total number of bins produced.

	3 Bins	4 Bins	5 Bins
Bin 0	0.0 - 0.33	0.0 - 0.25	0.0 - 0.2
Bin 1	0.33 - 0.66	0.25 - 0.5	0.2 - 0.4
Bin 2	0.66 - 1.0	0.5 - 0.75	0.4 - 0.6
Bin 3	-	0.75 - 1.0	0.6 - 0.8
Bin 4	-	-	0.8 - 1.0

for the given study.

The accuracy of the different methods and variables can be measured by comparing the number of correct events to incorrect events placed in each bin. In Figures 39 and 40 the percent of correct events placed in each bin is compared using the AMD-Gemini and CoMD models, respectively. The results are compared for using the charged particle multiplicity, the total Z=1-2 transverse energy, the 2-D raw neutron multiplicity versus charged particle multiplicity, and the 2-D raw neutron multiplicity versus total Z=1-2 transverse energy. Again, when 2 variables were used the procedure described above, in which the 1-D distribution was corrected for the slope of the 2-D distribution, was carried out.

The AMD-Gemini and CoMD simulations both show that the accuracy of the impact parameter selection greatly decreases for the more central collisions. This is expected due the lack of sensitivity that these variables exhibited for the more central collisions, as shown in Figure 34. For the most peripheral collisions (highest bin numbers), the percent of correct events is often above 80% demonstrating a relatively accurate impact parameter selection. For the lowest bin number (central collisions)

the b_{red} range predicted by the simulations is much larger then the expected range from Table VIII, which decreases the percent of correct events. Thus, the lower bins should be more accurately described as selecting the most violent collisions.

The choice of the variables used to perform the impact parameter binning, as shown in Figures 39 and 40, does not have a large affect on the accuracy. In the AMD-Gemini simulation, the results show that the use of the charged particle multiplicity improves the results for the peripheral collisions, while the Et_{12} show a slight improvement for the more central collisions. It does not appear that the addition of the second variable, the raw neutron multiplicity, has a significant effect on the accuracy. For the CoMD simulation, the different variable choices appear equivalent except for the charged particle multiplicity. The charged particle multiplicity appears be less accurate in the mid-peripheral collisions in comparison to the other choices.

Based on the AMD-Gemini and CoMD results, the 2 variable charged particle plus neutron multiplicity (modTotMult) method was chosen for the impact parameter selection for this study. The Et_{12} was not used because it did not show any significant improvement in the selection accuracy and poses a potential autocorrelation. Figures 41 and 42 show the b_{red} distribution associated with each bin using the modTotMult variable for the AMD-Gemini and CoMD simulations, respectively. The results show that the different bin selections do probe different regions of the b_{red} distribution even though significant overlap is present in some cases. In the following, the bin selection will be referred to in the form 5Bin3, where this represents the selection of Bin 3 from a total number of 5 bins.

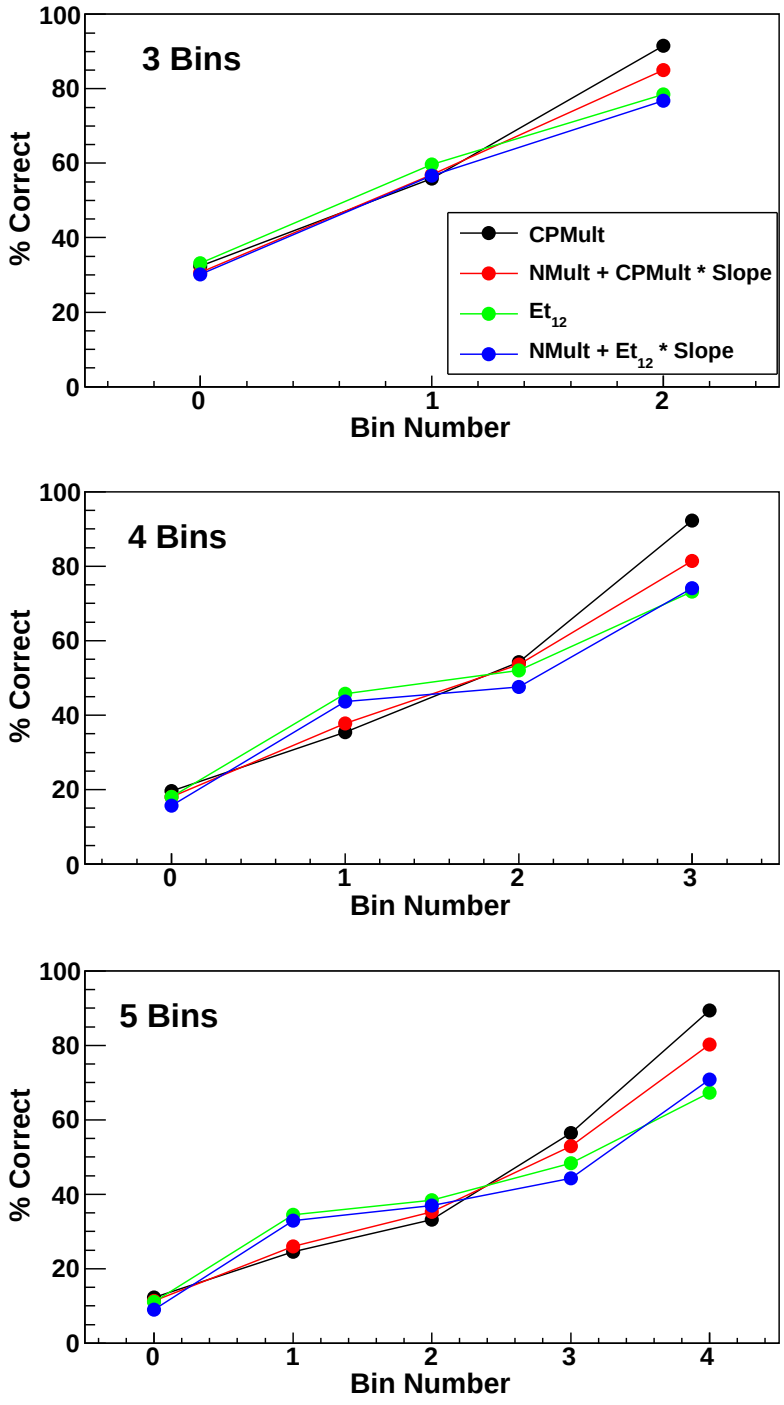

FIG. 39. The percent of correct events as a function of the bin number for the choice of 3 (Top), 4 (Middle), and 5 (Bottom) total bins from the AMD-Gemini simulation. The results are compared for four different choices of global variables as shown by the legend in the top panel.

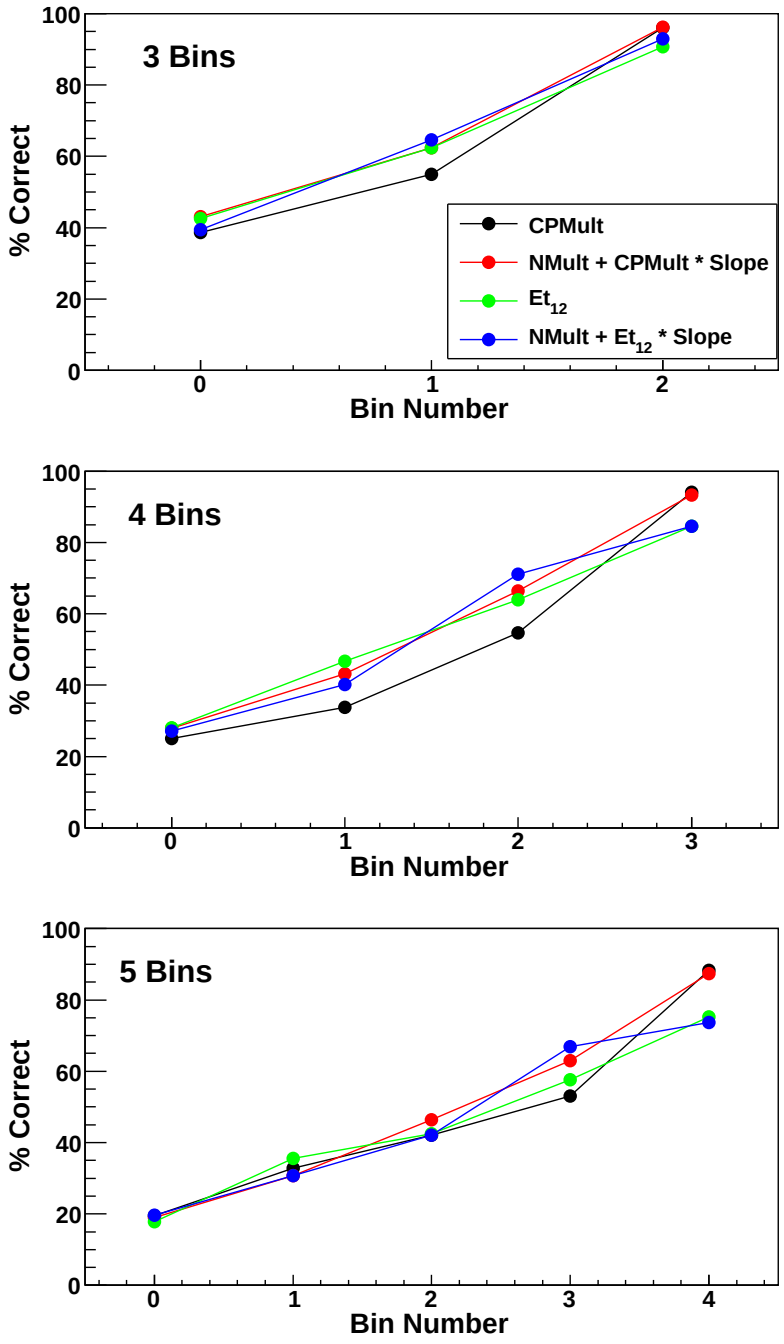

FIG. 40. Same as Figure 39, except results are from the CoMD simulation.

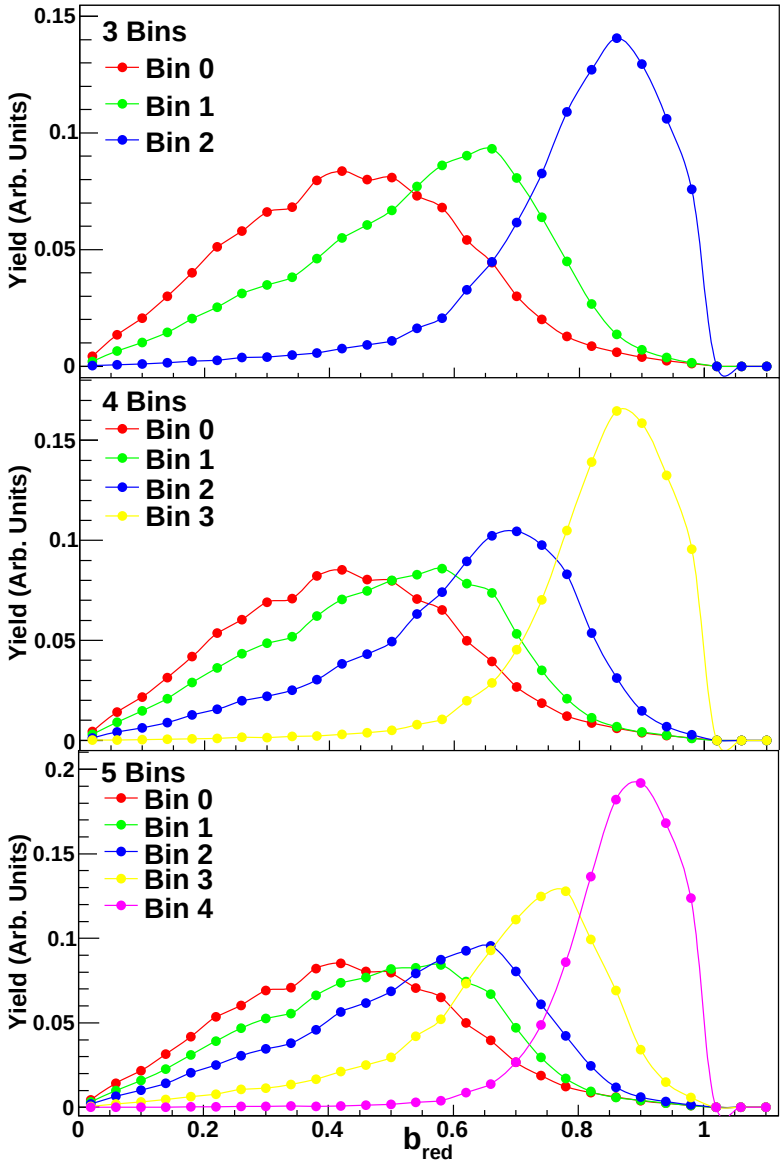

FIG. 41. Reduced impact parameter distributions from the AMD-Gemini simulation for the different bins produced using the modTotMult, Equation 4.1, variable. The total number of events for each distribution has been normalized to one. The distributions are shown for using 3 (Top), 4 (Middle), and 5 (Bottom) total bins.

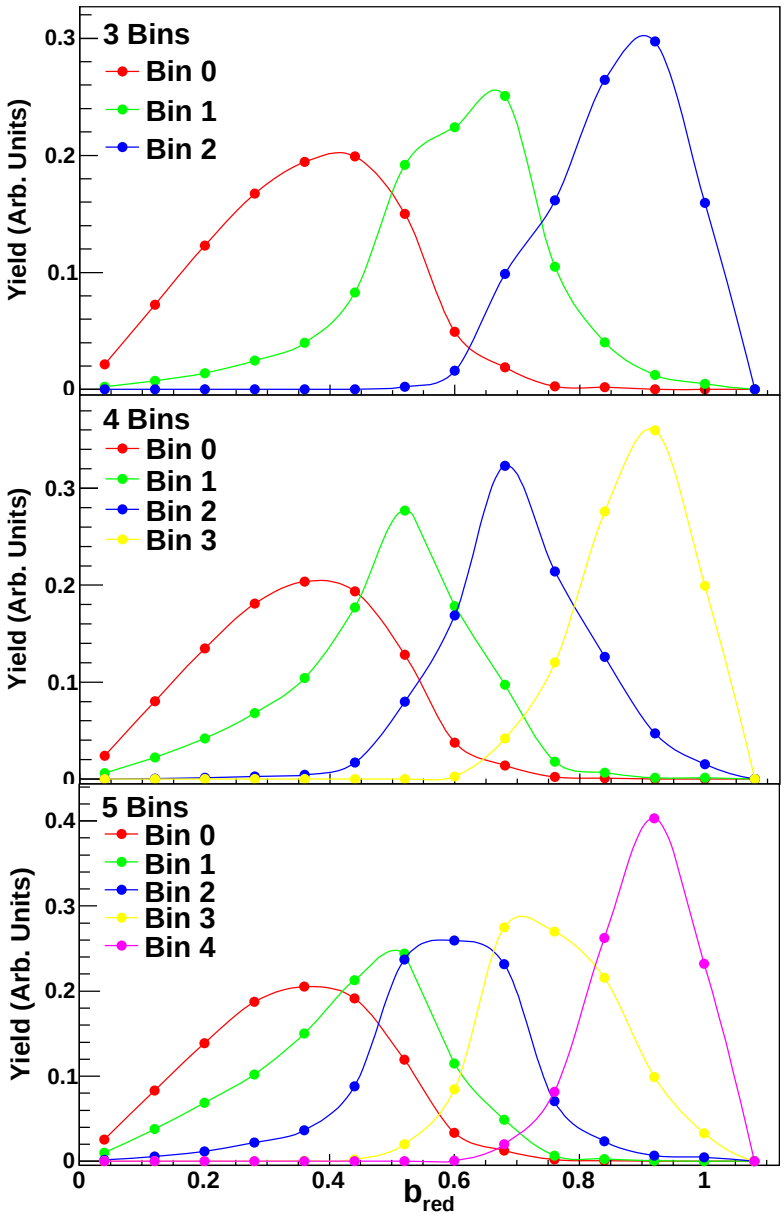

FIG. 42. Same as Figure 41, except results are from the CoMD simulation.

B. Reaction Plane Analysis

In studying the transverse flow below the balance energy, one is examining the in-plane enhancement of particle emission. Thus, for each event the reaction plane needs to be reconstructed in order to examine this enhancement. Different methods and techniques have been developed and studied for reaction plane reconstruction [153, 161, 162, 163, 164]. Three methods that have proven useful in the Fermi energy range are the transverse momentum analysis [163], the azimuthal correlations method [162], and the kinetic energy flow tensor [164].

In the transverse momentum analysis method a vector, Q, is constructed from the transverse momentum, p_t, of each fragment,

$$Q = \sum_{i \neq j}^{Mult} w_i \cdot p_{t,i} \tag{4.2}$$

where w_i is a weighting factor. The weight factor is generally taken to be +1 or -1 for particles with a center of mass rapidity, Ycm, greater than or less than zero, respectively. The phi angle of the constructed Q-vector represents the reconstructed reaction plane. It is important to note that the summation in Equation 4.2 is over all particles except for the particle of interest (POI) in order to avoid well known autocorrelations [163, 44]. Thus, the reaction plane is calculated for each particle in the event.

While the transverse momentum analysis method was originally developed for reactions well above the Fermi energy range, the azimuthal correlations method was designed specifically for lower energy reactions. In the Fermi energy range the observed in-plane enhancement is due to both the observation of the collective transverse flow and a collective rotational motion. The azimuthal correlations method attempts to take advantage of the in-plane enhancement due to rotational effects. The method

consists of projecting each event onto the p_x-p_y plane and fitting a linear function to the (p_x,p_y) points of each fragment. If collective flow and/or rotational motion are present the emission of the fragments will show an enhancement in the reaction plane and the slope of the linear function will represent the angle of the reaction plane. This method is implemented by finding the minimum deviation, D,

$$D^2 = \sum_{i \neq j}^{Mult} \left[p_{x,i}^2 + p_{y,i}^2 - \frac{(p_{x,i} + p_{y,i} \cdot a)^2}{1 + a^2} \right] \tag{4.3}$$

between the projected event and the linear function having a slope a. The slope of the line, a, that minimizes the deviation is found by taking the derivative of Equation 4.3 and setting it equal to zero [162]. Again, the POI is not used in the reaction plane analysis to remove autocorrelations. While the azimuthal correlations method provides an estimate of the reaction plane angle, it does not determine the forward flow side of the reaction. Therefore, the transverse momentum analysis is used to determine the forward flow side, while the azimuthal correlations method is used to determine the reaction plane. For example, the azimuthal correlations method, for a given POI, may provide a reaction plane of 95^o and the Q-vector provides a reaction plane of 260^o, thus the final reaction plane angle from the azimuthal correlation method would be 275^o (95^o+180^o).

The reaction plane can also be determined from the calculation of a tensor constructed from the momenta of the detected fragments. The tensor, F_{uv}, is defined as,

$$F_{uv} = \sum_{i \neq j}^{Mult} w_i \cdot p_i^u \cdot p_i^v \tag{4.4}$$

with w_i being a weight factor, u,v represent the x,y,z components of the momentum, and p_i^u as the u-component of the momentum for the i^{th} fragment. Thus, a 3x3 matrix can be created from F_{xx}, F_{xy}, F_{xz}, ..., F_{zz}. Upon diagonalization of the

matrix, the largest eigenvector from the tensor can be determined. The azimuthal angle of the largest eigenvector represents the reaction plane, while the polar angle is often referred to as the flow angle. As with the other methods, the POI is removed from the calculation of the tensor in order to avoid autocorrelations. In this analysis, the weight, w_i, in Equation 4.4 was taken to be $\frac{1}{2m_i}$, thus producing a kinetic energy tensor.

While the removal of the particle of interest in the determination of the reaction plane is important for avoiding autocorrelations, it also produces a lack of momentum conservation. Therefore, the difference between the reconstructed reaction plane angle and the angle of the POI, $\Delta\phi_{POI}$, will on average be larger then the true value. A larger $\Delta\phi_{POI}$ will correspond to a decreased in-plane momentum, Px. A common method to attempt to correct the lack of momentum conservation and account for the momentum of the removed POI is to add a velocity boost, v_b, to the other particles in the calculation of the reaction plane. The velocity boost represents a boost, in the transverse direction, of the other particles towards the POI. The velocity boost is defined as,

$$v_b = \frac{p_{t,POI}}{m_{sys} - m_{POI}} \tag{4.5}$$

where $p_{t,POI}$ represents the transverse momentum of the POI, m_{sys} is the total mass of the reaction system, and m_{POI} is the mass of the POI. As Equation 4.5 shows, the velocity boost is calculated assuming the the entire system has felt the recoil of the POI. The effect of the velocity boost can be observed in a typical flow plot (Figure 43) where the average in-plane momentum, $\langle Px/A \rangle$, is plotted against the reduced rapidity, $Y_r = Y_{cm}/Y_{cm,proj}$. Figure 43 shows the results with, red circles, and without, black circles, the addition of the velocity boost in the reaction plane calculation. The results show that the shape of the "flow" plot remains almost unchanged

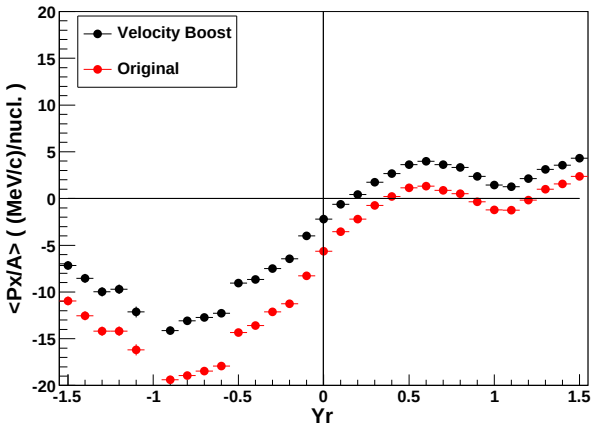

FIG. 43. Average in-plane momentum, $\langle Px/A \rangle$, for protons as a function of the reduced rapidity, Yr, for the ^{64}Ni system selecting 5Bin3. The azimuthal correlations method has been used to construct the reaction plane with (red circles) and without (black circles) a velocity boost correction.

after the velocity boost correction and the only significant difference observed is the overall increase in $\langle Px/A \rangle$. Therefore, the velocity boost helps to restore the symmetry around Y_r=0. In order to fully restore the symmetry, the recoil mass would need to be adjusted from m_{sys} to a smaller value, such as the mass of the projectile. However, in order to have a consistent velocity boost across all the impact parameter bins the recoil mass was assumed to be m_{sys} since this would not allow one to over correct the results. The effects of changing the recoil mass have been previously studied in Ref. [161] and had no significant effect on the final results. The velocity boost effects shown in Figure 43 are in good agreement with those previously observed in Refs. [162, 165] and will be used in the transverse flow analysis of Sections C and D.

The accuracy of the reaction plane determination can be experimentally estimated by randomly dividing each event into two halves and calculating the reaction plane for each sub-event [163, 162, 153]. The distribution of the difference between the two reaction plane angles, $\Delta\phi_{Halves}$, is shown in Figure 44 from the experimental

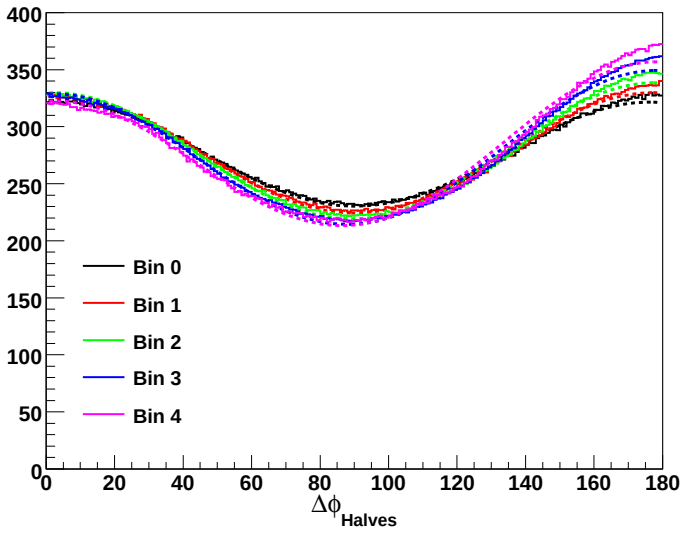

FIG. 44. Distributions of $\Delta\phi_{Halves}$ calculated using the azimuthal correlations method for 5 different impact parameter selection bins. The solid lines show the experimental results, for events with a charged particle multiplicity greater than three, from the ^{70}Zn system and the dashed lines represent fits to the data using Equation 4.6. The distributions are normalized to have the same area under the curve.

data. The experimental distributions are shown for events with a charged particle multiplicity greater than three for each of the different impact parameter selection bins. The standard deviation from the distribution $\Delta\phi_{Halves}$ can then be related to a measurement of the reaction plane accuracy [162].

The procedure from Ref. [162], described below, was used to estimate the standard deviation of the difference between the reconstructed and true reaction plane. The distributions in Figure 44 are assumed to be the combination of two Gaussian functions such that

$$\Delta\phi_{Halves} = C \cdot \left(R \cdot e^{\frac{-\phi^2}{2\sigma^2}} + e^{\frac{-(\phi-180)^2}{2\sigma^2}} \right) \tag{4.6}$$

with C representing a scaling constant, R is the ratio of the integral of the two

Gaussians, and σ is the standard deviation of the Gaussian functions. The dashed lines in Figure 44 represent the fit of Equation 4.6 to the distribution. The standard deviation of difference between the true reaction plane and the reconstructed reaction plane, σ_0, can be determined from

$$\sigma_0 = \frac{1}{2} \cdot \sigma \tag{4.7}$$

where σ represents the width extracted from the fit of Equation 4.6 to the $\Delta\phi_{Halves}$ distribution. Using Equation 4.7, with the fit results of the $\Delta\phi_{Halves}$ distributions, the accuracy of the reaction plane determination can be examined.

Before comparing the accuracy (σ_0), it is important to discuss the anti-correlation observed at 180° between the event halves in Figure 44. The peaks at 0° and 180° of the $\Delta\phi_{Halves}$ distribution demonstrates that the sub-events are likely to be either correlated or anti-correlated, respectively. The shape of this distribution is not surprising in the Fermi energy range since strong in-plane enhancement, due to rotational collective motion [162], and correlations between the event halves [166] have been observed. Similar distributions have been observed by Wilson *et al.* for the 35 MeV/u Ar + V system [162]. The results indicate that the reaction plane angle is well determined, strong peaking at 0° and 180°, however the forward flow side of the reaction plane varies between the event halves. Thus, a measurement of the reaction plane accuracy can still be achieved through estimating the widths of the distributions in Figure 44. Determing the forward flow side of the reaction plane is particularly important when examining the flow of intermediate mass fragments and is discussed in Section D.

The reaction plane resolution, σ_0, calculated from the three different reaction plane methods is shown in Figure 45 for each of the impact parameter bins. The results for all three methods show a consistent decrease in σ_0 for the more peripheral collisions, which is expected due to the strong alignment between the PLF and

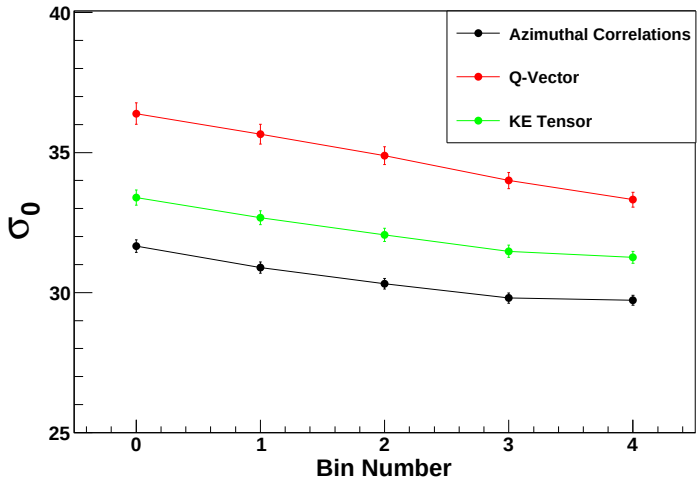

FIG. 45. Standard deviation of the difference between the true and reconstructed reaction plane, σ_0, plotted against the impact parameter selection bin number for events with a charged particle multiplicity > 3. Results are shown for the use of the Azimuthal Correlations (black), Transverse Momentum Analysis or Q-Vector (red), and Kinetic Energy Tensor (green) reaction plane methods for the ^{70}Zn system.

reaction plane. Furthermore, it is clear that the azimuthal correlations method produces the lowest σ_0 values and therefore provides the most accurate reaction plane determination. The range of the σ_0 values obtained are lower than those observed Wilson *et al.* [162] for the 35 MeV/u Ar + V system and demonstrates the ability of the NIMROD-ISiS array to reconstruct the reaction plane.

In studying the transverse flow in any energy regime, it is important to select quasi-complete events in order to ensure that the reconstructed reaction plane is a good representation of the true reaction plane. Previous works have used selections on total detected charge, fragments parallel velocity, and/or fragments parallel momentum to select "good" events [44, 167, 153]. In this work, a requirement was imposed for each event to have a total detected charge, SumZ, greater than 40% of

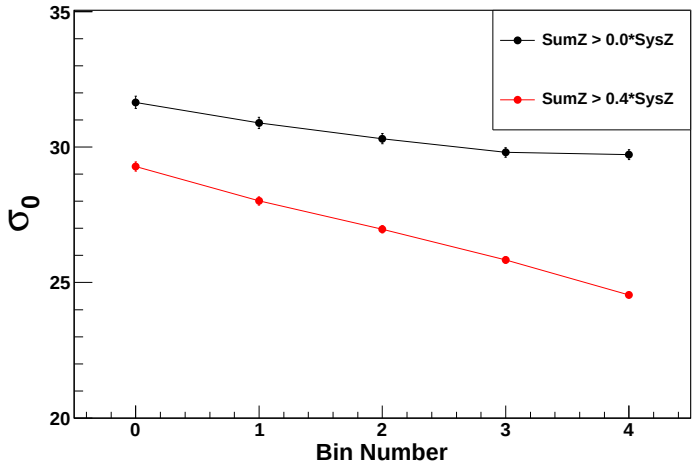

FIG. 46. Standard deviation of the difference between the true and reconstructed reaction plane, σ_0, plotted against the impact parameter selection bin number for the ^{70}Zn system. The azimuthal correlations method has been used for the experimental reaction plane calculation. The effect of requiring that the SumZ $> 40\% \cdot Z_{sys}$ (red) can be seen in comparison to events with only a charged particle multiplicity > 3 requirement (black).

the total charge of the colliding system ($\sum Z_{frag} > 40\% \cdot Z_{sys}$). This event selection criteria helps remove incomplete events and therefore improves the reaction plane resolution, as shown in Figure 46. The SumZ $> 40\% \cdot Z_{sys}$ event selection caused an average decrease of 11.5% in σ_0. In Figure 47 the reaction plane accuracy for the three experimental reaction systems is compared after applying the SumZ $> 40\% \cdot Z_{sys}$ criterion. The results demonstrate a consistent reaction plane determination between the different systems.

The experimental reaction plane resolution can be compared to the theoretical simulations in which the difference between the reconstructed and true reaction plane, $\Delta\phi_{rxnplane}$, can be calculated. In Figures 48 and 49 the distribution of $\Delta\phi_{rxnplane}$ is shown from the AMD-Gemini and CoMD simulations, respectively. The reaction

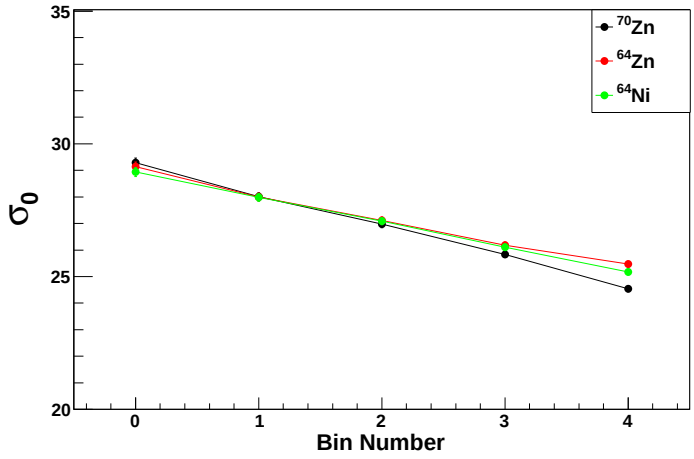

FIG. 47. Standard deviation of the difference between the true and reconstructed reaction plane, σ_0, plotted against the impact parameter selection bin number for the ^{70}Zn (black), ^{64}Zn (red), ^{64}Ni (green) systems. The azimuthal correlations method has been used for the experimental reaction plane calculation and the criteria of SumZ $> 40\% \cdot Z_{sys}$ and multiplicity > 3 have been applied.

plane was reconstructed using the azimuthal correlations method from the filtered theoretical data with the SumZ $> 40\% \cdot Z_{sys}$ criterion. The distributions are strongly peaked around 180° since the attractive mean-field causes the QP to rotate around the QT. Therefore, the QP, which defines the forward flow side, is moving ∼180° from the reaction plane and the reconstructed reaction plane, as mentioned above, should be 180° from the true reaction plane for reactions below the balance energy.

The true standard deviation, σ_{true}, of the reaction plane resolution from the simulations was extracted assuming that the distributions consisted of two Gaussian functions such that,

$$\Delta\phi_{rxnplane} = F + \left(C \cdot \left(R \cdot e^{\frac{-\phi^2}{2\sigma^2_{true}}} + e^{\frac{-(\phi-180)^2}{2\sigma^2_{true}}} \right) \right) \tag{4.8}$$

In summary, the azimuthal correlation method has been found to provide the

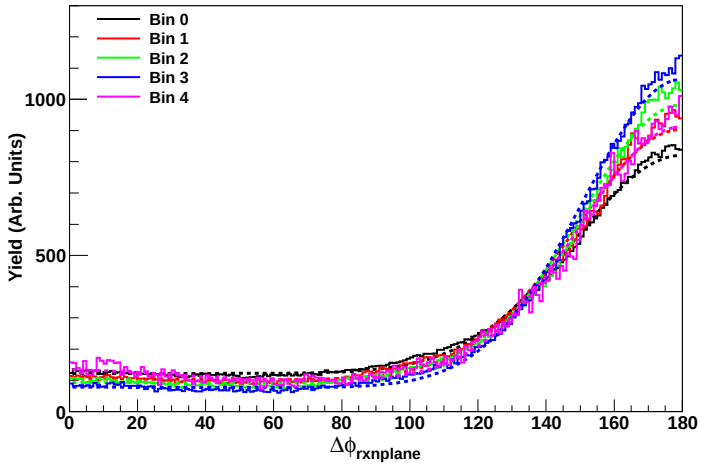

FIG. 48. The difference between the true and reconstructed reaction plane, $\Delta\phi_{rxnplane}$, is shown (solid lines) for each impact parameter selection bin number for the AMD-Gemini simulations. The dashed lines represent a fit to the data following from Equation 4.8. The azimuthal correlations method has been used to reconstruct the reaction plane from the filtered simulation and the SumZ $> 40\% \cdot Z_{sys}$ criterion was imposed. Each distribution has been normalized to the area under the curve.

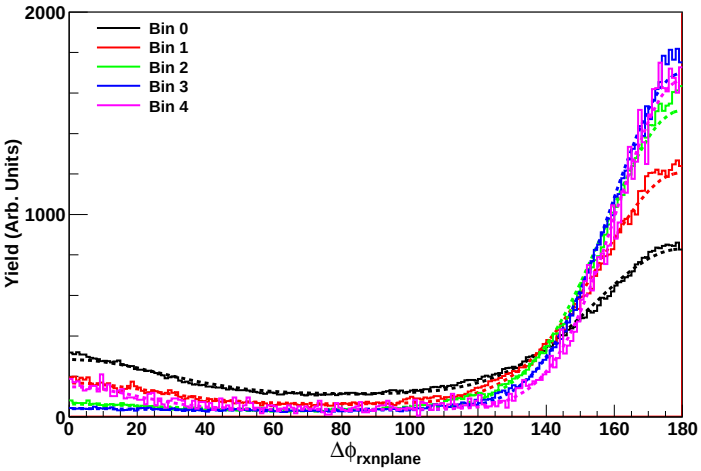

FIG. 49. Same as Figure 48, except results shown are from the CoMD simulation.

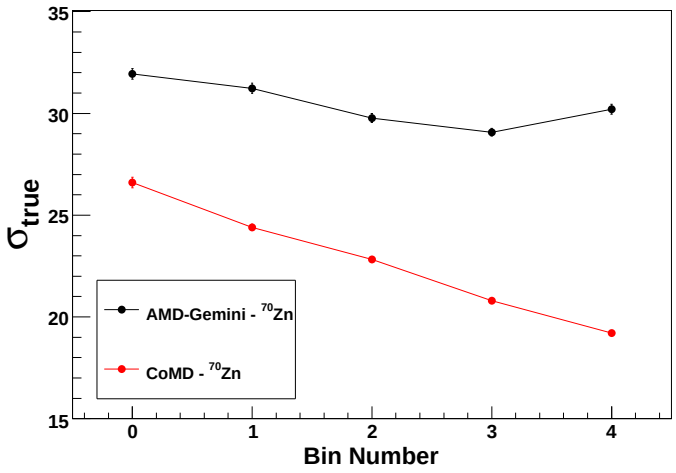

FIG. 50. Standard deviation of the difference between the true and reconstructed reaction plane, σ_{true}, plotted against the impact parameter selection bin number for the AMD-Gemini (black) and CoMD (red) simulations. The azimuthal correlations method has been used to reconstruct the reaction plane from the filtered simulation and the SumZ $> 40\% \cdot Z_{sys}$ criterion was imposed.

most accurate measurement of the reaction plane. The deviation from the reaction plane was decreased upon the requirement that the SumZ of each event be greater than 40% of the total charge of the system. The theoretical simulations allowed for a direct calculation of the standard deviation of the reaction plane calculation and were in good agreement with the experimental results using the event halves. In the following sections the transverse flow study is completed using the azimuthal correlations method for reaction plane reconstruction and an event criterion of SumZ $> 40\% \cdot Z_{sys}$.

C. Transverse Flow of Light Charged Particles (Z=1-2)

The investigation of the collective flow of isotopically identified fragments has been of interest due to possible signatures related to the density dependence of the symmetry energy [35, 34, 13]. In the low to intermediate energy regime there are only a few experimental results in which the transverse flow of isotopically identified fragments has been extracted [44, 66]. In the following, the flow of isotopically resolved particles is examined and isotopic/isobaric trends are explored. Also, the Stochastic Mean-Field model has been used to examine the sensitivity of the results to the density dependence of the symmetry energy.

1. Flow Parameter

The transverse flow is often quantified as the slope of the average in-plane momentum, $\langle Px \rangle$, over mid-rapidity. [44, 9, 8]. In Figure 51, the average in-plane momentum per nucleon is plotted as a function of the reduced rapidity for the different isotopically identified LCPs. The reduced rapidity, Yr, is defined as the ratio of the center-of-mass rapidity of the particle to the center-of-mass rapidity of the projectile, $\mathrm{Y}_{cm}/\mathrm{Y}_{cm,proj}$.

In mass symmetric collisions the reduced rapidity of the projectile and target are then defined as Yr = 1 and Yr = -1, respectively.

The solid line, shown in each panel of Figure 51, depicts a linear fit over the region -0.35 $\leq$ Y_r $\leq$ 0.35. The extracted slope of the linear fit represents the transverse flow of the LCPs and is referred to as the flow parameter. This range was chosen since the smooth curvature of the $\langle Px/A \rangle$ changes around Y_r $\cong$-0.35 due to the backward angle detector thresholds. The statistical error in the flow parameter was calculated from the error in the linear fit. Systematic errors associated with the fit range were estimated to be, on average, at most +1 and -0.4 (MeV/c)/A, by varying the fit range between -0.4 $\leq$ Y_r $\leq$ 0.4 and -0.15 $\leq$ Y_r $\leq$ 0.15. Unless noted, only the statistical errors are shown. The following light charged particle (LCP) results are presented for three different centrality bins: violent (3Bin0), mid-peripheral (3Bin1), and peripheral (3Bin2).

In examining Figure 51, it is clear that the shapes of the flow plots are not symmetric around Yr=0. In an perfect detector, or a simulation, one would expect a symmetric shape around Yr=0 since the systems under study are symmetric. The difference observed can be attributed to the lack of symmetry in the NIMROD-ISiS array. The backward angle detectors of the NIMROD-ISiS array have higher thresholds than the forward angle detectors. However, the lack of symmetry and detector thresholds do not prevent the extraction of the transverse flow for the light charged particles (LCPs). For heavier fragments, discussed in Section D, the backward angle thresholds require a different method for quantifying the flow.

2. Experimental LCP Results

The extracted transverse flow of the Z=1 and Z=2 particles is shown in Figure 52 as a function of the neutron-to-proton ratio of the colliding system, $(N/Z)_{sys}$. Fo-

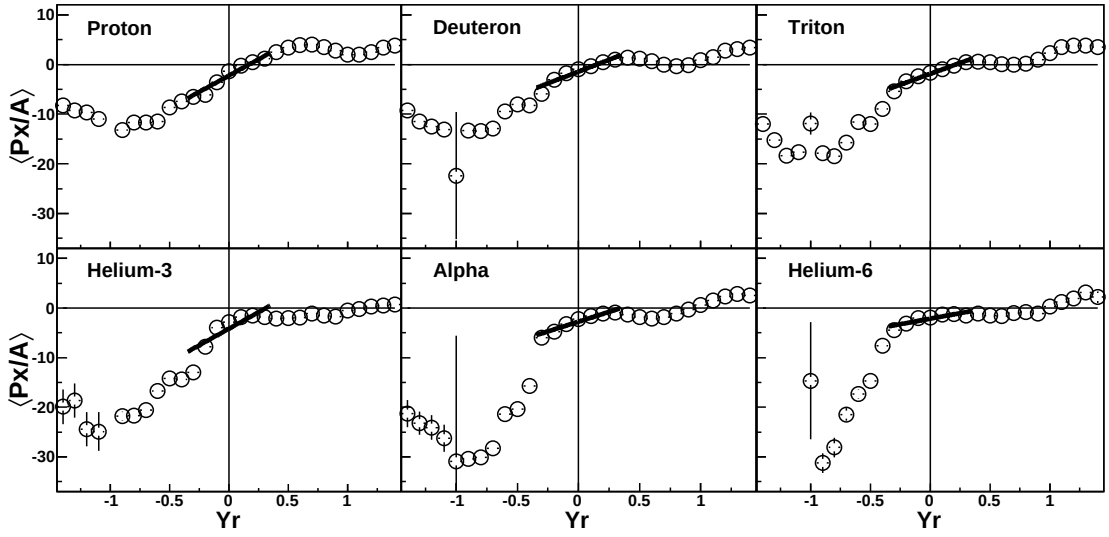

FIG. 51. Average in-plane momentum, $\langle Px/A \rangle$, as a function of the reduced rapidity for protons, deuterons, tritons, ^{3}He, alpha and ^{6}He particles. The results shown are from the mid-peripheral collisions (3Bin1) of the ^{64}Ni+^{64}Ni system. The solid black line represents a linear fit from -0.35 $\leq$ Y$_r$ $\leq$ 0.35.

cusing on the ^{64}Ni+^{64}Ni (N/Z=1.28) and ^{64}Zn+^{64}Zn (N/Z=1.13) systems, a clear dependence on on the $(N/Z)_{sys}$ is present. The results show an increased flow in the more neutron-rich system for the Z=1 and Z=2 particles. This is consistent with the previous observation by Pak *et al.* for Z=1-3 fragments from systems with the same mass (A_{sys}). [53]. The observed isospin dependence by Pak *et al.* was attributed to the isospin dependence of the mean-field and isospin-dependent nucleon-nucleon collisions [53, 56].

The results from the most neutron-rich ^{70}Zn (N/Z=1.33) system showed a decreased flow in comparison to the ^{64}Ni (N/Z=1.28) system. This demonstrates that the $(N/Z)_{sys}$ dependence of the transverse flow is not observed with the ^{70}Zn system. The difference between the A_{sys}=128 and A_{sys}=140 systems can be qualitatively understood through the dependence of the transverse flow on the attractive mean-field and repulsive nucleon-nucleon collisions, both of which scale with the mass of the system [48]. Therefore, below the balance energy the flow should decrease as a function of A_{sys} [48], due to the balance between the attractive mean field and nucleon-nucleon collisions, while also increasing as a function of $(N/Z)_{sys}$ [53], due to the isospin dependence of mean-field and isospin-dependent nucleon-nucleon collisions. The results from Figure 52 exhibit the effects of both the mass and isospin dependent components of the transverse flow.

The results of Figure 52 can be expanded upon through examining the flow per nucleon of isotopically identified light charged particles, as shown in Figure 53 for the mid-peripheral collisions. Again, an enhancement in the transverse flow from the ^{64}Ni system (solid black circles) is observed in comparison to the ^{64}Zn system (open pink circles) demonstrating that the $(N/Z)_{sys}$ dependence is also present for the Z=1 and Z=2 isotopes. This expands on the work of Pak *et al.* [53] and shows that the observed $(N/Z)_{sys}$ dependence of the Z=1 and Z=2 flow is not due to differing isotopic

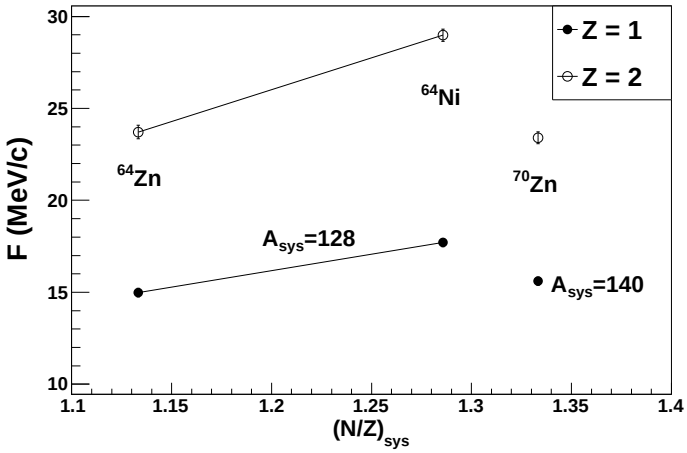

FIG. 52. The experimental flow parameters (F) for the Z=1 and Z=2 fragments are shown as a function of the N/Z of the colliding system, $(N/Z)_{sys}$, for the mid-peripheral collisions. The A_{sys}=128 systems are connected by a solid line.

distributions in the two systems. For example, the increased Z=1 flow in the more neutron-rich system could have potentially been due to an increased triton yield, since the Z=1 results represent a combination of all H isotopes.

Additionally, the results from the ^{70}Zn system (solid green squares) show for all isotopes, except tritons and ^{3}He, a decreased flow in comparison to the A_{sys}=128 systems, as expected from the Z=1 and Z=2 flow. This again illustrates the mass dependence of the transverse flow due to the attractive mean-field and nucleon-nucleon collisions. It is interesting to note, that the observed trend in the flow from the reaction systems is not seen for the triton and ^{3}He fragments where the flow from the ^{70}Zn system is larger than that from the ^{64}Zn system. This suggests that the flow of the A=3 fragments may be sensitive to a different reaction mechanism than the other fragments.

Isotopic and isobaric trends can also be explored from the extracted flow param-

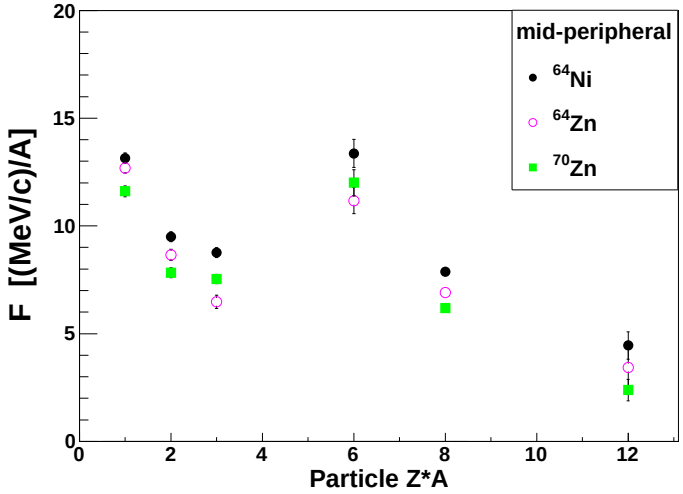

FIG. 53. The extracted flow parameters (F) per nucleon for the protons, deuterons, tritons, ^{3}He, alpha and ^{6}He particles are shown as a function of the mass times charge (Z*A) of the particle. Results are presented from ^{64}Ni, ^{64}Zn, and ^{70}Zn systems for mid-peripheral collisions as shown by the legend.

eters in Figure 53. A distinctive isotopic trend is observed, in which the transverse flow per nucleon is decreasing as a function of the mass, or N/Z, of the isotope. For the Z=1 isotopes, the protons exhibit the largest flow followed by deuterons and then tritons. Similarly, for the Z=2 isotopes, the ^{3}He fragments have the largest flow followed by the alpha particles and then ^{6}He fragments. A clear decrease in the flow with increasing neutron content is shown. This would suggest a smaller flow for neutrons in comparison to protons or that the neutron-rich fragments are originating from a different source, such as a neutron-rich neck region.

Examination of the transverse flow of the triton and ^{3}He fragments provides an isobaric comparison. The results, as shown in Figure 53, demonstrate an enhancement in the ^{3}He flow in comparison to the triton flow. This, again, indicates a decreased flow with increased neutron content. Therefore, in comparing fragments with a constant

charge (isotopes) or a constant mass (isobars) a consistent trend is observed, showing a decreased flow for the more n-rich fragments. Thus, these results (Figures 52-53) show that both the $(N/Z)_{sys}$ and the $(N/Z)_{frag}$ are important in describing the observed transverse flow results.

To further investigate the difference in the triton and ^{3}He flow the energy spectra of the particles were compared (Figure 54). The results are shown from rings 2, 8, 9 , and 10. The results from ring 2, as well as the other forward angle rings, show a relatively large difference between the triton and ^{3}He energy spectra. The triton energy spectra shows a much larger low energy component, often referred to as an evaporative component, than the ^{3}He fragments which are dominated by the higher energy component. This could potentially provide insight into the difference in the transverse flow. However, the flow is extracted from the mid-rapidity fragments which are largely detected in rings 8-10. The triton and ^{3}He energy spectra from these rings are shown in Figure 54. The results for the mid-rapidity triton and ^{3}He fragments (rings 8-10) do not show the large differences in the energy spectra observed in ring 2. Instead the energy spectra seem to indicate that the triton and ^{3}He fragments are coming from similar sources or mechanism. Therefore, it is unlikely that the decreased triton flow is due to a larger evaporative component since that is not present in the KE spectra for rings 8-10.

While the mid-peripheral reactions have been shown to provide the best signatures of the transverse flow [35, 34, 150], it is also interesting to examine the results in the more violent and peripheral collisions. The flow of the isotopically resolved particles from the most violent collisions is presented in Figure 55. The strong $(N/Z)_{sys}$ dependence of the flow is again observed as the flow from the ^{64}Ni system is increased relative to the ^{64}Zn system.

The expected decreased flow of the ^{70}Zn system with respect to the A_{sys}=128

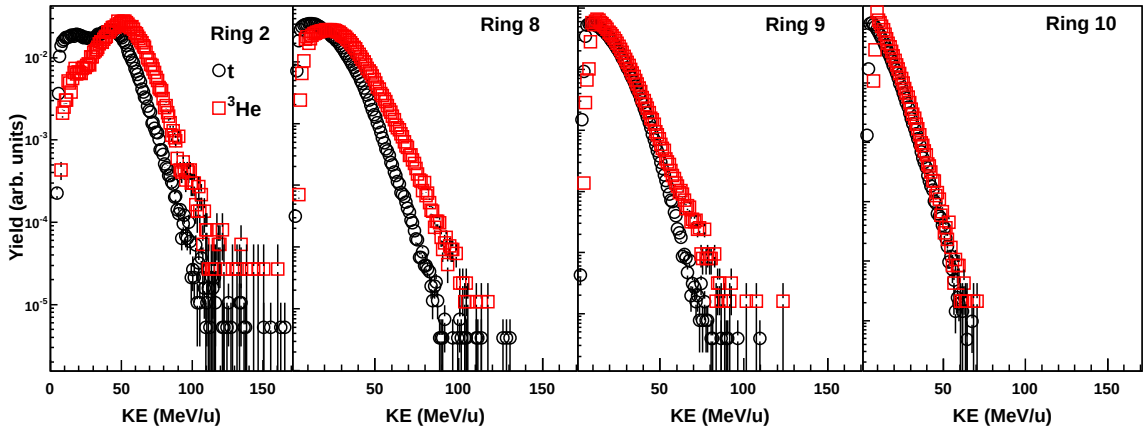

FIG. 54. Triton and ^{3}He kinetic energy distributions are compared for the mid-peripheral (3Bin1) ^{64}Ni+^{64}Ni collisions. The energy spectra from rings 2, 8, 9, and 10 are presented and the area of each distribution has been normalized to 1.

systems (due to the mass dependence) was only present in the proton, ^{3}He, alpha and ^{6}He particle flows for the most violent collisions (Figure 55). The deuteron and triton fragments present a different trend. Thus, while the $(N/Z)_{sys}$ dependence is very clear in both the violent and mid-peripheral collisions, with the ^{64}Ni flow larger than ^{64}Zn flow for all fragments, the mass dependence can vary. For example, the mid-peripheral triton and ^{3}He results, as well as the triton results from the violent collisions, all show an increased flow in the ^{70}Zn system in comparison to the ^{64}Zn system. As mentioned above, these differences may be indicate that different mechanisms are responsible for the production and/or flow of these fragments in the violent or mid-peripheral collisions.

Other than the deuteron and triton flow in the ^{70}Zn violent collisions, the isotopic and isobaric trends demonstrating a decreasing flow with increasing neutron content are clearly observed in both the violent and mid-peripheral results. However, the isotopic trend is not as strongly present in the violent collisions in comparison to the

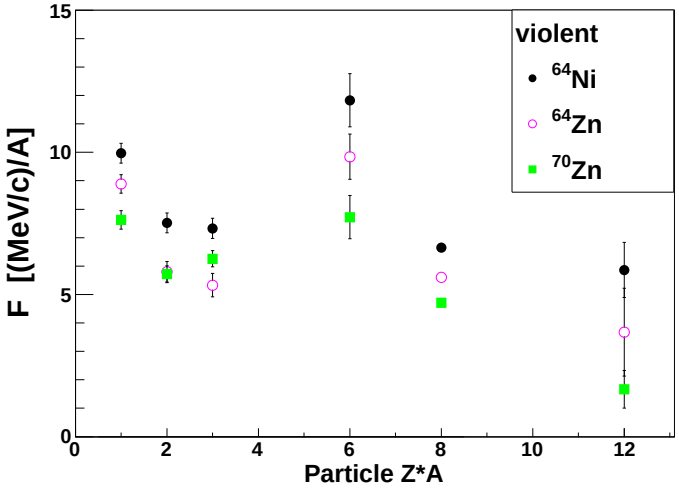

FIG. 55. Same as Figure 53 except results are presented for the violent collisions (3Bin0).

mid-peripheral collisions. In particular, the decreased flow between the deuteron and triton fragments, as well as alpha and ^{6}He fragments, is not as large in the violent collisions as it is in the mid-peripheral collisions. This shows that the central collisions are not as sensitive to the isotopic trends. While the isotopic trends are decreased, the isobaric trend is still relatively prominent in the violent collisions.

The transverse flow of the LCPs from the peripheral collisions is shown in Figure 56. The results show very strong isotopic and isobaric trends in the flow. As observed in the violent and mid-peripheral reactions, the transverse flow decreases with increasing neutron content for both the isotopes and isobars. It is also interesting to note that the system dependence of the transverse flow is not, in general, present for the peripheral reactions. There does appear to be a slight increase in the flow from the ^{64}Zn system relative to the ^{64}Ni and ^{70}Zn systems for the proton, deuteron, alpha, and ^{6}He particles. This presents an interesting change in the $(N/Z)_{sys}$ depedence of the transverse flow, where the flow is larger in the less neutron-

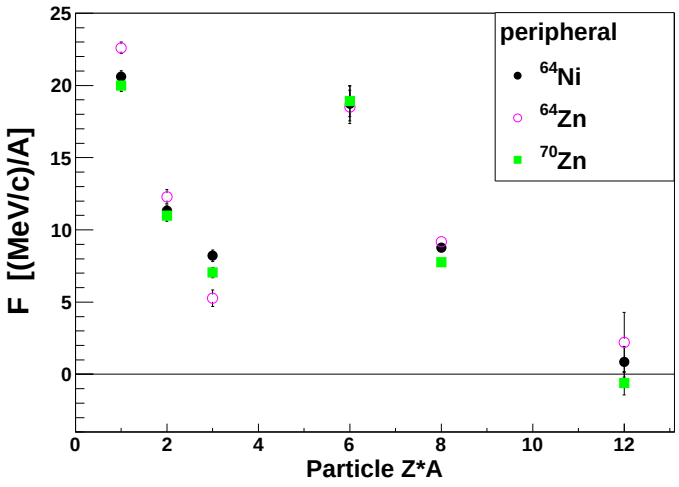

FIG. 56. Same as Figure 53 except results are presented for the peripheral collisions (3Bin2).

rich system for the peripheral collisions. Overall, for the peripheral collisions, the isotopic/isobaric trends become very strong while the system dependences are diminished. Thus, the mid-peripheral collision results are particularly interesting in that both the isotopic/isobaric trends and a relatively strong system dependence on the flow is observed.

The fragment flows from the violent, mid-peripheral, and peripheral collisions all present relatively consistent results for the isotopic and isobaric trends. Combined, they imply a differential movement of neutrons and protons in the mid-rapidity region of these Fermi energy heavy-ion collisions, where the proton movement enhances the flow and the neutron movement decreases the flow.

3. Stochastic Mean-Field Model Results

The transverse flow of the LCPs was investigated within the framework of the Stochastic Mean-Field (SMF) model [133, 134]. As discussed in Chapter III, the SMF model

uses the test-particle method to solve the Boltzmann-Langevin transport equation[135]. The potential used in the simulation allows for the density dependence of symmetry energy and the effective mass splitting to be examined independently. The potential was chosen such that the effective mass of the neutrons was greater than that of the protons ($m_n^* > m_p^*$). The simulation was stopped at 120 fm/c and a phase-space coalescence was applied to identify of the fragments. Thus, in comparing the experimental and theoretical results it is important to understand that the simulation provides information about the initial fragments emitted from the collision. However, previous theoretical results have shown that the magnitude of the transverse flow should saturate in <100 fm/c [49, 168, 51, 169]. Also, since the beam energy is below the balance energy the transverse flow extracted from the SMF model is negative. Therefore, in order to compare the SMF model to the experimental data, in which the flow is positive by convention, the sign of the flow from the SMF model was changed to be positive.

The $(N/Z)_{sys}$ dependence of the Z=1 particle flow was examined with the SMF model and compared to the experimental data in Figure 57. The magnitude of the Z=1 flow is underestimated by the SMF model in comparison to the experimental data. However, the trend of the flow between the systems can be examined. In particular, the results show that the difference in the Z=1 particle flow between the A_{sys}=128 systems is sensitive to the density dependence of the symmetry energy. Scalone *et al.* had previously suggested that the dependence of the LCP flow on the $(N/Z)_{sys}$ should be sensitive to symmetry potential [34].

In Figure 57, a 4.3% increase in the flow from the ^{64}Ni system relative to the ^{64}Zn system is produced with the stiff symmetry potential. The soft symmetry potential produced a 0.3% decrease in the flow between the ^{64}Ni and ^{64}Zn systems. In comparison, the experimental data showed an 8.3% increase in the Z=1 flow from the ^{64}Ni

system, relative to the ^{64}Zn system. Thus, the experimental trend was reproduced better using a stiff symmetry potential with the SMF model.

Furthermore, a decreased flow in the ^{70}Zn system, in comparison to the ^{64}Ni system, was observed for both the stiff and soft SMF results, as shown in Figure 57, which is again in agreement with the experimental data and demonstrates the mass dependence of the transverse flow. In comparing the ^{64}Zn and ^{70}Zn results the experimental data shows nearly equivalent flow, which represents a balance between the mass and $(N/Z)_{sys}$ dependences. The stiff SMF results show a similar trend, while the calculations with a soft symmetry potential show a decreased ^{70}Zn flow relative to the ^{64}Zn flow. Thus, the SMF model with a stiff symmetry potential appears to reproduce both the mass and $(N/Z)_{sys}$ dependence of the LCP flow. The Z=2 results from the SMF model are not shown in Figure 57 because there was no statistical difference in the flow between the three systems.

The $(N/Z)_{sys}$ dependence observed in the SMF results, discussed above, suggests a sensitivity to the low-density region of the symmetry potential. Below the saturation density, the soft symmetry potential is more repulsive for neutrons than the stiff potential. Thus, the repulsive potential decreases the flow in the neutron-rich ^{64}Ni system relative to the ^{64}Zn system in the soft case. In the stiff case the potential is less repulsive and therefore, the ^{64}Ni flow remains larger than the ^{64}Zn flow, as observed in the experimental data.

In Figure 58 the experimental isotopic LCP flow is compared to the SMF model for the mid-peripheral collisions. In general the magnitude of the fragment flows from the SMF model are larger than the experimental flow. This may be due to the reaction plane dispersion [166] present in the experimental analysis, which will decrease the extracted flow value. The SMF results are shown with respect to the true reaction plane and therefore, are not subject to any reaction plane dispersion.

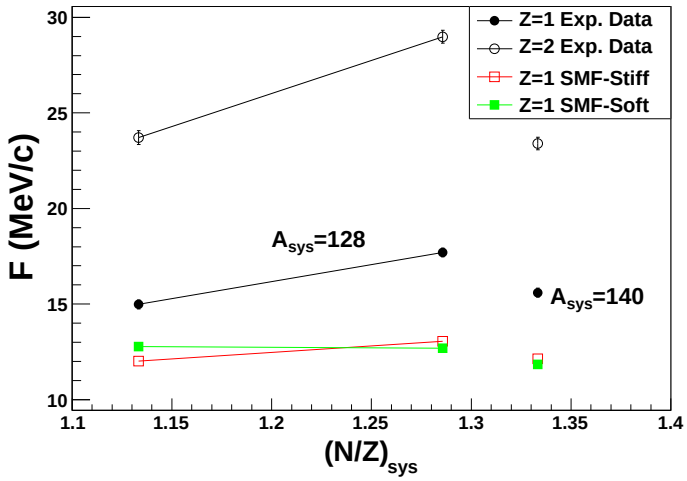

FIG. 57. The experimental flow parameters (F) for the Z=1 and Z=2 fragments are shown as a function of the N/Z of the colliding system, $(N/Z)_{sys}$, for the mid-peripheral collisions. The Stochastic Mean-Field (SMF) model results are shown for the Z=1 fragments for a stiff and soft $E_{sym}(\rho)$. The ^{64}Zn and ^{64}Ni systems, A_{sys}=128, are connected by a solid line.

However, isotopic/isobaric trends from the experiment are not affected by the reaction plane dispersion [166].

Despite the difference in magnitude of the flow, the agreement in the fragment flow trends between the model and the experimental data are impressive. Except for the proton flow, the SMF isotopic trends showed a decreasing flow with an increasing neutron content, as was observed in the experimental data. The SMF model is even able to reproduce the decreased difference between the deuteron and triton flow in the ^{70}Zn system showing that the isotopic trend is changing in the most massive system. This agreement between the fragment flow trends suggests that the SMF model is correctly calculating the differential movement of the neutrons and protons in the mean-field. Thus, in both the experiment and theory a decreased flow is observed with increasing neutron content of the fragments.

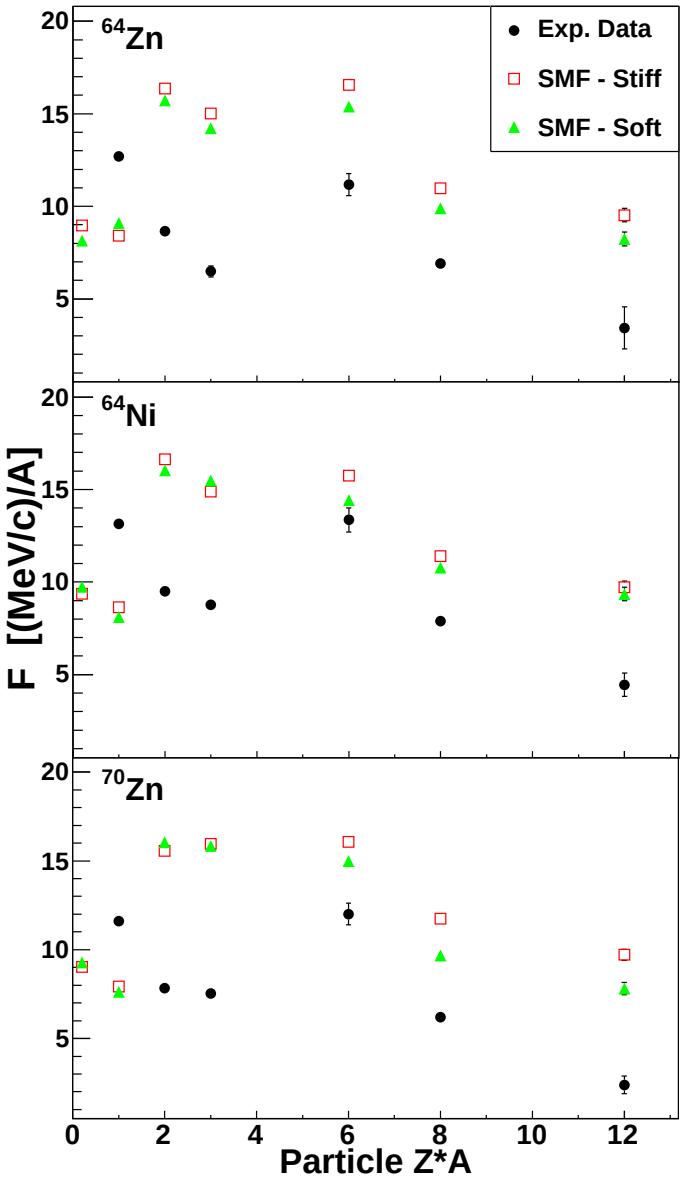

FIG. 58. Flow parameter (F) per nucleon is shown as a function of the mass times charge (Z*A) for the mid-peripheral collisions(3Bin1). The experimental data is shown in comparison to the Stochastic Mean-Field model results, for both a stiff and soft parameterization of the symmetry energy. The free neutron flow from the SMF model is offset with a Z*A = 0.1 for clarity.

The main discrepancy between the experimental and SMF results is that the proton flow in the SMF model is decreased relative to the deuteron and triton flows. This is attributed to the overproduction of the free nucleons due to the lack of n-body correlations in the mean-field approach [170]. This is an intrinsic problem with the one-body approach. Therefore, the additional free protons, that in reality should have been correlated with other nucleons, will decrease the flow relative to the correlated nucleons which are identified as fragments through the coalescence procedure. The overproduction of the protons was verified through examining the mid-rapidity yield of the LCPs from the SMF model in comparison to the experimental data, as shown in Figure 59. The silicon detector thresholds were applied to the SMF model results for the comparison and the mid-rapidity yield was determined from $0 \leq Y_r \leq 0.45$. The results, as expected, demonstrate a huge production of protons relative to the complex particles. The SMF model shows a nearly linear decrease in the LCP yield from deuterons to ^{6}He. Except for the alpha yield, this is in agreement with the experimental data. The increased alpha yield in the experiment is due to the n-body correlations that are not present in the mean-field simulation.

The LCP flow results between the SMF model and experimental data were also compared for the more violent collisions, as shown in Figure 60. The difference in the magnitude between the experimental and theoretical flow is increased. This may be the result of an increased reaction plane dispersion in the more central collisions where the reaction plane resolution is decreased. However, in general the results provide similar agreement with the trend of the LCP flow as was observed in the mid-peripheral collisions. The decreasing transverse flow with increased neutron content in the fragments is very prominent in the SMF results. Also, the proton flow from the SMF model is still not in agreement with the experimentally observed isotopic trend. It is worth noting that the SMF model, again, correctly predicts the trend of the

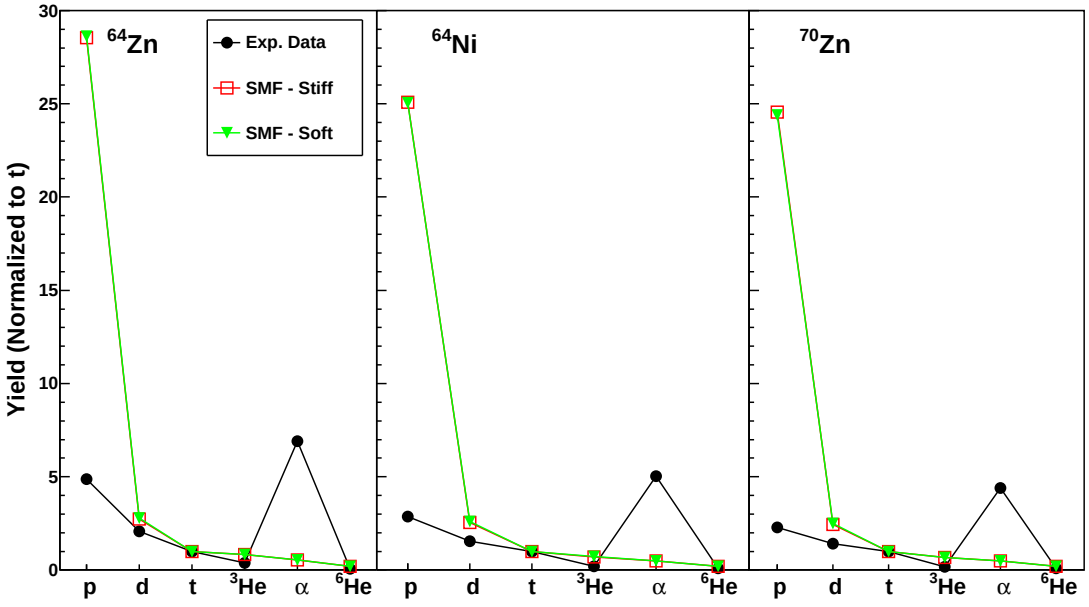

FIG. 59. Mid-rapidity yield ($0 \leq Y_r \leq 0.45$) for the LCPs, normalized to the triton yield, is presented for both the experimental data and the SMF simulation. The silicon detector thresholds have been applied to the SMF results.

deuteron and triton flow in the ^{70}Zn system, showing a slightly increased triton flow relative to the deuteron flow. Thus, both the experimental data and SMF calculation show a distinct change in the deuteron and triton flow in ^{70}Zn system in comparison to the ^{64}Ni and ^{64}Zn systems.

The ability of the SMF model to reproduce the observed isotopic trends demonstrates that the fragment flows are well reproduced by the one-body mean-field dynamics with a phase-space coalescence applied for recognition of the fragment identity. This is particularly interesting since the many-body correlations, often thought to be important in fragment production [171], are only partially accounted for in SMF model simulation. The agreement in the overall trends also suggests that emissions occurring at later times does not have a dominant affect on the observed fragment flow trends for these mid-peripheral collisions. This is expected since it has been shown that the magnitude of the transverse flow should saturate in <100 fm/c [49, 168, 51, 169].

The SMF model provides the opportunity to examine the sensitivity of the isotopically resolved fragment flows to the density dependence of the symmetry energy. In Figure 58 and 60 the results from the SMF model are shown with both a stiff and soft $E_{sym}(\rho)$. In general, the flow is decreased with the soft case which can be attributed to the low density behavior of the symmetry potential. As discussed above, at low density the soft symmetry potential is more repulsive for neutrons and will, therefore, decrease the flow in the neutron-rich systems.

The difference between the triton and ^{3}He flow is also shown to be sensitive, particularly in the mid-peripheral collisions, to $E_{sym}(\rho)$ as predicted previously by Scalone *et al.* [34]. In the ^{64}Ni system from Figure 58 the stiff symmetry potential produces a larger ^{3}He flow than triton flow, while the opposite is shown with the soft symmetry potential. The increased ^{3}He flow relative to the triton flow produced

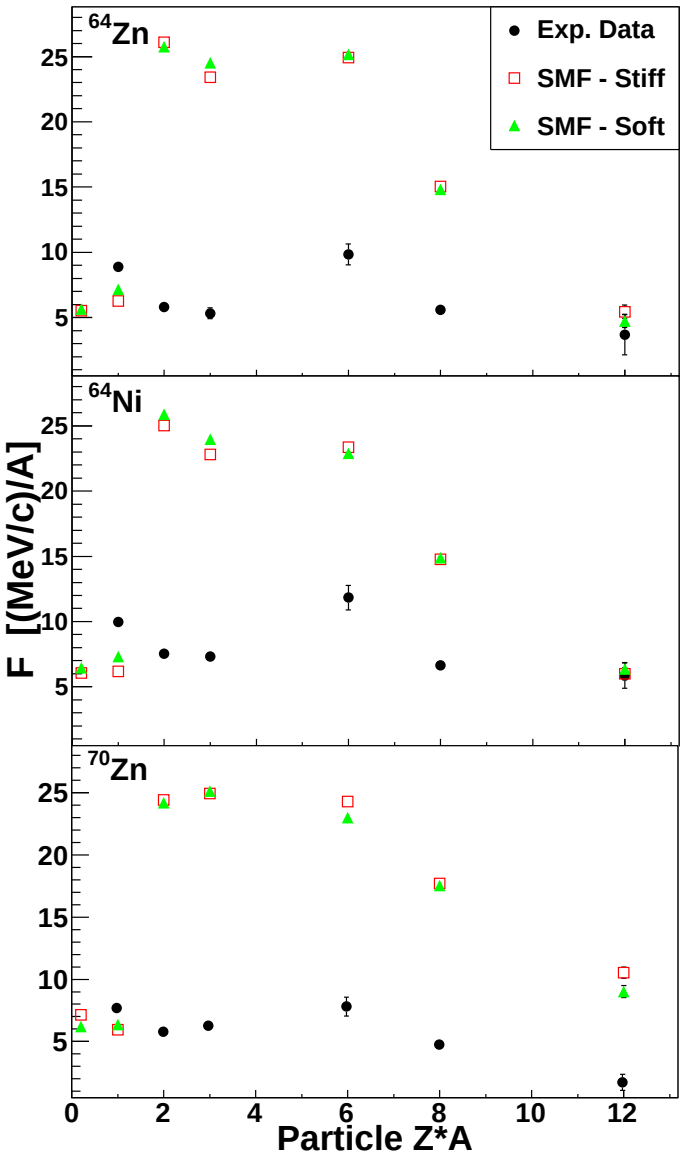

FIG. 60. Same as Figure 58 except the results are presented for the violent collisions (3Bin0).

by the stiff symmetry potential does improve the agreement between the SMF and experimental results. It is interesting to note that the triton-^{3}He differences appears to be more sensitive to the density dependence of the symmetry energy than the free neutron-proton flows, which have been consistently suggested to be strong observables for constraining $E_{sym}(\rho)$ [57, 13, 16, 58, 59, 60].

The results discussed above can be interpreted in terms of a more neutron-rich emission from the neck region in the stiff case [88]. The lower value of the stiff symmetry potential, with respect to the soft, during the expansion phase of the system leads to less repulsive dynamics, associated with a generally larger flow of the LCPs (see Figure 58). At the same time, the neutron excess is transferred towards the low-density neck region, from which light charge particles eventually emerge. The latter mechanism, that is sensitive to the derivative of the symmetry energy just below normal density, is also more effective in the stiff case producing a more neutron-rich neck region [88]. This is confirmed by examining the triton-^{3}He yield ratio as a function of the reduced rapidity for both the stiff and soft symmetry potential, as shown in Figure 61. An increased triton-^{3}He ratio is observed in the stiff case, relative to the soft, in the mid-rapidity region. The larger asymmetry of the neck region in the stiff case also explains the larger repulsion seen for tritons, with respect to ^{3}He, thus producing a decreased flow (see Fig. 58 middle panel).

In order to quantitatively compare the triton-^{3}He flow between the experiment and SMF calculations the percent difference was calculated as,

$$R_{3He-t} = \frac{F^{3He} - F^t}{F^{3He} + F^t} \tag{4.9}$$

where F^{3He} and F^t represent the flow parameter extracted for the ^{3}He and triton fragments. Thus, if $R_{3He-t} > 0$ the ^{3}He is larger than the triton flow and $R_{3He-t} < 0$ means the triton flow is larger then the ^{3}He flow. In Figure 62, R_{3He-t} is shown from

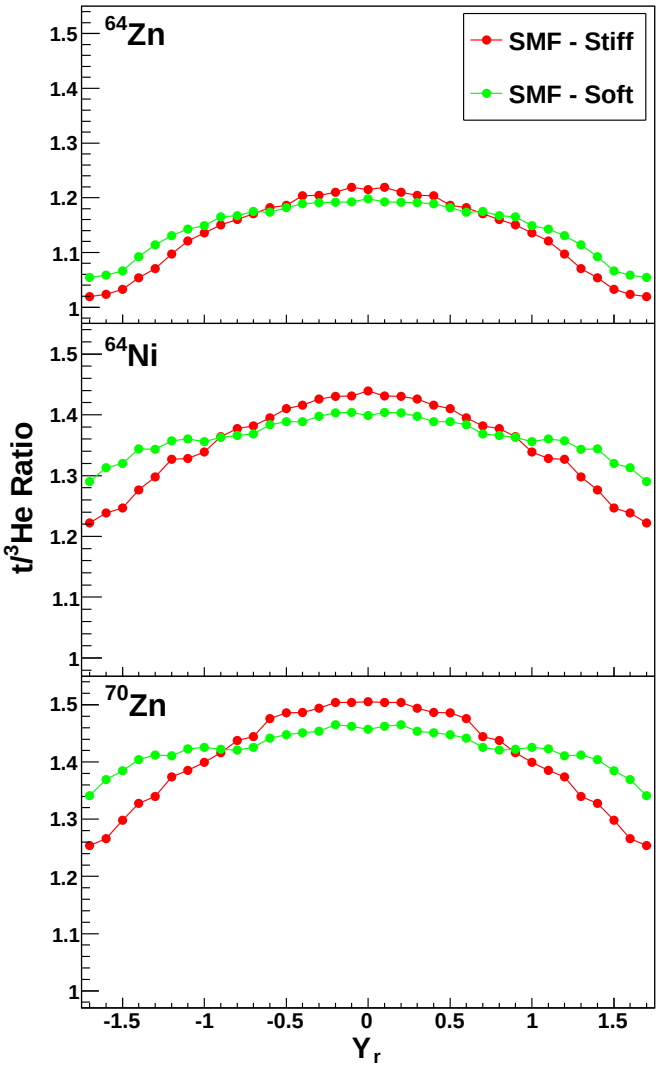

FIG. 61. Triton-^{3}He ratio as a function of the reduced rapidity (Y_r) is presented from the SMF simulation using both a stiff and soft symmetry potential for the ^{64}Zn, ^{64}Ni, and ^{70}Zn systems.

the experiment (blue fill area) and SMF model (circles) for the mid-peripheral (right panel) and most violent (left panel) collisions. The estimated systematic error in the experimental flow was accounted for and is shown by the dashed red line. The width of the blue fill area represents the statistical, or fit, error in extracting the transverse flow. The largest uncertainty comes from the statistical/systematic error present in the ^{3}He flow. The SMF model results are shown both with (black shapes) and without (grey shapes) applying the silicon detector thresholds. The results from the stiff and soft symmetry energy parameterizations with, $m_n^* > m_p^*$, are shown for each system as the closed and open circles, respectively. The effective mass splitting was examined for the mid-peripheral collisions of the ^{70}Zn system as shown in Figure 62.

The SMF model results, with and without the detector thresholds, demonstrate a sensitivity of the triton-^{3}He flow to the density dependence of the symmetry energy, specifically for the more neutron-rich ^{64}Ni and ^{70}Zn systems. In the ^{64}Zn system the R_{3He-t} value is not as sensitive to $E_{sym}(\rho)$ because the asymmetry of the system is smaller and therefore the magnitude of the symmetry potential is smaller. Applying the detector thresholds to the simulated data produced an overall enhancement in the magnitude of R_{3He-t}, moving it in closer agreement with the experiment. In general, the triton-^{3}He difference is underestimated by the SMF model. However, a stiff density dependence of the symmetry energy provides the better agreement with the experimental data. In particular, the stiff SMF results from the central ^{70}Zn and mid-peripheral ^{64}Ni are within the systematic error bars of the experimental data.

The SMF model demonstrates an unique interplay between the behavior of the symmetry potential at densities below and close to the saturation value in describing the fragment flows. The increased flow in the neutron-rich systems observed with the stiff symmetry potential suggests a sensitivity to the low density region, while the effect of the symmetry potential on the triton-^{3}He flow is influenced by the neck

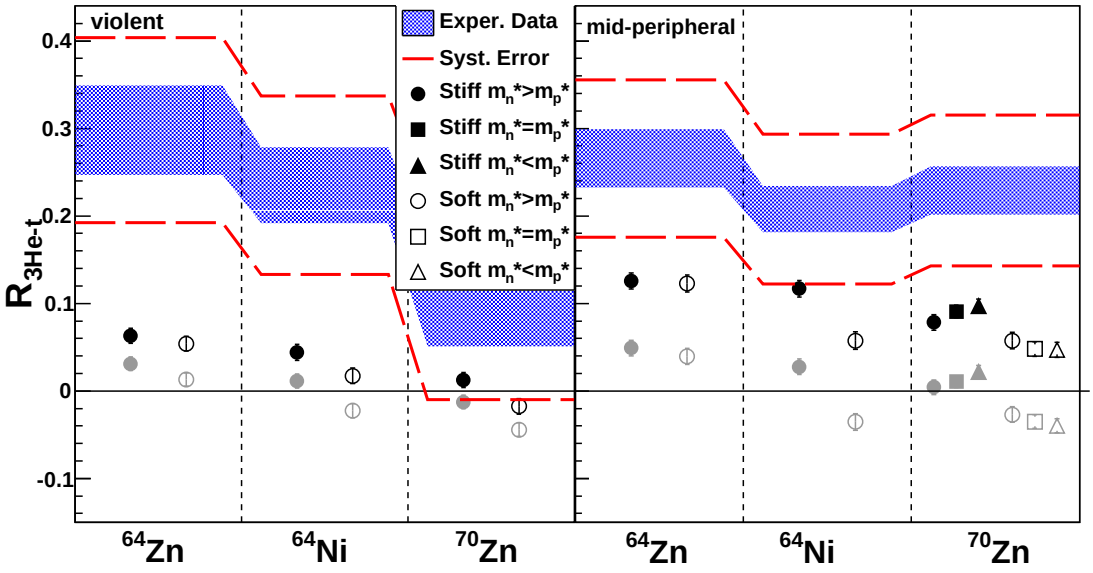

FIG. 62. R_{3He-t}, from Equation 4.9, is calculated from the ^{64}Ni, ^{64}Zn, and ^{70}Zn systems for the violent (Left panel) and mid-peripheral collisions (Right panel). The results from the experimental data, including the fit error, are represented by the faded blue region. The estimated systematic error in the experimental results is represented by the red dashed line. The SMF results are shown with (black) and without (faded grey) applying the silicon detector thresholds. As described by the legend, results with a soft and stiff density dependence of the symmetry energy are shown from the SMF model. For the mid-peripheral ^{70}Zn collisions the order of the effective mass splitting has been varied.

dynamics, that are sensitive to the derivative of the symmetry energy near normal density. While the SMF calculations were unable to fully reproduce the data, better agreement was observed with a stiff symmetry potential for the experimental features.

The importance of the neck dynamics, suggested by the SMF model, may also provide insight into the observation of the decreased flow with increasing neutron content of the LCPs (see Figs. 53-58). The *isospin migration* phenomenon [88, 38] represents the movement of neutrons and protons in opposite directions due to a density gradient. Thus, neutrons preferentially move towards the low-density neck region, while protons will travel towards a higher density region (near the saturation density), such as the projectile-like fragment (PLF). If the transverse flow is thought to represent the movement, or flow, of particles following the PLF and TLF then the proton movement, due to the isospin migration, may enhance the transverse flow. Likewise, the opposite movement of neutrons could diminish the flow. Thus, upon coalescence of the free nucleons the proton-rich fragments, such as ^{3}He, would exhibit an larger flow with respect to neutron-rich fragments, such as tritons. Further investigation of this concept is required, such as examining the LCP flow in isospin asymmetric systems where *isospin diffusion* [33] is present and may enhance the observed trends.

Another interesting observation is the sensitivity of the triton and ^{3}He flow to the isospin effective mass splitting. Determining the isospin dependence of the effective mass has become an important task, along with constraining $E_{sym}(\rho)$, and collective flow measurements have been suggested to be sensitive [172, 133, 173]. Recently, Li used experimental nucleon-nucleus scattering data to indirectly rule out an effective mass splitting of $m_n^* < m_p^*$ [174]. However, as seen in Figure 62 an effective mass splitting of $m_n^* < m_p^*$ with a stiff density dependence of the symmetry energy provides the largest R_{3He-t} value, which is the closest to the experimental data. While the

triton-^{3}He flow is sensitive to the effective mass splitting it is difficult to draw any definitive conclusions from these results.

4. Molecular Dynamics LCP Flow

The antisymmetrized molecular dynamics (AMD) [130] and constrained molecular dynamics (CoMD) [128, 129] models, along with Gemini [141], were used to explore the dynamical aspects of the transverse flow of light charged particles. A hybrid, or two-stage, approach has become a common method for simulating heavy-ion collisions. This consists of using a dynamical model, such as AMD or CoMD, to simulate the early stages of the collision coupled with a statistical model, such as Gemini, to de-excite the hot fragments to a final state. The hybrid approach has developed due to the extensive computational time required to simulate the entirety of a heavy-ion reaction with an AMD- or CoMD-type model. Therefore, the dynamical models are often stopped at a relatively early time stage, often around 300 fm/c, to minimize the computational requirements. Then the statistical decay calculation, which is extremely fast, is applied to allow for examination of the final cold fragment distribution from the reaction.

In using the hybrid approach it is important to understand the assumptions associated with the coupling to the statistical model. Around 300 fm/c, the dynamical model produces a distribution of fragments in phase-space which are likely dilute, deformed, and excited. However, from the dynamical simulation only the excitation energy, angular momentum, charge, and mass of the fragment are input into the Gemini model. Therefore, the statistical decay assumes that the fragment is in thermal equilibrium, spherical, and at the saturation density (ρ=0.16 fm^{-3}). Also, after applying the statistical model the fragments are propagated with no further nuclear or Coulomb interactions from the surrounding system. Thus, it is possi-

ble that correlations present before the application of the statistical model could be lost. It is clear that some of the dynamical aspects and correlations of the system may be sacrificed through the hybrid approach. Despite these limitations, the hybrid approach has been successfully used for the modeling of heavy-ion collisions [107, 130, 175, 176, 177, 32, 178]. Many of the comparisons have been focused on the reproduction of fragment yields and multiplicities, charge and mass distributions, and global event observables. However, a recent study by Hudan *et al.* suggested that the dynamical and statistical aspects of the collisions can not be decoupled, as the hybrid approach assumes [179].

Since the transverse flow should be strongly connected to the dynamics of the collision it provides an excellent observable to examine the validity of the hybrid approach. The AMD model was used to simulate the collision for 300 fm/c before the Gemini code was applied to the hot fragments. The CoMD model allowed for the reaction to be propagated to 3000 fm/c, which allows for a dynamical evolution and decay of the system. The Gemini code was still applied to decay any hot or unstable fragments still present at 3000 fm/c. Thus, examining the effect of the Gemini model can provide insight into how the assumptions associated with applying the statistical model affect the ability to accurately describe the dynamical nature of the collision.

In Figure 63 the transverse flow calculated from the AMD simulation for the LCPs is compared to the experimental data. The results are shown with and without applying Gemini at 300 fm/c. The addition of the Gemini de-excitation (solid triangles) produces a strong enhancement in the transverse flow in comparison to the flow at 300 fm/c (open squares). This was an unexpected result since the transverse flow is often thought to be a combination of collective and thermal motion [62, 9]. The thermal component of fragments momentum, or kinetic energy, should be random and therefore, decrease the collective motion. However, these results suggest that

even though the hot fragments are statistically de-excited, the original collective motion of the parent is the dominant component in the final momentum of the decayed fragment, which produces the increased transverse flow. For example, an excited PLF will be strongly aligned with the reaction plane and any fragments emitted from the PLF would also exhibit a strong in-plane enhancement.

Even though a reasonable explanation can explain the increased flow with respect to the Gemini de-excitation, the results are in conflict with previous theoretical studies which suggest that the magnitude of the transverse flow should saturate in <100 fm/c [49, 168, 51, 169]. The AMD-Gemini results of Figure 63 imply that the flow should increase well beyond 300 fm/c. This suggests that the fragments from the AMD calculations hold onto too much excitation energy and, therefore, the Gemini de-excitation has a large effect, even after 300 fm/c. If the original transport calculations are correct, suggesting a early saturation of the flow, then the statistical Gemini decay is producing an artificial increase in the flow.

In comparing the AMD results to the experimental data it appears that the transverse flow is not well described using the hybrid approach (AMD-Gemini). Except for the proton flow, both the magnitude and trend of the LCP flows are fully reproduced by AMD at 300 fm/c or AMD-Gemini. In order to improve the agreement between the AMD and experimental results, the magnitude of the LCP flows would need to decrease over time rather than increase as the AMD-Gemini results imply. However, both the AMD 300 fm/c and AMD-Gemini results are unable to reproduce the isotopic and isobaric trends. Therefore, it is difficult to determine whether the disagreement between the experiment and AMD-Gemini results are due to the dynamical stage or statistical decay of the reaction.

While the AMD results were unable to reproduce the experimental flow, a comparison of the filtered and unfiltered AMD-Gemini results demonstrates the presence

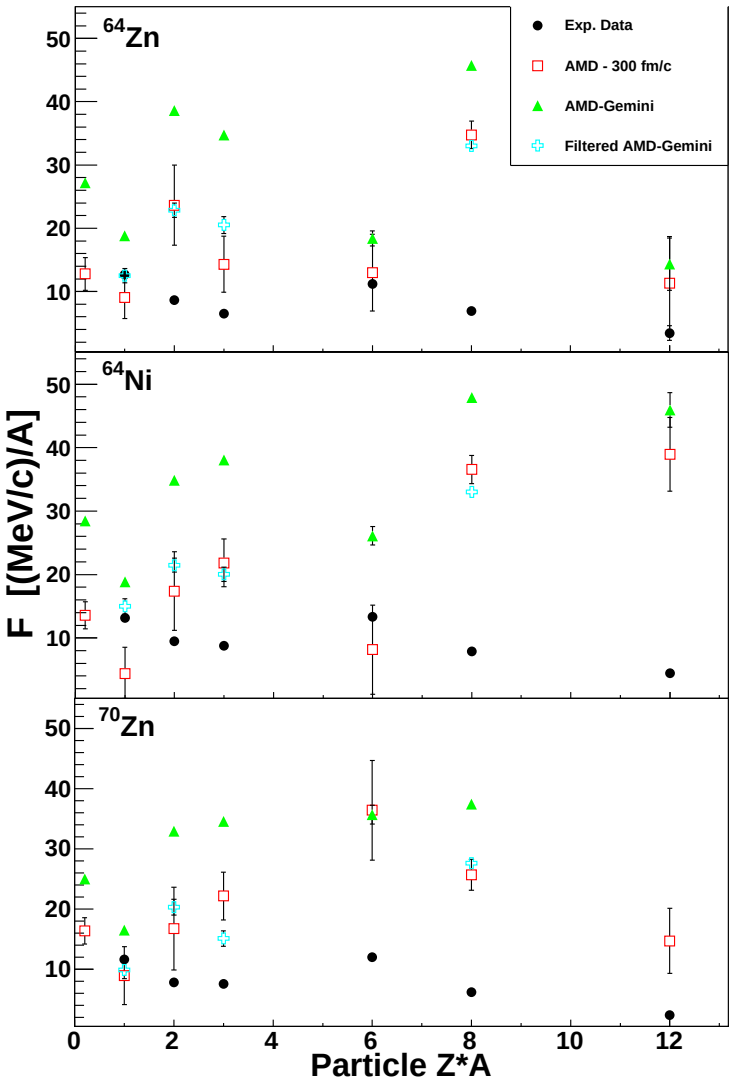

FIG. 63. Flow parameter (F) is shown as a function of the mass times charge (Z*A) for the light charged particles from the AMD simulation in comparison to the experimental data. The both the primary (300 fm/c) and final (300 fm/c + Gemini) flow parameters are shown from the AMD simulation, as well as the filtered AMD-Gemini results. The ^{3}He and ^{6}He results are not shown for the filtered AMD-Gemini since accurate fits over the mid-rapidity region could not be obtained.

of the experimental reaction plane dispersion. The reaction plane reconstruction method, used for the filtered AMD-Gemini results (open crosses), produces a decreased flow in comparison to the unfiltered results (solid triangles) in which the reaction plane angle is known. The results suggest that the reaction plane dispersion could decrease the magnitude of the flow by up to 50%.

The effect of the hybrid approach can be better examined using the CoMD model since the reactions were propagated for 3000 fm/c. Thus, the flow after the Gemini de-excitation can be compared to the flow calculated from a nearly complete dynamical evolution of the system. The comparison presented in Figure 64 provides the CoMD results from t=600 fm/c, t=600 fm/c + Gemini, and t=3000 fm/c + Gemini. It is important to note that at 3000 fm/c the Gemini decay has negligible affect on the LCP flow results and, therefore, is essentially equivalent to the 3000 fm/c (no Gemini) results. The results from the ^{64}Ni, ^{64}Zn, and ^{70}Zn systems are presented for completeness. However, the focus will be on the ^{70}Zn CoMD results due to a three-fold increase in the statistics relative to the other systems.

In comparison to the ^{70}Zn experimental data, the CoMD results at 600 fm/c and 3000 fm/c + Gemini are in relatively good agreement. It is impressive that the 3000 fm/c + Gemini results are able to reproduce the decreasing flow with increasing neutron content for the Z=2 isotopes. Furthermore, the 600 fm/c and 3000 fm/c + Gemini results show good agreement between each other, specifically for the protons and alpha particles which provide the best statistics. This demonstrates that the transverse flow has most likely saturated before 600 fm/c and thus, the results remain relatively unchanged at 3000 fm/c.

The application of Gemini at 600 fm/c has a drastic affect on the observed transverse flow. As observed in the AMD results, the Gemini decay causes an enhancement in the transverse flow, diminishing the agreement with the experimental data. Fur-

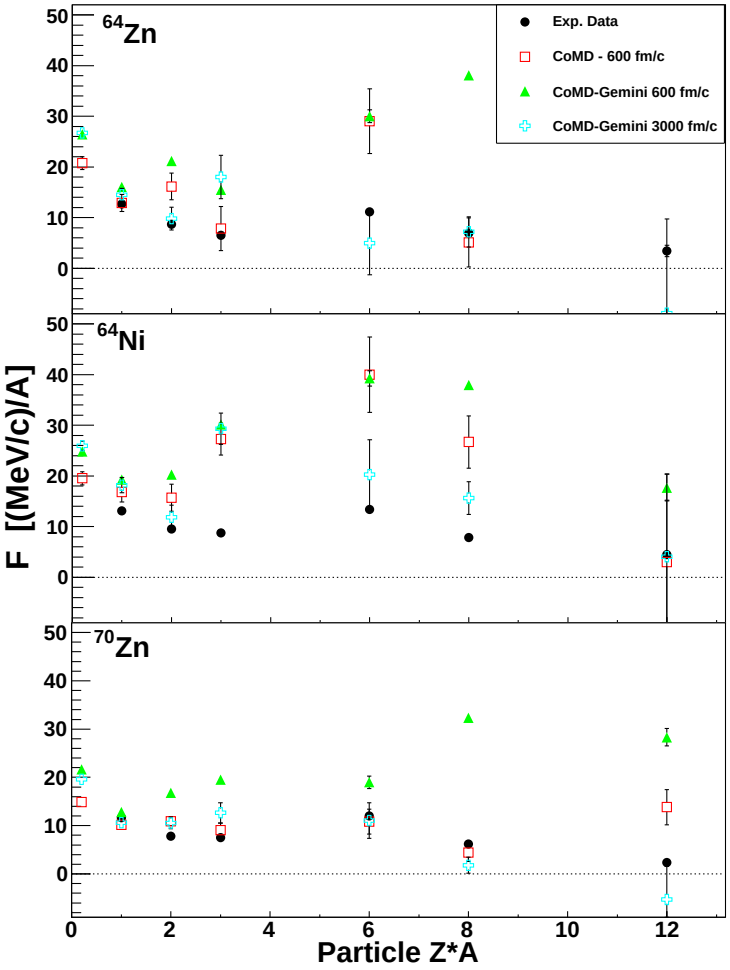

FIG. 64. Flow parameter (F) is shown as a function of the mass times charge (Z*A) for the light charged particles from the CoMD simulation in comparison to the experimental data. The CoMD results are presented from the calculation at 600 fm/c, 600 fm/c + Gemini, and 3000 fm/c + Gemini.

thermore, the isotopic trends are changed by the Gemini decay. For example, at 600 fm/c the CoMD results show a decreased alpha flow with respect to the ^{3}He flow. After applying Gemini, the alpha flow becomes larger than the ^{3}He flow which is not in agreement with the experimental data. In general, these results indicate that the dynamical evolution of the system has important consequences in determining the transverse flow which can not be represented through a statistical decay. Clearly, there are additional correlations, interactions, and/or fragmentation that the CoMD model is describing throughout the evolution up to 3000 fm/c that produce a much different phase-space distribution than the CoMD-Gemini hybrid model at 600 fm/c.

In order to further examine the hybrid approach, the time evolution of the transverse flow for the LCPs from the CoMD model is presented in Figure 65. It is important to notice that the flow is *not* shown per nucleon, in order to separate the flow of the isotopes for clarity. The transverse flow is shown as a function of time (solid circles) from the CoMD simulation up to 3000 fm/c at which point the Gemini model is applied (stars). Also, the 600 fm/c + Gemini results are shown as the solid squares for comparison. As previously predicted [49, 168, 51, 169], the transverse flow saturates very quickly for most of the fragments. Furthermore, the 3000 fm/c and 3000 fm/c + Gemini results are nearly equivalent demonstrating that the system has dynamically cooled to a final state and the Gemini decay, therefore, has little effect on the flow. In comparison, the 600 fm/c + Gemini results are widely different than the 3000 fm/c + Gemini results. This, as mentioned above, demonstrates that important information about the reaction system is lost in the coupling with Gemini.

It is interesting that the alpha particles do exhibit a further decrease in the flow between 1000 and 2000 fm/c. This could be thought of as random secondary decay component of the alpha particle momentum, which diminshes the collective motion or flow. Thus, the secondary decay from the dynamical calculation (CoMD) produces a

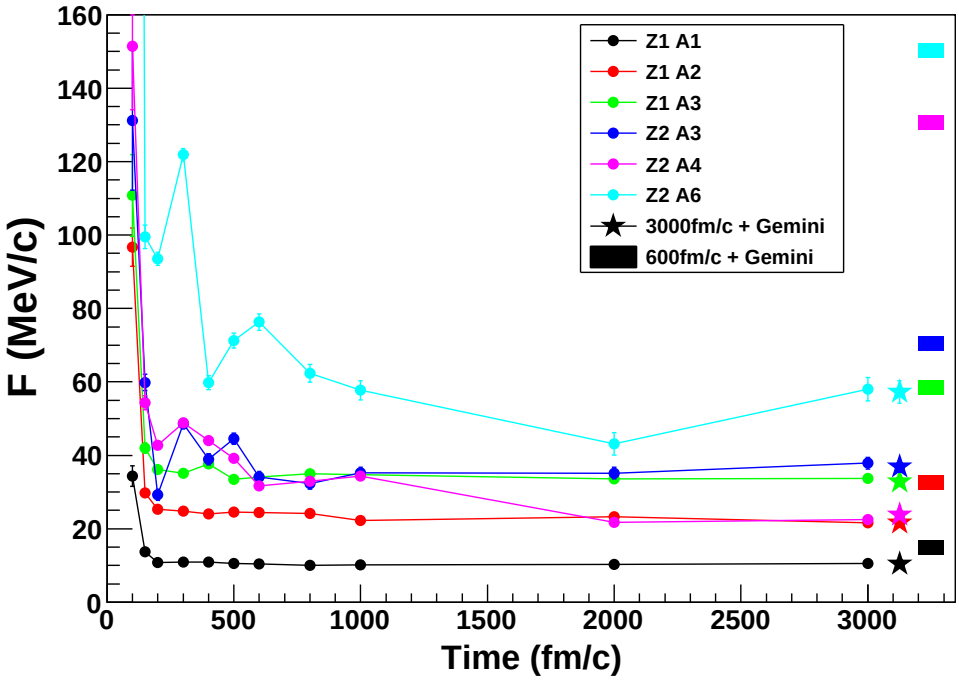

FIG. 65. Flow parameter for the LCPs is shown as a function of time from the CoMD simulation. The flow was extracted at different time steps (solid circles) up to 3000 fm/c and then the Gemini model was applied (stars). The CoMD 600 fm/c + Gemini results are shown as solid squares on the right side of the plot for comparison.

decreased flow while the statistical secondary decay (Gemini) increases the magnitude of the flow.

For comparison, the flow of protons and alpha particles from the AMD model as a function of time are shown in Figure 66. As mentioned, the AMD model was used to simulate the reaction for 300 fm/c before the Gemini code was applied to the hot fragments. The results show that the proton flow saturates very early in the reaction. However, the application of the Gemini code increases the proton flow after the saturation. Likewise, the alpha particle flow exhibits a large increase due to the Gemini de-excitation after it had appeared to saturate around 200 fm/c. The AMD and CoMD results both demonstrate the same trend with the flow appearing to saturate relatively early in the reaction and then increasing due to the Gemini de-excitation.

The energy spectra from the AMD and CoMD simulations were compared to the experiment in an attempt to determine why the Gemini decay has such a large effect on the transverse flow results. The proton energy spectra from the 300 fm/c AMD simulation with and without the Gemini decay are shown in Figure 67. The results are shown from rings 7-10 in order to examine the mid-rapidity region where the flow is extracted. While it is difficult to compare the results without the Gemini decay due to low statistics, the AMD + Gemini energy spectra are in excellent agreement with the experimental proton spectra. Thus, it appears that the AMD + Gemini hybrid approach is able to reproduce the kinetic properties of the reaction, even though the flow results were not reproduced.

The proton energy spectra from the CoMD simulation is compared to the experiment in Figure 68. The 600 fm/c, 600 fm/c + Gemini, and 3000 fm/c + Gemini proton energy spectra from the CoMD simulation are presented. Similar to the AMD energy spectra, the CoMD results are in excellent agreement with the experimental

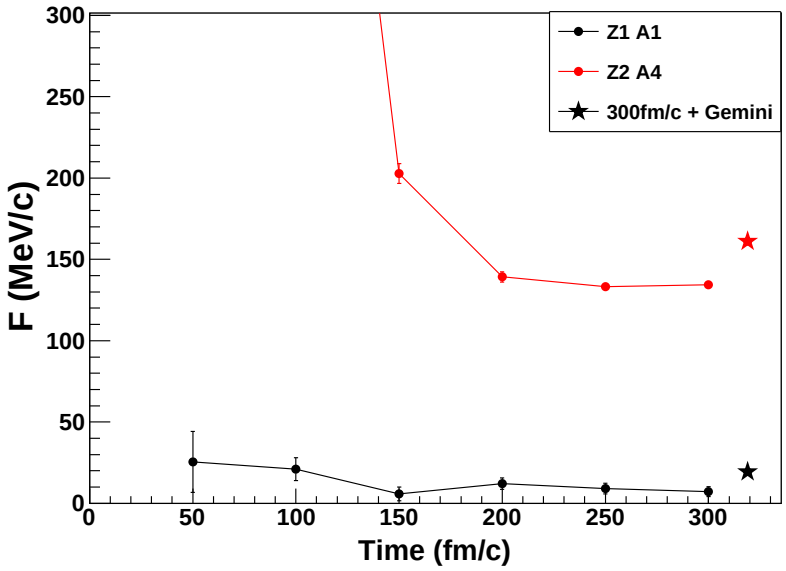

FIG. 66. Flow parameter for protons and alpha particles is shown as a function of time from the AMD simulation. The flow was extracted at different time steps (solid circles) up to 300 fm/c and then the Gemini model was applied (stars).

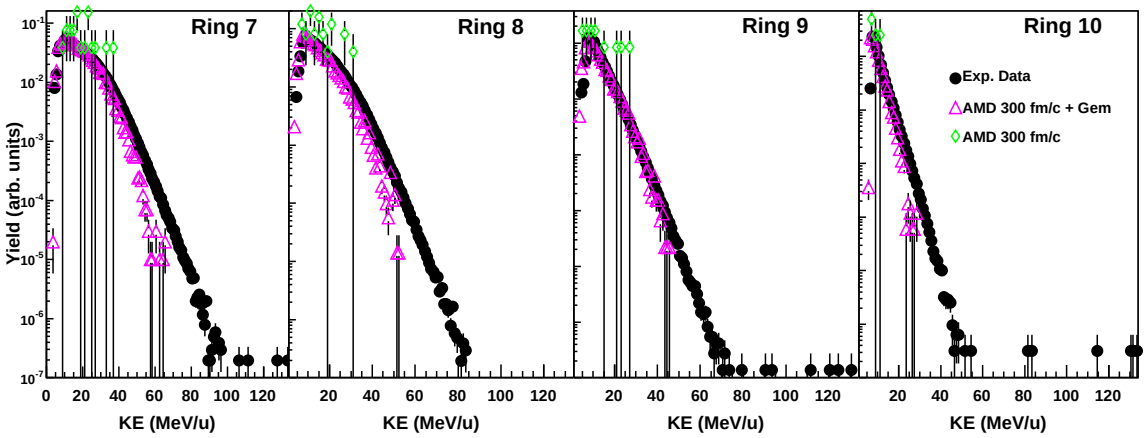

FIG. 67. Kinetic energy distribution of protons for Rings 7-10 from the experimental data (solid black circles) compared with the filtered AMD results at 300 fm/c with (pink open diamonds and without (green open triangles) applying the Gemini decay.

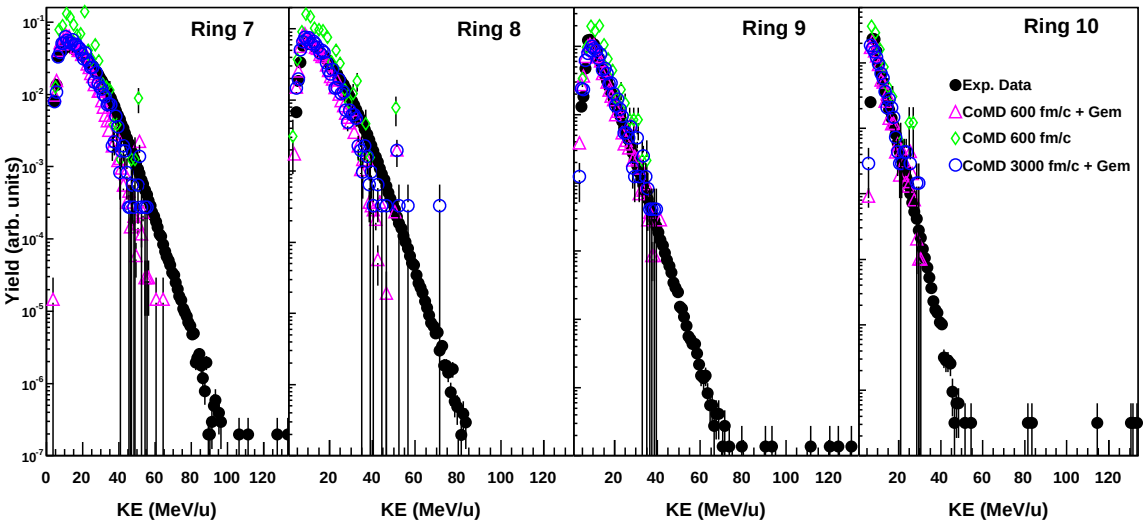

FIG. 68. Kinetic energy distribution of protons for Rings 7-10 from the experimental data (solid black circles) compared the 600 fm/c (open green diamonds), 600 fm/c + Gemini (open pink triangles), and 3000 fm/c + Gemini (open blue circles) filtered CoMD simulation.

data. It is particularly interesting that the 600 fm/c + Gemini proton energy spectra are nearly identical to the 600 fm/c (no Gemini) and 3000 fm/c + Gemini results, even though the LCP flow is significantly different. This, as well as the AMD results presented above, shows that the coupling of the dynamical and statistical models are able to reproduce the mid-rapidity energy spectra. This suggests that the flow results are sensitive to the dynamics and/or correlations present in the reaction that may be lost in the coupling of the models. Additional comparisons between the LCP energy spectra form the AMD and CoMD simulations with the experimental data are presented in Appendix E.

The reduced rapidity (Y_r) distributions of the protons, deuterons, tritons, and alpha particles from the AMD and CoMD simulations are shown in Figures 69 and 70, respectively. The effect of the Gemini model on the rapidity distribution was

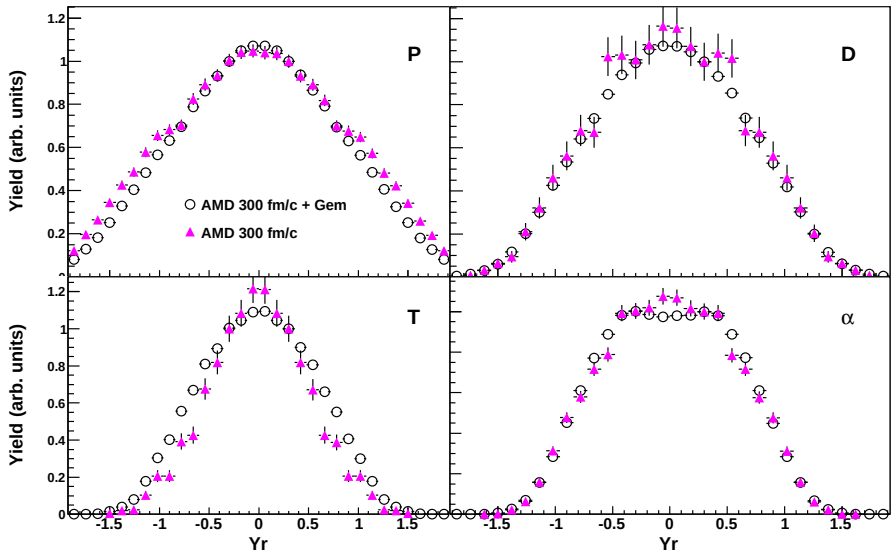

FIG. 69. Reduced rapidity (Y_r) distributions for protons (P), deuterons (D), tritons (T), and alpha (α) particles from the unfiltered AMD simulations at 300 fm/c with (open circles) and without (solid pink triangles) the Gemini decay.

examined since it could provide insight into strong flow enhancement observed due to the statistical decay. In general, applying the Gemini decay to the 300 fm/c AMD and 600 fm/c CoMD distributions has a relatively small effect. The rapidity distributions from the AMD simulation are slightly narrower, except for the protons, without the Gemini decay. Thus, it appears that the Gemini decay produces more particles near the rapidity of the projectile or target, most likely due to the decay of the QP and QT.

The only significant differences in the CoMD results (Figure 70) are observed for the alpha particles. The results show that applying Gemini to the 600 fm/c distribution has no effect, yet the flow results differ. In comparison, the 600 fm/c (no Gemini) and 3000 fm/c alpha particle rapidity distributions do show some differences while providing similar LCP flow results. These observations suggest that the rapidity distributions may not be strongly connected to the flow observables. This seems

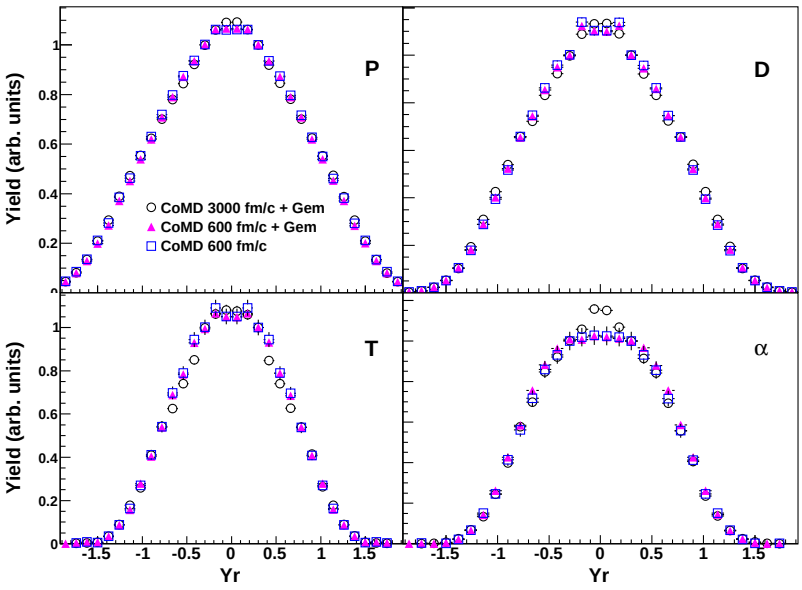

FIG. 70. Reduced rapidity (Y_r) distributions for protons (P), deuterons (D), tritons (T), and alpha (α) particles from the unfiltered CoMD simulations at 3000 fm/c + Gemini (open circles), 600 fm/c + Gemini (solid pink triangles), and 600 fm/c (open blue square).

reasonable since the flow does not depend on the yield of the particles but rather their correlation with the reaction plane.

Overall, the results indicate strong evidence that coupling of the dynamical and statistical models does not provide an accurate description of the heavy-ion reactions. While the hybrid approach has been shown to allow for the reproduction of a variety of kinetic observables and fragmentation yields it is unable to describe flow observables which are sensitive to the dynamics of the reactions. This demonstrates the need for simulations that can provide a complete description of the heavy-ion collisions with reasonable computational requirements, such as the CoMD model. This could then provide a consistent description of the dynamics, fragmentation, and kinetic properties for comparison to the experimental data.

5. LCP Summary

In summary, the transverse flow of LCPs from 35 MeV/u Zn and Ni systems has been investigated. The Z=1 and Z=2 transverse flow was shown to be dependent on both $(N/Z)_{sys}$ and A_{sys}. Furthermore, the flow of the isotopically identified LCPs was also shown to be sensitive to $(N/Z)_{sys}$ and A_{sys} expanding on the previous work of Pak *et al.* [53]. Isotopic and isobaric comparisons revealed a decreased flow with an increased neutron content of the fragment, representing a differential movement, or flow, of neutrons and protons. The experimental LCP flow results were compared to the SMF model in order to investigate their sensitivity to the density dependence of the symmetry energy. While many of the experimental trends were well reproduced by the SMF model, the magnitude of the flow did not match that of the experimental data. The SMF model showed good agreement with the observed isotopic trends (decreased flow with increased neutron content), except for the protons. The increase of the Z=1 particle flow with increasing $(N/Z)_{sys}$ and the triton-^{3}He flow difference were both shown to be sensitive to the symmetry potential. These results suggested that the fragment flows are sensitive to the behavior of the symmetry potential below normal nuclear density and to the related neck dynamics. The agreement with experimental data was better with a stiff density dependence of the symmetry energy.

A comparison of the LCP flow with the AMD and CoMD models demonstrated the important dynamical components necessary to describe experimental results. In particular, the use of statistical de-excitation models, such as Gemini, before the system has cooled to a near final state can drastically modify the observed transverse flow for the LCPs. Therefore, in order to accurately describe the LCP transverse flow it is important to use a single description of the reaction rather than a two-stage approach.

D. Transverse Flow of Intermediate Mass Fragments (Z≥3)

The heavier, or intermediate, mass fragments (IMFs) provide a new probe, in comparison to the light charged particles (LCPs), for examining the mechanisms responsible for the transverse flow. Previous research has suggested that the IMFs may be more sensitive to the collective motion present in the collisions due to a decreased thermal motion [62, 63]. Therefore, the IMFs may be more sensitive to the mean-field component of the transverse collective flow.

1. Quantifying IMF Transverse Flow ($\overline{\langle Px \rangle}$)

The backward angle energy thresholds in the NIMROD-ISiS array cause incomplete detection of the intermediate mass fragments. Therefore, it is difficult to extract an accurate slope measurement from the mid-rapidity region. Thus, the IMF flow had to be quantified differently than the LCP flow discussed above. Options that had previously been used included extracting the slope from only the positive Y_r region or mirroring the positive Y_r shape onto the negative Y_r side of the flow plot [46, 180]. However, in both of these cases one is still dependent on obtaining a good linear fit over a small region and, therefore, small fluctuations can cause large deviations in the fit and associated slope.

In order to provide a more consistent and accurate measurement, the transverse flow of the IMFs was extracted as the average in-plane momentum, $\overline{\langle Px/A \rangle}$, from $0.0 \leq Y_r \leq 0.45$. Thus, the measurement does not require a linear fit and is a simple measurement of the amount of in-plane momentum. This procedure has been suggested and used in previous studies to examine the collective flow [165, 181, 182, 49]. In calculating the $\overline{\langle Px/A \rangle}$, from $0.0 \leq Y_r \leq 0.45$, it is important for the "flow" plot to cross the (0,0) point. Otherwise the $\overline{\langle Px/A \rangle}$ obtained will be distorted due

to the negative offset and will not represent the flow of the particles. Thus, before calculating the $\overline{\langle Px/A \rangle}$ a manual offset correction was applied to the data such that it crossed the (0,0) point. The $\overline{\langle Px/A \rangle}$ could then be calculated. As a cross comparison, this method was applied to the LCPs where the linear fit method was also applicable. While the absolute values differ, since one is comparing a slope to an average, the trends remained consistent for the isotopically identified fragments demonstrating that both methods allow for the quantification of the transverse flow.

It should be noted that the velocity boost is not necessary with this method since the offset is manually corrected. This was verfied by examining the $\overline{\langle Px/A \rangle}$ for different IMFs with and without the velocity boost. In both cases the exact same $\overline{\langle Px/A \rangle}$ was extracted.

In examining the extracted IMF flow it was observed that for the central and mid-impact parameter collisions the heaviest fragments exhibited a negative flow. Negative flow has been previously observed in the Fermi energy regime yet an understanding of the results has not been fully achieved [44, 183, 46]. The negative flow was observed in the the more central collisions and one proposed explanation was that this arises from an anti-correlation between the IMF's azimuthal angle and the reconstructed reaction plane [44, 46]. The experimental results of the IMF flow, $\overline{\langle Px/A \rangle}$, are shown in Figure 71 as open circles. The negative flow increases for fragments with Z$\geq$3.

The reason for the negative flow can be explained by the removal of the POI in the calculation of the reaction plane. As described in Section B, the reaction plane is calculated separately for each particle in order to remove autocorrelations. Thus, the reaction plane angle is largely determined from the heavy fragments of the event, which should be well aligned with the reaction plane. However, in a central collision the reaction plane calculated for a Z=8 fragment, which is likely the heaviest detected fragment in the event, will likely be determined solely by LCPs. Thus, it was observed

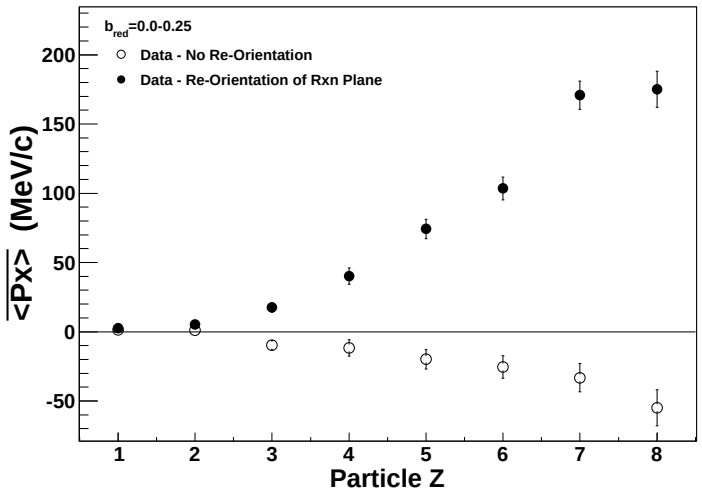

FIG. 71. Transverse flow, $\overline{\langle Px \rangle}$, for Z=1-8 fragments from the 4Bin0 centrality selection (violent collisions). The results are from the ^{70}Zn system and are shown both without (open circles) and with (solid circles) the reaction plane re-orientation method.

that when removing a heavy POI there was a significant probability that the reaction plane would be oriented 180^o from the reaction plane calculated with the heavy POI, as suggested in Refs. [44] and [46]. Therefore, the heavy fragment will exhibit a negative flow, as shown in Figure 71, since the reaction plane is most likely pointed 180^o from the fragment.

To correct the observed anti-correlation, it is proposed that after calculating the reaction plane without the POI, the reaction plane can be *re-oriented* using the reaction plane calculated from the entire event. If the difference between the reaction plane calculated without the POI and the reaction plane calculated using the entire event was greater than 90°, then the original reaction plane was rotated 180° (re-orientation). The resulting heavy fragment flow, with the re-orientation of the reaction plane, is shown as the solid black circles in Figure 71. As expected,

the heavy fragments no longer exhibit a negative flow but rather show an increasing positive transverse flow.

The effect of the reaction plane re-orientation on the $\langle Px \rangle$ versus Y_r plots is shown in Figure 72 for ^{16}O fragments. The shape of the $\langle Px \rangle$ is shown both before (solid black circles) and after (red triangles) the reaction plane re-orientation. As suggested above, the largest difference is observed in the violent, or central, collisions where the heavy fragment has a large effect on the reaction plane calculation. A minimal difference is observed in the most peripheral bin, 5Bin4, since the ^{16}O is no longer the dominant factor in the reaction plane calculation, due to other heavy fragments in the event. Figure 72 also demonstrates why the IMF flow had to be calculated as the average $\langle Px \rangle$, since it is clear that the mid-rapidity slope could not be extracted due to the incomplete detection at Y_r <0.0.

Theoretical simulations, in which the true reaction plane is known, were used to examine the validity of the proposed reaction plane re-orientation method. In Figure 73 the results from the CoMD simulation are presented. The simulated events were filtered to match the experimental data and the IMF flow, $\overline{\langle Px \rangle}$, was extracted. As shown, the negative IMF flow is present without the reaction plane re-orientation (open circles). After applying the reaction plane re-orientation method to the CoMD data, the extracted IMF flow is positive and increasing with the increased fragment charge. The filtered results from the CoMD simulation are in good agreement with the experimental observations presented in Figure 71. The IMF flow calculated from the true reaction plane is also shown in Figure 73. The true IMF flow from the unfiltered CoMD simulation is positive and increases with the fragment charge. Therefore, it is clear the the reaction plane re-orientation method helps correct the IMF flow results. The magnitude of the flow from the re-orientation method is overestimated, as shown for the Z=5-9 fragments. Therefore, the strength of the reaction-plane re-orientation

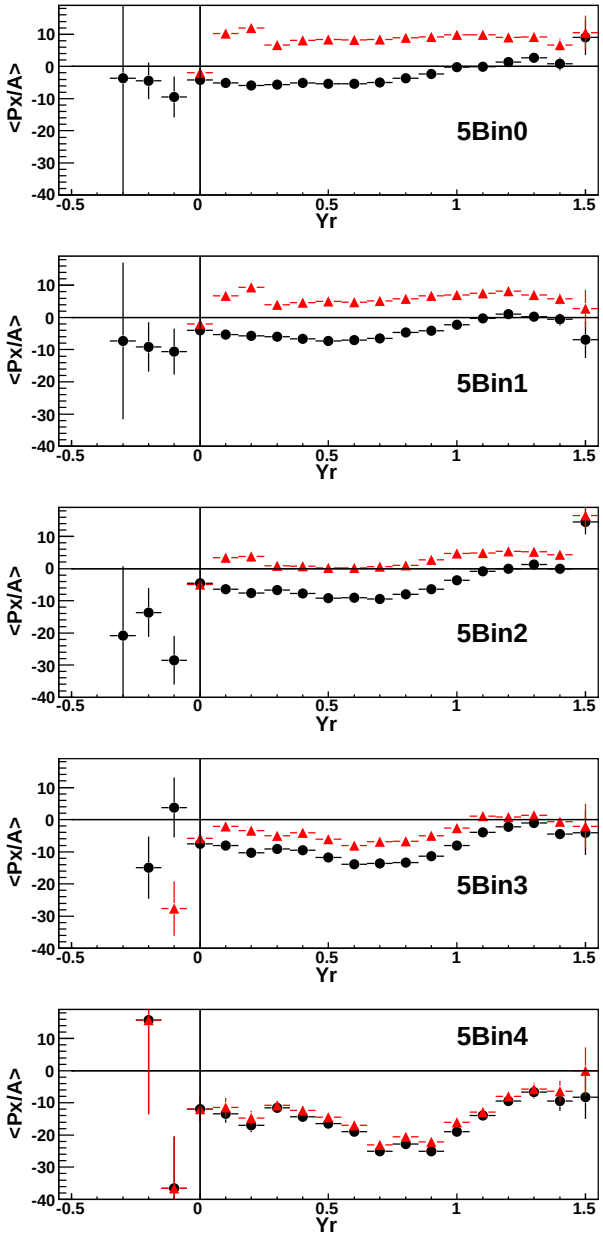

FIG. 72. Average in-plane momentum, $\langle Px/A \rangle$, is plotted as a function of the reduced rapidity, Y_r, for ^{16}O fragments with (red triangles) and without (black circles) re-orientation of the reaction plane. Results are shown for 5 different impact parameter selections from the ^{70}Zn system.

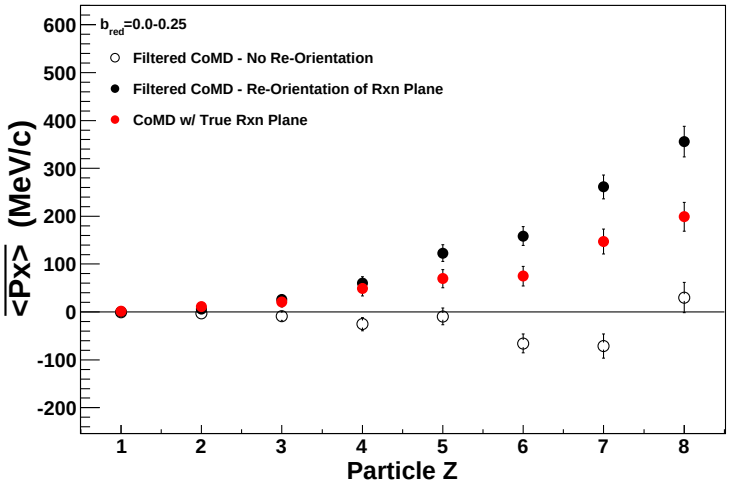

FIG. 73. Transverse flow, $\overline{\langle Px \rangle}$, is shown for Z=1-8 fragments from the ^{70}Zn+^{70}Zn CoMD simulation. The filtered CoMD results were used to calculate $\overline{\langle Px \rangle}$ with (solid black circles) and without (open circles) the reaction plane re-orientation method. The exact IMF flow, calculated relative to the true reaction plane, from the unfiltered simulation is shown as red circles. The results are shown from the 4Bin0 centrality selection.

method is that the trend and correct sign of the IMF flow is reproduced allowing for system to system comparisons to be studied.

Additional justification for the reaction plane re-orientation method is presented in Figure 74. The IMF flow calculated from the unfiltered AMD-Gemini and SMF simulations are compared to the experimental IMF flow. The results show that the re-orientation method is required for the experimental data in order to reproduce the sign and trend of the fragment flows, as suggested by the CoMD model results. The IMF flow results presented in the following sections were determined using the reaction plane re-orientation method.

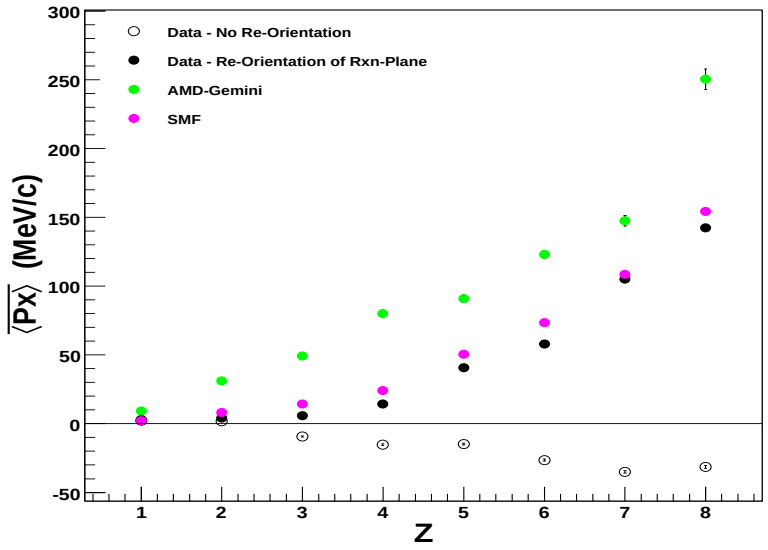

FIG. 74. Transverse flow, $\overline{\langle Px \rangle}$, is plotted as a function of the fragment charge from the ^{64}Ni system. The experimental results are shown with (solid black circles) and without (open circles) re-orientation of the reaction plane. For comparison unfiltered AMD-Gemini (green circles) and BGBD (pink circles) results are shown, in which the true reaction plane has been used to calculate the IMF flow. The simulated and experimental results are both from the 4Bin1 centrality selection.

2. IMF Flow Results and Discussion

As discussed in Chapter I, the transverse collective flow has been shown to depend on both the mass and N/Z of the colliding system. The examination of the balance energy demonstrated that the transverse flow was strongly dependent on the mass, A_{sys}, of the colliding system [48]. The balance energy followed an $A_{sys}^{-1/3}$ power law which represents a balance between the attractive mean-field potential which scales with the surface, $A_{sys}^{2/3}$, and the repulsive nucleon-nucleon collisions which should scale with the interaction volume, A_{sys} [48, 16]. Pak *et al.* have shown that the transverse collective flow for light particles with Z=1-3, as well as the balance energy, increases with an increasing neutron to proton ratio of the system, $(N/Z)_{sys}$ [53, 54]. The isospin dependence of the transverse flow and balance energy was attributed to the isospin dependent potential and in-medium nucleon-nucleon cross sections [55, 56]. Along with the mass-dependent mechanisms (mean-field and nucleon-nucleon collisions), the Coulomb potential should also have an important role in the observed transverse flow [56, 55, 184]. The IMF flow results presented below experimentally show, for the first time, the dependence of the transverse flow on the charge of the system, or the Coulomb potential.

The transverse flow, $\overline{\langle Px \rangle}$, for Z=1-9 particles is shown in Figure 75 for five centrality bins, ranging from Bin 0 (most violent collisions) to Bin 4 (most peripheral collisions). The expected increase in the transverse flow with the increasing charge of the fragments is clear [53, 9, 63]. However, a decrease in the magnitude of the flow from the central to peripheral bins is observed rather than the typical maximum flow in the mid-peripheral collisions (Bin 2) [53, 9]. While the un-filtered AMD-Gemini results showed a maximum flow for the mid-peripheral collisions, the filtered results demonstrated the same trend shown in the experimental data (Figure 75). This

was attributed to the reaction plane re-orientation method, which overestimates the magnitude of the flow in the most violent collisions (Bins 0-1) with respect to the mid-peripheral selection.

In Bin 0 the $\overline{\langle Px \rangle}$ of the IMFs from the ^{64}Ni and ^{64}Zn systems are nearly equivalent and larger than the ^{70}Zn system. This can be understood through the mass dependence of the transverse flow which is related to the balance energy relationship derived by Westfall *et al.* [48]. Thus, one would expect the ^{70}Zn (A_{sys}=140) system to exhibit a decreased flow in comparison to the A_{sys}=128 systems, since it has a lower balance energy due to the increased number of repulsive NN-collisions relative to the attractive mean-field potential.

In the peripheral reactions, Bins 3 and 4, the $\overline{\langle Px \rangle}$ of the IMFs from the Zn systems become nearly equivalent and decreased with respect to the ^{64}Ni system. This represents a clear dependence on the charge of the system for the IMF flow. The larger repulsive Coulomb force in the Zn (Z=30) systems causes a decreased flow in comparison to the ^{64}Ni (Z=28) system. The increased effect of the charge-dependent forces, relative to the mass-dependent forces, in the peripheral collisions may be due to the decreased interaction volume. For example, the number of NN-collisions would be greatly diminished in the peripheral reactions. This presents clear evidence of the charge dependence of the transverse flow.

A separation of the IMF flow between all 3 systems occurs in the mid-peripheral reactions (Bin 2). The IMF flow from the ^{64}Zn system is less than that from the ^{64}Ni system yet larger than the ^{70}Zn flow, exhibiting a behavior between the extremes of the mass (Bin 0) and charge (Bin 4) dependent flow. The difference between the mid-peripheral IMF flow in the ^{64}Ni and ^{64}Zn systems is similar to the $(N/Z)_{sys}$ dependence observed by Pak *et al.* for LCPs in A_{sys}=116 systems [53]. However, in context with the results from the IMF flow of the ^{70}Zn system, which has a similar $(N/Z)_{sys}$ as the

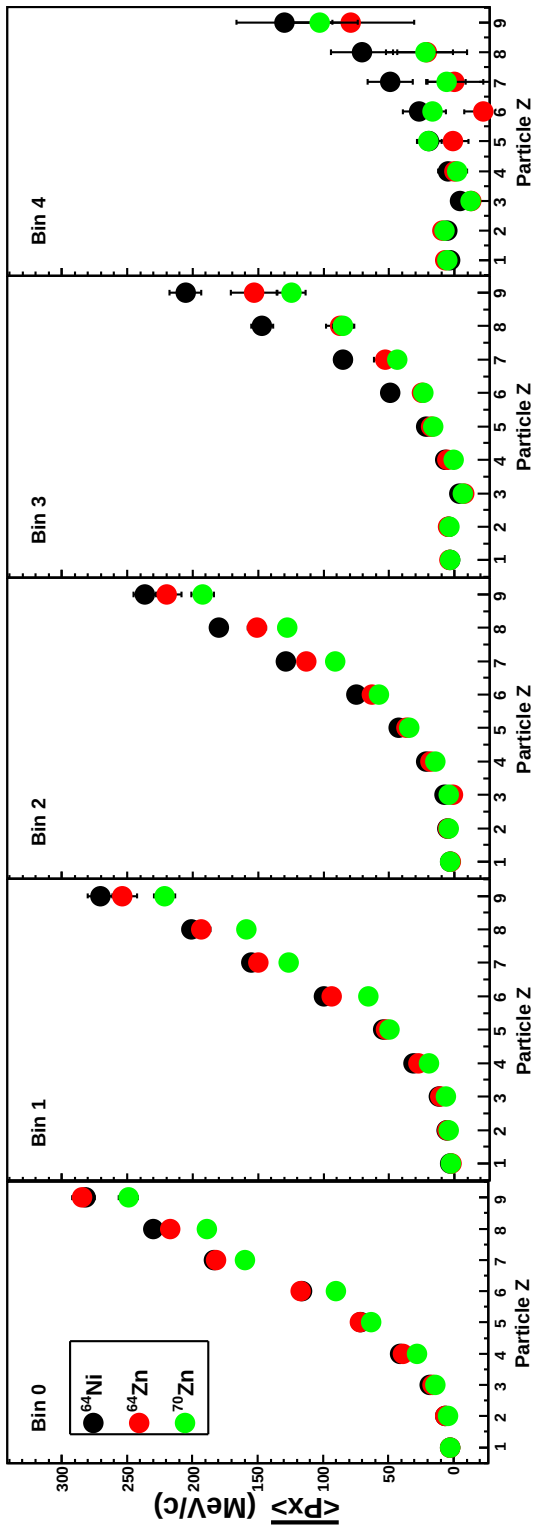

FIG. 75. Transverse flow, $\overline{\langle Px \rangle}$, for Z=1-9 particles in five different centrality bins. Bin 0 represents the most violent collisions, while Bin 4 represents the most peripheral. The results are shown for the ^{64}Ni, ^{64}Zn, and ^{70}Zn systems as shown in the legend.

^{64}Ni system, the $(N/Z)_{sys}$ dependence between the A_{sys}=128 IMF flow appears to be due to a balancing between the mass and charge dependent mechanisms.

In order to examine this trend more quantitatively the ratio

$$R_{Flow} = \frac{\overline{\langle Px/A\rangle}_{^{64}Zn} - \overline{\langle Px/A\rangle}_{^{70}Zn}}{\overline{\langle Px/A\rangle}_{^{64}Ni} - \overline{\langle Px/A\rangle}_{^{70}Zn}} \tag{4.10}$$

can be used to define the magnitude of the flow from the ^{64}Zn system in comparison to the ^{64}Ni and ^{70}Zn systems. Thus, when R_{Flow}=1 the IMF flow of the ^{64}Zn system equals that of the ^{64}Ni system and when R_{Flow}=0 the ^{64}Zn and ^{70}Zn systems have equivalent values of flow. In Figure 76, the individual R_{Flow} values of the Z=6-9 fragments and the average R_{Flow} value of Z=4-9 fragments are plotted as a function of the centrality bin number. The results exhibit a systematic trend from $R_{Flow} \cong 1$, for the most violent collisions, to $R_{Flow} \cong 0$, for the most peripheral reactions. The dashed black line in Figure 76 represents a perfect transition of R_{Flow}=1 for Bin 0 to R_{Flow}=0 for Bin 4 (results from Bin 4 are not shown due to statistics). Thus, the experimental results, which follow the dashed line, demonstrate a nearly perfect transitsion. The trend, observed in Figures 75 and 76, shows a transition from the IMF's $\overline{\langle Px\rangle}$ being strongly dependent on the mass of the system to a dependence on the charge of the system.

3. Anti-symmetrized Molecular Dynamics (AMD) Results

The observed mass to charge dependence of the IMF transverse flow should be sensitive to the density dependence of the symmetry energy since there is a mean-field component to the flow. Scalone *et al.* predicted that the difference in the transverse flow of LCPs from two systems with the same mass and differing $(N/Z)_{sys}$ would be sensitive to $E_{sym}(\rho)$ [34]. Therefore, changing the isospin-dependent part of the mean-field should effect the balance between the mass and charge dependent forces.

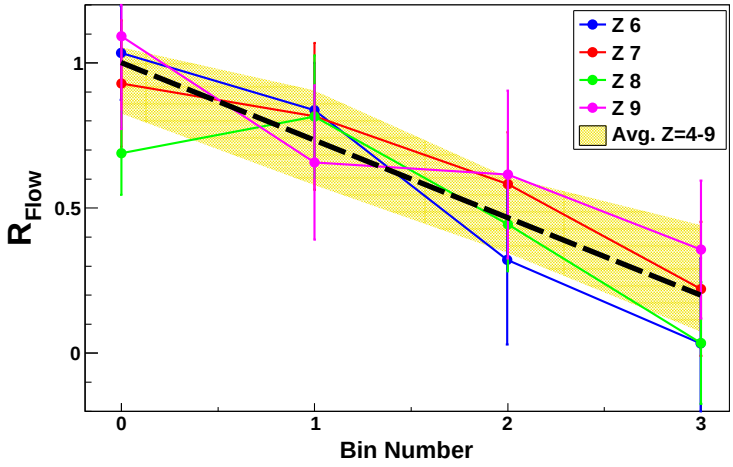

FIG. 76. R_{Flow}, as described in Eq. 4.10, is plotted against the centrality bin number for Z=6-9 fragments. The average R_{Flow} value for Z=4-9 fragments is shown as the yellow area. The black dashed line represents a perfect transition from R_{Flow}=1 for Bin 0 to R_{Flow}=0 for Bin 4. The results from the most peripheral collisions (Bin 4) have been excluded due to the increased error.

The antisymmetrized molecular dynamics with wave packet Diffusion and Shrinking (AMD-DS) model [130] was used to investigate the sensitivity of the IMF flow to $E_{sym}(\rho)$. As mentioned in Chapter III, the dynamics of the reaction were simulated up to a time of 300 fm/c, after which the GEMINI code [141] was used to statistically de-excite the hot fragments. The momentum dependent Gogny and Gogny-AS effective interactions provided an incompressibility of symmetric nuclear matter of K=228 MeV while allowing for the density dependence of the symmetry energy to be varied [130]. The Gogny and Gogny-AS interactions produce a soft and stiff density dependence of the symmetry energy, respectively. While the AMD-Gemini simulation was unable to reproduce the LCP trends, it was able to reproduce the experimental IMF flow trends shown in Figure 75. Thus, the dependence of the IMF flow on the isospin-dependence of the nuclear interaction can be examined.

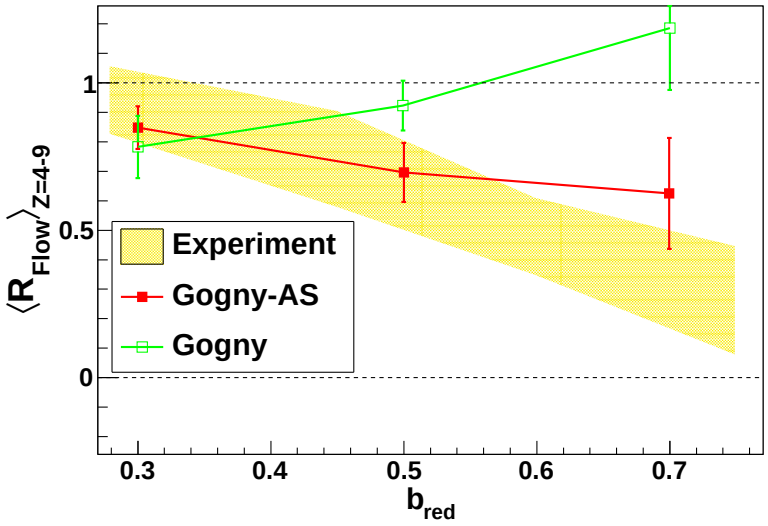

FIG. 77. Average R_{Flow} for Z=4-9 fragments ($\langle R_{Flow} \rangle_{Z=4-9}$) is plotted as a function of the reduced impact parameter, b_{red}, for the experimental data (yellow area) and the unfiltered AMD-Gemini simulation with both a stiff (red squares) and soft (green open squares) $E_{sym}(\rho)$.

In Figure 77 the average R_{Flow} value for Z=4-9 fragments is shown as a function of b_{red} from the AMD-Gemini simulations in comparison to the experimental data. The experimental results are equivalent to those presented in Figure 76 except that R_{Flow} is shown as a function of the average b_{red} of each centrality bin. The average b_{red} was determined using the filtered molecular dynamics simulations to provide an estimate of the impact parameter range selected in each centrality bin. The impact parameter for each event of the AMD-Gemini simulation was known and, therefore, the average b_{red} values shown in Figure 77 are exact. While the same experimental procedure discussed above were used to extract the IMF flow, the AMD-Gemini results (Figure 77) were not filtered due to statistical limitations.

The results shown in Figure 77 demonstrate that the differences in the IMF flow between systems has a strong sensitivity to the density dependence of the symme-

try energy. The Gogny-AS interaction, or stiff $E_{sym}(\rho)$, clearly demonstrates the best agreement with the experimental data, showing a decreasing $\langle R_{Flow} \rangle_{Z=4-9}$ value with increasing b_{red}. In comparison, the soft symmetry energy parameterization, or Gogny interaction, is unable to reproduce the experimental trend. In the Gogny calculation the ^{64}Zn flow increases relative to the ^{64}Ni flow, eventually becoming larger ($R_{Flow} > 1$). This is related to the larger symmetry energy at low-density for the Gogny interaction, which is more repulsive for the more neutron-rich ^{64}Ni system relative to the ^{64}Zn system. The isospin-dependent part of the Gogny-AS interaction is less repulsive at low-density and therefore, the ^{64}Ni flow remains larger than the ^{64}Zn flow producing agreement with the experimental data. It is clear that the isospin-dependent part of the interaction is an important component in describing the observed transition from a mass to charge dependence of the IMF transverse flow.

4. Comparison with Constrained Molecular Dynamics (CoMD) and Stochastic Mean-Field (SMF) Models

Along with the AMD-Gemini simulation presented above, the CoMD [129] and SMF [133] models were also used to examine the sensitivity of the IMF flow results to the density dependence of the symmetry energy. To review, in the CoMD model the reaction was dynamically evolved up to 3000 fm/c. This allowed for the dynamical de-excitation of most of the hot fragments. After 3000 fm/c the GEMINI code was used to break-up any unstable or long-lived excited fragments. The SMF model was used to simulate the dynamics up to 120 fm/c and a phase-space coalescence was applied to obtain the fragment identities. Thus, the fragments obtained from the SMF model do not represent a final cold distribution. In all of the models (AMD/CoMD/SMF) the interaction or mean-field potential used produces an EoS with a compressibility, K, between 200-230 MeV. Therefore, the symmetric part of the EoS was kept relatively constant and

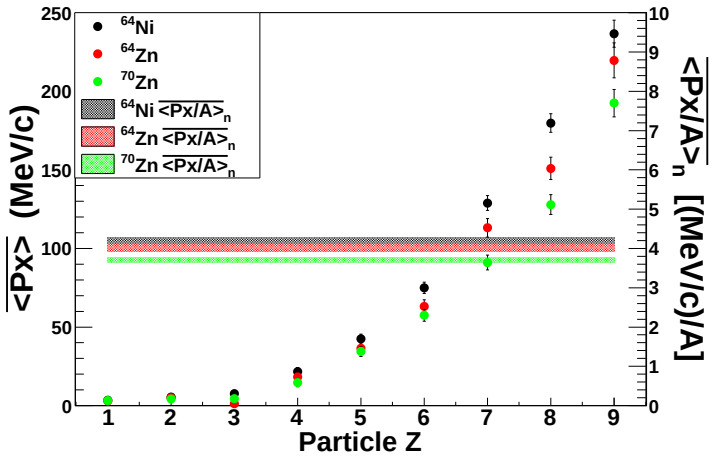

FIG. 78. Transverse flow, $\overline{\langle Px \rangle}$ (left axis), for Z=1-9 particles from mid-peripheral collisions in the the ^{70}Zn+^{70}Zn, ^{64}Zn+^{64}Zn, and ^{64}Ni+^{64}Ni collisions. The nucleon-weighted flow, $\overline{\langle Px/A \rangle}_n$ (right axis), results for each system are shown by the solid lines, representing the combination of the Z=3-9 fragment flows.

the different density dependences of the symmetry energy could be examined.

The experimental transverse flow, $\overline{\langle Px \rangle}$, for Z=1-9 particles is shown in Figure 78 for only the mid-peripheral collisions. As observed in Figure 75, a separation of the IMF flow between all 3 systems is observed in which the IMF's $\overline{\langle Px \rangle}$ from the ^{64}Zn system is less than that from the ^{64}Ni system yet larger than the ^{70}Zn flow. This was interperted as a balance between the mass-dependent mechanisms (mean-field and NN-collisions), which would cause the A_{sys}=128 systems to have equivalent flow, and the charge-dependent mechanisms (Coulomb potential), which would cause the Zn systems to have similar flow.

In order to improve statistics for comparison with the theoretical simulations, the Z=3-9 fragments were combined into an average nucleon-weighted in-plane mo-

mentum defined as

$$\langle Px/A \rangle_n = \left(\sum_{f=0}^{N_f} \omega_f \left(Px/A \right)_f \right) \div N_n \tag{4.11}$$

where N_f (N_n) is the total number of fragments (nucleons) in a given rapidity window each with an in-plane momentum per nucleon of $(Px/A)_f$. The weight (ω_f) of each fragment was set to the number of nucleons in the fragment. The nucleon-weighted transverse flow, $\overline{\langle Px/A \rangle_n}$, was then extracted over the range $0.0 \leq Y_r \leq 0.45$ for each system. Therefore, the nucleon-weighted flow provides decreased error due to the increased statistics of combining the Z=3-9 fragments in this fashion. The experimental nucleon-weighted flow from each system is shown in Figure 78 as the solid colored lines. The R_{Flow} value was then calculated as shown in Eq. 4.10 from the nucleon-weighted flow of each system.

In the mid-peripheral reactions the experimental nucleon-weighted flow from each system followed the trend that was observed from the IMF flows in Figure 78. A value of R_{Flow}=0.61±0.14 was calculated from the experimental data, representing that the nucleon-weighted flow from ^{64}Zn system was below that of the ^{64}Ni system and above the ^{70}Zn system.

The R_{Flow} value was also calculated from the nucleon-weighted flow for the AMD-Gemini, CoMD, and SMF simulations. It should be noted that since the SMF model was stopped at t=120 fm/c the nucleon-weighted flow was constructed from all fragments with Z≥3 in order to better approximate the nuclear flow of the heavy fragments.

Unlike the AMD-Gemini simulation results presented above, the SMF and CoMD results were unable to reproduce the observed experimental trend, in which the IMF flow was dependent on the mass of the system in the central collisions and the charge of the system in the peripheral collisions. In the SMF model the disagreement was

largely due to an overestimation of the ^{70}Zn system flow in both the central and peripheral collisions relative to the ^{64}Zn and ^{64}Ni systems. The CoMD model showed nearly equivalent flow from the Zn systems in the central collisions and separation between the Zn system in the peripheral collisions. These differences demonstrate the varying descriptions of the IMF flow between the AMD, CoMD, and SMF models.

While the models differed in the central and peripheral collisions, a consistency was observed in the mid-peripheral collisions. In these reactions the separation in the nucleon-weighted flow between all three systems was present, as shown in Figure 78, for the AMD-Gemini, CoMD, and SMF simulations. This offers the opportunity to compare the theoretical results, where they provide a consistent description of the IMF flow, to the experimental data. Specifically, the sensitivity to $E_{sym}(\rho)$ for the IMF, or nucleon-weighted, flow can be examined from the simulated mid-peripheral collisions.

It is interesting that the models provide similar predictions for the mid-peripheral IMF flow, yet can vary in the central and peripheral regions. This may be connected to the "dynamical" fragment production in mid-rapidity region, which is directly connected to the flow, since it reaches a maximum in the mid-peripheral collisions [70]. Since the AMD, CoMD, and SMF models simulate the dynamical stage of the reaction it seems reasonable that the best agreement would, therefore, be achieved in mid-peripheral collisions, where the dynamical aspects of the mid-rapidity fragments are the most important. For example, in the more central or peripheral collisions, where the models differ, the statistical decay component of the mid-rapidity fragments may become increasingly important.

The R_{Flow} values from the different symmetry energy parameterizations of each model are compared to the experimental data (red fill area) in Figure 79. As expected from the comparison with the AMD model presented above, the stiff density

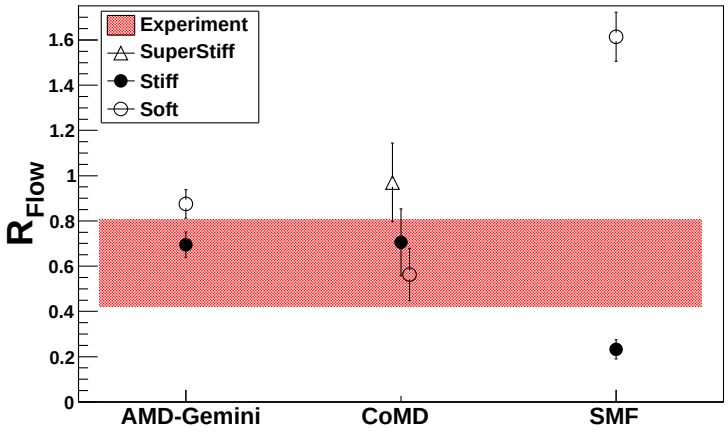

FIG. 79. R_{Flow} value from the nucleon-weighted flow of the mid-peripheral reactions is shown for the different symmetry energy parameterizations of the AMD-Gemini, CoMD and SMF models. The experimental value is represented by the red fill area.

dependence of the symmetry energy, or Gogny-AS interaction, is in excellent agreement with the experimental results. The best agreement between the CoMD and experiment was achieved with the stiff and soft symmetry energy parameterizations in comparison to the super-stiff calculation. The SMF model showed the greatest difference between the stiff and soft $E_{sym}(\rho)$. Unfortunately, neither the stiff or soft SMF results agreed with the data. However, the stiff SMF calculation was closer to the experimental result than the soft calculation. These theoretical results demonstrate that the separation of the nucleon-weighted flow between systems is a sensitive observable to the density dependence of the symmetry energy and a stiff $E_{sym}(\rho)$ provided improved the agreement with the experimental data.

In the SMF model the difference between the two calculations can be connected to the low density behavior of the symmetry energy. In the soft case the symmetry potential will decrease the attractive mean-field potential for the neutron-rich systems,

while a stiff symmetry potential will increase the attractive mean-field for proton rich systems. Therefore, the symmetry potential will decrease the attractive mean-field of the ^{64}Ni system (N/Z=1.33) more then the ^{64}Zn system (N/Z=1.13). This should produce a larger decrease in the ^{64}Ni IMF flow in comparison to the ^{64}Zn IMF flow. The soft SMF results showed that the IMF flow from the ^{64}Zn system was larger than that of the ^{64}Ni IMF flow producing a R_{Flow} >1, as shown in Figure 79. In the case of the stiff symmetry potential, which is less repulsive for the neutron-rich systems, the ^{64}Ni IMF flow is larger than the ^{64}Zn IMF flow producing R_{Flow} ∼0.25. The same trend is seen also in AMD calculations, though the results corresponding to the two different $E_{sym}(\rho)$ are much closer. The opposite trend observed in the CoMD model may suggest that, due to the different model ingredients, that the IMF flow results are sensitive to a different density domain. If the IMF flow from the CoMD model is originating from a region above the saturation density then the isospin-dependent part of the interaction would have the opposite effect relative to the low-density region, thus, explaining the difference in the observed trend in comparison to the AMD and SMF results.

The form of the different $E_{sym}(\rho)$ from the AMD, CoMD, and SMF models can be compared in Figure 80. In the examined energy region, 35 MeV/u, the maximum density achieved in the reaction is most likely 1.5 $\rho/\rho_\circ$ and the mid-rapidity IMFs may be originating from a low density neck region, as suggested by the AMD and SMF results [107, 185, 186]. Therefore, in comparing the symmetry energy parameterizations one should examine the region below 1.5 $\rho/\rho_\circ$. As shown in Figure 80, the stiff AMD, stiff and soft CoMD, and stiff SMF symmetry energy parameterizations (shown in red), which provided the better agreement with the experimental data, are all similar below 1.5 $\rho/\rho_\circ$. Thus, a relatively consistent agreement from three different theoretical models is achieved. It also should be noted that the stiff parameterizations

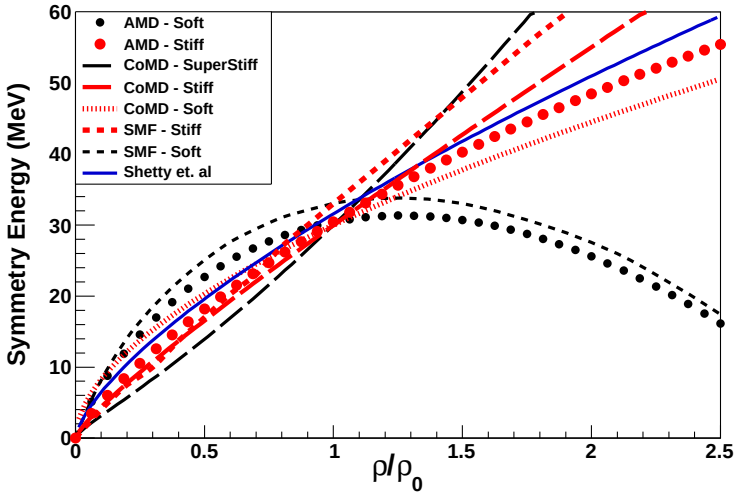

FIG. 80. Density dependence of the symmetry energy obtained from the interactions used in the AMD, CoMD, and SMF models. The stiff $E_{sym}(\rho)$, which provided the best agreement with the experimental data, from each model is shown in red. For comparison, the $E_{sym}(\rho)$ extracted from the work of Shetty *et al.* is shown by the solid black line [18].

from the simulations are in good agreement with current predictions of the density dependence of the symmetry energy [28, 18, 13]. For comparison the results from Shetty *et al.* are shown in Figure 80 as the solid blue line [18].

5. IMF Summary

In summary, the transverse flow of IMFs has been investigated for the 35 MeV/u ^{70}Zn+^{70}Zn, ^{64}Zn+^{64}Zn, and ^{64}Ni+^{64}Ni systems. The results demonstrated that the IMF flow depended strongly on the mass of the system in the violent collisions and the charge of the system in the peripheral collisions. This suggests that the repulsive Coulomb potential becomes an increasingly important component to the transverse flow in the more peripheral collisions in comparison to the attractive mean-field and repulsive nucleon-nucleon collisions. The transition of the IMF flow depending on the

mass of the system to the charge of the system was shown to be strongly sensitive to the density dependence of the symmetry energy using the AMD-Gemini simulation. The comparison between the experimental data and AMD-Gemini results provides strong evidence supporting a stiff density dependence of the symmetry energy. The CoMD and SMF model results were compared to the experimental data for the mid-peripheral collisions. The results provided additional evidence of the sensitivity of the IMF flow to the density dependence of the symmetry energy. For all three of the theoretical simulations (AMD/CoMD/SMF), better agreement with the experimental data was achieved with a stiff density dependence of the symmetry energy. These results, therefore, provide strong evidence of a stiff density dependence of the symmetry energy.

CHAPTER V

CORRELATIONS WITH PROJECTILE-LIKE FRAGMENTS AND EMISSION ORDER OF LIGHT CHARGED PARTICLES

Peripheral collisions can often be characterized by the formation of a projectile-like (PLF) and target-like (TLF) fragment along with the emission of light charged particles (LCPs). The NIMROD-ISiS array allows for detection of the PLF fragments and the associated LCPs. The lab-frame kinetic energy of the TLF prohibits detection in the array due to the silicon detector thresholds. In this chapter the correlation of LCPs are examined with respect to the detected PLFs. This provides an opportunity to examine the dynamics and mechanisms of the fragments produced from the neck, or mid-rapidity, region.

It is important to note that throughout the chapter the term PLF will be used to describe the heaviest fragment detected in any given event. Therefore, in a central collisions the heaviest detected fragment may have a Z=5 and is not truly a "projectile-like" fragment. However, the discussion is focused on the results from PLFs with a charge near that of the projectile. Furthermore, all events must have passed the criterion that the total detected charge, SumZ, be greater than 40% of the charge of the total system ($\sum Z_{frag} > 40\% \cdot Z_{sys}$). This helps to eliminate events in which the heaviest fragment from the event was not actually detected in the NIMROD-ISiS array.

Section A of the chapter describes how the event classification, based on the PLF charge, is correlated to the impact parameter and reaction plane. In Section B the experimental results are presented showing the correlation observed between the PLF and the mid-rapidity LCPs. The results suggest that the correlations are connected to the average order of emission of the mid-rapidity LCPs. Theoretical simulations

were used to validate the relationship between the mid-rapidity LCP's correlation with the PLF and the average order of emission as demonstrated in Section C. A summary of the experimental and theoretical results are provided in Section D.

A. Event Classification by PLF Charge

In examining the neck emission process it is important to separate events according to a consistent ordering parameter since the size and mechanisms of the mid-rapidity region may change from the most central to peripheral collisions [70]. In the following the charge of the projectile-like fragment (PLF) is used for event classification. Molecular dynamics simulations have been used to examine the correlation between the PLF charge and the impact parameter of the event.

In Figure 81 the reduced impact parameter, b_{red}, for each simulated event is plotted against the charge of the PLF for the antisymmetrized molecular dynamics and constrained molecular dynamics simulations (refer to Section C for details on the AMD and CoMD simulations). The results shown have been filtered using a software replica of the NIMROD-ISiS array and the SumZ $> 40\% \cdot Z_{sys}$ criterion has been applied. Thus, the correlation observed between the PLF Z and b_{red} should also be present in the experimental data. The PLF Z and b_{red} demonstrate an almost linear relationship for PLFs with Z=15-30. This shows that selecting events by the charge of the PLF, for PLFs with Z$\gtrsim$15, should provide a relatively well-defined impact parameter selection. Below a PLF Z $\approx$ 15 it appears that the heaviest detected fragment can be associated with a wide variety of impact parameters.

The relationship between the azimuthal angle of the PLF and the reaction plane can also be examined. For very peripheral collisions, where the PLF charge is close to that of the projectile, the azimuthal angle of the PLF should be strongly correlated

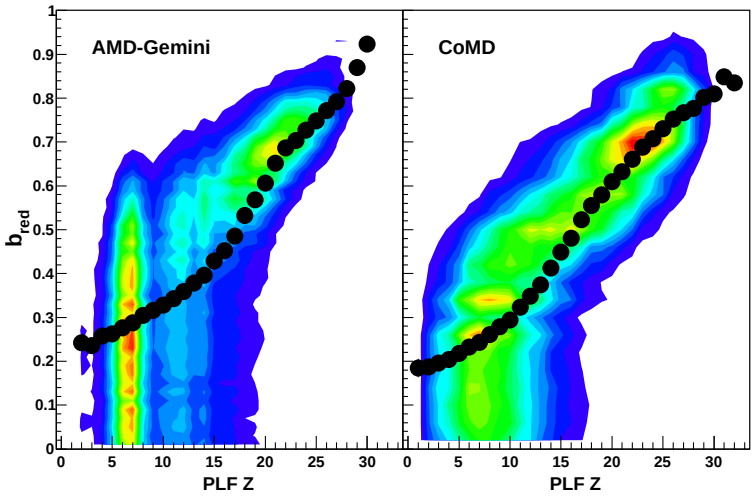

FIG. 81. Contour plot depicting the relationship between the charge of the detected PLF and the reduced impact parameter, b_{red}, of the event, where $b_{red}=b/b_{max}$ with $b_{max}=10$ fm. The black closed circles represent the average value for each PLF Z. Results are shown from the filtered AMD-Gemini (left) and CoMD (right) simulations for the ^{70}Zn system.

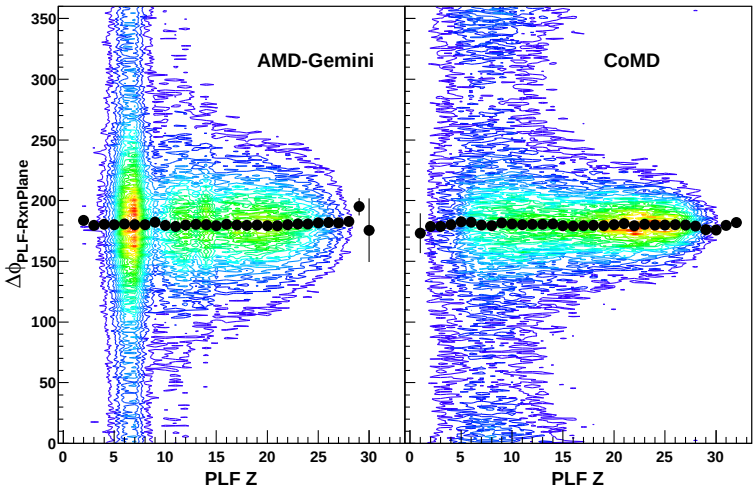

FIG. 82. Contour plot depicting the relationship between the charge of the detected PLF and the difference between the reaction plane and PLF azimuthal angle, $\Delta\phi_{PLF-RxnPlane}$. The black closed circles represent the average value for each PLF Z. Results are shown from the filtered AMD-Gemini (left) and CoMD (right) simulations for the ^{70}Zn system.

with the reaction plane angle. This correlation is again examined using the filtered molecular dynamics simulations, in which the known reaction plane can be compared to the azimuthal angle of the PLF. The difference between the reaction plane and PLF angle, $\Delta\phi_{PLF-RxnPlane}$, is shown versus the PLF charge in Figure 82. The results demonstrate that the average $\Delta\phi_{PLF-RxnPlane}$, shown as solid black circles, is almost perfectly anti-aligned (180°) from the reaction plane. The 180° anti-alignment with the reaction plane is due to the dominance of the attractive mean-field below the balance energy [48, 16]. Therefore, there is still a strong correlation between the PLF and reaction-plane. Figures 81 and 82 demonstrate that selecting classes of events by the charge of the PLF provides both an impact parameter selection as well as a correlation with the reaction-plane for PLF Z$\gtrsim$15.

B. Experimental Results

1. PLF Scaled Transverse Flow (Corr-Flow)

The correlation between the PLF and LCPs has been investigated through a transverse flow-type analysis. The transverse flow is commonly examined by plotting the average fragment momentum in the reaction plane as a function of rapidity. In the following the average momentum of the LCPs *in the plane of the PLF*, $\langle p_x \rangle$, was calculated and examined as a function of the rapidity. This will be referred to as *corr-flow*, representing the flow of particles correlated with the PLF. In Ref. [187] a scale-invariant flow analysis was carried out in order to compare the transverse flow at varying energies. In a similar manner, we investigated the calculation of a scale-invariant corr-flow in order to compare the correlation of LCPs among different PLFs. In the following, different methods for scaling the PLF-plane momentum and rapidity of the particles are discussed and a comparison of each method is presented in Figure 83.

Following Ref. [187] a scale-invariant transverse flow can be calculated as,

$$\tilde{p}_x^{sProj} = \frac{p_{x,frag}/A_{frag}}{p_{z,proj}^{cm}/A_{proj}} \tag{5.1a}$$

$$\tilde{Y}^{sProj} = \frac{Y_{frag}^{cm}}{Y_{proj}^{cm}} \tag{5.1b}$$

where $\tilde{p}_x^{sProj}$ represents the PLF-plane momentum per nucleon of the fragment ($p_{x,frag}/\mathrm{A}_{frag}$) scaled by the parallel momentum per nucleon of the projectile in the center-of-mass ($p_{z,proj}^{cm}/\mathrm{A}_{proj}$) and $\tilde{Y}^{sProj}$ represents the fragment center-of-mass rapidity (Y_{frag}^{cm}) scaled by the center-of-mass rapidity of the projectile (Y_{proj}^{cm}). The sProj scaling, as mentioned, was originally used to compare the flow at different energies and therefore is not sensitive to the properties of the PLF.

In order to account for the PLF properties, $\tilde{p}_x^{sPLF}$ and $\tilde{Y}^{sPLF}$ were calculated as

$$\tilde{p}_x^{sPLF} = \frac{p_{x,frag}/A_{frag}}{p_{z,PLF}^{cm}/A_{PLF}} \tag{5.2a}$$

$$\tilde{Y}^{sPLF} = \frac{Y_{frag}^{cm}}{Y_{PLF}^{cm}} \tag{5.2b}$$

where the center-of-mass fragment rapidity (Y_{frag}^{cm}) is scaled by the center-of-mass rapidity of the PLF (Y_{PLF}^{cm}) and the fragment PLF-plane momentum ($\mathrm{p}_{x,frag}/\mathrm{A}_{frag}$) is scaled by the center-of-mass parallel momentum of the PLF ($p_{z,PLF}^{cm}/A_{PLF}$). In this case both $\tilde{p}_x^{sPLF}$ and $\tilde{Y}^{sPLF}$ are invariant with respect to different PLFs. Therefore, the scaling is denoted by the sPLF label.

For comparison, the PLF-plane momentum of the fragment ($p_{x,frag}$) was divided by the total transverse momentum of the fragment ($p_{t,frag}$) as,

$$\tilde{p}_x^{stFrag} = \frac{p_{x,frag}}{p_{t,frag}} = v_1 \tag{5.3}$$

and the average $\tilde{p}_x^{stFrag}$ was plotted against $\tilde{Y}^{sPLF}$ from Equation 5.2. The stFrag scaling of p_x is often used in examining the transverse flow and is referred to as the directed flow represented as v_1 [188, 35, 189]. However, in this case $\tilde{p}_x^{stFrag}$ is not invariant with the PLF.

Finally, a transverse PLF scaling, $\tilde{p}_x^{stPLF}$, was calculated as,

$$\tilde{p}_x^{stPLF} = \frac{p_{x,frag}/A_{frag}}{p_{t,PLF}^{cm}/A_{PLF}} \tag{5.4}$$

where the PLF-plane transverse momentum of the fragment ($p_{x,frag}/\mathrm{A}_{frag}$) is scaled by the transverse momentum of the PLF ($p_{t,PLF}^{cm}/\mathrm{A}_{PLF}$). The average $\tilde{p}_x^{stPLF}$ was, again, plotted against the $\tilde{Y}^{sPLF}$. The stPLF scaling is PLF-invariant since both $\tilde{p}_x^{stPLF}$ and $\tilde{Y}^{sPLF}$ are scaled relative to the properties of the PLF.

The discussed scalings, Eqs. 5.1-5.4, are compared in Figure 83 for the correlation

of alpha particles with both a Z=4 and Z=25 PLF. The results for the Z=4 PLFs and alpha particles (left panel) show a constant $\langle \tilde{p}_x \rangle \cong 0$, which demonstrates that there are no significant correlations. A $\langle \tilde{p}_x \rangle \cong 0$ is representative of a random emission of alpha particles with respect to the Z=4 PLF. This is expected as events with a Z=4 heaviest fragment consist of a wide range of impact parameters, as shown in Figure 81. Therefore, the Z=4 fragments and alpha particles may be originating from the same source, such as a compound nucleus in the more central collisions, and do not exhibit any interaction. In contrast, strong correlations are observed between the Z=25 PLF and α particle demonstrating that the emission of the α particle is affected by the PLF. Also, the choice of scaling method has a distinct effect on the shape of the $\langle \tilde{p}_x \rangle$ vs. $\tilde{Y}$ plot.

The scaling by the projectile, defined in Eq. 5.1 ($\langle \tilde{p}_x^{sProj} \rangle$ vs. $\tilde{Y}^{sProj}$), shows the smallest correlations between the α particle and Z=25 PLF in comparison to the other methods, as shown in Figure 83. This is because the properties, such as the rapidity or momentum, of the PLF were not used in the scaling. Whereas, in Eq. 5.2 ($\langle \tilde{p}_x^{sPLF} \rangle$ vs. $\tilde{Y}^{sPLF}$) the PLF-plane momentum and rapidity of the α particles were scaled relative to the properties of the PLF. Thus, both the x-axis and y-axis are invariant with respect to the PLF. The results of the sPLF scaling show a distinct decrease, or bump, in $\langle \tilde{p}_x \rangle$ around $\tilde{Y}$=1 which is not evident in the sProj scaling. This represents a correlation, or interaction, between the alpha particles and PLF at $\tilde{Y}$=1. Therefore, the invariant PLF scaling (sPLF) appears to provide a better examination of the correlations between the PLF and fragments.

The stFrag scaling (Eq. 5.3) presented a similar shape or correlation as the sPLF scaling (Eq. 5.2) for the Z=25 PLFs and alpha particles. This suggests that the main difference between the sProj and sPLF/stFrag scalings is due to the calculation of $\tilde{Y}$, which is equivalent in for the sPLF and stFrag scaling, with $\tilde{Y}$ representing the

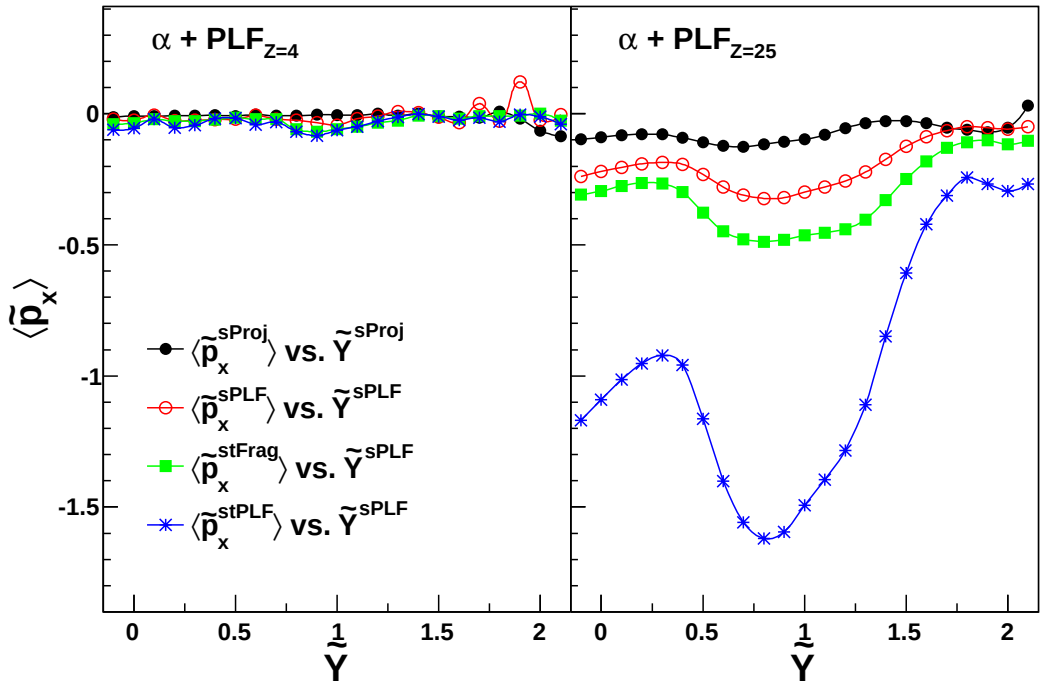

FIG. 83. Average scaled PLF-plane momentum, $\langle \tilde{p}_x \rangle$, of alpha particles in correlation with Z=4 (Left Panel) and Z=25 (Right Panel) PLFs is shown as a function of the scaled rapidity ($\tilde{Y}$). The presented results are from the 35 MeV/u ^{70}Zn+^{70}Zn system. The scaled momentum and rapidity have been calculated as described in Eqs. 5.1-5.4.

rapidity of the fragment relative to the PLF. Whereas $\tilde{Y}^{sProj}$ is scaled relative to the projectile rapidity which is a constant. Thus, the strong correlations observed between the PLFs and alpha particles in Figure 83 are enhanced by scaling the rapidity of the fragment by the PLF rapidity.

In examining the results from the Eq. 5.4 scaling (stPLF), in Figure 83, two distinct regions are present. A mid-rapidity region ranging from $0.0 \leq \tilde{Y} \leq 0.45$ and a PLF region from $0.5 \leq \tilde{Y} \leq 1.5$, in which there appears to be a Coulomb-bump due to the alpha particle interaction with the PLF. While these features are also present in the sPLF and stFrag scalings, they appear more prominent with the stPLF scaling. It is interesting to note that the strongest correlations appear when the alpha particle PLF-plane momentum was scaled relative to the transverse momentum of the PLF ($\langle \tilde{p}_x^{stPLF} \rangle$). Therefore, if the observed PLF-plane momentum of the alpha particles had been simply due to the inherit transverse motion of the PLF, the strong correlations observed in Figure 83 would be scaled out using the stPLF scaling. Thus, the stPLF scaling helps removes the inherent transverse momentum of the event which allows for the correlation between the fragment and PLF to become more pronounced. Therefore, the following analysis is performed using the scaling of $\langle \tilde{p}_x^{stPLF} \rangle$ vs. $\tilde{Y}^{sPLF}$ presented in Eq. 5.4 and for simplicity will be denoted as $\langle \tilde{p}_x \rangle$ vs. $\tilde{Y}$.

2. Mid-Rapidity Slope

Using the scaling from Eq. 5.4, the slope of the $\langle \tilde{p}_x \rangle$ (Eq. 5.4) over the mid-rapidity region can provide information about the movement of the fragments with respect to the PLF. For example, a positive slope would imply that on average the fragments are moving towards, or following, the PLF. In order to investigate the movement of the mid-rapidity fragments a linear fit was applied to the $\langle \tilde{p}_x \rangle$ vs. $\tilde{Y}$ plot from $-0.1 \leq \tilde{Y} \leq 0.45$. The fit range focuses on the forward rapidity fragments since we are

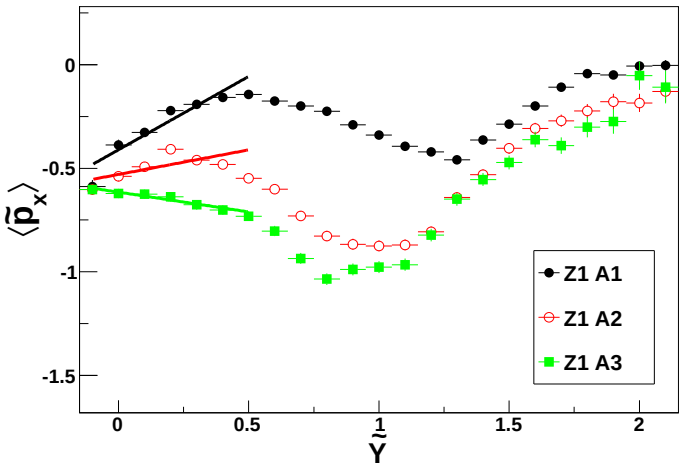

FIG. 84. The average scaled PLF-plane momentum, $\langle \tilde{p}_x \rangle$, of protons, deuterons, and tritons is shown as a function of the scaled rapidity, $\tilde{Y}$. The solid lines represent linear fits over the range -0.1$\leq \tilde{Y} \leq$0.45.

examining correlations with the PLF and also excludes any backward angle detector threshold effects. Figure 84 presents $\langle \tilde{p}_x \rangle$ plotted against $\tilde{Y}$ for protons, deuterons, and tritons in correlations with a Z=24 PLF. The linear fit is shown as the solid colored line for each isotope. The slope of the linear fit is then used to quantify the average movement of the particles and, as mentioned previously, will be referred to as the corr-flow (flow of particles *correlated* with the PLF).

The slopes observed in Figure 84 suggest that the mid-rapidity protons, deuterons, and tritons are moving in different directions with respect to the PLF. The positive slope exhibited by the protons would imply that they are, on average, moving toward or are more aligned with the PLF. In contrast, the tritons appear to move in the opposite directions, away from the PLF, implied by the negative slope or corr-flow.

The mid-rapidity slope ($\partial \langle \tilde{p}_x \rangle / \partial \tilde{Y}$) was extracted for the protons, deuterons, and tritons in correlation with PLFs of charge Z=3 to Z=30. In Figure 85, the extracted slopes are plotted as a function of the charge of the PLF. The results demonstrate

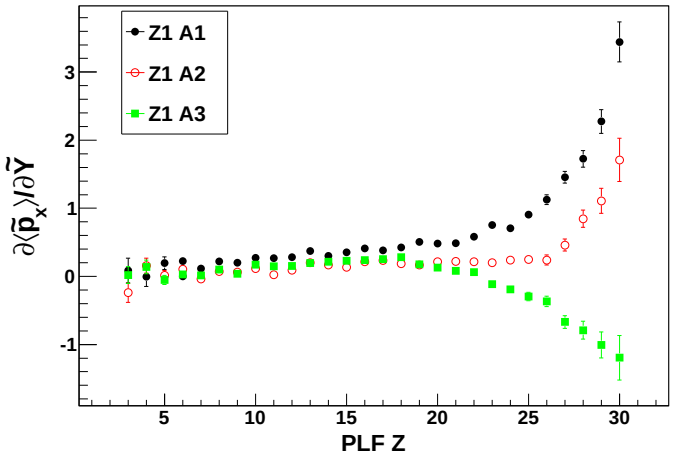

FIG. 85. The slope of the mid-rapidity particles, $\partial\langle\tilde{p}_x\rangle/\partial\tilde{Y}$, shown as a function of the PLF charge for protons, deuterons, and tritons.

that beyond a PLF Z=20 the magnitude and sign of the proton, deuteron, and triton slopes are drastically different. In particular, the difference increases with increasing charge, or size, of the PLF. As suggested above, these results suggest that the protons, deuterons, and tritons have different trajectories relative to the PLF.

3. Order of Emission

We propose that the different trajectories of the mid-rapidity fragments, shown in Figure 85 are connected to their proximity to the PLF and TLF at their time of formation. Figure 86 presents a simplified illustration of the possible effect of the PLF-TLF proximity to the mid-rapidity fragments. If the mid-rapidity fragment is emitted while in a close proximity to the PLF and TLF (left side of Figure 86) then the Coulomb potential would likely force the fragment trajectory to be anti-aligned, or perpendicular, with the PLF-TLF axis. This would result in a negative slope of $\langle\tilde{p}_x\rangle$. If the formation of the fragment occurs at a later time, where the PLF-TLF

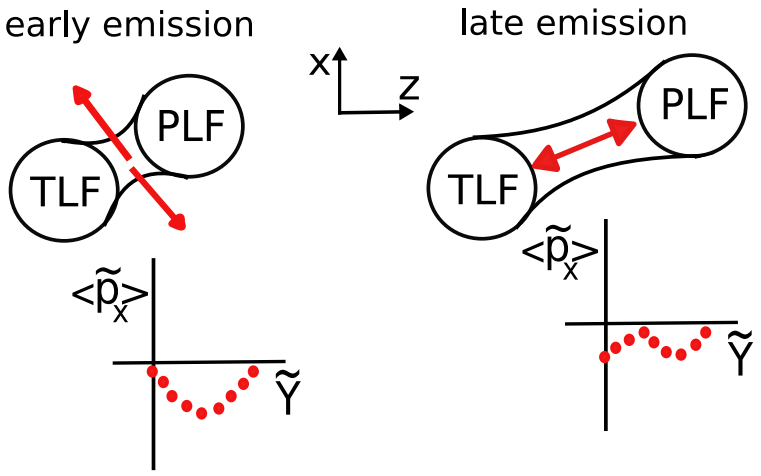

FIG. 86. Simple illustration of the proposed PLF-TLF proximity effect on the mid-rapidity fragments. The left side depicts the mechanism producing negative slopes due to an early emission of fragments. The right side shows a later emission of mid-rapidity fragments producing a positive slope.

proximity is decreased, then it is possible for a more aligned emission to occur (right side of Figure 86). Particles following the trajectory of the PLF would produce a positive slope value or corr-flow. In general, the aligned emission or positive corr-flow can be understood from previous studies of the transverse flow which suggest that the attractive mean-field would cause the nuclear matter, or particles, to flow in the direction of the PLF [8, 48, 16, 56, 55].

In the context that the slope of the mid-rapidity fragments is associated with the PLF-TLF proximity, or the time of emission, then the results from Figure 85 would suggest that the average order of emission for the mid-rapidity Z=1 isotopes is $\tau_t < \tau_d < \tau_p$, where τ is the average time of emission. In Figure 87 the extracted slopes are shown for the Z=1 (top panel) and Z=2 (bottom panel) isotopes as a function of the PLF charge. In order to improve statistics, events were combined by binning the PLFs based on their charge, as shown by the x-axis of Figure 87. Combing the

events with different PLFs is possible since the scaling used (Eq. 5.4) is invariant to the PLF. The corr-flow of the Z=1 isotopes, shown in Figure 87, shows the same trends that were observed before binning the events (Figure 85).

As previously mentioned, the separation between the proton, deuteron, and triton slopes increases with an increasing PLF charge. This may be understood by the increased Coulomb force that would be imparted on the mid-rapidity fragments from a higher PLF charge. Thus, events with a larger PLF Z should be more sensitive to the average order of emission of the particles.

The corr-flow of the Z=1 isotopes is compared between the ^{70}Zn+^{70}Zn, ^{64}Zn+^{64}Zn, and ^{64}Ni+^{64}Ni systems in the top panel of Figure 87. The results from all three system are not presented for the Z=2 isotopes because the error bars, from the linear fits, were larger than the differences between the systems. The results for the Z=1 isotopes show that the corr-flow of the fragments is sensitive to the colliding system. The absolute magnitude of the slope was the largest for the ^{64}Zn (N/Z=1.13) system followed by the ^{64}Ni (N/Z=1.28) and then ^{70}Zn (N/Z=1.33) systems. This demonstrates a dependence on the neutron to proton ratio of the colliding system, $(N/Z)_{sys}$, where the corr-flow decreases with an increasing $(N/Z)_{sys}$. Specifically, the protons and tritons show a strong sensitivity to the $(N/Z)_{sys}$ with an increased positive and negative flow, respectively, in the ^{64}Zn system.

The comparison of the corr-flow between systems is interesting with respect to the standard flow results from Chapter IV Section C. The standard isotopic flow results presented a general trend with the largest flow was from the ^{64}Ni system followed by the ^{64}Zn system and then the ^{70}Zn system. Thus, for the systems with the same A_{sys}, the flow increased with the $(N/Z)_{sys}$, as expected from previous studies [53]. However, the corr-flow shows a decreasing flow with increasing $(N/Z)_{sys}$. This demonstrates that the corr-flow, which examines the correlation with the PLF rather than the

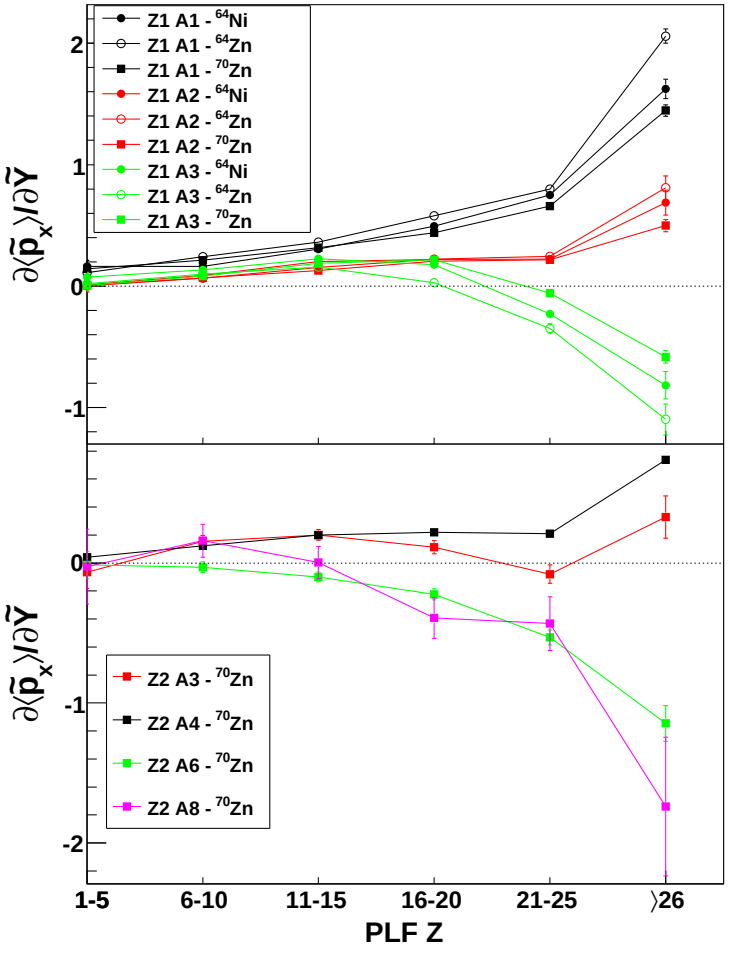

FIG. 87. The extracted slopes, $\partial \langle \tilde{p}_x \rangle / \partial \tilde{Y}$, for the Z=1 (top panel) and Z=2 (bottom panel) isotopes, are shown as a function of the binned PLF charge. Results from the 35 MeV/u ^{70}Zn+^{70}Zn, ^{64}Zn+^{64}Zn, and ^{64}Ni+^{64}Ni systems are presented for the Z=1 isotopes. Results from the Z=2 isotopes are shown only from the ^{70}Zn+^{70}Zn system.

reaction plane, is sensitive to different mechanisms of the reaction than the standard flow analysis.

In the bottom panel of Figure 87 the slopes extracted from the Z=2 isotopes are shown. Following the argument connecting the magnitude and sign of the slope to the average order of emission, the results suggest that the ^{6}He and ^{8}He fragments are on average emitted in the early stages of the collision followed by the ^{3}He fragments and then alpha particles. It is very interesting that the most neutron-rich fragments (triton, ^{6}He, ^{8}He) are on average formed early in the mid-rapidity region in comparison to the more proton-rich fragments. This provides additional information about the formation of a neutron-rich mid-rapidity or neck region. Previous studies have shown an increased N/Z content in the neck region [70, 71, 80, 81, 82, 83, 84] and these results suggest that this may be connected to the early formation of neutron-rich fragments in the mid-rapidity region.

In Figure 88 the extracted slopes from the corr-flow of elemental Z=1-4 fragments are presented. The Z=1 and Z=2 results show an increasing positive corr-flow as a function of the binned PLF charge. This would suggest that all the Z=1 and Z=2 fragments have a relatively late emission time, which produces the positive slopes. However, when we examine the isotopically resloved Z=1 and Z=2 fragments it is clear that the dynamics can vary widely, as shown in Figure 87. These results demonstrate the importance of separately examining the isotopically resolved fragments since the results of the elementally identified Z=1 and Z=2 fragments, from Figure 88, are clearly dominated by the proton and alpha particle dynamics, respectively. Thus, the interesting differences between the different isotopes are lost.

The corr-flow was also investigated for the Z=3 and Z=4 fragments, as shown in Figure 88, as a function of the PLF binned charge. Based on the presented arguments the results imply that the mid-rapidity Z=3 and Z=4 fragments have, on average, a

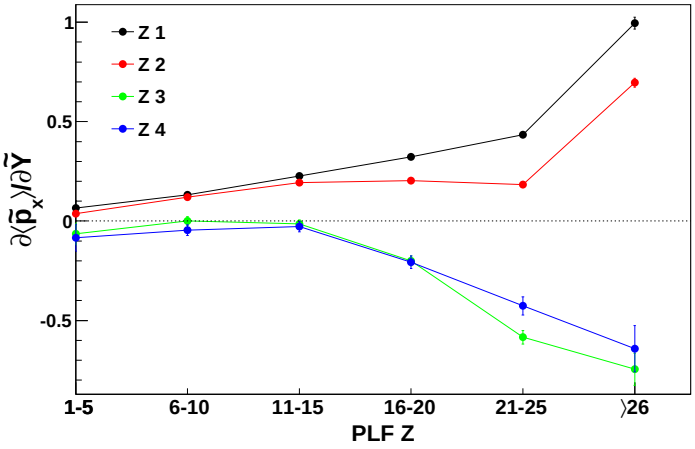

FIG. 88. The extracted slopes, $\partial \langle \tilde{p}_x \rangle / \partial \tilde{Y}$, for the Z=1, 2, 3 and 4 fragments shown as a function of the binned PLF charge. Results are from the 35 MeV/u ^{70}Zn+^{70}Zn system.

relatively early emission time. Differences in the corr-flow for isotopically resloved Z=3 and Z=4 fragments was also examined and showed consistent results with the elemental results presented in Figure 88. The large negative slopes suggest that the Z=3 and Z=4 fragments would be emitted on a time-scale comparable to that of the triton, ^{6}He, and ^{8}He fragments. This begins to present a picture that the fragments commonly observed to show an increased mid-rapidity production (such as the triton, ^{6}He, Z=3 and Z=4 fragments) are being produced on a relatively early time scale.

Additional evidence that the extracted slope, or corr-flow, is connected to the average emission order is presented in Figure 89. In each PLF charge bin, the PLFs were separated based on their relative velocity in comparison to the projectile. Then the corr-flow slope was extracted for alpha particles. If the extracted slope was correlated to the proximity of the PLF and TLF then a decreased slope would be expected for events in which the PLF velocity is dampened since the proximity of the PLF to the mid-rapidity particles would be increased. As expected, the extracted

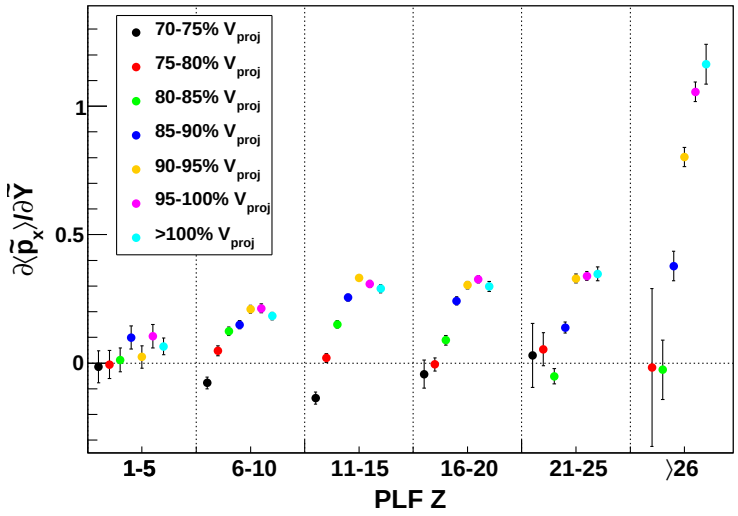

FIG. 89. The extracted slopes, $\partial \langle \tilde{p}_x \rangle / \partial \tilde{Y}$, for alpha particles are shown as a function of both the velocity and charge of the PLF. In each PLF charge bin the slope was extracted from events in which the velocity of the PLF was within a certain percentage of the velocity of the projectile, as described by the legend.

slopes are consistently decreased for the more dampened PLF events, as shown in Figure 89. In particular, it is interesting to note that for some of the most dampened events, in which the PLF velocity is 70-75% of the projectile velocity, a negative slope is extracted. This implies that the close proximity of the PLF and TLF to the mid-rapidity alpha particles effects the dynamics such that the Coulomb forces produce a negative flow. The largest effects were observed in the Z≥26 PLF bin where the largest Coulomb forces would be present. As shown, a very strong correlation between the magnitude of the slope and the PLF velocity is observed. Events in which the PLF is moving at nearly the speed of the projectile shows large positive slopes due to the fast separation between the PLF and TLF, which produces a decreased proximity to the mid-rapidity alpha particles..

The results presented in Figure 89 provided further experimental evidence that the extracted slope from the corr-flow can be connected to the proximity of the PLF and TLF to the mid-rapidity particles and therefore is associated with the time of emission or fragment formation. In combination with the results from Figures 87 and 88 it appears that on average the triton, ^{6}He, ^{8}He, Z=3 and Z=4 fragments are emitted early in the mid-rapidity region followed by deuteron and ^{3}He fragments and lastly the emission of the proton and alpha particles.

C. Theoretical Simulations

While the experimental data suggests a connection between the corr-flow and order of emission of the mid-rapidity fragments it is important to explore this idea in the context of simulations where the PLF-TLF proximity, strength of the Coulomb potential, and time of fragment formation can be examined.

1. Coulomb Trajectory

The Coulomb trajectory of mid-rapidity particles was examined through a Monte Carlo simulation in which the proximity of the PLF and TLF was varied. A depiction of the Coulomb trajectory simulation is shown in Figure 90. The initial configuration consisted of particle placed directly in between the PLF and TLF. The PLF and TLF were each represented by a sphere containing 30 protons with a radius of 4.9 fm, which is representative of a ^{70}Zn nucleus. In the simulation the PLF and TLF were propagated at a velocity of 0.13%c with a center-of-mass angle of θ_{cm}=13° and θ_{cm}=193°, respectively. The velocity was chosen to match the center-of-mass velocity of the 35 MeV/u ^{70}Zn+^{70}Zn reaction. The θ_{cm} of the PLF corresponds to detection in the forward most ring of the NIMROD-ISiS array. The velocity vector of the mid-

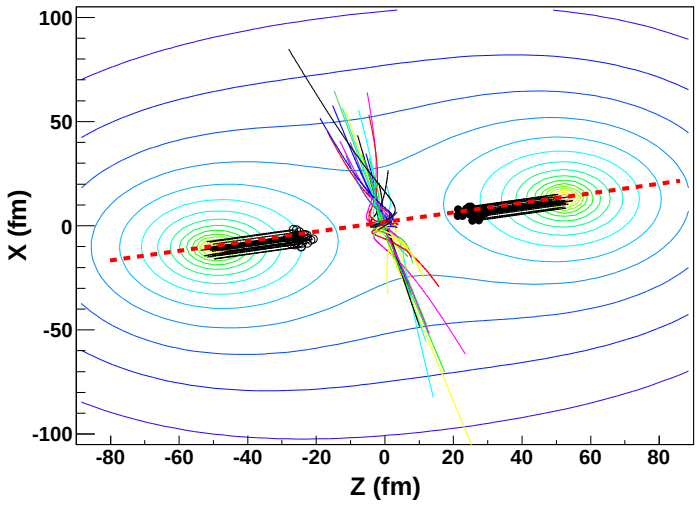

FIG. 90. Trajectories of the PLF, TLF, and mid-rapidity particles are shown from the Coulomb trajectory calculations in which the initial distance of the PLF and TLF was 25 fm from the mid-rapidity particle. The initial position of the PLF (TLF) is shown as the black filled (open) circles and the solid black lines represent the trajectory of the PLF (TLF). The contour lines depict the Coulomb potential produced from the final position of the PLF and TLF. The trajectories of the mid-rapidity particles are shown as solid lines originating from the (0,0) position. For clarity only 50 of the 5500 mid-rapidity particle trajectories are shown. The red dashed line represents the average initial trajectory of the mid-rapidity particles under no influence of the PLF-TLF Coulomb field.

rapidity particle was randomly determined from a Maxwell-Boltzmann distribution with T=6 MeV. However, the x-component of the velocity (v_x) was adjusted such that the center-of-mass angle of the mid-rapidity particles (θ_{cm}) was similar to that of the PLF or TLF. Thus, the initial trajectories represents a scenario in which a mid-rapidity particle is emitted and is following, or is aligned, with the motion of the PLF or TLF. In Figure 90 the dashed red line represents the average initial trajectory of the mid-rapidity particles, which is directed along the PLF-TLF axis.

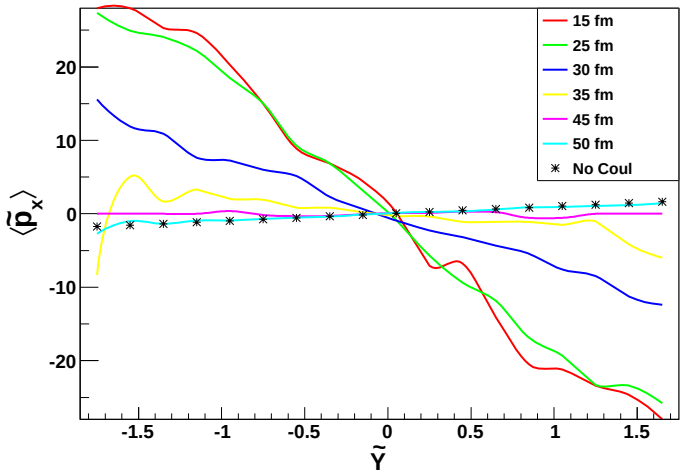

FIG. 91. Average scaled PLF-plane momentum, $\langle \tilde{p}_x \rangle$, is shown as a function of the scaled rapidity ($\tilde{Y}$) calculated from the Coulomb trajectory simulation. The proximity of the PLF and TLF to the mid-rapidity particle was varied as described by the legend.

After determining the initial conditions for the simulation the mid-rapidity fragment, PLF, and TLF were propagated for 200 fm/c. The trajectories of the PLF and TLF, shown as the solid black lines in Figure 90, were propagated without effects of Coulomb forces. The mid-rapidity fragment was propagated within the Coulomb field produced by the PLF and TLF, which is represented by the contour lines in Figure 90. The simulation was carried out 5500 times in order to obtain the average trajectory of the mid-rapidity particles. After propagation for 200 fm/c the final PLF-plane momentum and scaled rapidity for each particle was used to examine the $\langle \tilde{p}_x \rangle$ against $\tilde{Y}$, as shown in Figure 91, for different initial PLF-TLF proximities.

The results from the Coulomb trajectory simulation, shown in Figure 91, demonstrate the strong effect that the proximity of the PLF-TLF can have on the trajectory of the mid-rapidity fragments and therefore, the slope that would be extracted from the $\langle \tilde{p}_x \rangle$ versus $\tilde{Y}$ plot. When the distance of the PLF and TLF from the mid-rapidity

particle was small, 15-25 fm, the strong Coulomb potential forces the particle to move perpendicular to the PLF-TLF axis, as shown in Figure 90, thus producing a negative slope. As the distance of the PLF and TLF from the mid-rapidity particle is increased the initial trajectory of the particle is disturbed less by the Coulomb field and the strong negative flow is diminished. For example, at a PLF-TLF distance of 45-50 fm from the mid-rapidity particle the slope becomes very similar to the positive slope that would be extracted from the initial trajectory of the particles in which there is no PLF-TLF Coulomb field (asterisks Figure 91).

The Coulomb trajectory results demonstrated that in a simple scenario, in which the nuclear force is neglected, the mid-rapidity particle trajectory is strongly effected by the proximity of the PLF and TLF. Both the positive and negative corr-flow observed in the experiment were qualitatively reproduced through varying the distance of the PLF and TLF from the particle. Thus, the magnitude and sign of the corr-flow slope in the peripheral reactions appears to be very sensitive to the Coulomb field produced by the PLF and TLF. The Coulomb trajectory results provide evidence that the experimental corr-flow results could be used as a probe to the average emission order of the fragments.

2. Classical Molecular Dynamics (CMD)

The classical molecular dynamics (CMD) model [124, 125] provides a more sophisticated simulation than the Coulomb trajectory calculation in which the nuclear force and dynamical mid-rapidity particle production is included. The CMD model was used to simulate the 35 MeV/u ^{70}Zn+^{70}Zn reactions up to a time of 400 fm/c. The CMD results were filtered with a software replica of the NIMROD-ISiS array which accounts for geometry and energy thresholds of the detector.

Unlike the Coulomb trajectory calculation, the proximity of the PLF and TLF

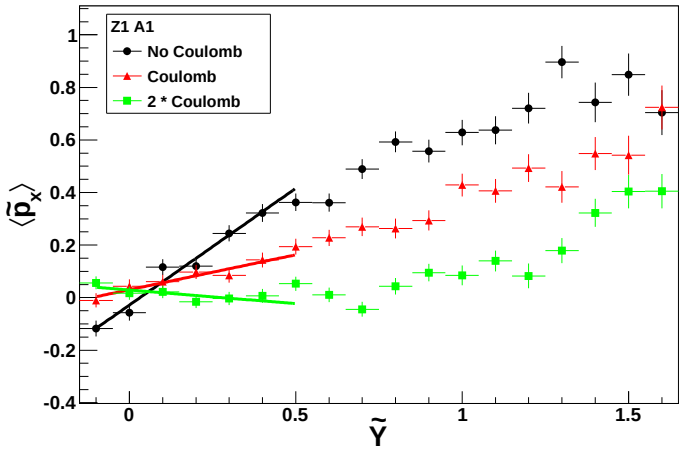

FIG. 92. Average scaled PLF-plane momentum, $\langle \tilde{p}_x \rangle$, is shown as a function of the scaled rapidity ($\tilde{Y}$) for protons in correlation with a PLF Z=21-25 from the filtered CMD simulations at 400 fm/c. The magnitude of the Coulomb potential was varied as described by the legend. A linear fit, represented by the solid colored lines, over the mid-rapidity region is shown for each of the CMD results.

can not be controlled at the time of emission of the mid-rapidity particles in the CMD model since it is a dynamical simulation in which the particle emission is occurring throughout the reaction. Therefore, in order to investigate the effect of the Coulomb potential of the PLF and TLF on the mid-rapidity, or neck, region the magnitude of the potential was varied. In Figure 92 the $\langle \tilde{p}_x \rangle$ is shown as a function of $\tilde{Y}$ for protons in correlation with PLFs with Z=21-25. The results show how the repulsive Coulomb potential competes against the attractive nuclear force in defining the trajectories of the mid-rapidity protons.

When the Coulomb potential was *not* used in the CMD simulation, the trajectory of the protons was determined from a combination of nucleon-nucleon collisions and the nuclear force. Without the repulsive Coulomb potential, a relatively large positive slope was extracted from the corr-flow, as shown by the solid black line in Figure 92.

The magnitude of the slope was decreased when the Coulomb potential was taken into account in the simulation, as shown by the solid red line. When the strength of the Coulomb potential was doubled, the corr-flow actually becomes negative, as shown by the solid green line. Thus, a balance between the attractive nuclear force and repulsive Coulomb force in the trajectory of the mid-rapidity fragments is observed.

The CMD results present a situation in which the magnitude of the Coulomb potential is strongly connected to the resulting corr-flow. An increased Coulomb potential produced a negative flow due to the particles being repulsed away from the PLF and TLF. In the experimental data, this would imply that the particles which exhibited a negative flow must have felt a stronger Coulomb force, likely from the PLF and TLF, than the positive flow particles which must have felt a smaller Coulomb force relative to the nuclear force. Therefore, the observation of a negative corr-flow should be associated with an early time of emission, since the particles would have to be in close vicinity to the PLF-TLF. At the later stages of the reaction, the Coulomb field in the mid-rapidity region would not be as strong and therefore, a positive corr-flow could be observed.

3. Antisymmetrized Molecular Dynamics (AMD)

The antisymmetrized molecular dynamics with wave packet diffusion and shrinking model (AMD) [130] was used to examine the average order of emission the LCPs in the mid-rapidity region. The CMD and Coulomb trajectory simulations provided evidence supporting the idea that the corr-flow of the LCPs and IMFs is connected to the average order of emission. However, these simulations do not provide a complete description of the heavy-ion collision. Therefore, in order to actually compare the experimentally determined emission order to theory, the AMD model was used (as well as the CoMD model in the following Section).

In AMD the Pauli Principle is respected at all times through the use of a Slater Determinant of Gaussian wave packets. The Gogny interaction was used in the simulation and the dynamics were propagated to a time of 300 fm/c. The remaining hot fragments at t=300 fm/c were statistically de-excited using the GEMINI code [141]. The AMD model coupled to GEMINI has been shown to accurately reproduce many observables from heavy-ion collisions [130, 107].

The relative production of the LCPs was examined at intervals of 50 fm/c throughout the simulated collisions. In particular, the production of particles in the mid-rapidity region was studied in reference to the final yield at t=∞, which is represented by the final distribution calculated from the GEMINI code. Each event was tagged according to the charge of the PLF at t=∞ and the %Yield, defined as

$$\%Yield = \frac{Yield(t = \tau)}{Yield(t = \infty)} \times 100\%, \tag{5.5}$$

was calculated where Yield(t=τ) represent the yield of a given particle type at some time, τ, and Yield(t=∞) is the particle yield after the GEMINI de-excitation. Therefore, the %Yield represents the relative yield produced at each time step. In Figure 93 the %Yield, calculated for particles with $0.0 \leq \tilde{Y} \leq 0.45$ (mid-rapidity region), is shown as a function of time for events in which the final PLF Z=20-24.

The results shown in Figure 93 are in good agreement with the emission order results implied from the experimental data. The %Yield is shown up to a time of 300 fm/c, which is when the GEMINI code was applied. The %Yield of the Z=1 isotopes (top panel) shows that a large mid-rapidity triton production occurs relatively early in comparison to the deuterons and protons. The results show that >80% of the mid-rapidity protons are being produced due to the statistical decay (GEMINI) in comparison to the dynamical formation. The percent production of the deuterons is slightly larger than the protons implying an earlier average emission. The Z=1

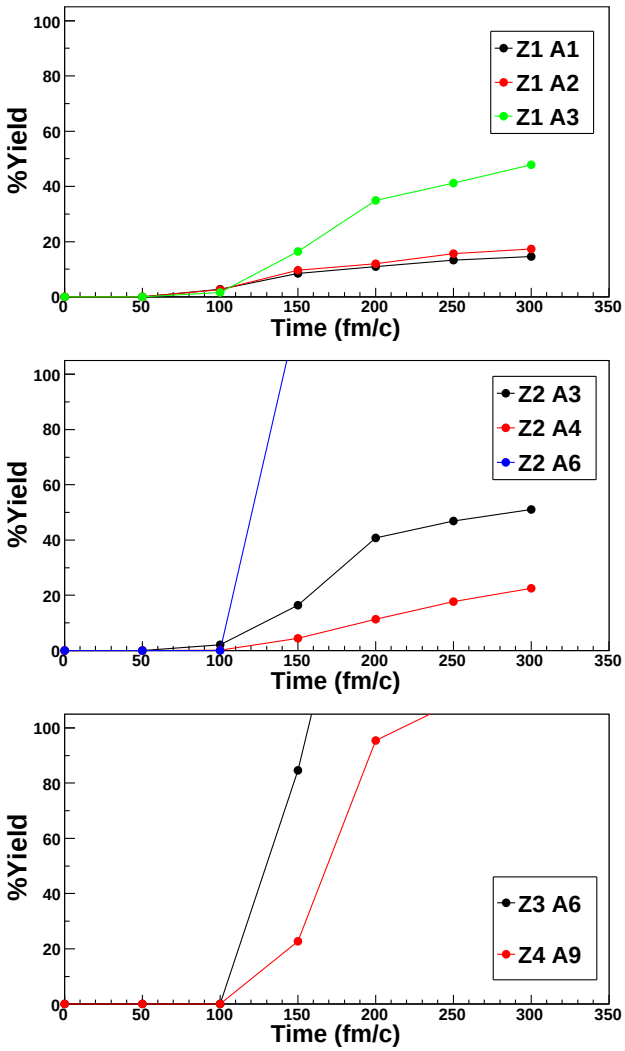

FIG. 93. Mid-rapidity %Yield as a function of time for different particle types from the AMD simulation. The results are shown for events in which the final (t=∞) PLF Z=21-25.

AMD-GEMINI results follow the experimental corr-flow results in which the slope decreased from protons to deuterons to tritons.

The $\%Yield$ results for the Z=2 isotopes (middle panel of Figure 93) are also in agreement with the emission order determined from the corr-flow. The mid-rapidity ^{6}He fragments are produced very quickly early in the collision, followed by the ^{3}He fragments and the alpha particles which on average were emitted during the later stages of the reaction. The ^{6}He fragments show a %Yield greater than 100% at 150 fm/c which represents that some of the produced ^{6}He actually break-up at a later time step. Therefore, any ^{6}He that were to reach the detector would likely have had to been produced or formed very early. Again, the extracted order of emission is in agreement with the experimentally determined order of emission for the Z=2 isotopes.

The results for the mid-rapidity ^{6}Li and ^{9}Be fragments (bottom panel), which are the dominant Z=3 and Z=4 isotopes, represent a relatively early emission time for the total produced yield. The results, like the ^{6}He, suggest that some of the ^{6}Li and ^{9}Be fragments break-up at the later stages since the %Yield value increases beyond 100%. Again, these results support the experimental corr-flow results which suggested that the Z=3 and Z=4 fragments were emitted relatively early and exhibited a corr-flow similar to the tritons and ^{6}He.

The overall results from the AMD-GEMINI simulation demonstrated good agreement with the emission order determined from the experimental corr-flow for the mid-rapidity particles. While experimentally the average emission time was not able to be extracted for a more direct comparison, the trend of the average emission order for the Z=1-4 fragments is the same between the experiment and AMD calculation.

4. Constrained Molecular Dynamics (CoMD)

Along with the AMD model, the CoMD model [128, 129] was also utilized to explore the average emission order of the Z=1-4 fragments. In the CoMD model the Pauli Principle is described through examining the occupation probability at each time step. This allows for a faster simulation of the heavy-ion collisions. Therefore, in the CoMD model the fragment production was examined up to t=3000 fm/c. The GEMINI code was used to de-excite any remaining hot fragments after 3000 fm/c.

The %Yield results from the CoMD simulation are shown in Figure 94. As mentioned, the fragment production can be evaluated over a longer time scale, in comparison to AMD, providing a better illustration of the evolution of the system. The results show that after 3000 fm/c GEMINI has a minimal effect on the particle yields, except for alphas. Thus, these results provide an opportunity to compare the experimental results to a more consistent description of the heavy-ion collision. In applying the GEMINI afterburner, one has to assume that the fragments have reached thermal equilibrium, are spherical (not deformed), and at normal nuclear density. These assumptions may likely affect the description of the mid-rapidity production. Thus, the CoMD results allow us to examine the production rates through dynamical evolution of the system, in which the fragment density and deformation is respected.

The overall trend in the production from CoMD is in good agreement with the predictions by the AMD model. The largest difference between the CoMD and AMD simulations is the difference between the proton and deuteron production rates. In the AMD model the deuteron production is just slightly increased with respect to the proton production and in the CoMD model there is a significant difference in the %Yield of the deuterons and protons. However, the average order of emission is consistent between the different descriptions of the collisions.

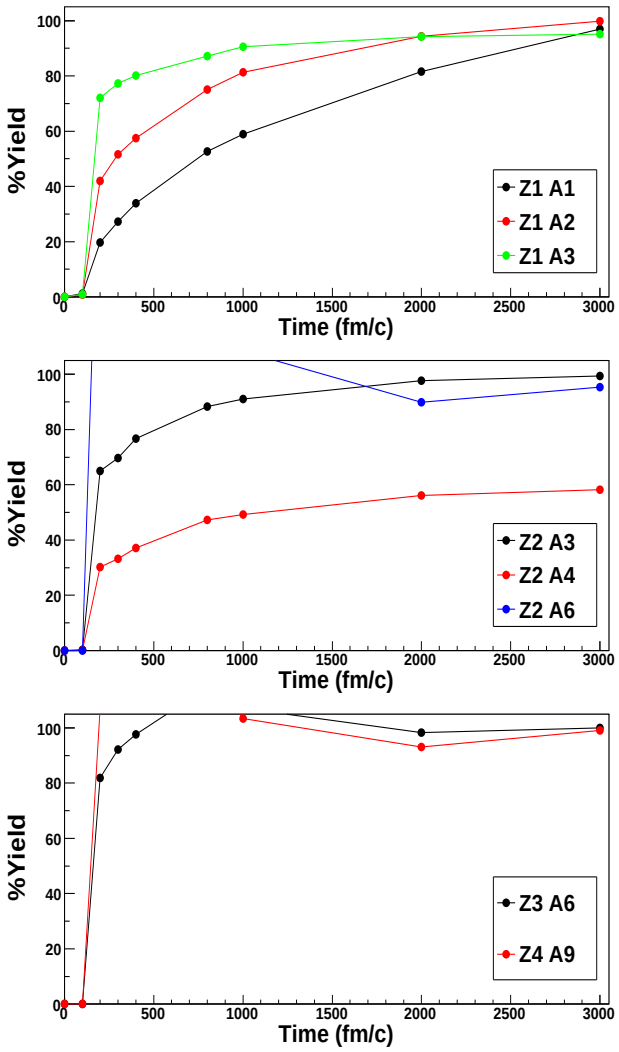

FIG. 94. Mid-rapidity %Yield as a function of time for different particle types from the CoMD simulation. The results are shown for events in which the final (t=∞) PLF Z=21-25.

The average emission order from the CoMD model (Figure 94) is in good agreement with the experimentally determined emission order from the corr-flow measurements. The CoMD results depict a scenario in which the mid-rapidity region is preferentially populated with triton, ^{6}He, Z=3, and Z=4 fragments at the early stages of the reaction, which was also suggested by the experimental results. Along with the AMD results, the CoMD simulations demonstrates that the emission order of the Z=1-4 fragments found from the experimental data was correctly determined.

5. Statistical Multifragmentation Model (SMM)

The dynamical simulations provide evidence that the corr-flow is related to the average emission time, or PLF proximity, of the mid-rapidity particles. However, the dynamical simulations do not provide information, for example, on why the tritons would be preferentially emitted into the mid-rapidity region in comparison to protons. The Statistical Multifragmentation Model (SMM) [143] has been used to examine how the proximity of the second source can change the break-up of QP and therefore, produce an enhanced emission of specific particle types into the mid-rapidity region.

The Deep-Inelastic Transfer (DIT) code of Tasson-Got [190] was used to simulate the dynamical stage of the 35 MeV/u ^{70}Zn+^{70}Zn collisions. The DIT model provides a hot QP and hot QT from a stochastic nucleon exchange process which are then de-excited by the SMM model. The angular momentum (J), excitation energy, charge, and mass of the QP and QT are calculated from DIT and are input into the SMM model. It is important to note that in the DIT model there is no particle or fragment production, besides the hot QP and QT. Therefore, the dynamical production of mid-rapidity particles is neglected. Any mid-rapidity production is due purely to the statistical de-excitation of the hot QP and QT. However, the production of the different particle types in the mid-rapidity region can still be investigated.

The SMM model has been modified [148, 149] such that Coulomb field produced by the nearby QT is accounted for in the fragmentation of the hot QP or vice versa. The particle distribution and Coulomb acceleration of the fragments are modified by the Coulomb energy of two body (PLF and TLF) system, as described in Refs. [148] and [149]. Therefore, the fragmentation of the hot QP in the presence of the QT can be investigated as a function of the QP-QT proximity. It should be noted that the nuclear force of the second source is not accounted for in the break-up of the QP. In the following, the proximity will be represented by the amount of time in which the QP and QT were propagated after the DIT interaction before the SMM fragmentation. Results will be shown in which the QP and QT were propagated for 20, 50, and 80 fm/c before fragmentation, as well as the effect of neglecting the second source proximity. Thus, a time = 80 fm/c represents an increased PLF-TLF distance and a decreased Coulomb field in the mid-rapidity region, in comparison to a time = 20 fm/c.

The corr-flow for alpha particles in correlation with PLFs of Z$\geq$26 is shown in Figure 95 from the DIT-SMM calculation. The average scaled PLF-plane momentum, $\langle \tilde{p}_x \rangle$, is shown as a function of the scaled rapidity ($\tilde{Y}$) both with and without the proximity of the second source (QT). The results demonstrate that the dynamics or trajectories of the alpha particles are not largely affected by the proximity of the second source. In all cases shown in Figure 95 the extracted slope would be negative.

It is interesting to note that the results without proximity and with proximity after 80 fm/c do show a slight positive slope around $\tilde{Y}$=0. Also, the magnitude of the negative slope does increase with increasing proximity (20-50 fm/c). This again shows that the negative slope increases with early emission time, or closer PLF-TLF proximity. Overall the DIT-SMM results are not able to reproduce the experimental corr-flow results, in which a strong positive corr-flow was observed for alpha particles.

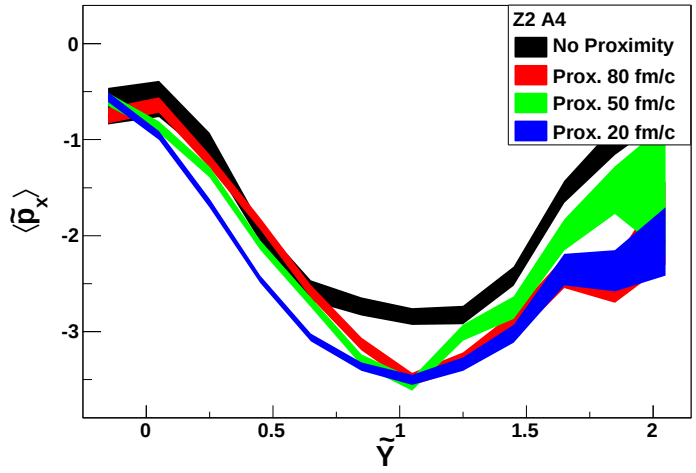

FIG. 95. Average scaled PLF-plane momentum, $\langle \tilde{p}_x \rangle$, is shown as a function of the scaled rapidity ($\tilde{Y}$) for alpha particles in correlation with PLF Z$\geq$26. The DIT-SMM simulation results are shown with and without the proximity effect as shown in the legend.

This may be due to the lack of a dynamical component to the mid-rapidity fragments in the statistical DIT-SMM simulation. Thus, the focus of the SMM simulations was to attempt to learn why the different particle types may be preferentially emitted in the mid-rapidity region in relation to the proximity of a second source.

An important aspect that the DIT-SMM simulation does reproduce is the dip or bump in the $\langle \tilde{p}_x \rangle$ versus $\tilde{Y}$ plot around $\tilde{Y}$=1, as shown in Figure 95. The same feature is observed in the experimental data, shown in Figures 83 and 84. If one combines the dip around $\tilde{Y}$=1 from the QP break-up with the mid-rapidity region from the Coulomb trajectory simulation (Figure 91) the shape of the experimental corr-flow can be qualitatively reproduced. This implies that the experimental results represent a combination of dynamical and statistical emissions from both a mid-rapidity source and QP break-up, respectively.

The LCP yield from the SMM simulation with and without the second source

proximity was compared to the experimental data. In Figure 96 the proton, deuteron, triton, and alpha particle yield is shown as a function of $\tilde{Y}$ for the experimental and filtered DIT-SMM results for events with a PLF Z=21-25. The results demonstrate that the proximity of the second source has a large effect on the particle distribution along $\tilde{Y}$. Except for protons, an increased proximity of the second source increases the production of the mid-rapidity fragments. For example, without the proximity effect the triton distribution is bimodal depicting a relatively isotropic break-up of the QP and QT. The addition of the second source proximity causes the triton yield to become strongly peaked in the mid-rapidity region. Furthermore, the fragment distributions in which the second source proximity is present are in much better agreement with the experimental data. This suggests that the fragments detected in the experiment are formed in the presence of the second source. Thus, the dynamics should be sensitive to the second source proximity, or time of emission of the fragment.

The total mid-rapidity fragment production presented in Figure 96 can be viewed as the overlapping mid-rapidity emission from the QP and QT. In Figure 97 the unfiltered QP and QT yield is presented as a function of the scaled rapidity for protons, deuterons, and tritons. Without the proximity of the second source (black lines), the QP and QT results represent a relatively isotropic emission centered around $\tilde{Y} = 1$ and -1, respectively. Thus, a small mid-rapidity production is observed due to the overlap of the QP and QT emission. The effect of the second source proximity, as discussed above, produces an enhancement in the production of the deuterons and tritons in between the PLF and TLF. Thus, even though SMM is a statistical break-up model the second source proximity effect is able to enhance the mid-rapidity production improving the agreement with the experiment.

The increased mid-rapidity fragment production has been further examined in

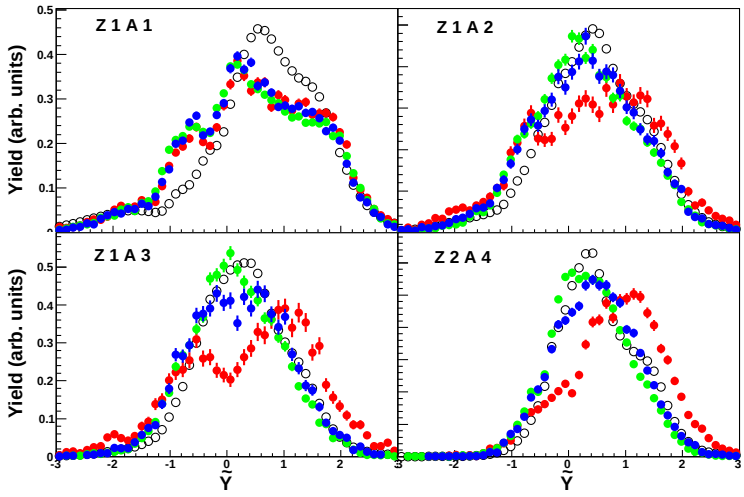

FIG. 96. Proton, deuteron, triton, and alpha yield is shown as a function of the scaled rapidity ($\tilde{Y}$) for events with a PLF Z=21-24. The experimental data (open circles) is compared to the filtered DIT-SMM results without proximity (red circles) and with proximity at 80 fm/c (blue circles) and 20 fm/c (green circles).

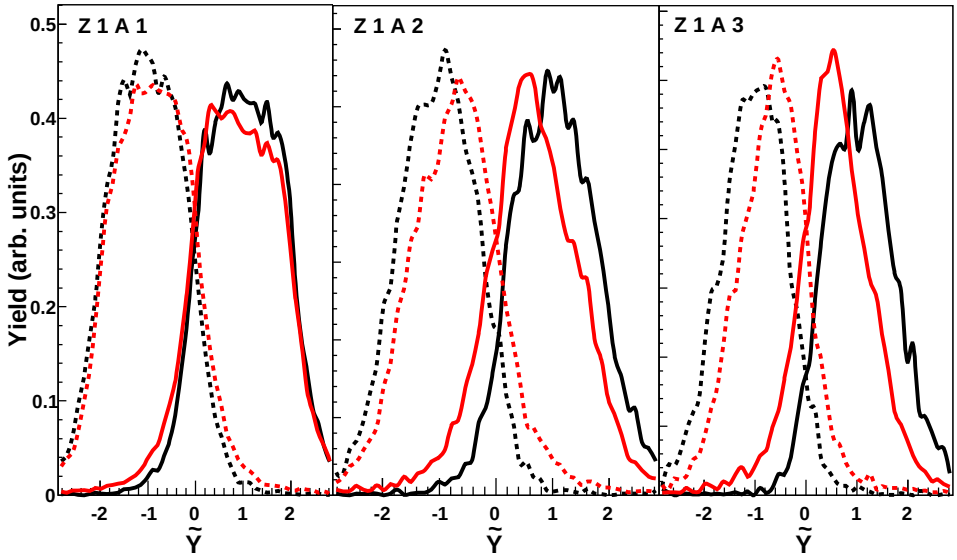

FIG. 97. Proton, deuteron, and triton yield is shown as a function of the scaled rapidity ($\tilde{Y}$) for events with a PLF Z=21-24 from the unfiltered SMM calculation. The yield from the QP (solid lines) and QT (dashed lines) are shown separately, both with a second source proximity of 50 fm/c (red lines) and without the proximity effect (black lines).

Figure 98. The ratio

$$R_{Yield} = \frac{Yield(\tilde{Y} < 1)}{Yield(Total)} \times 100\% \tag{5.6}$$

was calculated from the unfiltered fragments originating from only the QP (the QT break-up was not included). Therefore, R_{Yield} represents the percentage of fragments emitted behind the PLF, Yield($\tilde{Y} < 1$), relative to the total yield produced by the QP break-up, Yield(Total). An isotropic emission pattern should produce $R_{Yield} = 50\%$. The results in Figure 98 show that without the proximity of the second source (solid circles) all the fragments have a R_{Yield} value just below 50%. This represents a slight preference for the fragments to be emitted in front of the PLF. This anisotropy is due the angular momentum of the fragmenting QP. As shown, R_{Yield} is almost exactly 50% when the angular momentum of the QP, from DIT, and the second source proximity were neglected (open circles). Thus, without the second source proximity isotopic emission is observed from the fragmenting QP and QT.

The proximity of the second source has a large effect on the R_{Yield} values, as shown in Figure 98. It is clear that the proximity of the second source produces much stronger anisotropies in the fragment emission than the angular momentum effects. In all cases the R_{Yield} value becomes greater than 50% when including the second source proximity illustrating an enhanced production of particles behind the PLF. This preferential backward emission can be understood through the changing Coulomb energy of the system. With the addition of the second source proximity it becomes more favorable to emit light and neutron-rich fragments into the mid-rapidity region where the Coulomb potential is larger. Thus, the PLF, which has the largest charge in the event, is preferentially emitted forward of most the fragments (away from the TLF) in order to minimize the Coulomb energy. These results are in agreement with the a previous study by Botvina and Mishustin showing how the

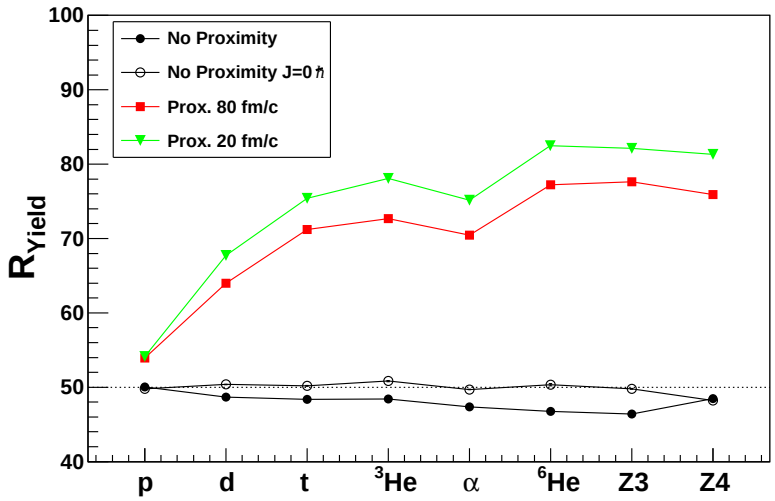

FIG. 98. R_{Yield}, from Eq. 5.6, is shown for proton, deuteron, triton, ^{3}He, alpha, ^{6}He, Z=3 and Z=4 particles for the break-up of the unfiltered QP from the DIT-SMM calculation. The results are shown for events that produced a PLF Z=20-24 with and without the proximity of the second source as described by the legend. The R_{Yield} value is also shown for the QP break-up neglecting the angular momentum (J=0$\hbar$).

proximity of a second source can effect the distribution of IMFs from the QP break-up [149].

In context with the experimental corr-flow results, it is interesting to examine the preferential mid-rapidity emission of the Z=1 and Z=2 isotopes. The experimental results suggested that the average emission order for Z=1 fragments was tritons followed by deuterons and then protons. The results in Figure 98 provide an alternative explanation for why the tritons would feel the most Coulomb. A strong increase in R_{Yield} is observed with the increasing N/Z of the Z=1 isotopes. Thus, it is more energetically favorable to emit the triton fragments into the mid-rapidity region then protons due to their larger N/Z or decreased Coulomb potential ($Z^2/A^{1/3}$). Therefore, the tritons should, on average, feel a larger Coulomb force due to the proximity of the PLF-TLF. The R_{Yield} for the protons remains near 50% with or without the second source proximity due to a large charge to mass ratio of 1.

The emission of the Z=2 fragments can also be investigated. Based on the experimental corr-flow results the ^{8}He and ^{6}He fragments are on average emitted before the ^{3}He fragments which are followed by alpha particle emission. However, these results are different then the Z=1 isotope emission order which follows a decreasing Coulomb potential (tritons→deuterons→protons). Based on the Coulomb potential of the Z=2 fragments, the alpha particles should be preferentially emitted in the mid-rapidity region over the ^{3}He fragments. However, the results in Figure 98 show that a larger percent of the ^{3}He fragments are emitted in the mid-rapidity region in comparison to the alpha particles. This is likely due to the large binding energy of alpha particles, relative to ^{3}He, which will increase the overall probability for emission and, as a result, decrease the R_{Yield} value. Thus, the SMM simulation supports the experimental results which suggest that the ^{6}He fragments would feel the largest Coulomb potential and exhibit the most negative corr-flow followed by the ^{3}He fragments and lastly the

alpha particles.

The R_{Yield} results are also shown for the Z=3 and Z=4 fragments in Figure 98. The R_{Yield} values demonstrate a strong preference for emission of the Z=3 and Z=4 fragments into the mid-rapidity region with the second source proximity. This again indicates a favored emission of the Z=3 and Z=4 fragments into the mid-rapidity region with a close PLF and TLF proximity. Thus, the Z=3 and Z=4 fragments would exhibit a negative corr-flow due to the PLF and TLF proximity, as was observed in the experimental data.

While the DIT-SMM model did not allow for the investigation of the emission order of the fragments since it assumes a simultaneous break-up of the QP and QT, it did show that the Coulomb energy of the system, or proximity of the second source, has an important role in where a fragment is preferentially emitted (forward or backward of the PLF). The enhancement of preferential mid-rapidity emission from the SMM results were in good agreement with the order of emission determined from the experimental PLF-slope results. This suggests that the increased Coulomb potential in the mid-rapidity region, especially in the early stages of the collisions, causes a preferential emission of the more neutron-rich LCPs and Z=3-4 IMFs which will then exhibit a negative corr-flow.

The SMM results provide a picture of the formation of the mid-rapidity region that is consistent with the interpertation of the Stochastic Mean-Field simulation from Chapter IV Section C. In order for the SMM simulation to match the experimental data, the proximity of the second source is needed which produces a movement of neutrons toward the mid-rapidity region before the statistical decay. In the dynamical SMF calculation the results, from Chapter IV, where interperted in the context of the isospin migration phenomenon [88, 38], which is the movement of neutrons towards the low-density mid-rapidity region while protons move the opposite direction toward

the QP or QT. Thus, in both the statistical and dynamical simulation the differential movement of neutrons and protons near the neck is important for understanding the experimental data.

D. PLF Correlations Summary

The correlation of LCPs (Z=1-2) and IMFs (Z=3-4) with PLFs has been investigated for the 35 MeV/u ^{70}Zn+^{70}Zn, ^{64}Zn+^{64}Zn, and ^{64}Ni+^{64}Ni systems. The flow of the LCPs in the PLF-plane (corr-flow) has been studied using the new scaling method presented in Equation 5.4. The results demonstrated very strong correlations of the mid-rapidity LCPs and IMFs with the PLF in the peripheral events.

The magnitude of the corr-flow, taken as the slope over the mid-rapidity region, was very sensitive to the different Z=1 and Z=2 isotopes. Thus, demonstrating that the different isotopes exhibit different dynamical characteristics. The corr-flow of the LCPs and IMFs in the mid-rapidity region was suggested to be sensitive to the proximity of the PLF-TLF and therefore, the order of emission of the mid-rapidity LCPs/IMFs could be obtained. The results indicated that on average the order of emission for the Z=1 isotopes starts with tritons followed by deuterons and then, lastly, protons. The Z=2 isotopes presented an average emission order beginning with the early emission of ^{8}He and ^{6}He followed by ^{3}He and then alpha particles. The Z=3 and Z=4 IMFs showed no significant isotopic effects but rather that the IMFs had a relatively early emission time due to the strong negative corr-flow.

These results depict a scenario in which the mid-rapidity, or neck, region is first populated by the neutron-rich fragments (tritons, ^{6}He, ^{8}He) and IMFs (at least Z=3 and Z=4). This is particularly interesting in context with previous studies that have observed an increased production of n-rich LCPs and IMFs in the neck-region in

comparison to the QP break-up [36]. Thus, the increased neutron content in the neck-region may be due to the preferential emission of n-rich fragments during the early stages of the reaction.

A variety of theoretical models and simulations were used to demonstrate the validity of the connection between the corr-flow and order of emission.

1. The Coulomb trajectory simulation showed that the slope of the corr-flow is strongly sensitive to the distance between the mid-rapidity particle and the PLF-TLF. A close proximity of the PLF-TLF to the mid-rapidity particle would produce a negative corr-flow.
2. The CMD model demonstrated that the magnitude of the Coulomb force felt by the mid-rapidity particles directly effected the slope of the corr-flow. In particular, an increased Coulomb potential caused the protons' positive corr-flow to become negative.
3. The average order of emission of the LCPs/IMFs was extracted from the AMD and CoMD models. The extracted average order of emission was in direct agreement with the experimentally obtained emission order from the corr-flow interpertation.
4. The SMM model was used to examine the results in the context of a fragmenting QP and QT system. The SMM results showed a preferential emission of n-rich fragments and IMFs into the mid-rapidity region when the QP decayed in the proximity of the QT because this minimized the Coulomb energy of the system.

Together, all the simulations and models provide a consistency in the relationship between the corr-flow and the emission of the LCPs/IMFs. In particular, the AMD and CoMD models were able to confirm the experimentally determined average order

of emission.

In conclusion, a new method, the corr-flow, has been developed to examine the dynamics of the mid-rapidity LCPs and IMFs in peripheral collisions. The resulting trajectory of the particles, or slope of the corr-flow, was shown to be sensitive to their average order of emission. Thus, new insight into the neck, or mid-rapidity, production mechanism is presented in which the increased neutron enrichment appears to be connected to a preferential emission of n-rich particles relatively early in the reaction.

CHAPTER VI

CONCLUSIONS

Determining the form of the nuclear Equation of State (EoS) is an important goal that has been recognized by the DOE/NSF Nuclear Science Advisory Committee in the 2007 Long Range Plan [191]. In particular, the EoS of asymmetric nuclear matter is crucial for understanding the properties of neutron stars and the effective nucleon-nucleon interaction. With the construction of new facilities, such as the Facility for Rare Isotope Beams (FRIB) [192], that will allow for increasingly neutron-rich heavy-ion collisions to be studied, it is imperative to identify probes that can be used to constrain the nuclear EoS. In this dissertation, the transverse flow of light charged particles (LCPs) and intermediate mass fragments (IMFs) have been shown to be sensitive to the EoS. Furthermore, new insight into the dynamics of the heavy-ion collisions have been achieved through examination of mid-rapidity fragments, or the neck-like structure, present in mid-peripheral and peripheral collisions.

The transverse flow of for proton, deuteron, triton, ^{3}He, alpha, and ^{6}He particles was investigated. The Z=1 and Z=2 transverse flow was shown to be dependent on both the $(N/Z)_{sys}$ and A_{sys}. Furthermore, the flow of the isotopically identified LCPs was also shown to be sensitive to the $(N/Z)_{sys}$ and A_{sys}, which expanded on the previous work of Pak *et al.* [53]. Isotopic and isobaric comparisons revealed a decreased flow with an increased neutron content of the fragment suggesting a differential movement of mid-rapidity protons and neutrons. The experimental LCP flow results were compared to the SMF model in order to investigate their sensitivity to the density dependence of the symmetry energy. The SMF model was able to reproduce the isotopic and isobaric trends for all the LCPs, except protons. Both the dependence of the Z=1 flow on the $(N/Z)_{sys}$ and the difference between the triton-^{3}He

flow were shown to sensitive to the form of the density dependence of the symmetry energy used in the simulation. Better agreement with experimental data was achieved with a stiff density dependence of the symmetry energy. These results suggested that the fragment flows are sensitive to the behavior of the symmetry potential below normal nuclear density and to the related neck dynamics, specifically the isospin migration phenomenon.

A comparison of the LCP flow with the AMD and CoMD models demonstrated the important dynamical components necessary to describe experimental results. In particular, the use of statistical de-excitation models, such as Gemini, before the system has cooled to a near final state can drastically modify the observed transverse flow. Therefore, in order to accurately describe the LCP transverse flow it is important to use a single dynamical description of the reaction rather than a two-stage approach. More generally, this demonstrates the need for theoretical simulations, such as the CoMD model, that can provide a single description of heavy-ion collisions from start to finish with reasonable computational time requirements.

The IMFs provided a new probe, in comparison to the light charged particles (LCPs), for examining the mechanisms responsible for the transverse flow. The results demonstrated that the IMF flow depended strongly on the mass of the system in the most violent collisions and the charge of the system in the peripheral collisions. This suggests that the repulsive Coulomb potential becomes an increasingly important component to the transverse flow in the more peripheral collisions in comparison to the attractive mean-field and repulsive nucleon-nucleon collisions. The transition of the IMF flow depending on the mass of the system to the charge of the system was shown to be strongly sensitive to the density dependence of the symmetry energy using the AMD-Gemini simulation. The comparison between the experimental data and AMD-Gemini results provides strong evidence supporting a stiff density dependence

of the symmetry energy. The CoMD and SMF model results were compared to the experimental data for the mid-peripheral collisions. The results provided additional evidence of the sensitivity of the IMF flow to the density dependence of the symmetry energy. For all three of the theoretical simulations (AMD/CoMD/SMF), better agreement with the experimental data was achieved with a stiff density dependence of the symmetry energy.

Together, the LCP and IMF results demonstrate the potential, and current ability, for transverse flow experiments to be used to constrain the density dependence of the symmetry energy. The theoretical comparisons presented in this work all showed better agreement with the experimental data when a stiff density dependence of the symmetry energy is used in the calculation. The symmetry energy at normal nuclear density ($\rho_\circ = 0.16$ fm^{-3}) and the slope (L) extracted from the different forms of the density dependence of the symmetry used in the simulations are presented in Table IX. The slope is defined as,

$$L = 3\rho_\circ \frac{\partial E_{sym}(\rho)}{\partial \rho}|_{\rho_\circ} \tag{6.1}$$

which represents the derivative of the symmetry energy around $\rho_\circ$. The $E_{sym}(\rho_\circ)$ and L values that provided the better agreement with the experimental data (shown in bold in Table IX) are in excellent agreement with current constraints on the density dependence of the symmetry energy [28, 193] and provide strong evidence supporting a stiff $E_{sym}(\rho_\circ)$.

The correlation of mid-rapidity LCPs (Z=1-2) and IMFs (Z=3-4) with projectile-like fragments (PLFs) was investigated. A new method was developed to examine the "flow" of the particles with respect to the PLF. The invariant PLF-scaled flow allowed for the dynamics of the mid-rapidity proton, deuteron, triton, ^{3}He, alpha, ^{6}He, ^{8}He, Z=3, and Z=4 particles to be studied. The results demonstrated very strong

TABLE IX. Symmetry energy at normal nuclear density and slope (L) values from the different forms of the density dependence of the symmetry energy used in the theoretical simulations. The parameterization that provided better agreement with the experimental data are in bold.

Simulation	Form	$E_{sym}(\rho_\circ)$	Slope (L)
AMD	**Stiff**	**30.5**	**65**
	Soft	30.5	21
SMF	**Stiff**	**33**	**95**
	Soft	33	19
CoMD	Super-Stiff	30	105
	Stiff	**30**	**78**
	Soft	**30**	**51**

correlations of the mid-rapidity LCPs and IMFs with the PLF in the peripheral events. Theoretical simulations were used to show that the PLF-scaled flow of particles was connected to their average order of emission. The results indicated that on average the order of emission for the Z=1 isotopes starts with tritons followed by deuterons and then, lastly, protons. The Z=2 isotopes presented an average emission order beginning with the early emission of ^{8}He and ^{6}He followed by ^{3}He and then alpha particles. The Z=3 and Z=4 IMFs showed no significant isotopic effects but rather that the IMFs had a relatively early emission time due to the strong negative corr-flow. These results depict a scenario in which the mid-rapidity, or neck, region is first populated by the neutron-rich fragments (tritons, ^{6}He, ^{8}He) and IMFs (at least Z=3 and Z=4). This is particularly interesting in context to the observed increased production of n-rich LCPs and IMFs in the neck-region in comparison to the QP break-up [36]. Thus, the increased neutron content in the neck-region may be due to

the preferential emission of n-rich fragments during the early stages of the reaction. The experimental results were in good agreement with the average order of emission extracted from the antisymmetrized molecular dynamics and constrained molecular dynamics models. The statistical multifragmentation model showed that the reason for the observed order of emission may be related to the break-up of the quasi-projectile in the presence of an external Coulomb field, due to the quasi-target, which can cause a preferential emission of n-rich particles into the mid-rapidity region. Overall, new insight about the neck, or mid-rapidity, production mechanism was discovered in which the increased neutron enrichment appears to be related to a preferential emission of n-rich particles relatively early in the reaction.

Together, the transverse flow analysis and mid-rapidity study provide new experimental results that describe the differential movement of neutrons and protons in Fermi energy heavy-ion collisions. This has been connected to the EoS for asymmetric nuclear matter through comparison with theoretical simulations and has, thus, added new results that suggest a stiff density dependence of the symmetry energy. Further, experimental and theoretical efforts could provide stringent constraints on the nuclear EoS using the methods and data provided in this work.

REFERENCES

[1] G. R. Choppin, J. O. Liljenzin, and J. Rydberg, *Radiochemistry and Nuclear Chemistry* (Butterworth-Heinemann, Woburn, 2002).

[2] G. Friedlander, J. W. Kennedy, E. S. Macias, and J. M. Miller, *Nuclear and Radiochemistry* (John Wiley and Sons, New York, 1981).

[3] G. Audi and A. H. Wapstra, Nucl. Phys. **A595**, 409 (1995).

[4] B. A. Li and U. Schroder, editors, *Isospin Physics in Heavy-Ion Collisions at Intermediate Energies* (NOVA Science, Huntington, 2001).

[5] A. Ono, Prog. Theor. Phys. Supp. **146**, 378 (2002).

[6] C. Fuchs and H. H. Wolter, Eur. Phys. J. A. **30**, 5 (2006).

[7] P. Danielewicz, R. Lacey, and W. G. Lynch, Science **298**, 1592 (2002).

[8] S. Das Gupta and G. D. Westfall, Physics Today **46**, 34 (1993).

[9] W. Reisdorf and H. G. Ritter, Annu. Rev. Nucl. Part. Sci. **47**, 663 (1997).

[10] N. Herrmann, J. P. Wessles, and T. Wienold, Annu. Rev. Nucl. Part. Sci. **49**, 581 (1999).

[11] D. J. Magestro, W. Bauer, and G. D. Westfall, Phys. Rev. C **62**, 041603(R) (2000).

[12] S. Shlomo, V. M. Kolomietz, and G. Colo, Eur. Phys. J. A **30**, 23 (2006).

[13] B. A. Li, L. W. Chen, and C. M. Ko, Phys. Rep. **464**, 113 (2008).

[14] D. V. Shetty and S. J. Yennello, arXiv:1002.0313v1 [nucl-ex] (2009).

[15] V. Baran, M. Colonna, V. Greco, and M. Di Toro, Phys. Rep. **410**, 335 (2005).

[16] B. A. Li, C. M. Ko, and W. Bauer, Int. J. Mod. Phys. **E7**, 147 (1998).

[17] A. W. Steiner, M. Prakash, J. M. Lattimer, and P. J. Ellis, Phys. Rep. **411**, 325 (2005).

[18] D. V. Shetty, S. J. Yennello, and G. A. Souliotis, Phys. Rev. C **76**, 24606 (2007).

[19] J. M. Lattimer and M. Prakash, Science **304**, 536 (2004).

[20] L. W. Chen, C. M. Ko, and B. A. Li, Phys. Rev. C **72**, 64309 (2005).

[21] B. A. Li, Nucl. Phys. **A708**, 365 (2002).

[22] T. Klahn *et al.*, Phys. Rev. C **74**, 035802 (2006).

[23] P. G. Krastev and B. A. Li, Phys. Rev. C **76**, 55804 (2007).

[24] R. J. Furnstahl, Nucl. Phys. **A706**, 85 (2002).

[25] J. R. Stone, J. C. Miller, R. Koncewicz, P. D. Stevenson, and M. R. Strayer, Phys. Rev. C **68**, 034324 (2003).

[26] B. Li, Phys. Rev. Lett. **88**, 192701 (2002).

[27] B. A. Li, Nucl. Phys. **A708**, 365 (2002).

[28] M. B. Tsang, Y. Zhang, P. Danielewicz, M. Famiano, Z. Li, W. G. Lynch, and A. W. Steiner, Phys. Rev. Lett. **102**, 122701 (2009).

[29] M. A. Famiano, T. Liu, W. G. Lynch, M. Mocko, A. M. Rogers, M. B. Tsang, M. S. Wallace, R. J. Charity, S. Komarov, D. G. Sarantites, L. G. Sobotka, and G. Verde, Phys. Rev. Lett. **97**, 052701 (2006).

[30] T. X. Liu, W. G. Lynch, M. B. Tsang, X. D. Liu, R. Shomin, W. P. Tan, G. Verde, H. F. Xi, H. S. Xu, B. Davin, Y. Larochelle, R. de Souza, R. J. Charity, and L. G. Sobotka, Phys. Rev. C **76**, 034603 (2007).

[31] S. Kowalski, J. B. Natowitz, S. Shlomo, R. Wada, K. Hagel, J. Wang, T. Materna, Z. Chen, Y. G. Ma, L. Qin, and A. S. Botvina, Phys. Rev. C **75**, 014601 (2007).

[32] M. Huang, Z. Chen, S. Kowalski, Y. G. Ma, R. Wada, T. Keutgen, K. Hagel, M. Barbui, A. Bonasera, *et al.*, Phys. Rev. C **81**, 044620 (2010).

[33] M. B. Tsang, T. X. Liu, L. Shi, P. Danielewicz, C. K. Gelbke, X. D. Liu, W. G. Lynch, W. P. Tan, G. Verde, A. Wagner, H. S. Xu, W. A. Friedman, L. Beaulieu, B. Davin, R. de Souza, Y. Larochelle, T. Lefort, R. Yanez, V. E. Viola, R. J. Charity, and L. G. Sobotka, Phys. Rev. Lett. **92**, 062701 (2004).

[34] L. Scalone, M. Colonna, and M. Di Toro, Phys. Lett. B **461**, 9 (1999).

[35] M. Di Toro, S. J. Yennello, and B. A. Li, Eur. Phys. J. A **30**, 153 (2006).

[36] M. Di Toro, A. Olmi, and R. Roy, Eur. Phys. J. A **30**, 65 (2006).

[37] V. Baran, M. Colonna, M. Di Toro, V. Greco, M. Zielinska-Pfabe, and H. H. Wolter, Nucl. Phys. **A703**, 603 (2002).

[38] V. Baran, M. Colonna, and M. Di Toro, Nucl. Phys. **A730**, 329 (2004).

[39] L. G. Sobotka, Phys. Rev. C **50**, 1272(R) (1994).

[40] R. E. Renfordt, D. Schall, R. Bock, R. Brockmann, J. W. Harris, A. Sandoval, R. Stock, H. Strobele, *et al.*, Phys. Rev. Lett. **53**, 763 (1984).

[41] H. A. Gustafsson, H. H. Gutbrod, B. Kolb, H. Lohner, B. Ludewigt, A. M. Poskanzer, T. Renner, H. Riedesel, *et al.*, Phys. Rev. Lett. **52**, 1590 (1984).

[42] M. B. Tsang, R. M. Ronningen, G. Bertsch, Z. Chen, C. B. Chitwood, D. J. Fields, C. K. Gelbke, *et al.*, Phys. Rev. Lett. **57**, 559 (1986).

[43] C. A. Ogilvie, W. Bauer, D. A. Cebra, J. Clayton, S. Howden, J. Karn, A. Nadasen, A. Vander Molen, G. D. Westfall, W. K. Wilson, and J. S. Winfield, Phys. Rev. C **42**, 10(R) (1990).

[44] D. Cussol, T. Lefort, J. Peter, G. Auger, C. O. Bacri, F. Bocage, B. Borderie, *et al.*, Phys. Rev. C **65**, 44604 (2002).

[45] D. Krofcheck, W. Bauer, G. M. Crawley, S. Howden, C. A. Ogilvie, A. Vander Molen, G. D. Westfall, *et al.*, Phys. Rev. C **46**, 1416 (1992).

[46] D. J. Magestro, W. Bauer, O. Bjarki, J. D. Crispin, M. L. Miller, M. B. Tonjes, A. M. Vander Molen, and G. D. Westfall, Phys. Rev. C **61**, 021602(R) (2000).

[47] D. Krofcheck, W. Bauer, G. M. Crawley, C. Djalali, S. Howden, C. A. Ogilvie, A. Vander Molen, G. D. Westfall, *et al.*, Phys. Rev. Lett. **63**, 2028 (1989).

[48] G. D. Westfall, W. Bauer, D. Craig, M. Cronqvist, E. Gualtieri, S. Hannuschke, D. Klakow, *et al.*, Phys. Rev. Lett. **71**, 1986 (1993).

[49] A. Bonasera, F. Gulminelli, and J. Molitoris, Phys. Rep. **243**, 1 (1994).

[50] J. Rizzo, P. Chomaz, and M. Colonna, Nucl. Phys. **A806**, 40 (2008).

[51] A. D. Sood and P. R. K., Phys. Rev. C **69**, 054612 (2004).

[52] B. A. Li and A. T. Sustich, Phys. Rev. Lett. **82**, 5004 (1999).

[53] R. Pak, W. Benenson, O. Bjarki, J. A. Brown, S. A. Hannuschke, R. A. Lacey, B. A. Li, *et al.*, Phys. Rev. Lett. **78**, 1022 (1997).

[54] R. Pak, B. A. Li, W. Benenson, O. Bjarki, J. A. Brown, S. Hannuschke, *et al.*, Phys. Rev. Lett. **78**, 1026 (1997).

[55] C. Liewen, Z. Fengshou, and J. Genming, Phys. Rev. C **58**, 2283 (1998).

[56] B. A. Li, Z. Ren, C. M. Ko, and S. J. Yennello, Phys. Rev. Lett. **76**, 4492 (1996).

[57] B. A. Li, Phys. Rev. Lett. **85**, 4221 (2000).

[58] G. C. Yong, B. A. Li, and L. W. Chen, Phys. Rev. C **74**, 064617 (2006).

[59] W. Trautmann, M. Chartier, Y. Leifels, R. C. Lemmon, Q. Li, J. Lukasik, A. Pagano, P. Pawlowski, P. Russotto, and P. Wu, Prog. Part. Nucl. Phys. **62**, 425 (2009).

[60] W. Trautmann, M. Chartier, Y. Leifels, R. C. Lemmon, Q. Li, J. Lukasik, A. Pagano, P. Pawlowski, P. Russotto, and P. Z. Wu, arXiv:0907.2822v1 [nucl-ex] (2009).

[61] G. C. Yong, B. A. Li, L. W. Chen, and X. C. Zhang, Phys. Rev. C **80**, 44608 (2009).

[62] F. Rami, P. Crochet, R. Dona, B. de Schauenburg, P. Wagner, J. P. Alard, A. Andronic, *et al.*, Nucl. Phys. **A646**, 367 (1999).

[63] M. J. Huang, R. C. Lemmon, F. Daffin, W. G. Lynch, C. Schwarz, M. B. Tsang, C. Williams, P. Danielewicz, *et al.*, Phys. Rev. Lett. **77**, 3739 (1996).

[64] M. D. Partlan, S. Albergo, F. Bieser, F. P. Brady, Z. Caccia, D. A. Cebra, A. D. Chacon, J. Chance, Y. Choi, *et al.*, Phys. Rev. Lett. **75**, 2100 (1995).

[65] T. Z. Yan, Y. G. Ma, X. Z. Cai, D. Q. Fang, G. C. Lu, W. Q. Shen, W. D. Tian, *et al.*, Chin. Phys. Lett. **24**, 3388 (2007).

[66] J. Lukasik and W. Trautmann, arXiv:0708.2821 [nucl-ex] (2007).

[67] C. P. Montoya, W. G. Lynch, D. R. Bowman, G. F. Peaslee, N. Carlin, R. de Souza, C. K. Gelbke, W. B. Gong, *et al.*, Phys. Rev. Lett. **73**, 3070 (1994).

[68] R. Wada, M. Gonin, M. Gui, K. Hagel, Y. Lou, D. Utley, B. Xiao, D. Miller, J. B. Natowitz, *et al.*, Nucl. Phys. **A548**, 471 (1992).

[69] J. Toke, B. Lott, S. P. Baldwin, B. M. Quednau, W. U. Schroder, L. G. Sobotka, J. Barreto, R. J. Charity, *et al.*, Nucl. Phys. **A583**, 519 (1995).

[70] J. Lukasik, J. Benlliure, V. Metivier, E. Plagnol, B. Tarnian, M. Assenard, G. Auger, *et al.*, Phys. Rev. C **55**, 1906 (1997).

[71] E. Plagnol, J. Lukasik, G. Auger, C. O. Bacri, F. Bellaize, N.and Bocage, B. Borderie, *et al.*, Phys. Rev. C **61**, 014606 (1999).

[72] L. Stuttge, J. C. Adloff, B. Bilwes, R. Bilwes, F. Cosmo, M. Glaser, G. Rudolf, and F. Scheibling, Nucl. Phys. **A539**, 511 (1992).

[73] D. E. Fields, K. Kwiatkowski, K. B. Morley, E. Renshaw, J. L. Wile, S. J. Yennello, and R. G. Viola, V. E.and Korteling, Phys. Rev. Lett. **69**, 3713 (1992).

[74] J. E. Sauvestre, J.-L. Charvet, R. Dayras, C. Volant, B. Berthier, R. Legrain, R. Lucas, *et al.*, Phys. Lett. B **335**, 300 (1994).

[75] J. Boger, S. Kox, G. Auger, J. M. Alexander, A. Narayanan, M. A. McMahan, *et al.*, Phys. Rev. C **41**, 801(R) (1990).

[76] S. Piantelli, L. Bidini, G. Poggi, M. Bini, G. Casini, P. R. Maurenzig, A. Olmi, G. Pasquali, A. A. Stefanini, and N. Taccetti, Phys. Rev. Lett. **88**, 52701 (2002).

[77] S. Hudan, R. Alfaro, L. Beaulieu, B. Davin, Y. Larochelle, T. Lefort, V. E. Viola, H. Xu, R. Yanez, R. de Souza, *et al.*, Phys. Rev. C **70**, 031601(R) (2004).

[78] A. B. McIntosh, S. Hudan, J. Black, D. Mercier, C. J. Metelko, R. Yanez, R. de Souza, A. Chbihi, M. Famiano, *et al.*, Phys. Rev. C **81**, 034603 (2010).

[79] L. Gingras, A. Chernomoretz, Y. Larochelle, Z. Y. He, L. Beaulieu, G. C. Ball, F. Greiner, D. Horn, R. Roy, M. Samri, *et al.*, Phys. Rev. C **65**, 061604(R) (2002).

[80] D. Theriault, J. Gautheir, F. Grenier, F. Moisan, C. St.-Pierre, R. Roy, B. Davin, S. Hudan, *et al.*, Phys. Rev. C. **74**, 051602(R) (2006).

[81] J. F. Dempsey, R. J. Charity, L. G. Sobotka, G. J. Kunde, S. Gaff, C. K. Gelbke, T. Glasmacher, M. J. Huang, R. C. Lemmon, W. G. Lynch, *et al.*, Phys. Rev. C **54**, 1710 (1996).

[82] S. Piantelli, P. R. Maurenzig, A. Olmi, L. Bardelli, M. Bini, G. Casini, A. Mangiarotti, *et al.*, Phys. Rev. C **76**, 061601(R) (2007).

[83] R. Planeta, F. Amorini, A. Anzalone, L. Auditore, V. Baran, A. Benisz, I. Berceanu, A. Bonasera, *et al.*, Phys. Rev. C. **77**, 014610 (2008).

[84] S. Hudan, R. Alfaro, B. Davin, Y. Larochelle, H. Xu, L. Beaulieu, T. Lefort, R. Yanez, R. de Souza, R. J. Charity, L. G. Sobotka, *et al.*, Phys. Rev. C **71**, 054604 (2005).

[85] R. Laforest, E. Ramakrishan, D. J. Rowland, A. Ruangma, E. M. Winchester, E. Martin, and S. J. Yennello, Phys. Rev. C **59**, 2567 (1999).

[86] D. V. Shetty, A. Keksis, A. Ruangma, G. A. Souliotis, M. Veselsky, E. M. Winchester, S. J. Yennello, K. Hagel, Y. G. Ma, *et al.*, Phys. Rev. C **68**, 054605 (2003).

[87] J. Rizzo, M. Colonna, V. Baran, M. Di Toro, H. H. Wolter, and M. Zielinska-Pfabe, Nucl. Phys. **A806**, 79 (2008).

[88] R. Lionti, V. Baran, M. Colonna, and M. Di Toro, Phys. Lett. B **625**, 33 (2005).

[89] G. Verde, A. Chbihi, R. Ghetti, and J. Helgesson, Eur. Phys. J. A **30**, 81 (2006).

[90] C. J. Gelderloos, J. M. Alexander, N. N. Ajitanand, E. Bauge, A. Elmaani, *et al.*, Phys. Rev. Lett. **75**, 3082 (1995).

[91] Z. Y. He, G. M. Jin, Z. Y. Li, L. M. Duan, G. X. Dai, B. G. Zhang, *et al.*, Eur. Phys. J. A **1**, 61 (1998).

[92] E. W. Cornell, T. M. Hamilton, D. Fox, Y. Lou, R. T. de Souza, *et al.*, Phys. Rev. Lett. **77**, 4508 (1996).

[93] E. De Flilippo, A. Pagano, J. Wilczynski, F. Amorini, A. Anzalone, L. Auditore, V. Baran, I. Berceanu, J. Blicharska, J. Brzychczyk, A. Bonasera, B. Borderie, *et al.*, Phys. Rev. C **71**, 044602 (2005).

[94] G. Casini, P. G. Bizzeti, P. R. Maurenzig, A. Olmi, A. A. Stefanini, J. P. Wessles, R. J. Charity, R. Friefelder, A. Gobbi, N. Herrmann, *et al.*, Phys. Rev. Lett. **71**, 2567 (1993).

[95] D. Durand, J. Colin, J. F. Lecolley, C. Meslin, M. Aboufirassi, B. Bilwes, *et al.*, Phys. Lett. B **345**, 397 (1995).

[96] S. Hudan, A. S. Botvina, R. Alfaro, L. Beaulieu, B. Davin, Y. Larochelle, T. Lefort, V. E. Viola, H. S. Xu, R. Yanez, R. T. deSouza, T. X. Liu, X. D. Liu, W. G. Lynch, R. Shomin, W. P. Tan, M. B. Tsang, A. Vander Molen, A. Wagner, H. F. Xi, R. J. Charity, and L. G. Sobotka, arXiv:nucl-ex/0308031v2 (2003).

[97] M. Jandel, A. S. Botvina, S. J. Yennello, G. A. Souliotis, D. V. Shetty, E. Bell, and A. Keksis, J. Phys. G: Nucl. Part. Phys. **31**, 29 (2005).

[98] R. Ghetti, J. Helgesson, G. Lanzano, E. De Flilippo, M. Geraci, S. Aiello, S. Cavallaro, A. Pagano, *et al.*, Nucl. Phys. **A765**, 307 (2006).

[99] R. Ghetti, J. Helgesson, V. Avdeichikov, B. Jakobsson, N. Colonna, G. Tagliente, H. W. Wilschut, and K. V. L., arXiv:nucl-ex/0507029v1 (2005).

[100] L. W. Chen, C. M. Ko, and B. A. Li, Nucl. Phys. **A729**, 809 (2003).

[101] R. Ghetti and J. Helgesson, Nucl. Phys. **A752**, 480c (2005).

[102] S. Wuenschel, K. Hagel, R. Wada, J. Natowitz, S. J. Yennello, Z. Kohley, C. Bottosso, L. W. May, W. B. Smith, D. V. Shetty, B. C. Stein, S. N. Soisson, and G. Prete, Nucl. Instrum. Methods Phys. Res. A **604**, 578 (2009).

[103] Micromatter Co. 18218 18th AVE NW Arlington, WA 98223.

[104] Specials thanks to John Greene at ANL traget lab for the speedy target fabrication.

[105] Trace Sciences International Inc. www.tracesciences.com.

[106] E. Bell, *N/Z Equilibration*, PhD thesis, Texas A&M University, 2005.

[107] R. Wada, T. Keutgen, K. Hagel, Y. G. Ma, J. Wang, M. Murray, L. Qin, P. Smith, J. B. Natowitz, R. Alfarro, J. Cibor, M. Cinausero, Y. E. Masri, D. Fabris, E. Fioretto, A. Keksis, S. Kowalski, M. Lunardon, A. Makeev, N. Marie, E. Martin, Z. Majka, A. Martinez-Davalos, A. Menchaca-Rocha, G. Nebbia, G. Prete, V. Rizzi, A. Ruangma, D. V. Shetty, G. Souliotis, P. Staszel, M. Veselsky, G. Viesti, E. M. Winchester, S. J. Yennello, W. Zipper, and A. Ono, Phys. Rev. C **69**, 044610 (2004).

[108] K. Kwiatkowski, D. S. Bracken, K. B. Morley, J. Brzychczyk, E. Renshaw-Foxford, K. Komisarcik, V. E. Viola, N. R. Yoder, J. Dorsett, J. Poehlman, N. Madden, and J. Ottarson, Nucl. Instrum. Methods Phys. Res. A **360**, 571 (1995).

[109] R. P. Schmitt, L. Cooke, G. Derrig, D. Fabris, B. Hurst, J. B. Natowitz, G. Nebbia, D. OKelly, B. Srivastava, W. Turmel, D. Utley, H. Utsunomiya, and R. Wada, Nucl. Instrum. Methods Phys. Res. A **354**, 487 (1995).

[110] J. Pouthas, B. Borderie, R. Dayras, E. Plagnol, M. F. Rivet, F. Saint-Laurent, J. C. Steckmeyer, G. Auger, C. O. Bacri, S. Barbey, A. Barbier, A. Benkirane, J. Benlliure, B. Berthier, E. Bougamont, P. Bourgault, P. Box, R. Bzyl, B. Cahan, Y. Cassagnou, D. Charlet, J. L. Char-vet, A. Chbihi, T. Clerc, N. Copinet, D. Cussol, M. Engrand, J. M. Gautier, Y. Huguet, . Jouniaux, J. L. Laville, P. L. Botlan, A. Leconte, R. Legrain, P. Lelong, M. L. Guay, L. Martina, C. Mazur, P. Mosrin, L. Olivier, J. P. Passerieux, S. Pierre, B. Piquet, E. Plaige, E. C. Pollacco, B. Raine, A. Richard, J. Ropert, C. Spitaels, L. Stab, D. Sznajderman, L. Tassan-got, J. Tillier, M. Tripon, P. Vallerand, C. Volant, P. Volkov, J. P. Wieleczko, and G. Wittwer, Nucl. Instrum. Methods Phys. Res. A **357**, 418 (1995).

[111] G. F. Knoll, *Radiaton Detection and Measurement* (John Wiley & Sons, Ann Arbor, 2000).

[112] W. R. Leo, *Techniques for Nuclear and Particle Physics Experiments.* (Spring-Verlag, New York, 1994).

[113] B. Davin, R. T. deSouza, R. Yanez, Y. Larochelle, R. Alfaro, H. S. Xu, A. Alexander, K. Bastin, L. Beaulieu, J. Dorsett, G. Fleener, L. Gelovani, T. Lefort, J. Poehlman, R. J. Charity, L. G. Sobotka, J. Elson, A. Wagner, T. Liu, X. D. Liu, W. G. Lynch, L. Morris, R. Shomin, W. P. Tan, M. B. Tsang, G. Verde, and J. Yurkon, Nucl. Instrum. Methods Phys. Res. A **473**, 302 (2001).

[114] Pico Systems www.pico-systems.com.

[115] L. W. May, Z. Kohley, S. Wuenschel, K. Hagel, S. N. Soisson, G. A. Souliotis, B. C. Stein, R. Wada, and S. J. Yennello, To Be Submitted .

[116] S. Wuenschel, K. Hagel, L. W. May, R. Wada, and S. J. Yennello, AIP Conf. Proc. **1099**, 816 (2009).

[117] G. A. Souliotis, M. Veselsky, D. V. Shetty, L. Trache, and S. J. Yennello, Nucl. Phys. **A746**, 526c (2004).

[118] S. Wuenschel, *Temperature and Scaling Studies from Projectile Fragmentation of* $^{86,78}Kr+^{64,58}Ni$ *at 35 MeV/A*, PhD thesis, Texas A&M University, 2009.

[119] Code for two-body kinematic caluclation provided by T. Keutgen and Y.E. Masri (FNRS and IPN, Universit Catholique de Louvain, B-1348 Louvain-Neuve, Belgium).

[120] C. Dugauquez, *Production de particules chargees legeres et multiplicites neutroniques associees dans les reactions p+Si and a+Si de 20 a 64 MeV*, PhD thesis, Universite Catholique de Louvain, 2005.

[121] C. Dufauquez, Y. E. Masri, V. Roberfroid, J. Cabrera, T. Keutgen, J. Van Mol, P. Demetriou, and R. J. Charity, Nucl. Phys. **A773**, 24 (2006).

[122] F. Hubert, R. Bimbot, and H. Gauvin, At. Data Nucl. Data Tables **46**, 1 (1990).

[123] L. Tassan-Got, Nucl. Instrum. Methods Phys. Res. B **194**, 503 (2002).

[124] V. Latora, M. Belkacem, and A. Bonasera, Phys. Rev. Lett. **73**, 1765 (1994).

[125] M. Belkacem, V. Latora, and A. Bonasera, Phys. Rev. C **52**, 271 (1995).

[126] R. J. Lenk, T. J. Schlagel, and V. R. Pandharipande, Phys. Rev. C **42**, 372 (1990).

[127] V. Latora, A. Del Zoppo, and A. Bonasera, Nucl. Phys. **A572**, 477 (1994).

[128] M. Papa and A. Maruyama, T.and Bonasera, Phys. Rev. C **64**, 24612 (2001).

[129] M. Papa, G. Giuliani, and A. Bonasera, J. Comput. Phys. **208**, 403 (2005).

[130] A. Ono and H. Horiuchi, Prog. Part. Nucl. Phys. **53**, 501 (2004).

[131] A. Ono, Phys. Rev. C **59**, 853 (1999).

[132] A. Ono, S. Hudan, A. Chbihi, and J. D. Frankland, Phys. Rev. C. **66**, 014603 (2002).

[133] J. Rizzo, M. Colonna, M. Di Toro, and V. Greco, Nucl. Phys. **A732**, 202 (2004).

[134] V. Giordano, M. Colonna, M. Di Toro, V. Greco, and J. Rizzo, Phys. Rev. C **81**, 044611 (2010).

[135] P. Chomaz, M. Colonna, and J. Randrup, Phys. Rep. **389**, 263 (2004).

[136] J. Rizzo, M. Colonna, and A. Ono, Phys. Rev. C **76**, 024611 (2007).

[137] M. Colonna, M. Di Toro, A. Guarnera, S. Maccarone, M. Zielinska-Pfabe, and H. H. Wolter, Nucl. Phys. **A642**, 449 (1998).

[138] I. Bombaci, M. Prakash, M. Prakash, P. J. Ellis, J. M. Lattimer, and G. E. Brown, Nucl. Phys. **A583**, 623 (1995).

[139] C. Gale, G. F. Bertsch, and S. Das Gupta, Phys. Rev. C **41**, 1545 (1990).

[140] E. Santini, T. Gaitanos, M. Colonna, and M. Di Toro, Nucl. Phys. **A756**, 468 (2005).

[141] R. J. Charity, M. A. McMahan, G. J. Wozniak, R. J. McDonald, L. G. Moretto, D. G. Sarantites, L. G. Sobotka, *et al.*, Nucl. Phys. **A483**, 371 (1988).

[142] Charity, R.J., code GEMINI++, (www.chemistry.wustl.edu/rc/gemini++/).

[143] J. P. Bondorf, A. S. Botvina, A. S. Iljinov, I. N. Mishustin, and K. Sneppen, Phys. Rep. **257**, 133 (1995).

[144] N. Buyukcizmeci, R. Ogul, and A. S. Botvina, Eur. Phys. J. A **25**, 57 (2005).

[145] A. S. Botvina and I. N. Mishustin, Eur. Phys. J. A **30**, 121 (2006).

[146] A. S. Botvina, A. D. Jackson, and I. N. Mishustin, Phys. Rev. E **62**, R64 (2000).

[147] G. A. Souliotis, A. S. Botvina, D. V. Shetty, A. L. Keksis, M. Jandel, M. Veselsky, and S. J. Yennello, Phys. Rev. C **75**, 011601(R) (2007).

[148] A. S. Botvina, M. Bruno, M. D'Agostino, and D. H. E. Gross, Phys. Rev. C **59**, 3444 (1999).

[149] A. S. Botvina and I. N. Mishustin, Phys. Rev. C **63**, 061601(R) (2001).

[150] G. D. Westfall, Nucl. Phys. **A630**, 27 (1998).

[151] R. Pak, W. J. Llope, D. Craig, E. E. Gualtieri, S. Hannuschke, R. A. Lacey, J. Lauret, *et al.*, Phys. Rev. C **53**, 1469 (1996).

[152] J. C. Angelique, A. Buta, G. Bizard, D. Cussol, A. Peghaire, J. Peter, R. Popescu, G. Auger, *et al.*, Nucl. Phys. **A614**, 261 (1997).

[153] A. Andronic, J. Lukasik, W. Reisdorf, and W. Trautmann, Eur. Phys. J. A **30**, 31 (2006).

[154] J. De Sanctis, M. Masotti, M. Bruno, M. D'Agostino, E. Geraci, G. Vannini, and A. Bonasera, J. Phys. G **36**, 15101 (2009).

[155] C. A. Ogilvie, D. A. Cebra, J. Clayton, S. Howden, J. Karn, A. Vander Molen, G. D. Westfall, W. K. Wilson, and J. S. Winfield, Phys. Rev. C **40**, 654 (1989).

[156] F. Haddad, K. Hagel, J. Li, N. Mdiewayeh, J. B. Natowitz, R. Wada, B. Xiao, C. David, M. Freslier, and J. Aichelin, Phys. Rev. C **55**, 1371 (1997).

[157] C. David, M. Freslier, and J. Aichelin, Phys. Rev. C **51**, 1453 (1995).

[158] J. Peter, D. Cussol, G. Bizard, R. Brou, M. Louvel, J. P. Patry, R. Regimbart, *et al.*, Nucl. Phys. **A519**, 611 (1990).

[159] S. A. Bass, A. Bischoff, J. A. Maruhn, H. Stocker, and W. Greiner, Phys. Rev. C **53**, 2358 (1996).

[160] Y. G. Ma, J. B. Natowitz, R. Wada, K. Hagel, J. Wang, T. Keutgen, Z. Majka, M. Murray, L. Qin, *et al.*, Phys. Rev. C **71**, 54606 (2005).

[161] M. B. Tsang, R. T. de Souza, Y. D. Kim, D. R. Bowman, N. Carlin, C. K. Gelbke, *et al.*, Phys. Rev. C **44**, 2065 (1991).

[162] W. K. Wilson, R. Lacey, C. A. Ogilvie, and G. D. Westfall, Phys. Rev. C **45**, 738 (1992).

[163] P. Danielewicz and G. Odyniec, Phys. Lett. B **157**, 146 (1985).

[164] M. Gyulassy, K. A. Frankel, and H. Stocker, Phys. Lett. B **110**, 185 (1982).

[165] C. A. Ogilvie, D. A. Cebra, J. Clayton, P. Danielewicz, S. Howden, J. Karn, *et al.*, Phys. Rev. C **40**, 2592 (1989).

[166] J. Lukasik and W. Trautmann, arXiv:0603028 [nucl-ex] (2006).

[167] J. Peter, Nucl. Phys. **A545**, 173 (1992).

[168] R. Nebauer and J. Aichelin, Nucl. Phys. **A650**, 65 (1999).

[169] J. Zhang, S. Das Gupta, and C. Gale, Phys. Rev. C **50**, 1617 (1994).

[170] M. Colonna (private communication).

[171] A. Ono and J. Randrup, Eur. Phys. J. A **30**, 109 (2006).

[172] M. Di Toro, V. Baran, M. Colonna, G. Ferini, T. Gaitanos, V. Greco, J. Rizzo, and H. H. Wolter, Nucl. Phys. **A787**, 585 (2007).

[173] B. A. Li, C. B. Das, S. Das Gupta, and C. Gale, Nucl. Phys. **A735**, 563 (2004).

[174] B. A. Li, Phys. Rev. C **69**, 64602 (2004).

[175] M. Mocko, M. B. Tsang, D. Lacroix, A. Ono, P. Danielewicz, W. G. Lynch, and R. J. Charity, Phys. Rev. C **78**, 024612 (2008).

[176] Y. Fu, D. Q. Fang, Y. G. Ma, X. Z. Cai, W. D. Tian, H. W. Wang, and W. Guo, Chin. Phys. Lett. **26**, 082503 (2009).

[177] D. Lacroix, A. Van Lauwe, and D. Durand, Phys. Rev. C **69**, 054604 (2004).

[178] Z. Chen, S. Kowalski, M. Huang, R. Wada, T. Keutgen, K. Hagel, J. Wang, L. Qin, J. B. Natowitz, T. Materna, P. K. Sahu, and A. Bonasera, arXiv:1002.0319v1 [nucl-ex] (2010).

[179] S. Hudan, R. T. de Souza, and A. Ono, Phys. Rev. C **73**, 054602 (2006).

[180] A. Andronic, W. Reisdorf, N. Herrmann, P. Crochet, J. P. Alard, V. Barret, Z. Basrak, *et al.*, Phys.Rev. C **67**, 34907 (2003).

[181] A. Ono and H. Horiuchi, Phys. Rev. C **51**, 299 (1995).

[182] A. Ono, H. Horiuchi, and T. Maruyama, Phys. Rev. C **48**, 2946 (1993).

[183] J. Lukasik, G. Auger, M. L. Begemann-Blaich, N. Bellaize, R. Bittiger, F. Bocage, *et al.*, Phys. Lett. B **608**, 223 (2005).

[184] S. Soff, S. A. Bass, C. Hartnack, H. Stocker, and W. Greiner, Phys. Rev. C **51**, 3320 (1995).

[185] B. A. Li and L. W. Chen, Phys. Rev. C **72**, 64611 (2005).

[186] M. Di Toro, A. Olmi, and R. Roy, Eur. Phys. J. A **30**, 65 (2006).

[187] A. Bonasera and L. P. Csernai, Phys. Rev. Lett. **59**, 630 (1987).

[188] A. M. Poskanzer and S. A. Voloshin, Phys. Rev. C **58**, 1671 (1998).

[189] S. A. Voloshin, Phys. Rev. C **55**, 1630 (1997).

[190] L. Tassan-Got and C. Stefan, Nucl. Phys. **A524**, 121 (1991).

[191] NSAC Long Range Plan: Frontiers of Nuclear Science, http://www.er.doe.gov/np/nsac/nsac.html, 2007.

[192] http://www.frib.msu.edu/.

[193] L. W. Chen, C. M. Ko, B. A. Li, and J. Xu, arXiv:1004.4672v1 [nucl-th] (2010).

APPENDIX A

SCHEMATIC OF NIMROD-ISIS ARRAY RINGS

The following figures show schematic drawings of the detector configurations for each ring of the NIMROD-ISiS array. All detector numbers correspond to the values from the detectormap which relates the detector number to the correct ADC/QDC channel number. In Rings 2-9 the cesium-iodides are labeled as either CsIB, CsIR, or CsIL which represents the bottom, top-right, and top-left CsI. In the case of only 1 CsI in the top ring, the CsIR label was used by default (see Ring 2-3).

Unless noted the top of the figure represents a phi angle of 90^o in lab. The point of view for each ring comes from that of the target. Therefore, for the forward angle rings (2-11) the beam would be traveling into the figure and in the backward angle rings (12-15) the beam would be traveling out of the figure.

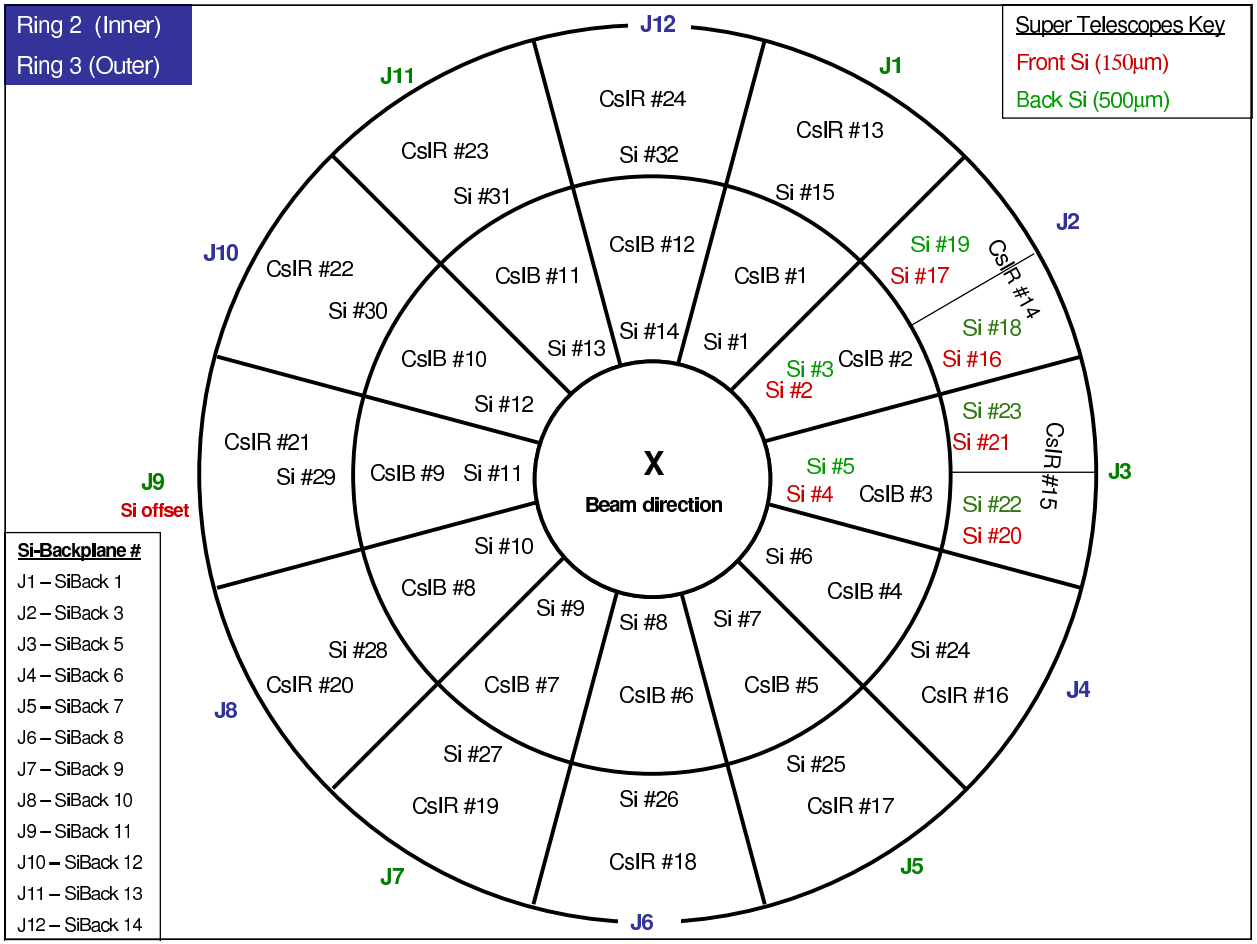

FIG. 99. Detector configuration for ring 2 (inner) and ring 3 (outer). The silicon and CsI(Tl) detector numbers are labeled according to the detectormap configuration. In the case of the super-telescope modules, the front (150μm) silicon is labeled in red while the back (500μm) silicon is labeled in green. In the lower left corner the detector number for each of the silicon back-planes is shown correlated with the "J" number of the module. The "J" numbers shown on the outside of the ring correspond to the microcontroller board that was used for that module.

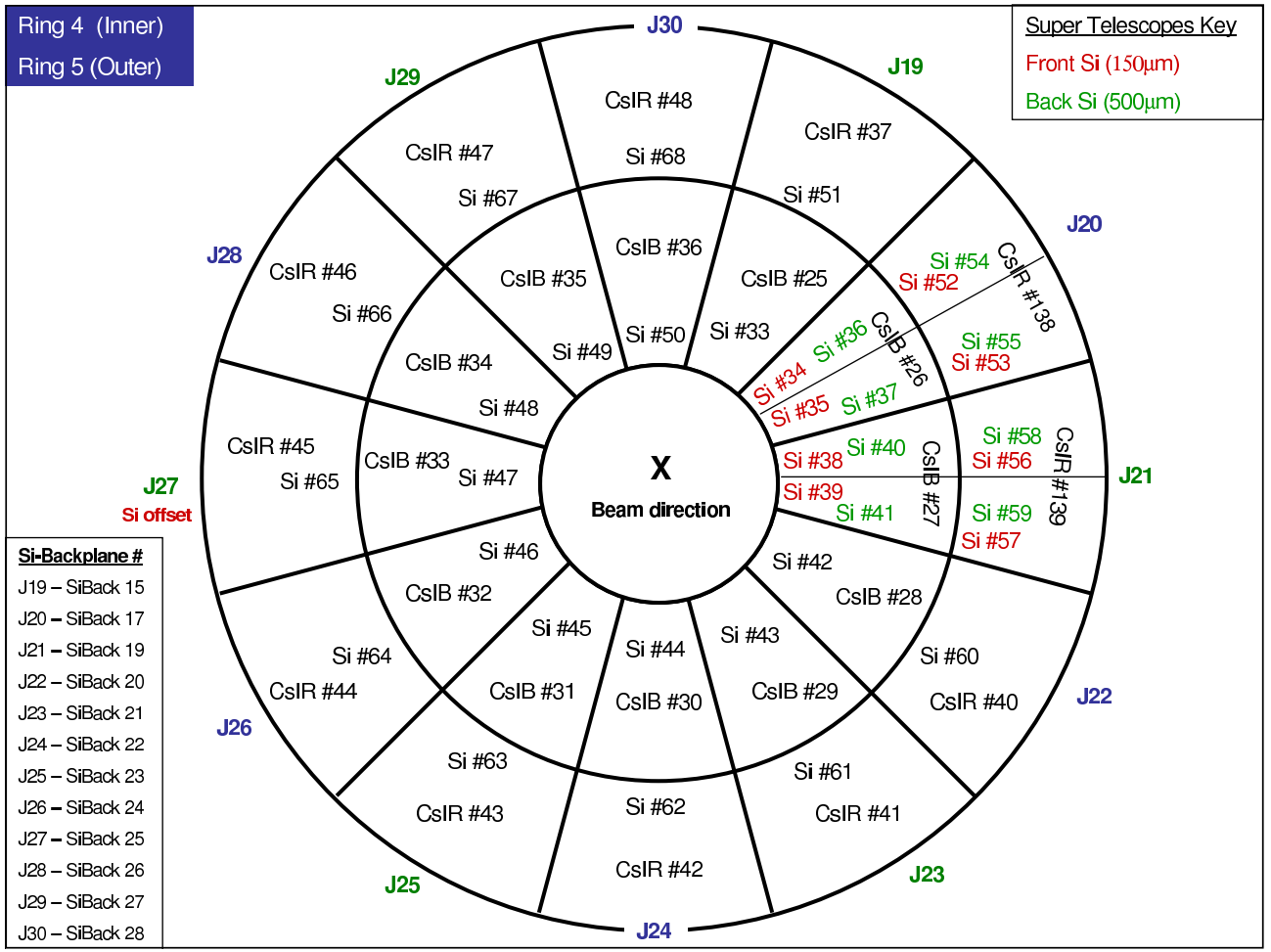

FIG. 100. Detector configuration for ring 4 (inner) and ring 5 (outer). The silicon and CsI(Tl) detector numbers are labeled according to the detectormap configuration. In the case of the super-telescope modules, the front (150μm) silicon is labeled in red while the back (500μm) silicon is labeled in green. In the lower left corner the detector number for each of the silicon back-planes is shown correlated with the "J" number of the module. The "J" numbers shown on the outside of the ring correspond to the microcontroller board that was used for that module.

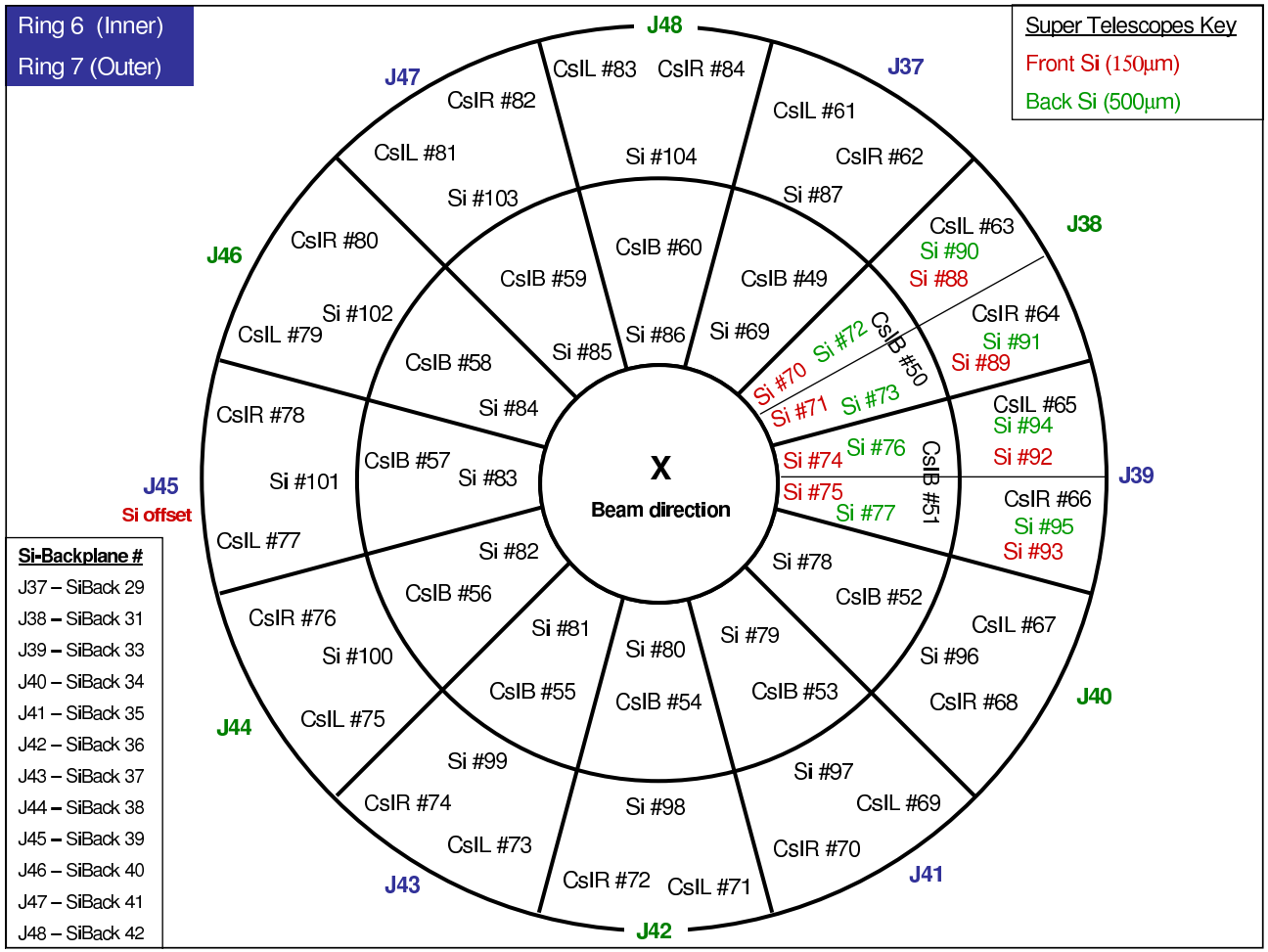

FIG. 101. Detector configuration for ring 6 (inner) and ring 7 (outer). The silicon and CsI(Tl) detector numbers are labeled according to the detectormap configuration. In the case of the super-telescope modules, the front (150μm) silicon is labeled in red while the back (500μm) silicon is labeled in green. In the lower left corner the detector number for each of the silicon back-planes is shown correlated with the "J" number of the module. The "J" numbers shown on the outside of the ring correspond to the microcontroller board that was used for that module.

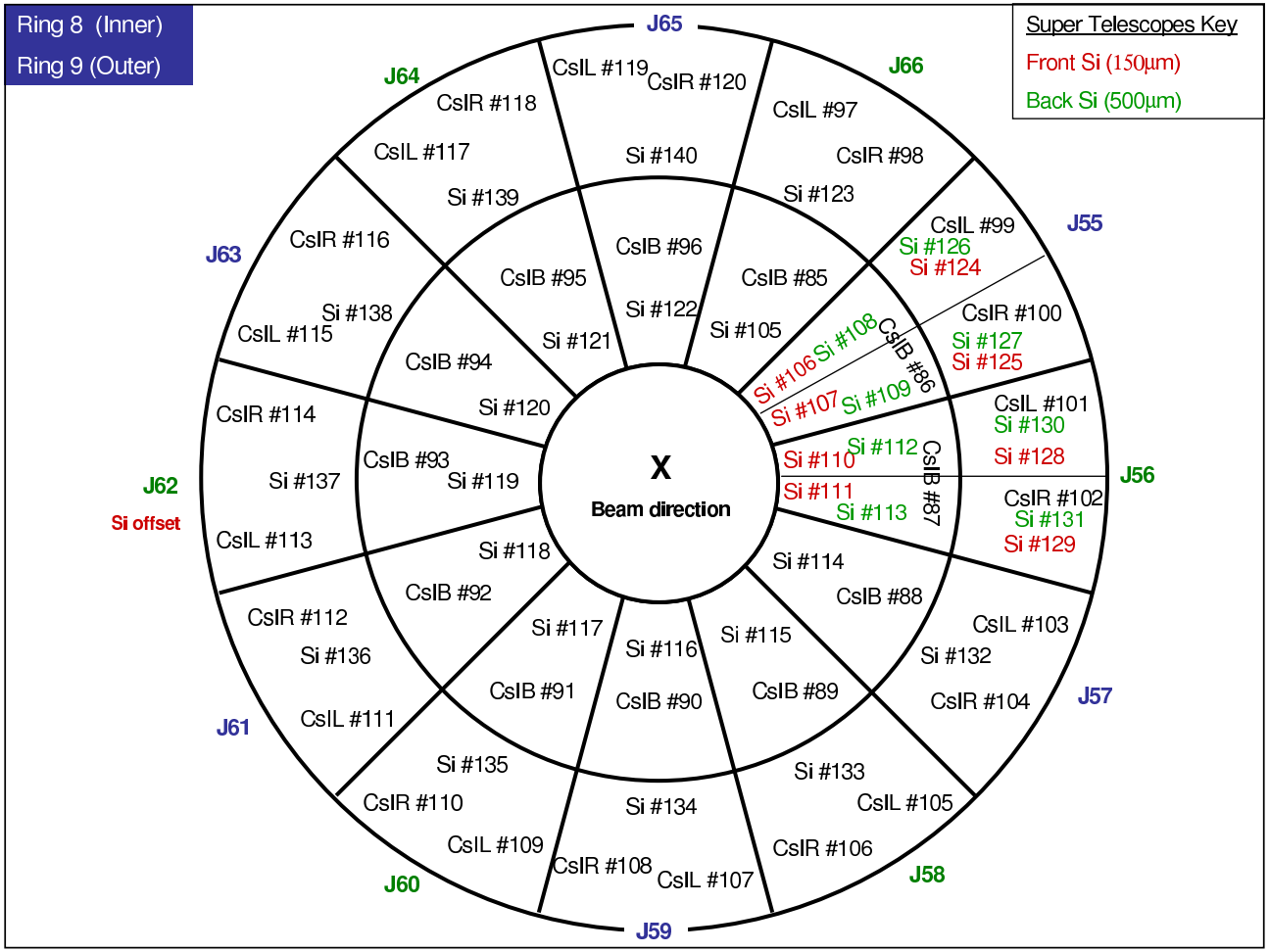

FIG. 102. Detector configuration for ring 8 (inner) and ring 9 (outer). The silicon and CsI(Tl) detector numbers are labeled according to the detectormap configuration. In the case of the super-telescope modules, the front (150μm) silicon is labeled in red while the back (500μm) silicon is labeled in green. The silicon back-plane signals were not collected for rings 8 and 9. The "J" numbers shown on the outside of the ring correspond to the microcontroller board that was used for that module.

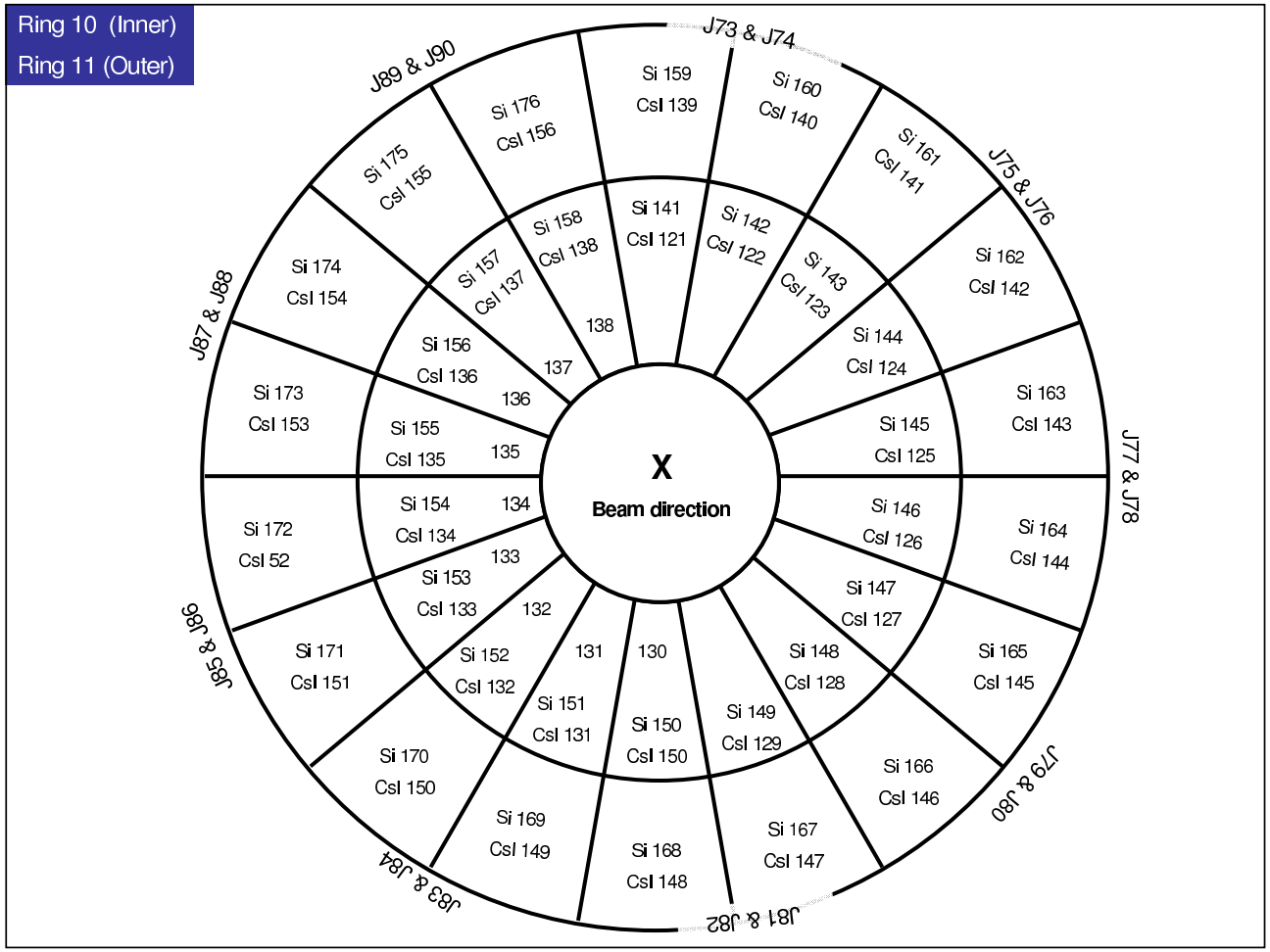

FIG. 103. Detector configuration for ring 10 (inner) and ring 11 (outer). The silicon and CsI(Tl) detector numbers are labeled according to the detectormap configuration. Rings 10-11 did have any supertelescope modules or silicon back-plane signals. The "J" numbers shown on the outside of the ring correspond to the signal feed-throughs on the outside of the chamber. A Zepto System microcontroller board was used for the silicon signals, while the CsI(Tl) signals were brought directly from the chamber to the electronics.

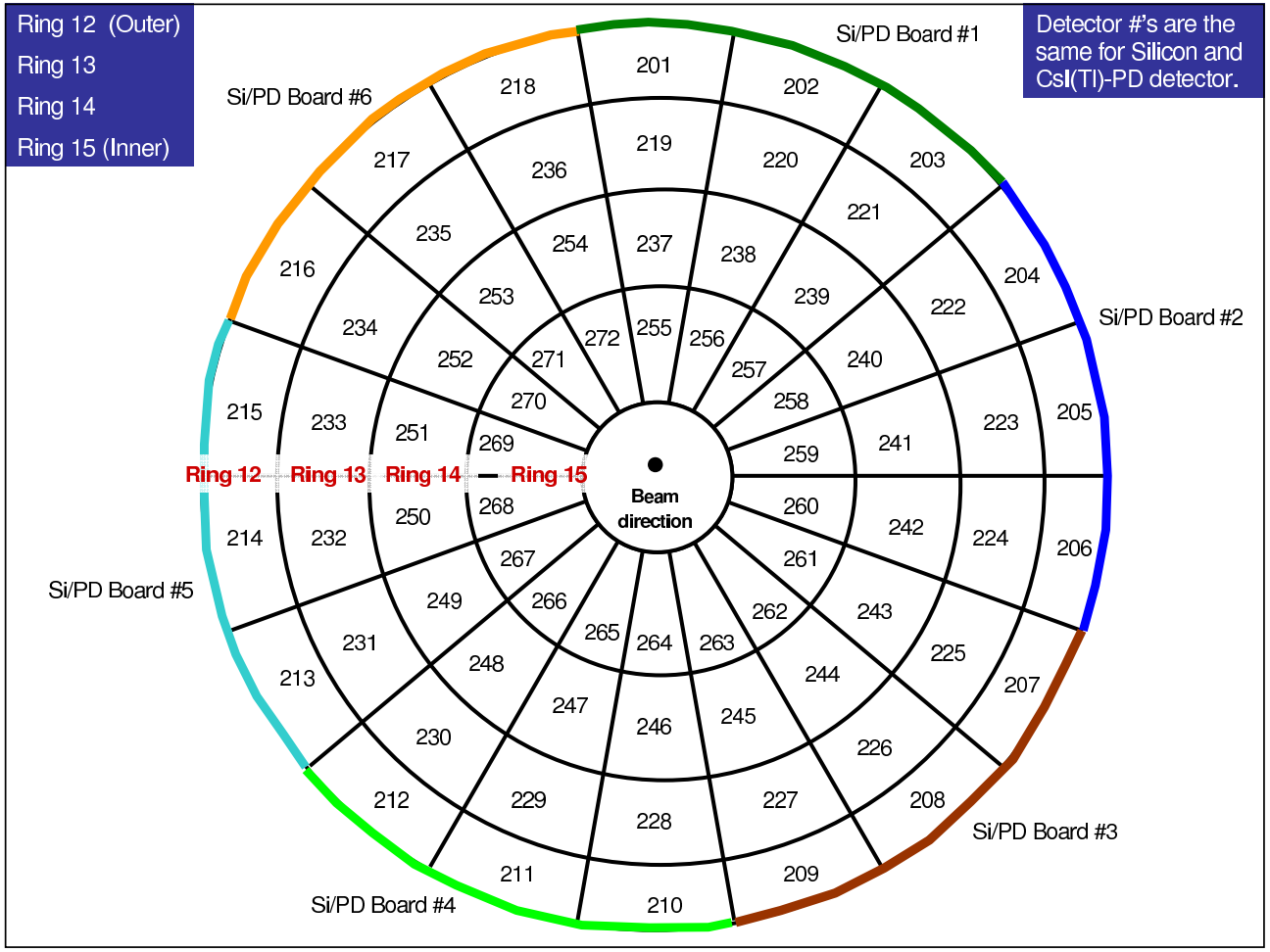

FIG. 104. Detector configuration for ISiS consisting of rings 12 (inner), 13, 14, and 15 (outer). The silicon and CsI(Tl) detector numbers are labeled according to the detectormap configuration. Photodiode detectors are coupled to CsI(Tl) for the light collection rather than PMTs. The Si-CsI detectors are grouped into six sections, each consisting of 12 Si-CsI detectors. Each of the six sections are labeled with a silicon and photodiode board number, which represents the Zepto system microcontroller board used for those detectors.

APPENDIX B

KINETIC ENERGY SPECTRA

The kinetic energy spectra are shown for each reaction system and ring of the NIMROD-ISiS array. The energy spectra for the different elements are offset in order to allow each spectra to be viewed. Small bumps in the low energy region of some spectra, specifically Z=1-2, are observed and can be attributed to the different thresholds for each isotope and the threshold differences between detectors.

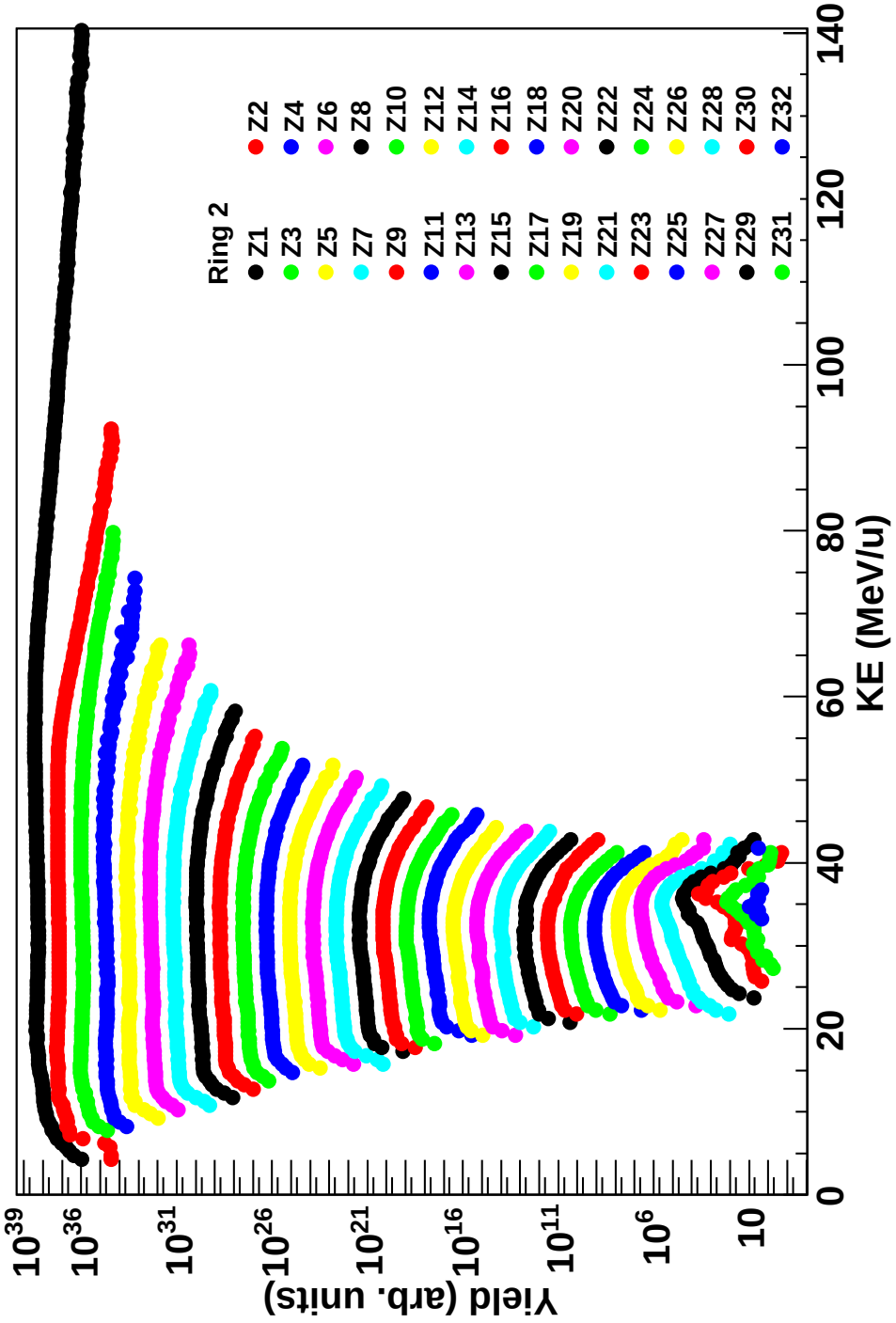

FIG. 105. Ring 2 energy spectra for the 35 MeV/u ^{64}Zn+^{64}Zn system.

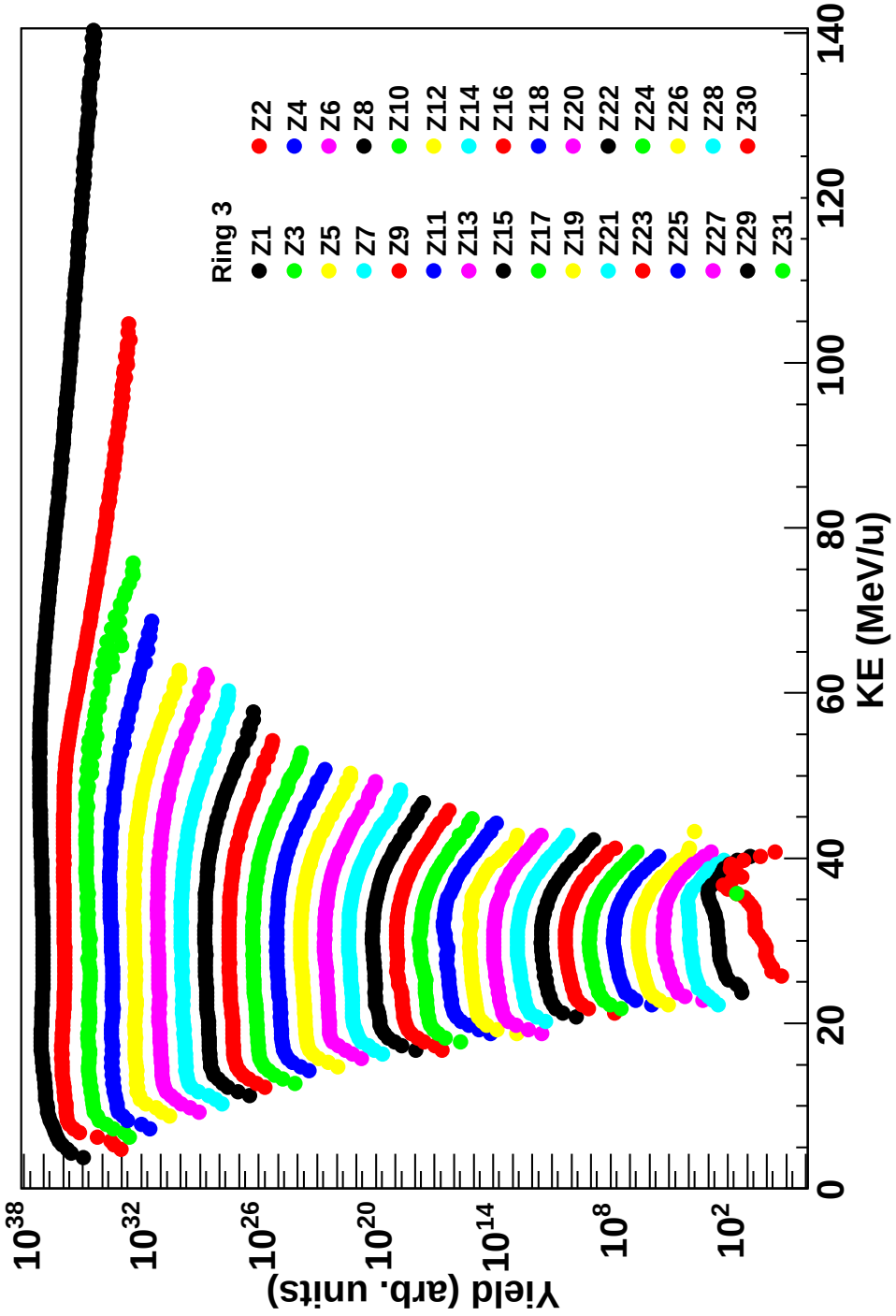

FIG. 106. Ring 3 energy spectra for the 35 MeV/u ^{64}Zn+^{64}Zn system.

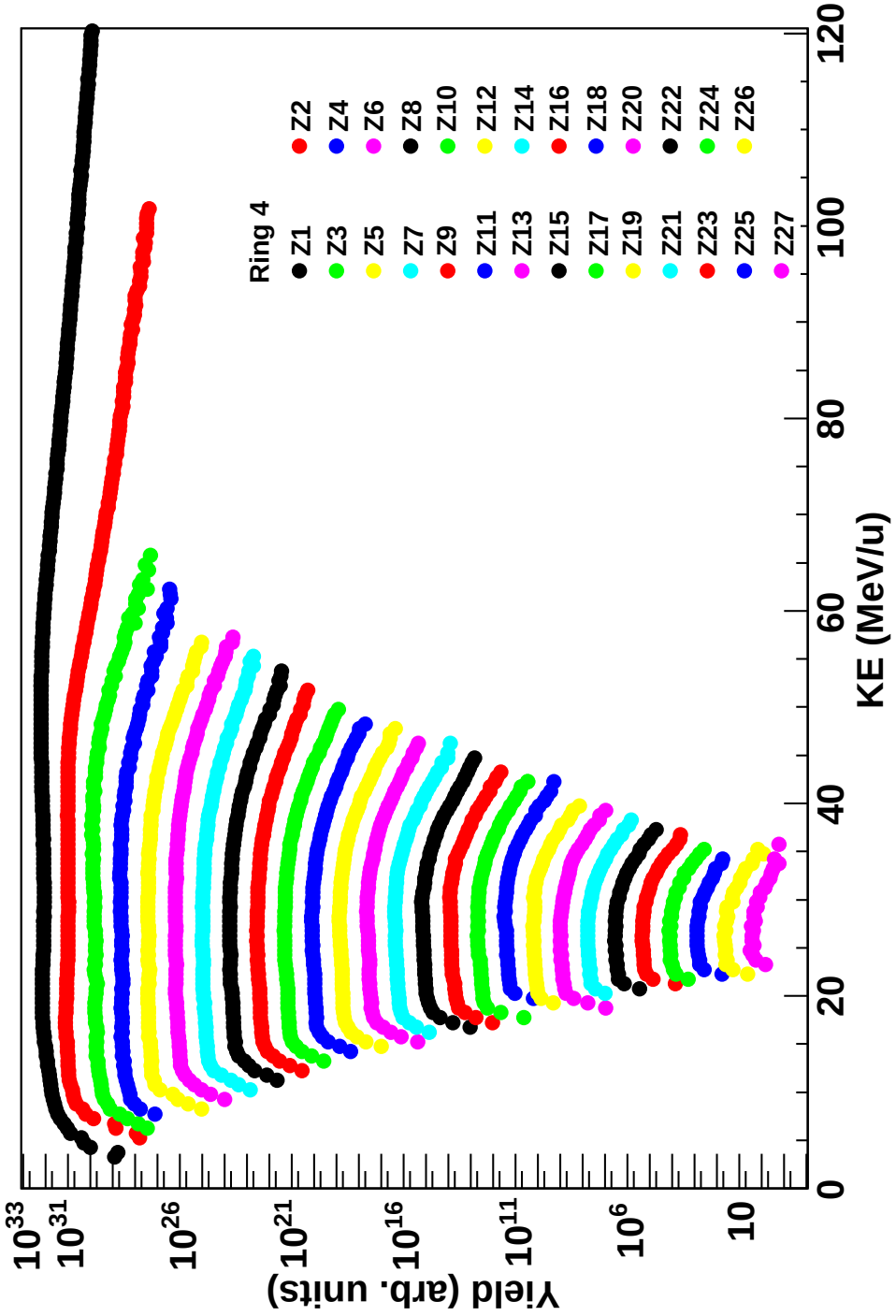

FIG. 107. Ring 4 energy spectra for the 35 MeV/u ^{64}Zn+^{64}Zn system.

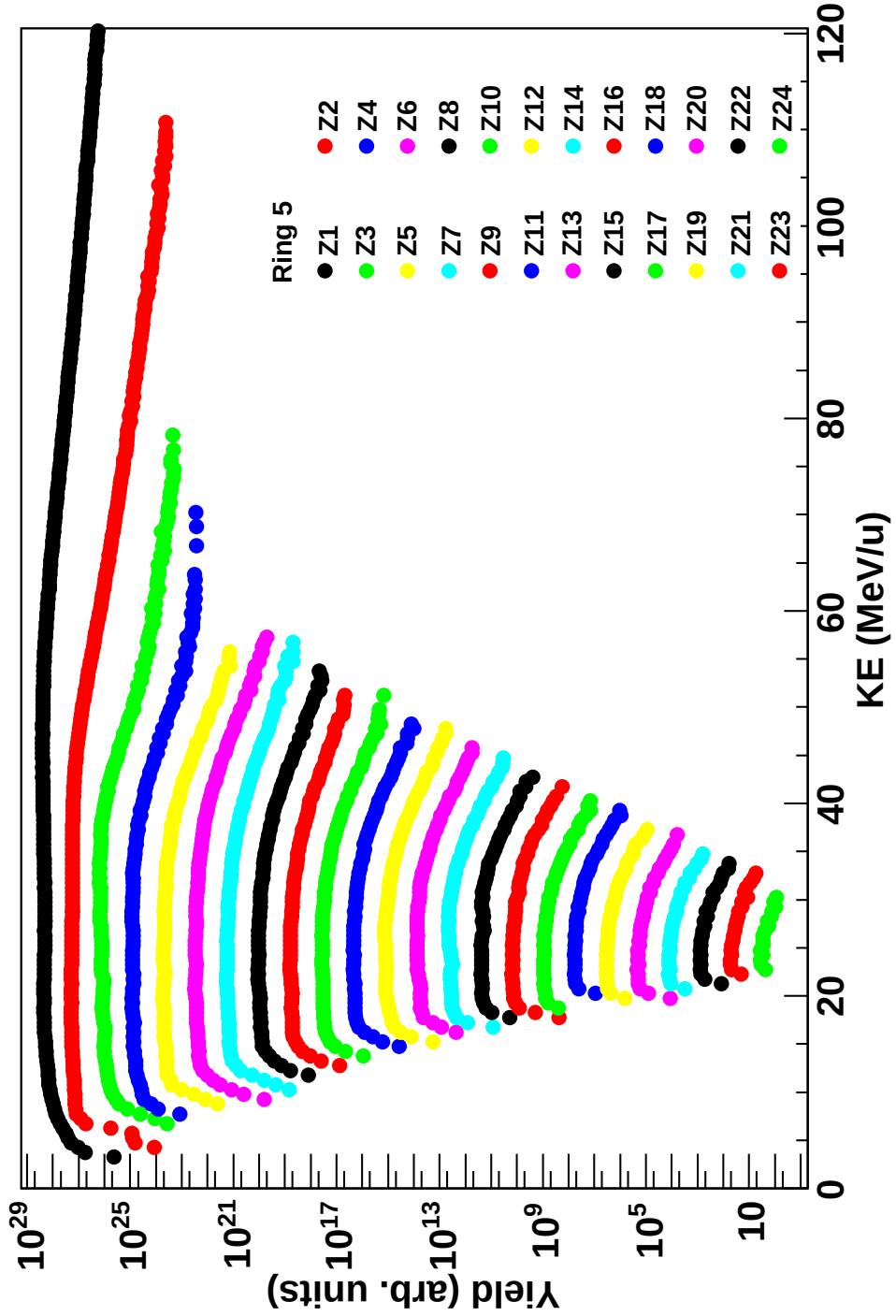

FIG. 108. Ring 5 energy spectra for the 35 MeV/u ^{64}Zn+^{64}Zn system.

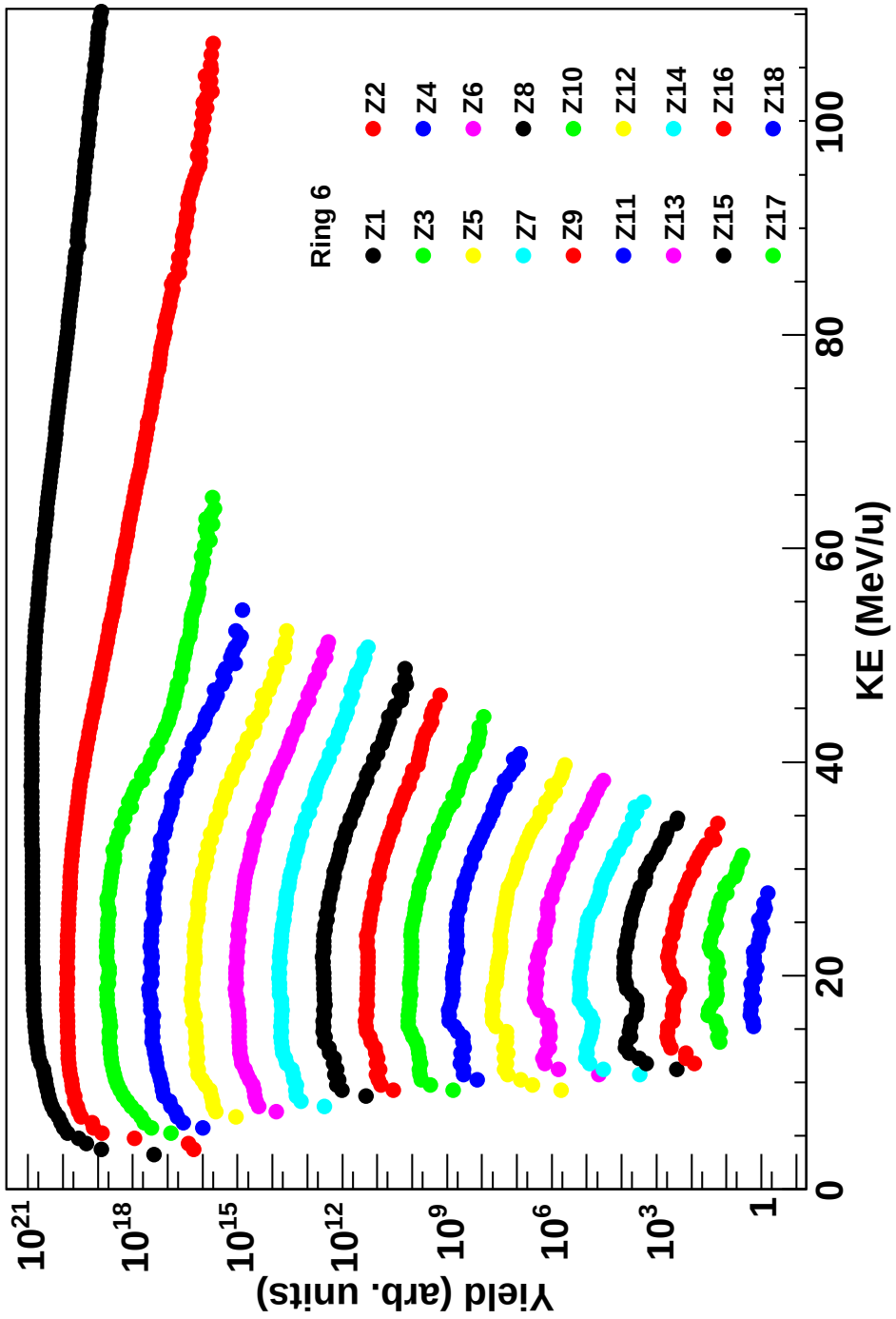

FIG. 109. Ring 6 energy spectra for the 35 MeV/u ^{64}Zn+^{64}Zn system.

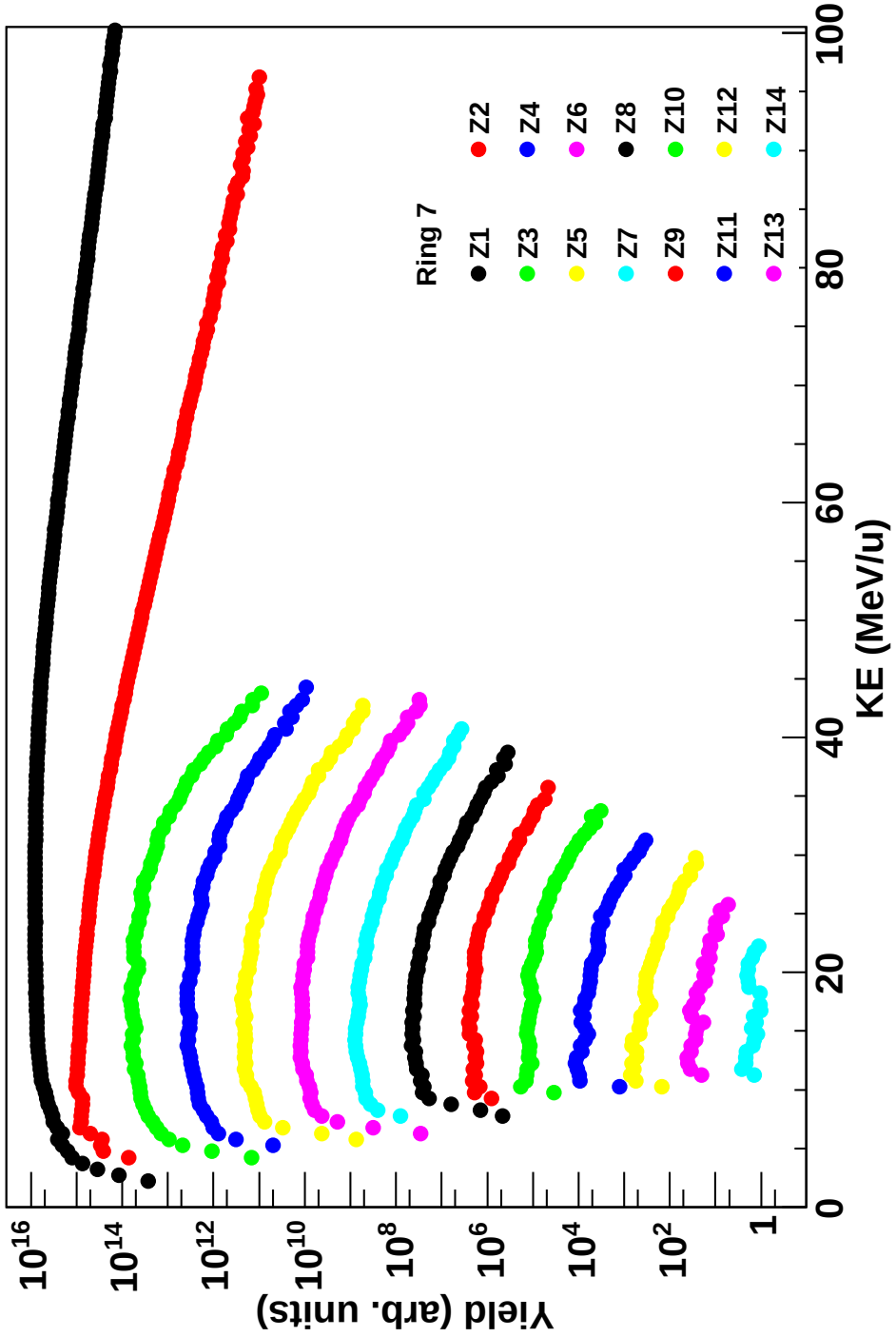

FIG. 110. Ring 7 energy spectra for the 35 MeV/u ^{64}Zn+^{64}Zn system.

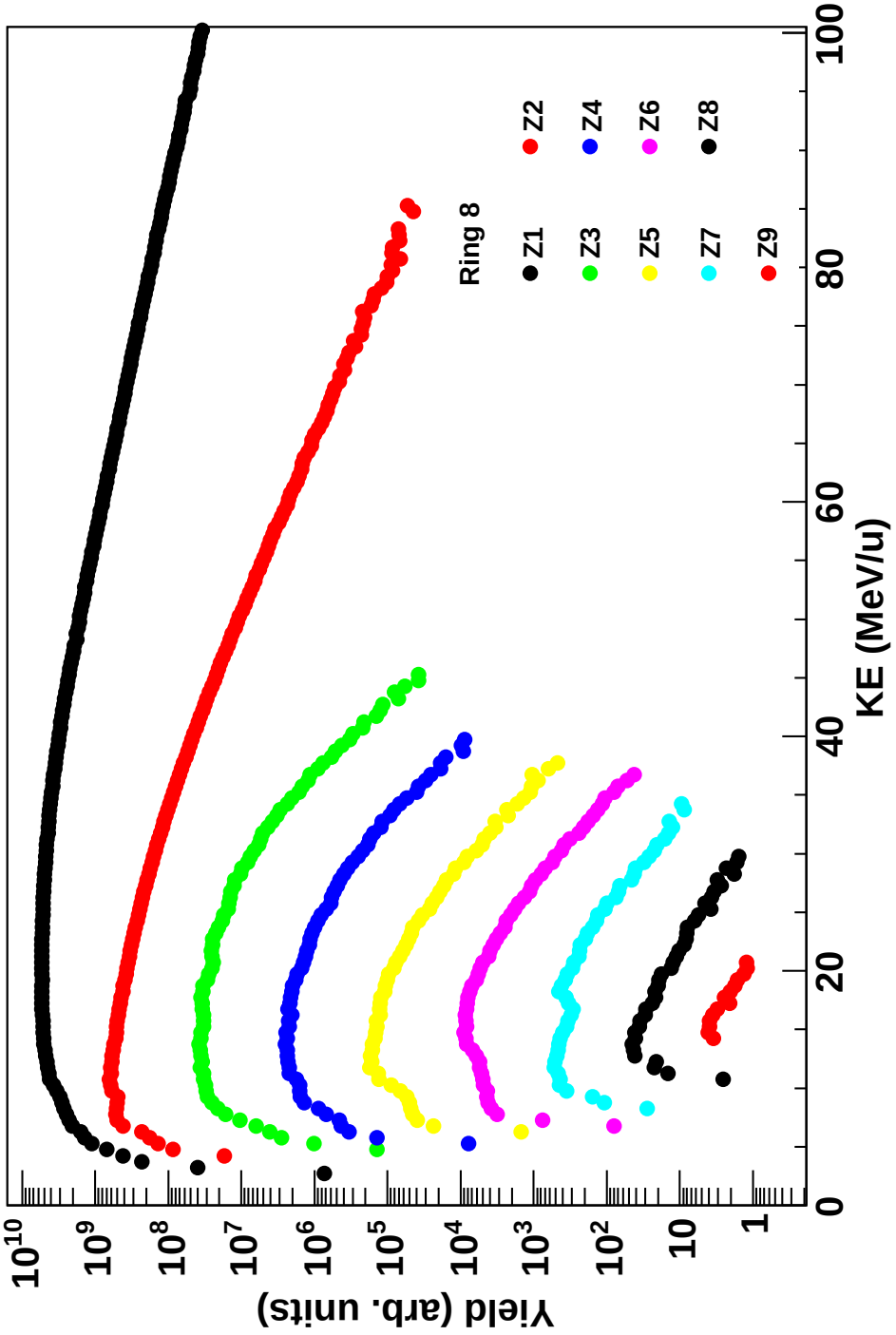

FIG. 111. Ring 8 energy spectra for the 35 MeV/u ^{64}Zn+^{64}Zn system.

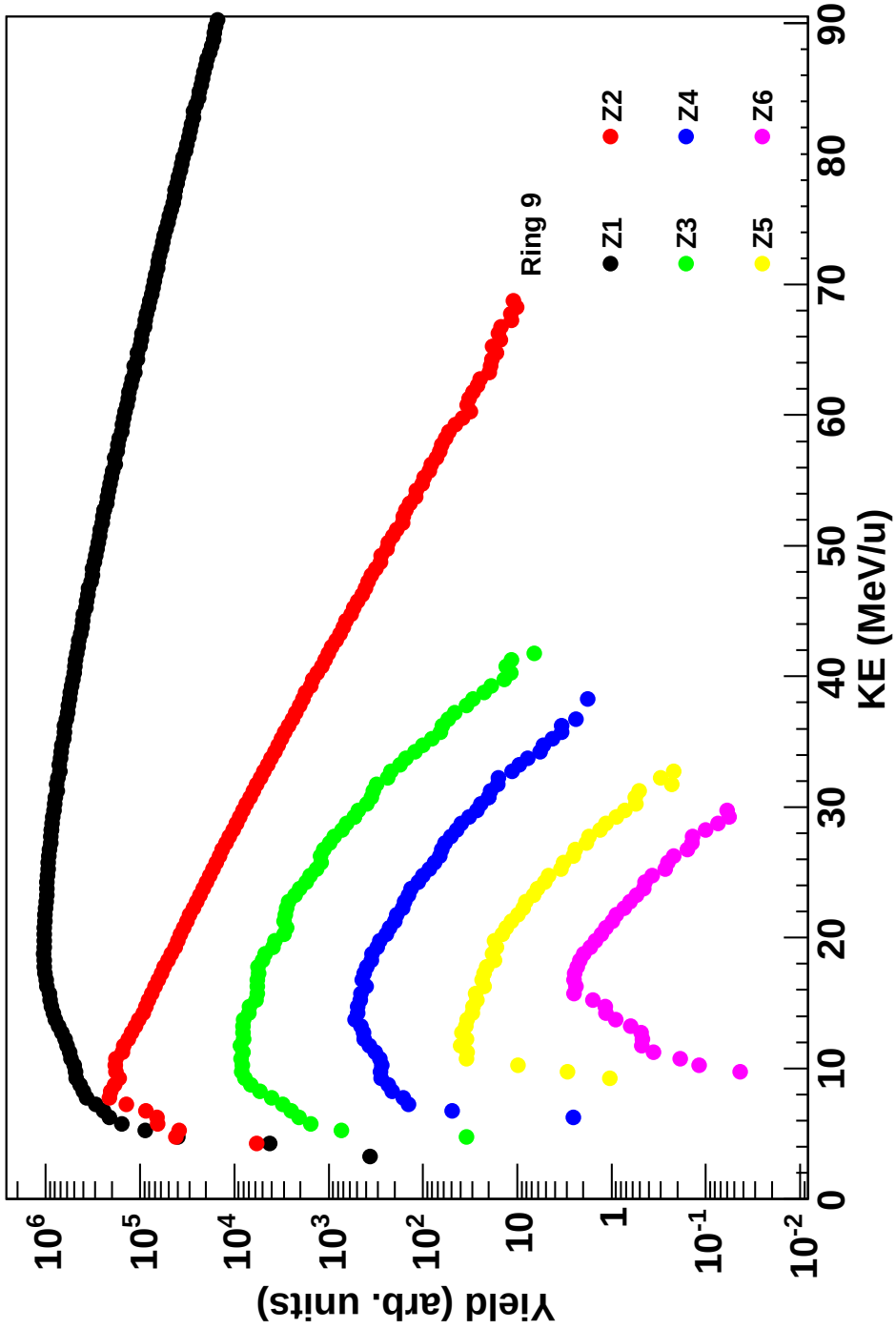

FIG. 112. Ring 9 energy spectra for the 35 MeV/u ^{64}Zn+^{64}Zn system.

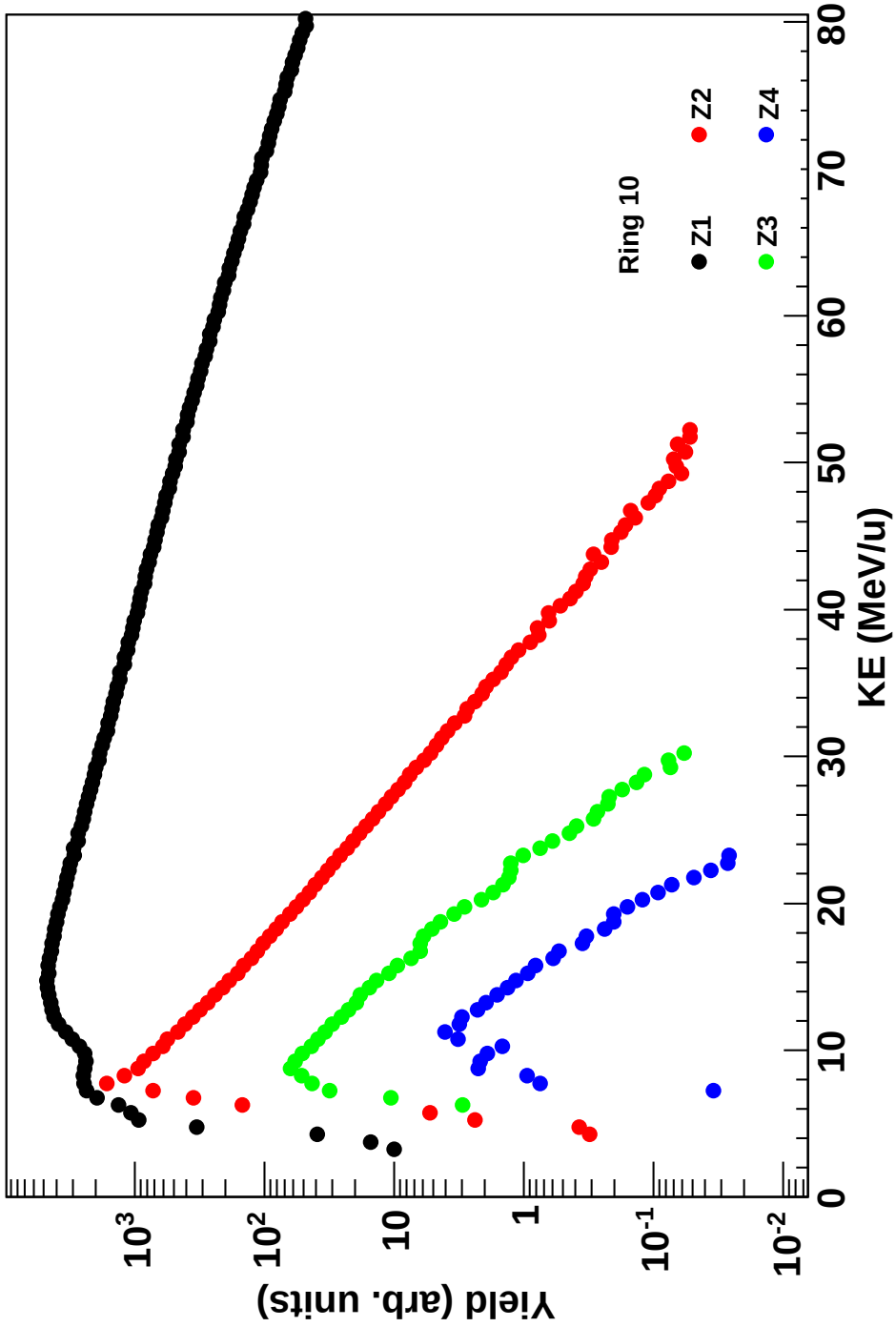

FIG. 113. Ring 10 energy spectra for the 35 MeV/u ^{64}Zn+^{64}Zn system.

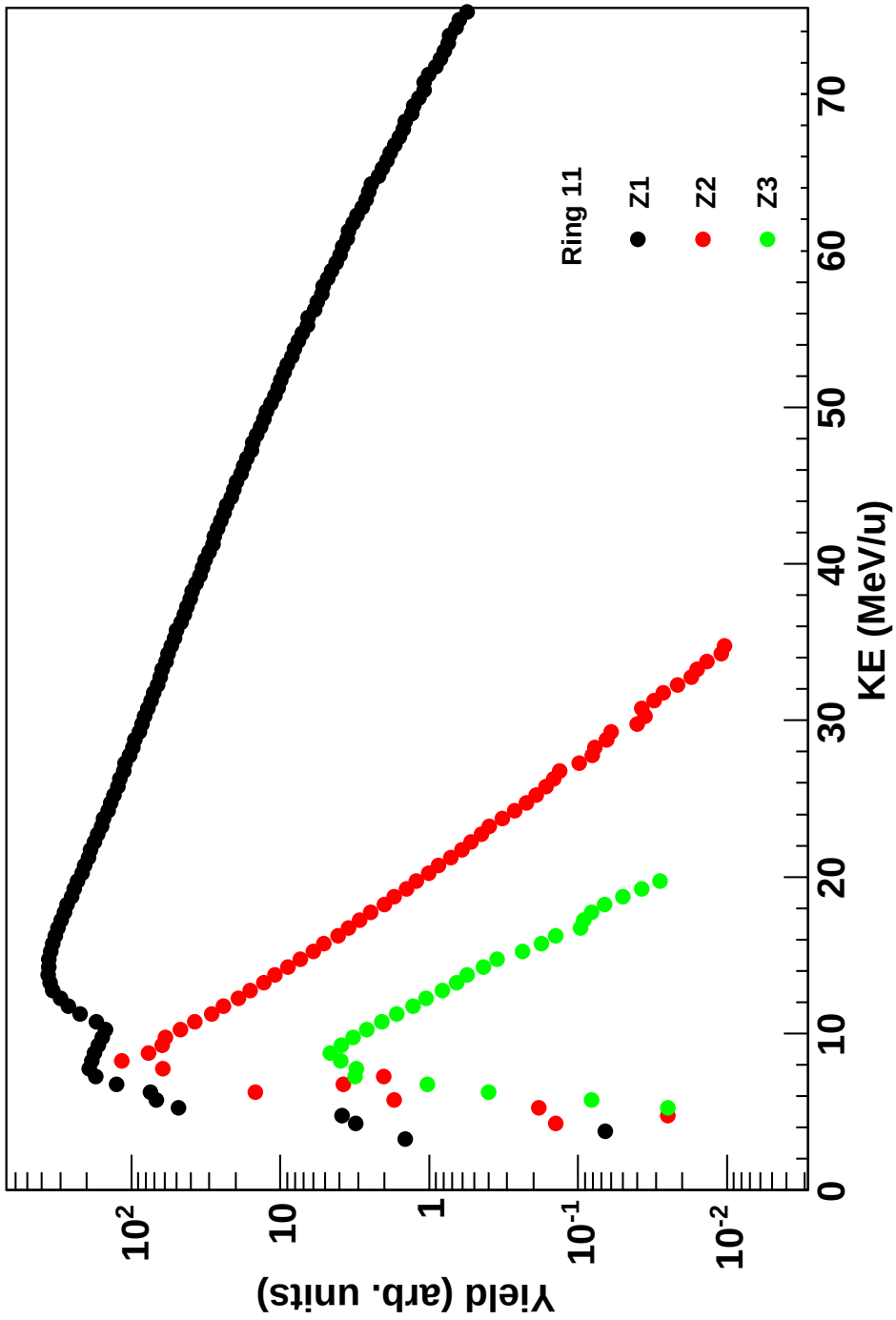

FIG. 114. Ring 11 energy spectra for the 35 MeV/u ^{64}Zn+^{64}Zn system.

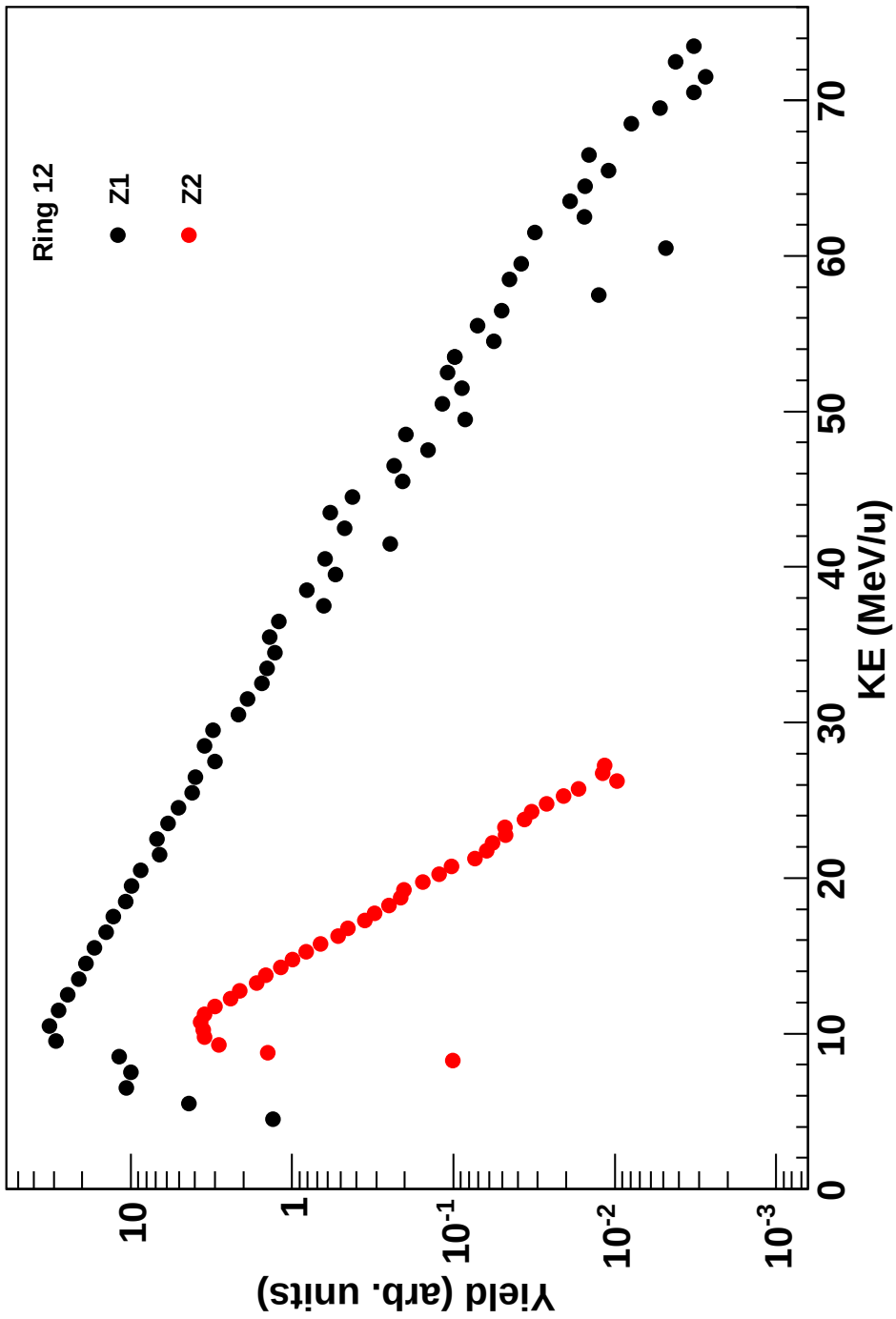

FIG. 115. Ring 12 energy spectra for the 35 MeV/u ^{64}Zn+^{64}Zn system.

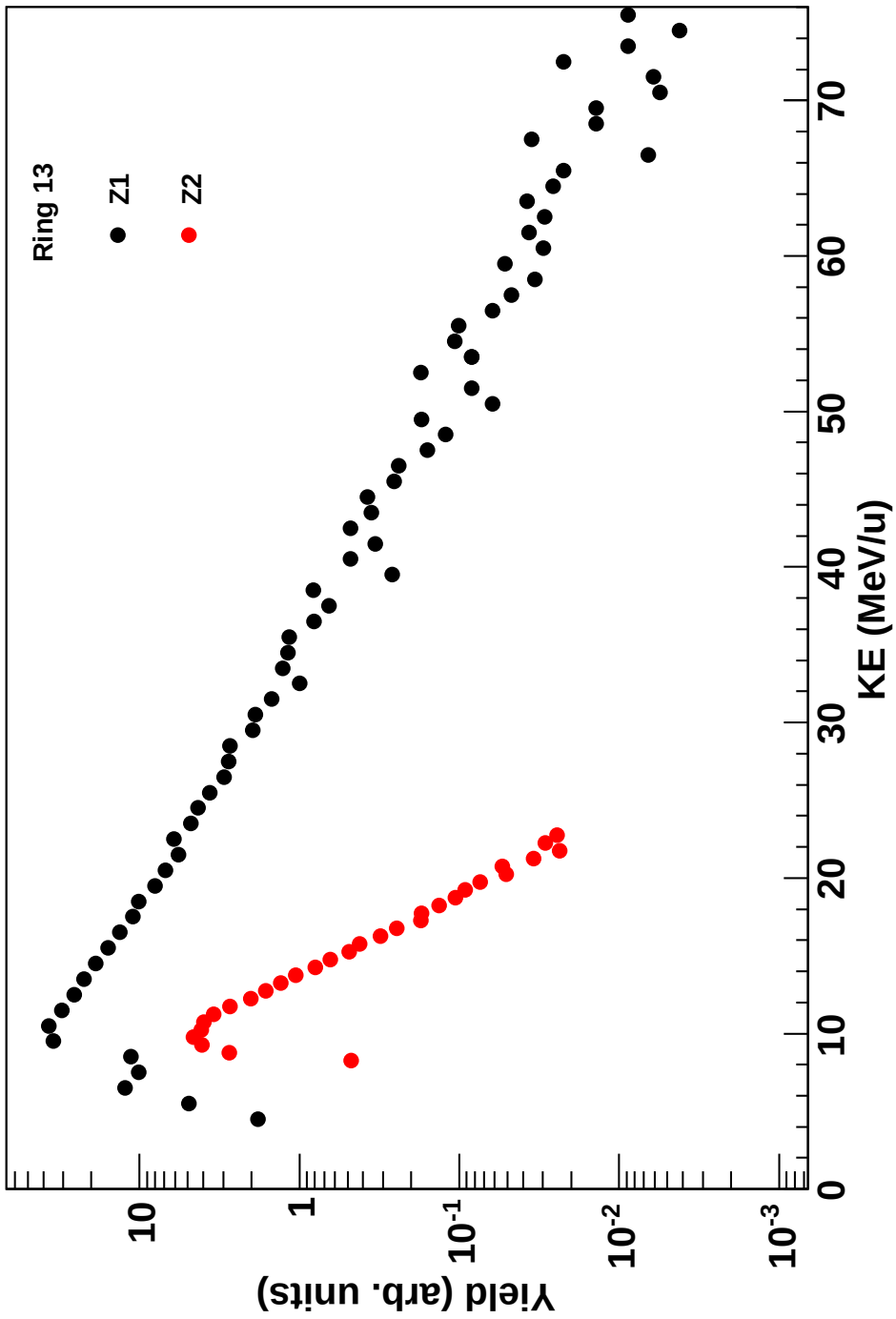

FIG. 116. Ring 13 energy spectra for the 35 MeV/u ^{64}Zn+^{64}Zn system.

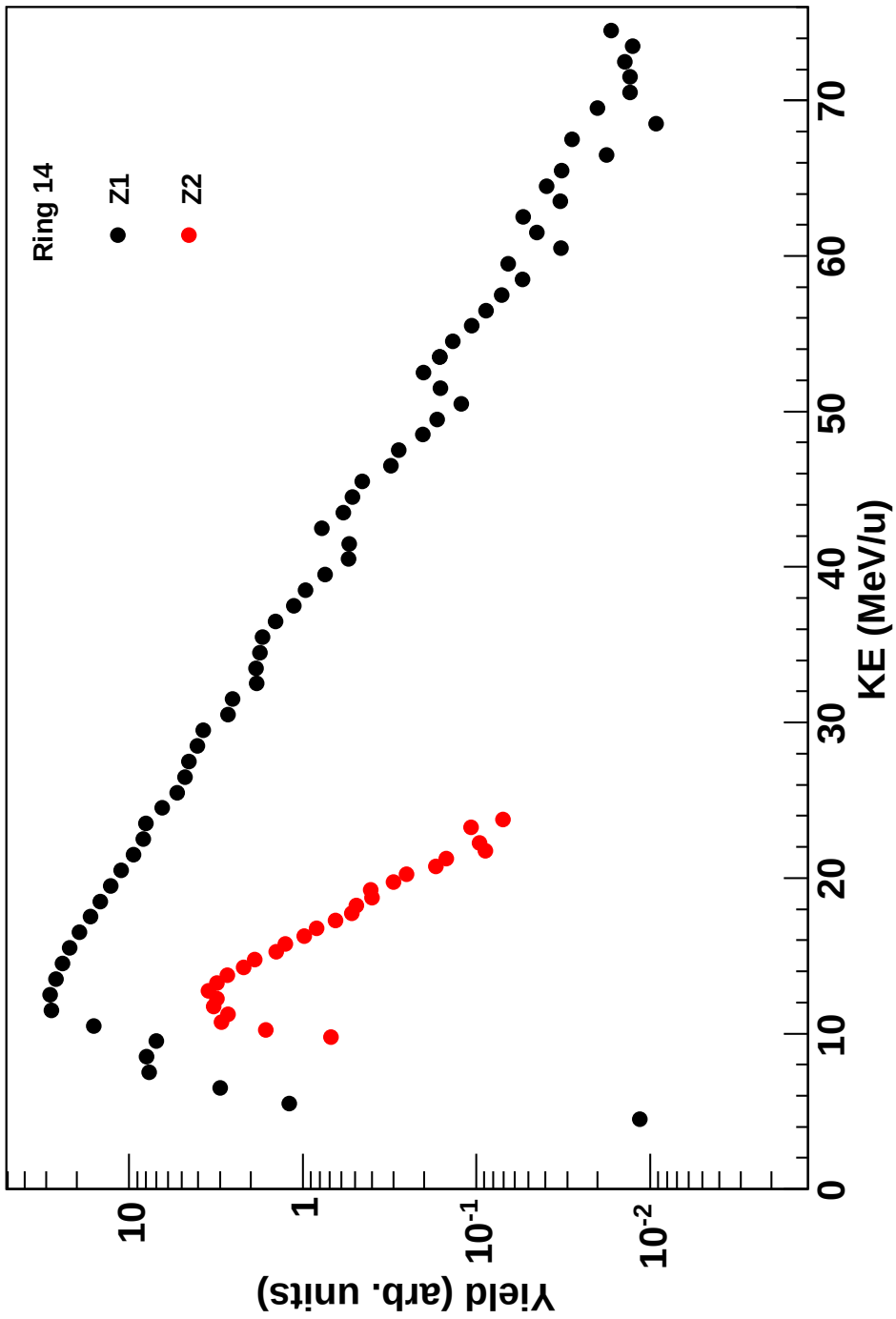

FIG. 117. Ring 14 energy spectra for the 35 MeV/u ^{64}Zn+^{64}Zn system.

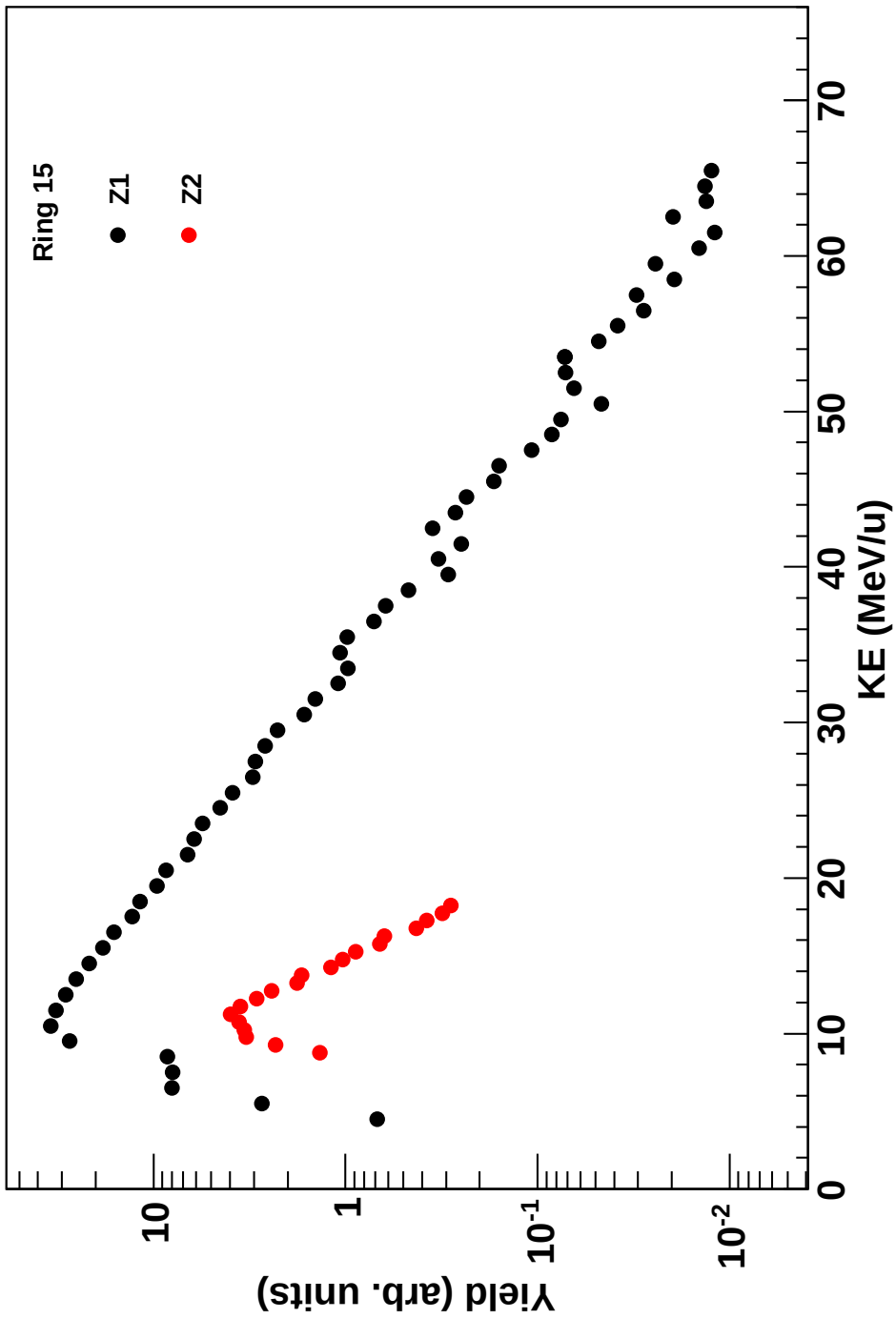

FIG. 118. Ring 15 energy spectra for the 35 MeV/u ^{64}Zn+^{64}Zn system.

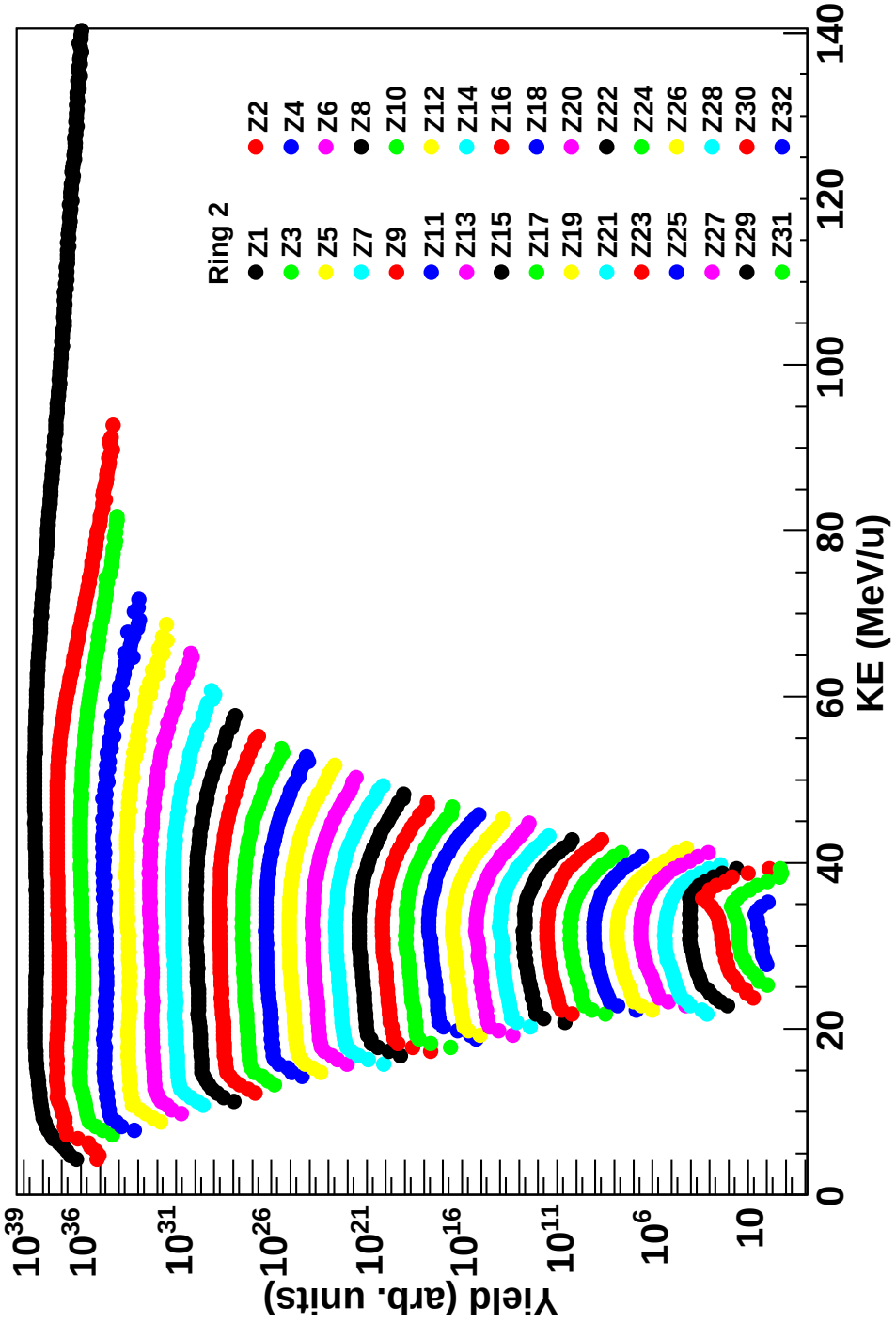

FIG. 119. Ring 2 energy spectra for the 35 MeV/u ^{70}Zn+^{70}Zn system.

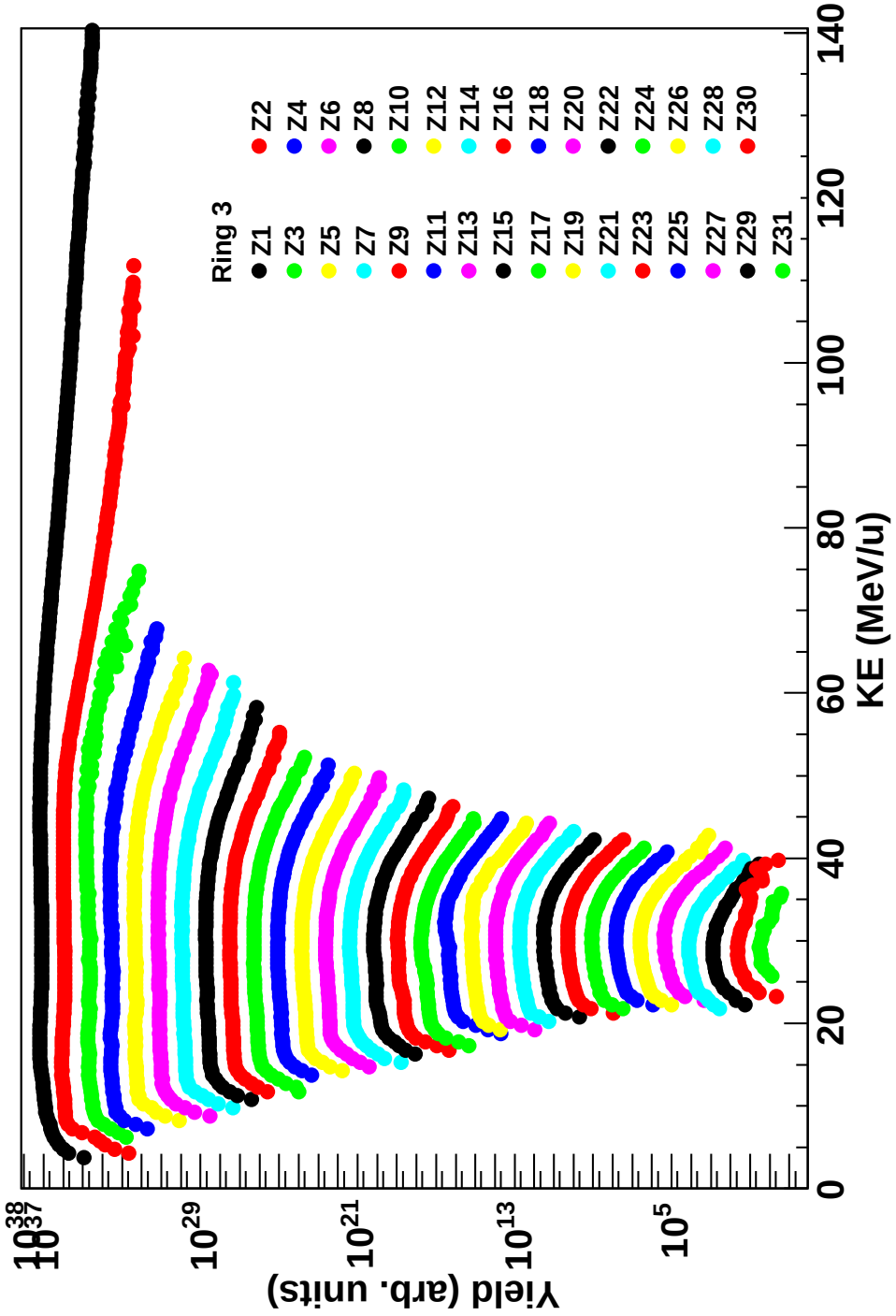

FIG. 120. Ring 3 energy spectra for the 35 MeV/u ^{70}Zn+^{70}Zn system.

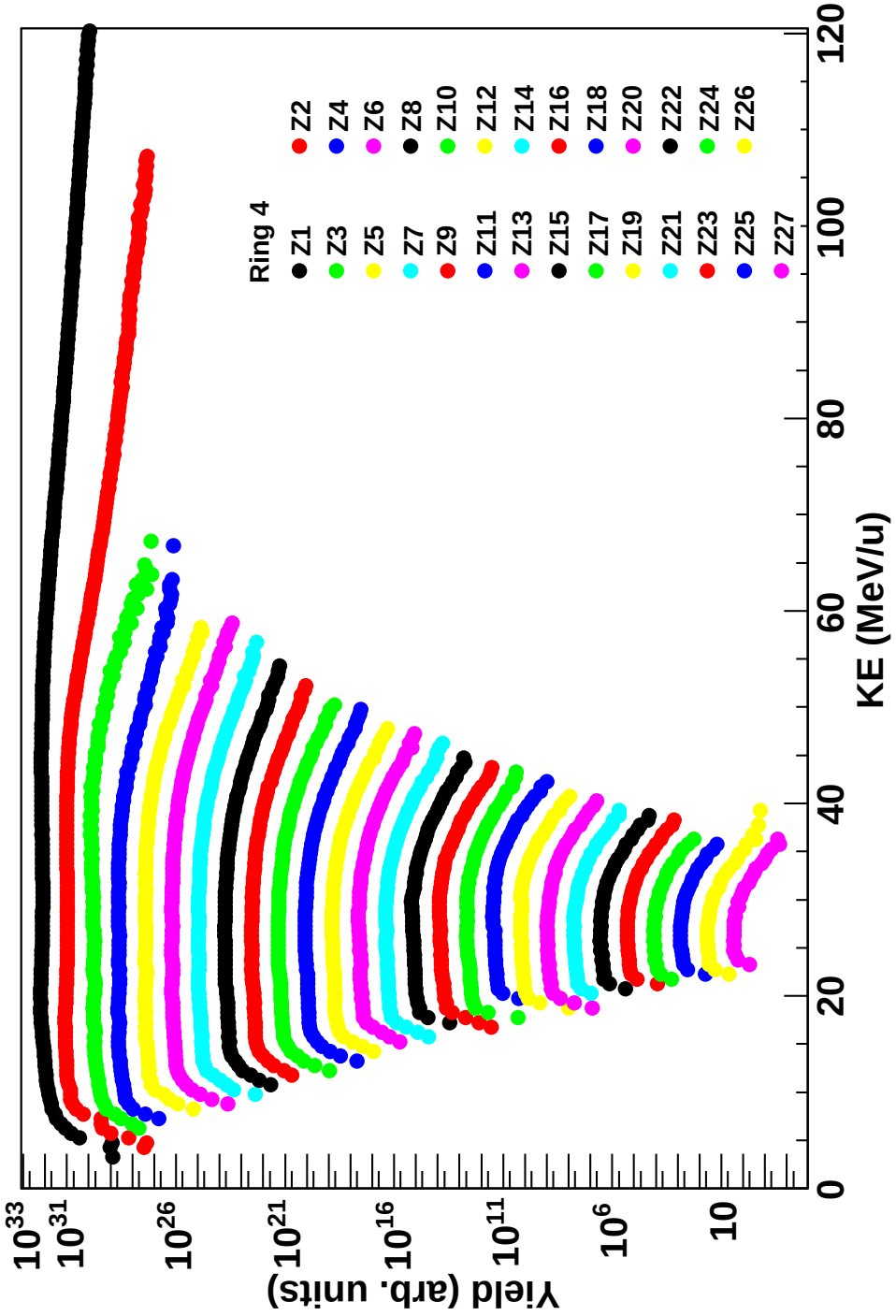

FIG. 121. Ring 4 energy spectra for the 35 MeV/u ^{70}Zn+^{70}Zn system.

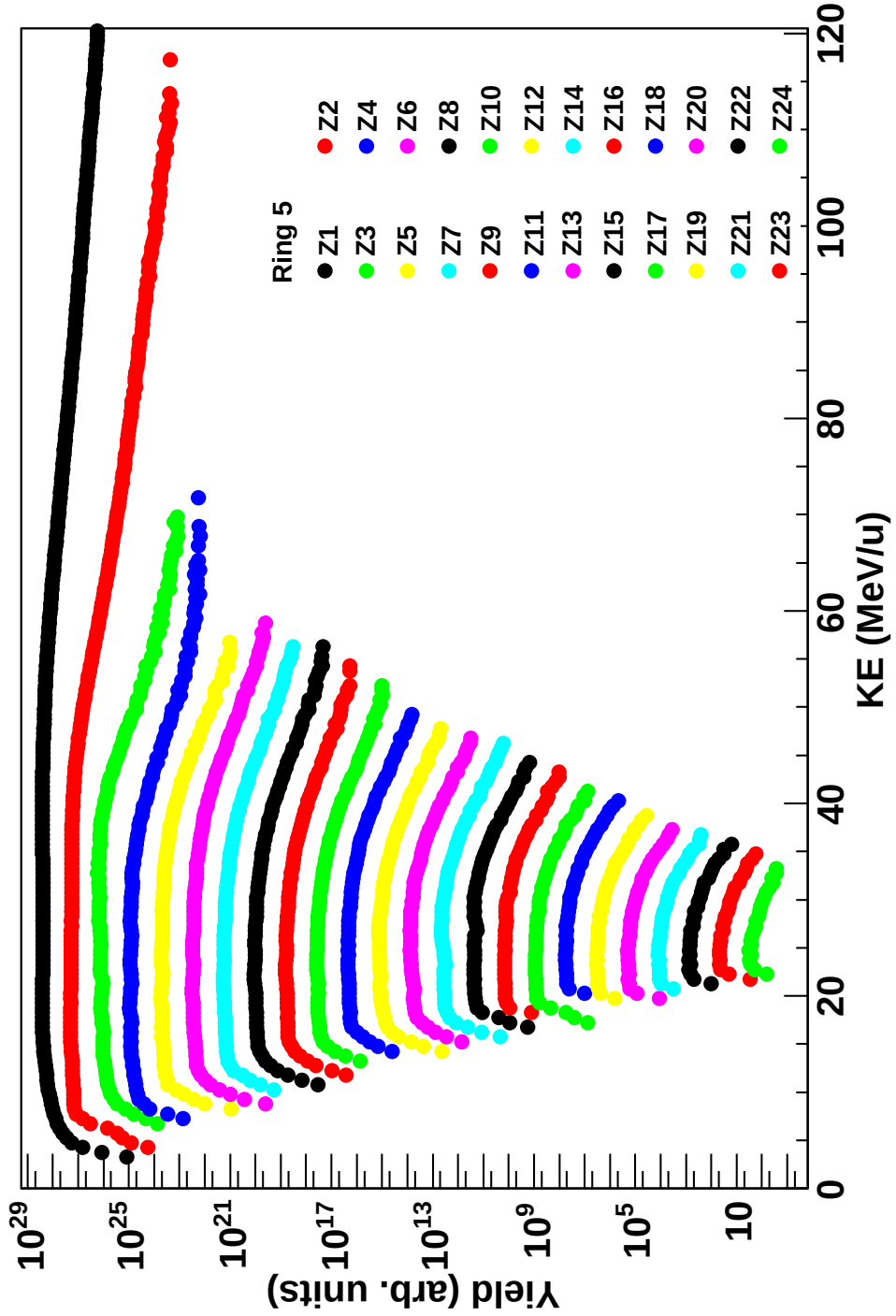

FIG. 122. Ring 5 energy spectra for the 35 MeV/u ^{70}Zn+^{70}Zn system.

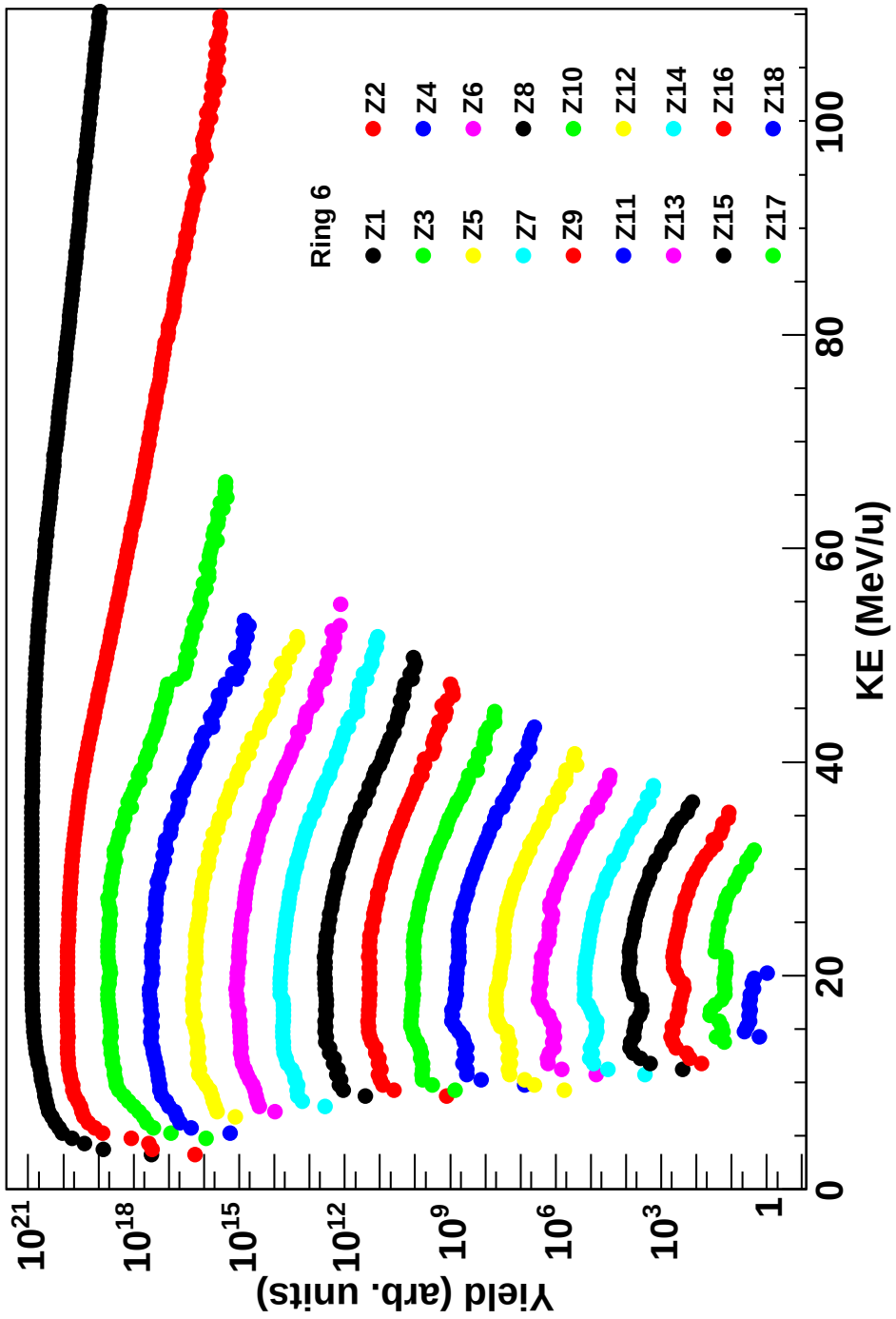

FIG. 123. Ring 6 energy spectra for the 35 MeV/u ^{70}Zn+^{70}Zn system.

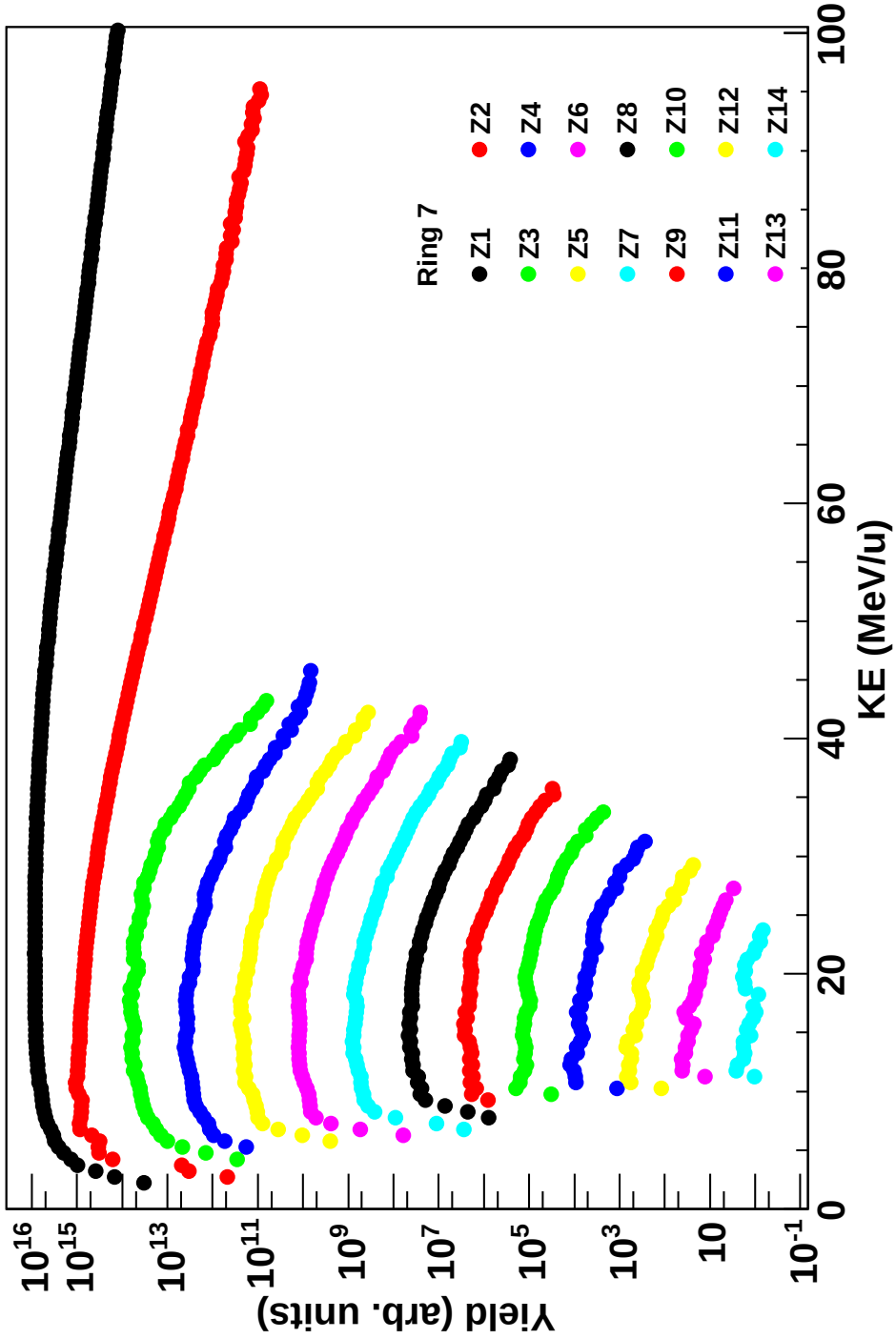

FIG. 124. Ring 7 energy spectra for the 35 MeV/u ^{70}Zn+^{70}Zn system.

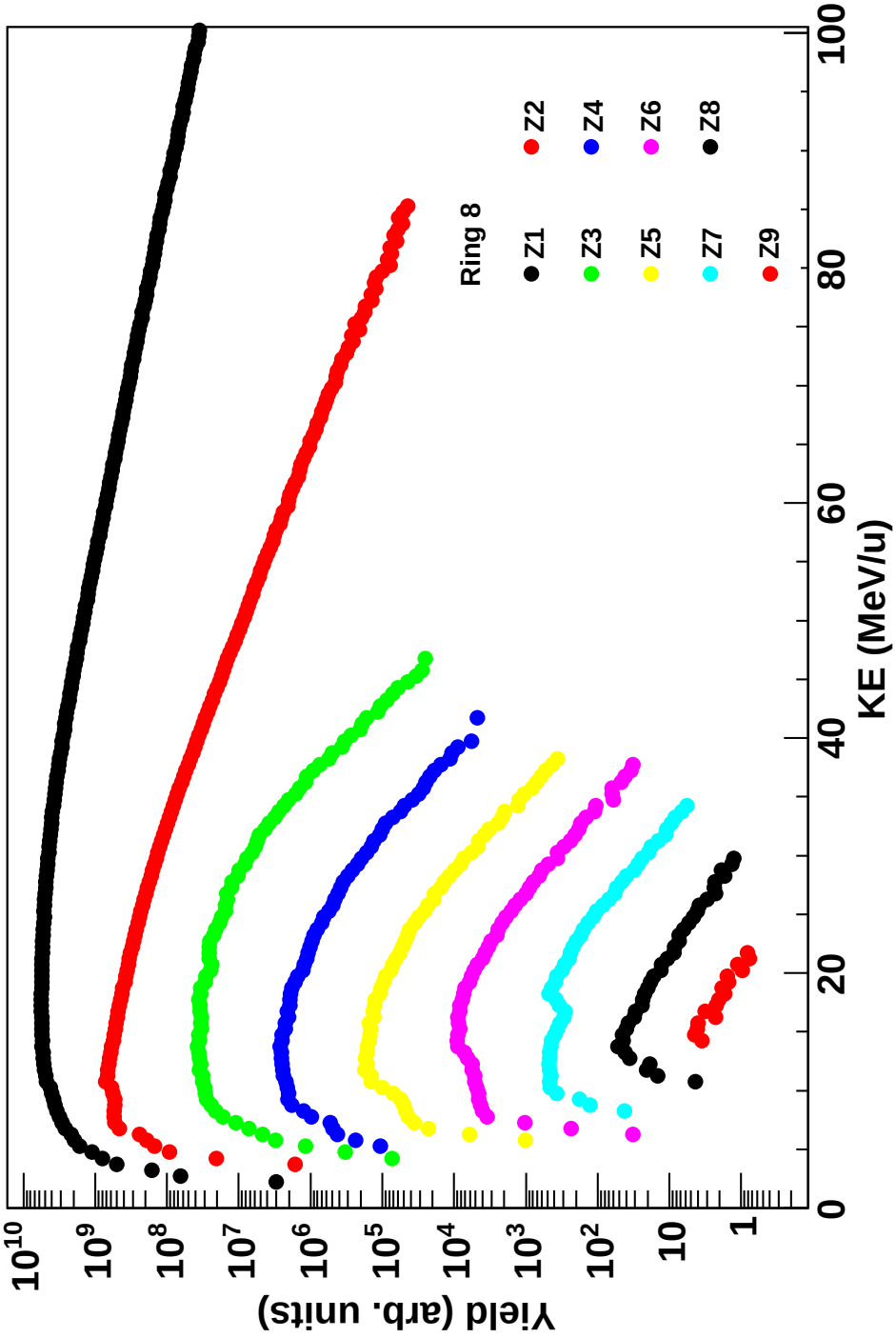

FIG. 125. Ring 8 energy spectra for the 35 MeV/u ^{70}Zn+^{70}Zn system.

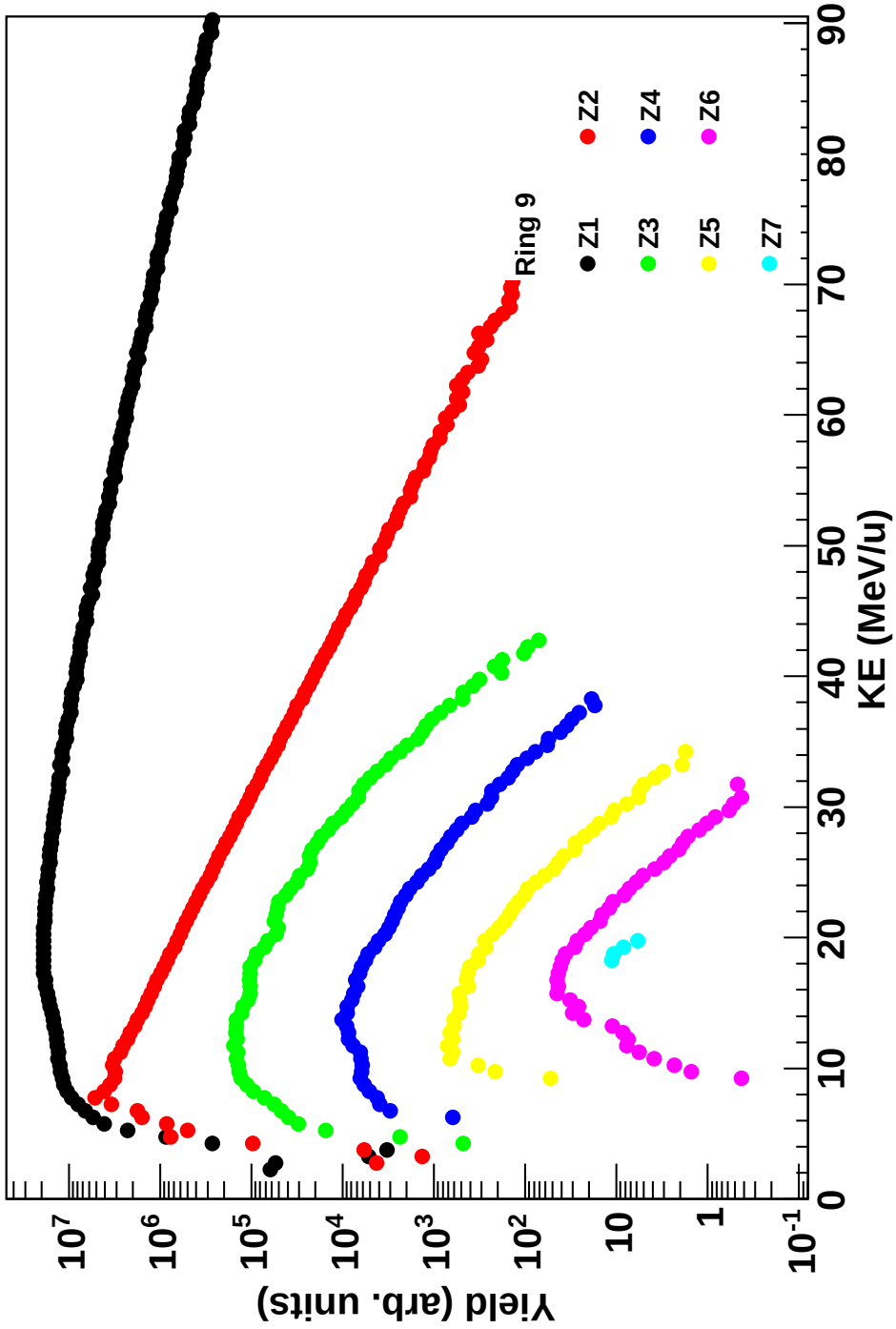

FIG. 126. Ring 9 energy spectra for the 35 MeV/u ^{70}Zn+^{70}Zn system.

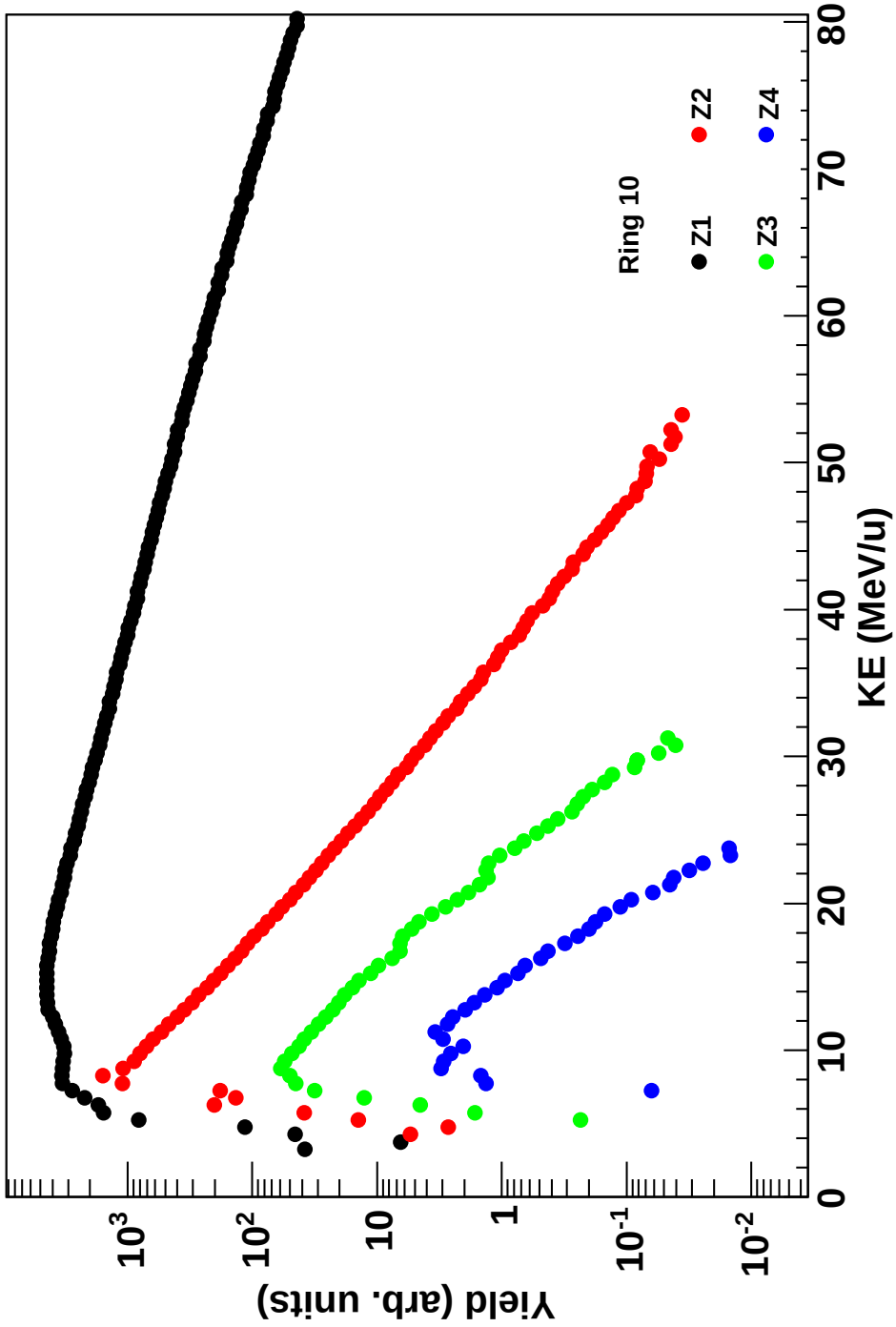

FIG. 127. Ring 10 energy spectra for the 35 MeV/u ^{70}Zn+^{70}Zn system.

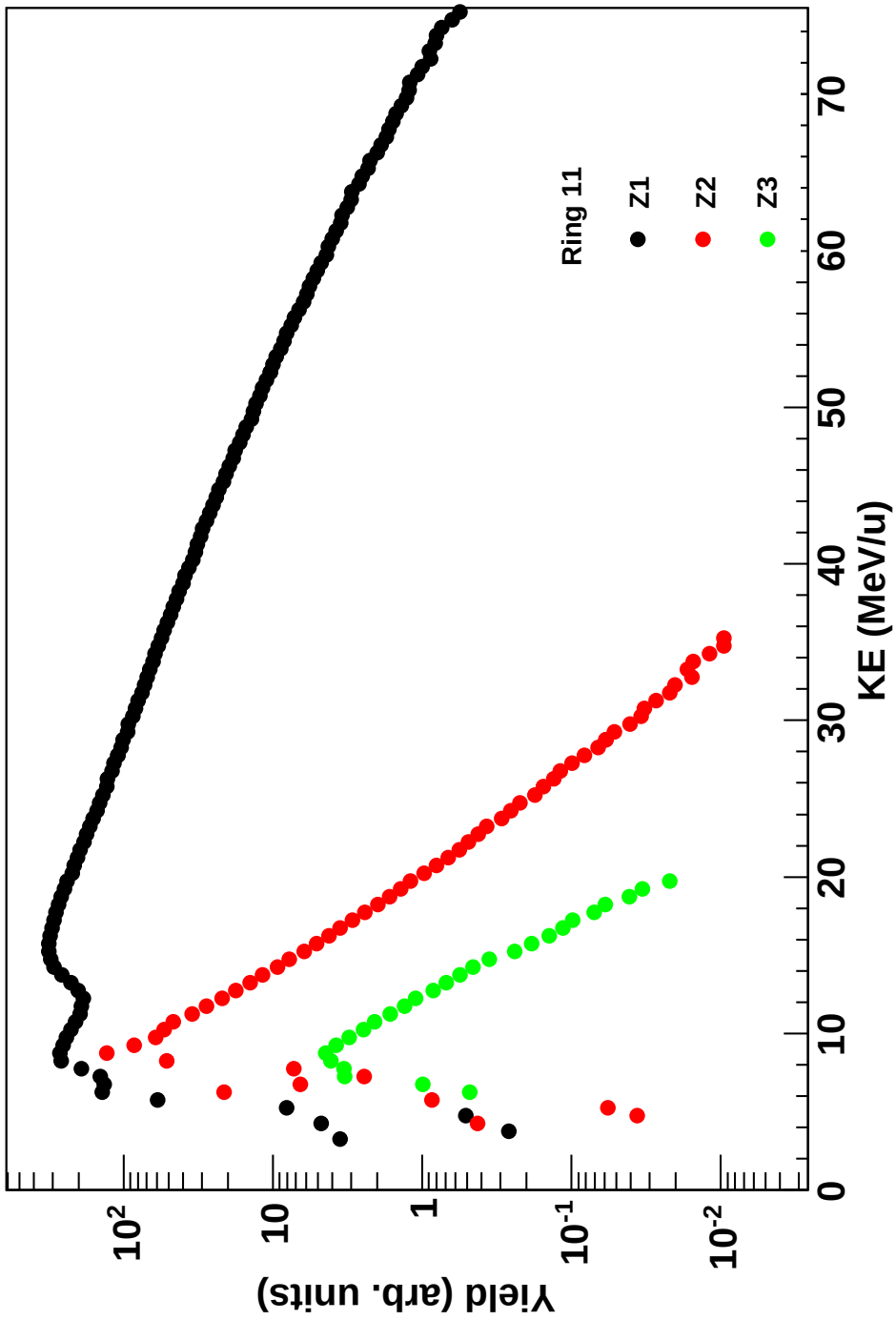

FIG. 128. Ring 11 energy spectra for the 35 MeV/u ^{70}Zn+^{70}Zn system.

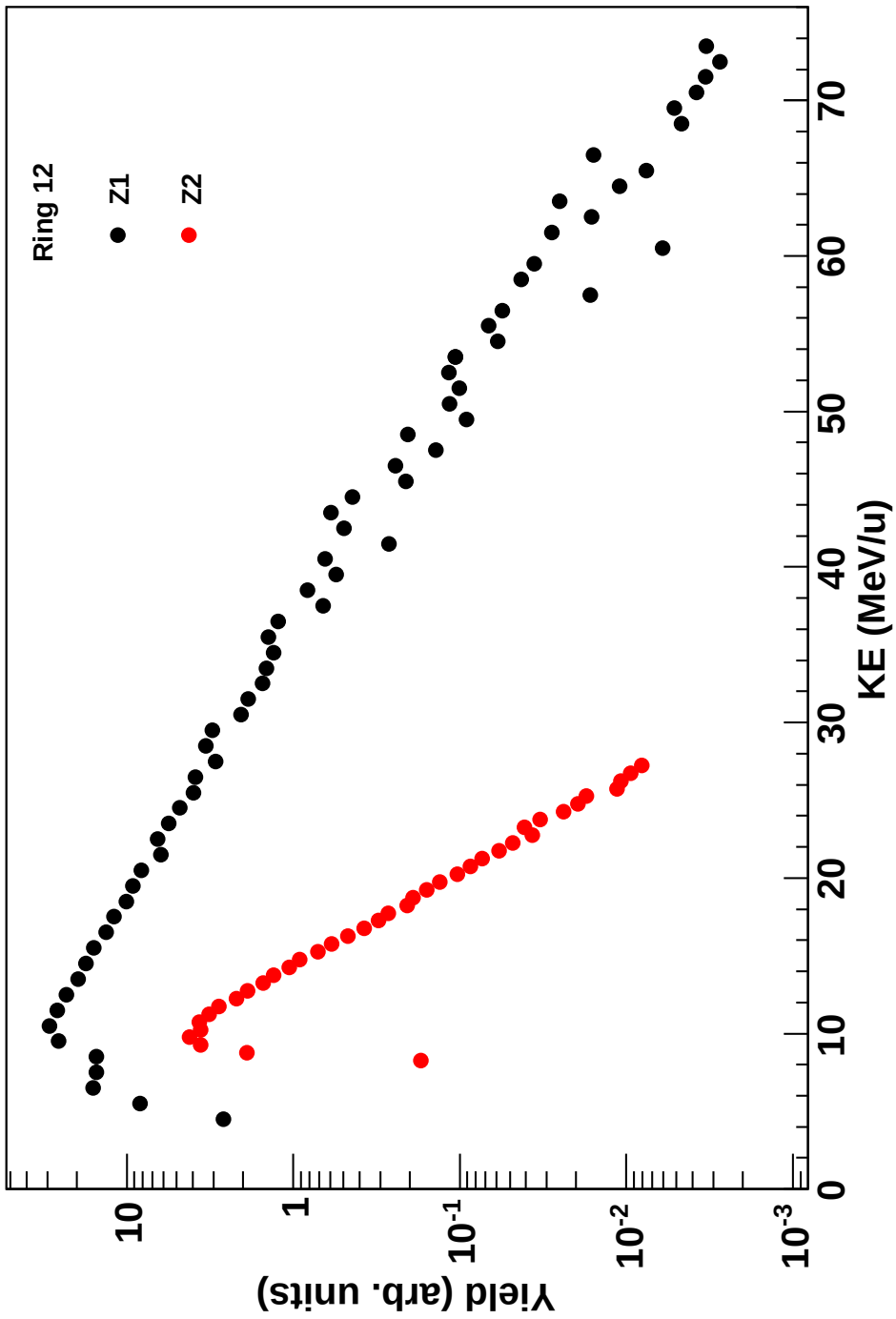

FIG. 129. Ring 12 energy spectra for the 35 MeV/u ^{70}Zn+^{70}Zn system.

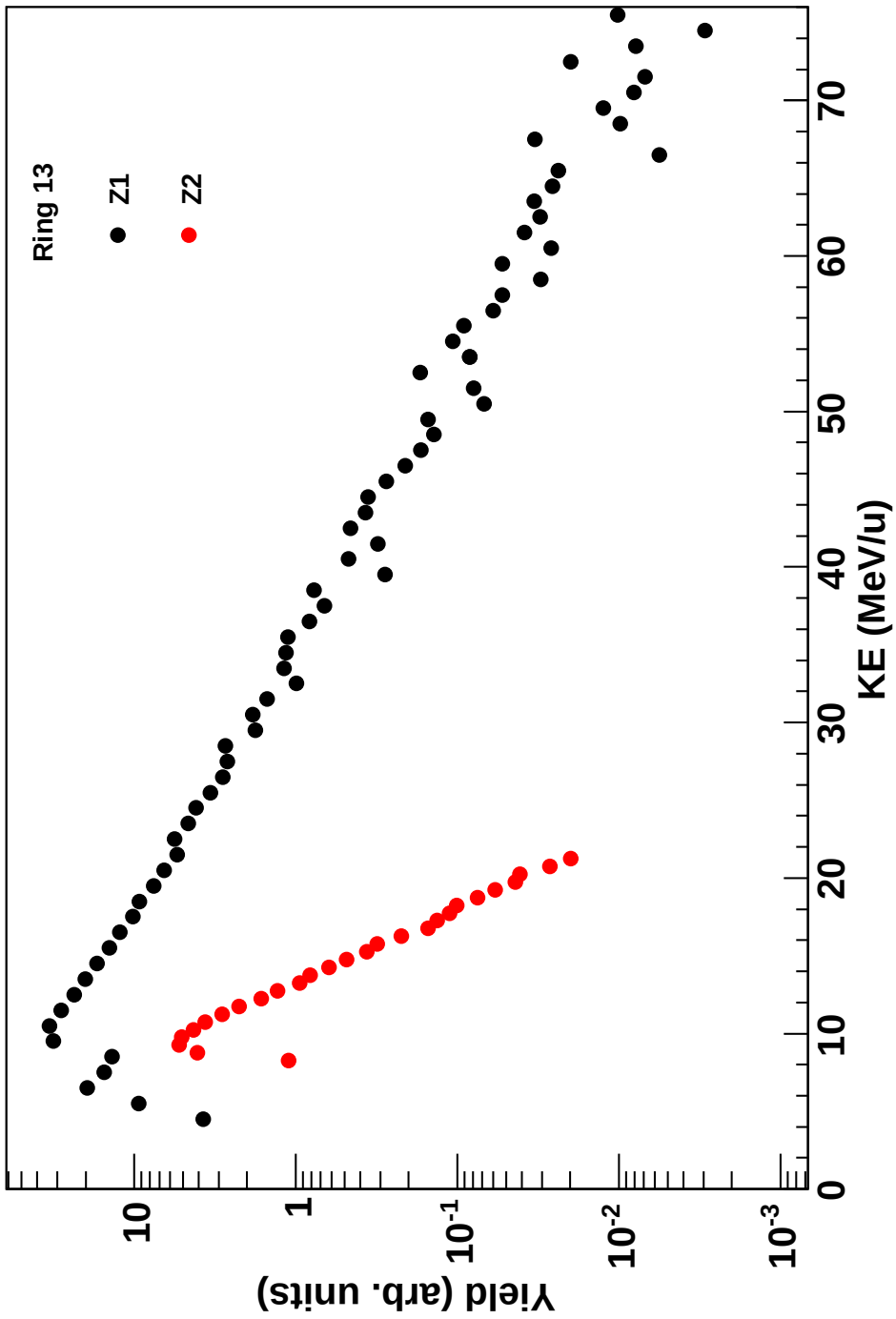

FIG. 130. Ring 13 energy spectra for the 35 MeV/u ^{70}Zn+^{70}Zn system.

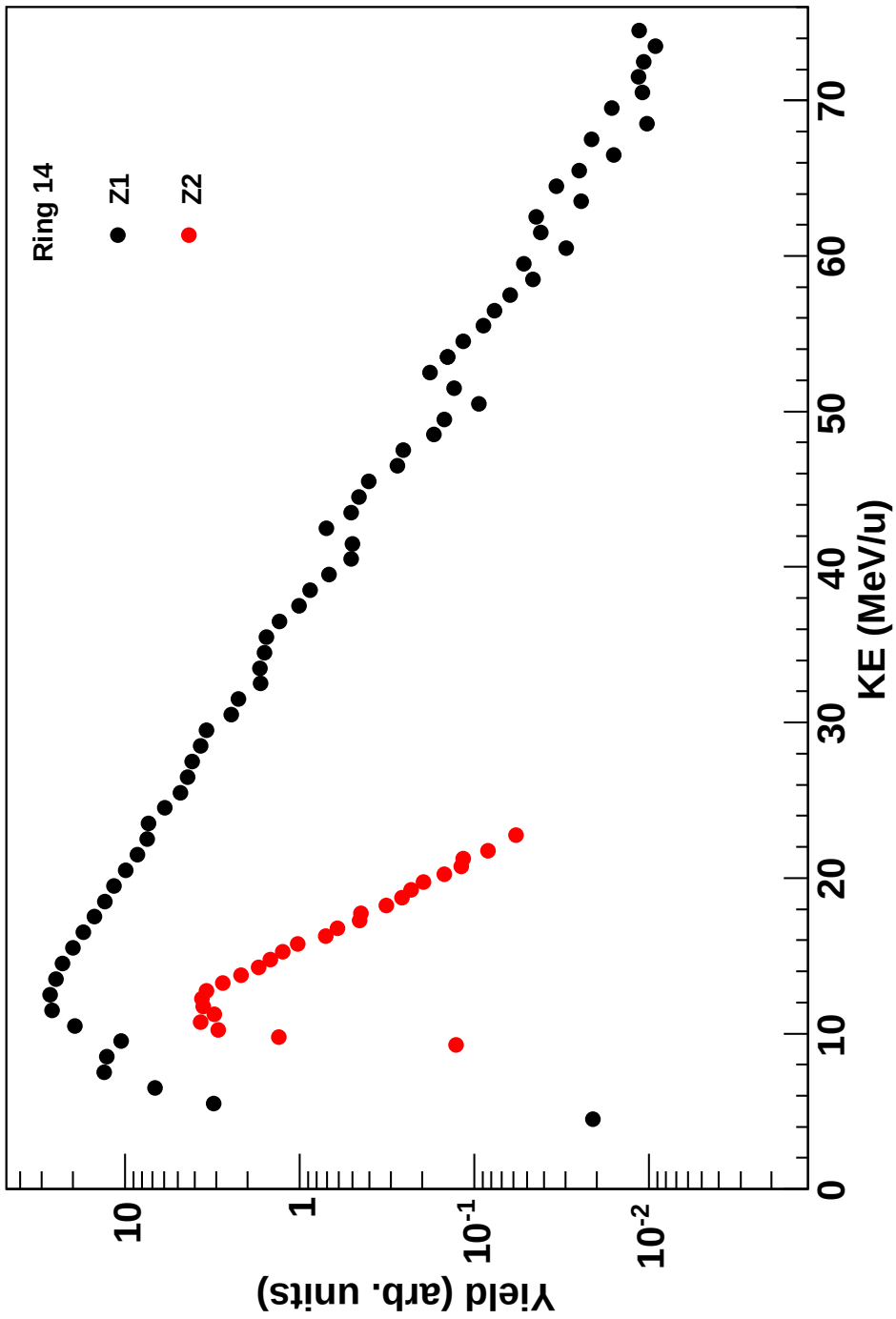

FIG. 131. Ring 14 energy spectra for the 35 MeV/u ^{70}Zn+^{70}Zn system.

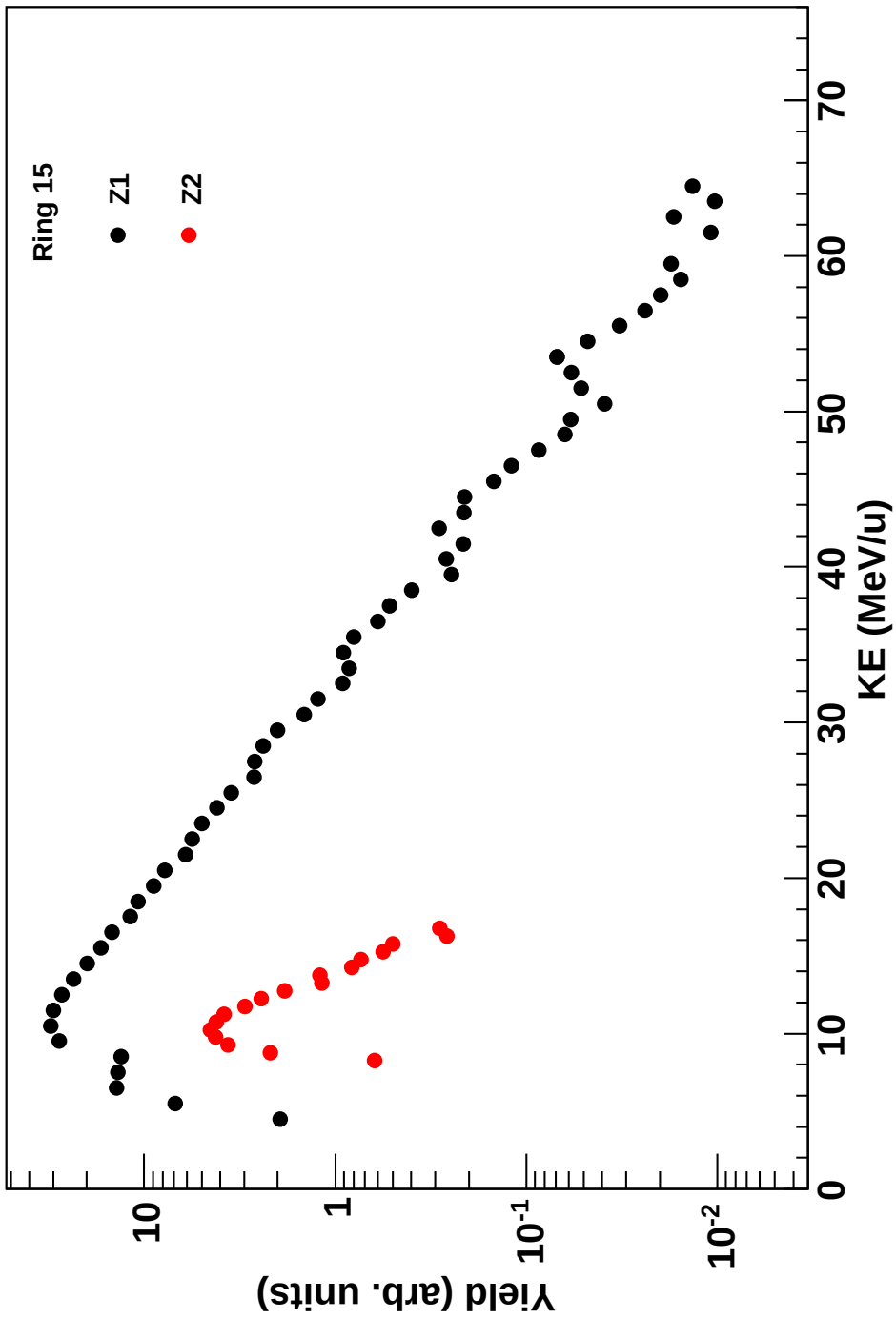

FIG. 132. Ring 15 energy spectra for the 35 MeV/u ^{70}Zn+^{70}Zn system.

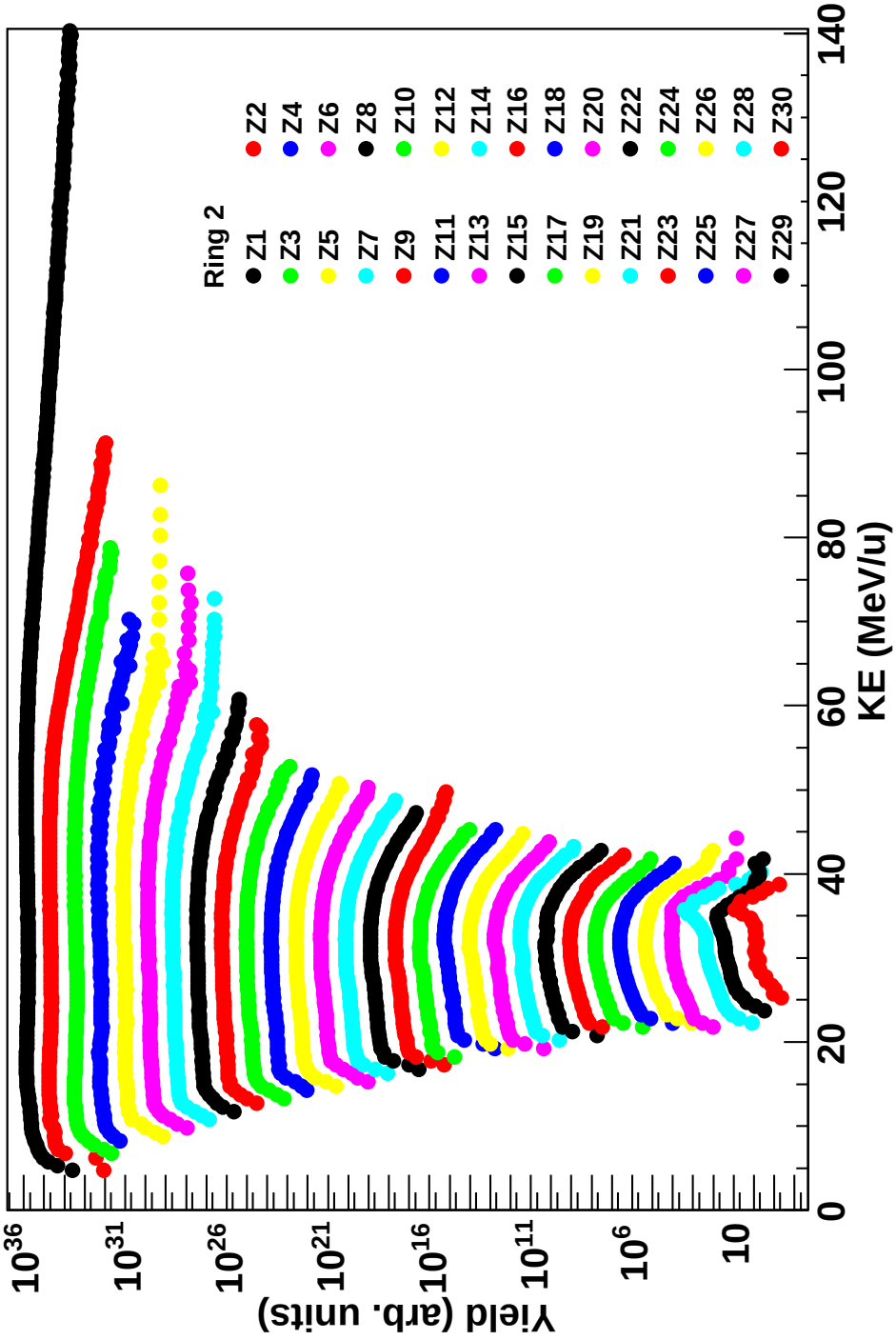

FIG. 133. Ring 2 energy spectra for the 35 MeV/u ^{64}Ni+^{64}Ni system.

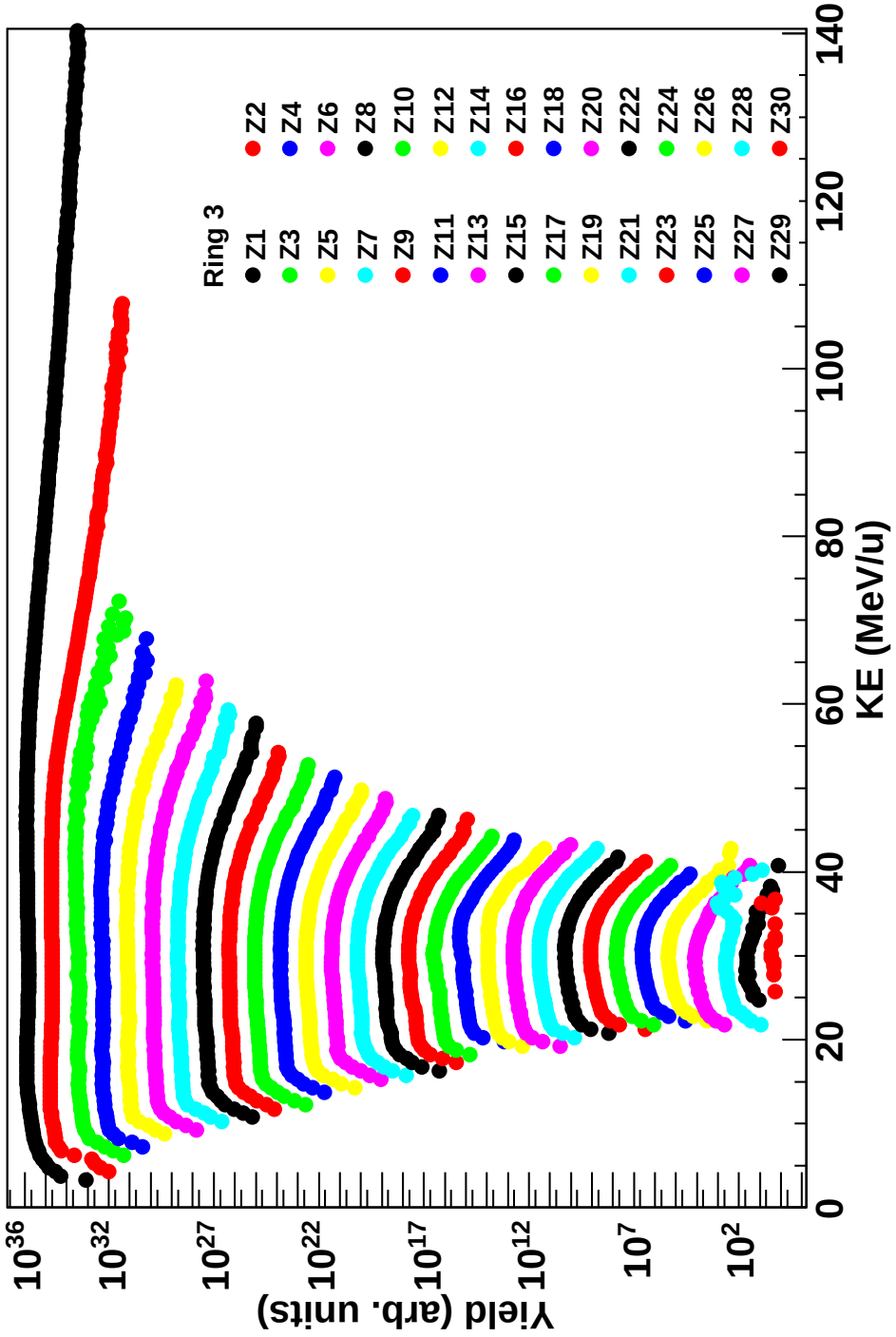

FIG. 134. Ring 3 energy spectra for the 35 MeV/u ^{64}Ni+^{64}Ni system.

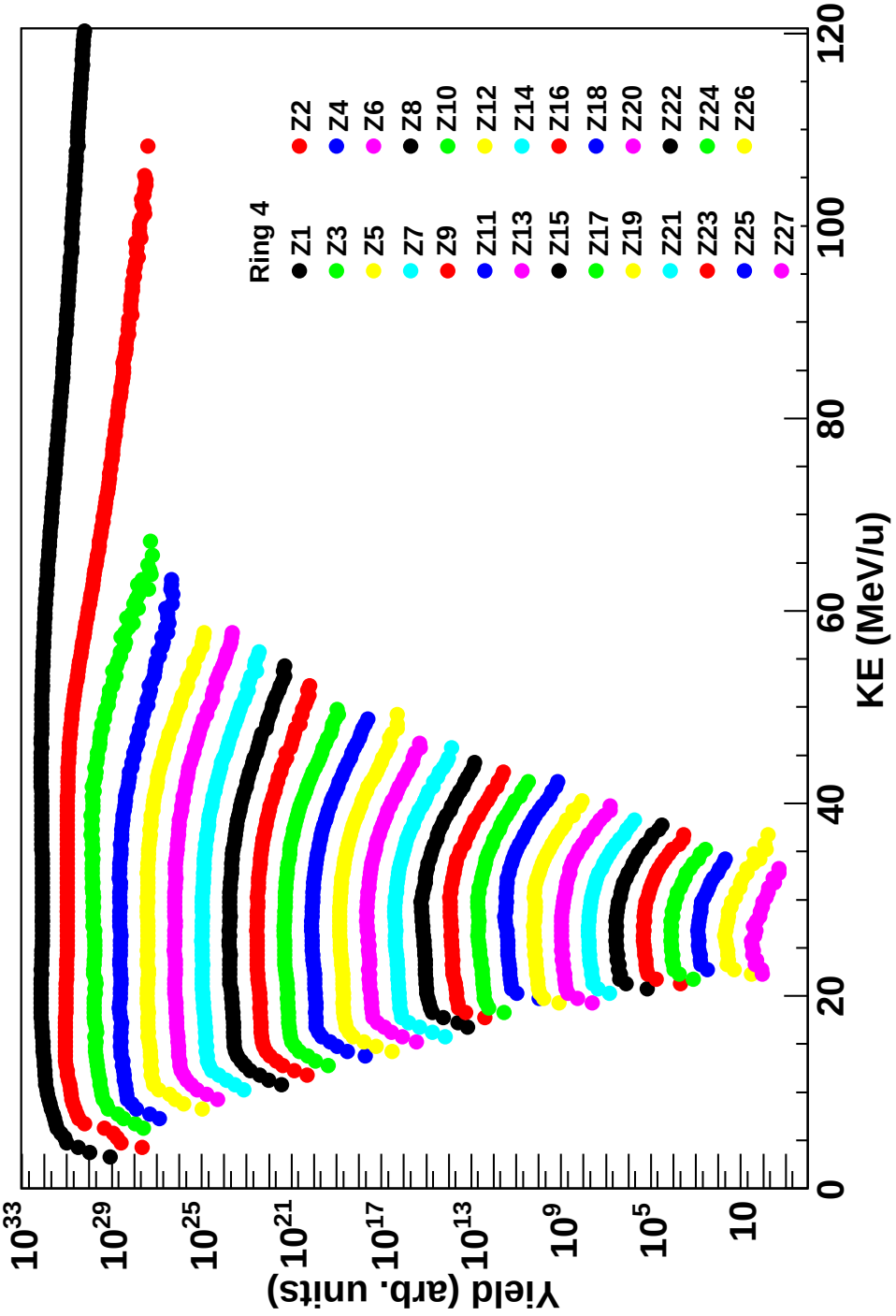

FIG. 135. Ring 4 energy spectra for the 35 MeV/u ^{64}Ni+^{64}Ni system.

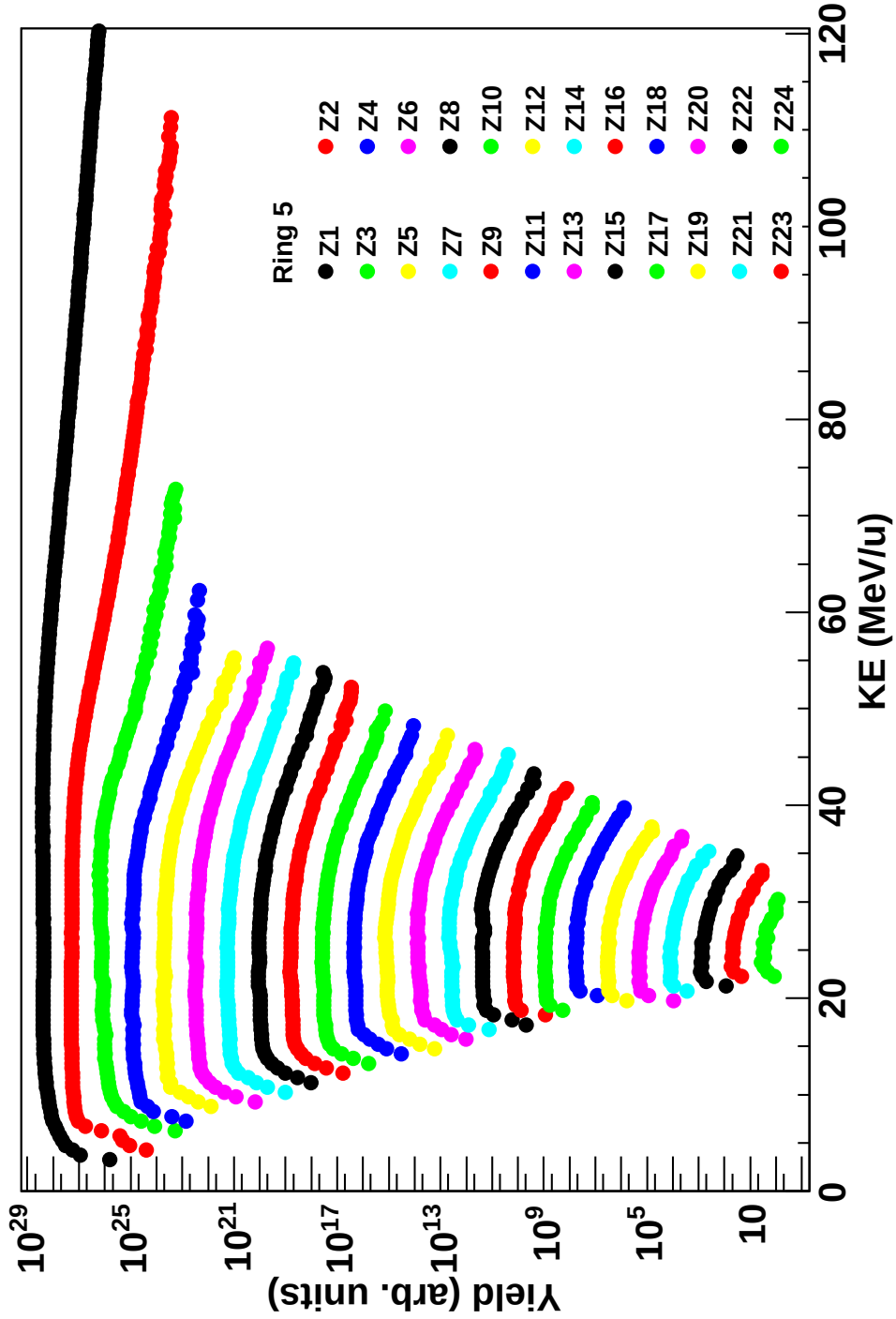

FIG. 136. Ring 5 energy spectra for the 35 MeV/u ^{64}Ni+^{64}Ni system.

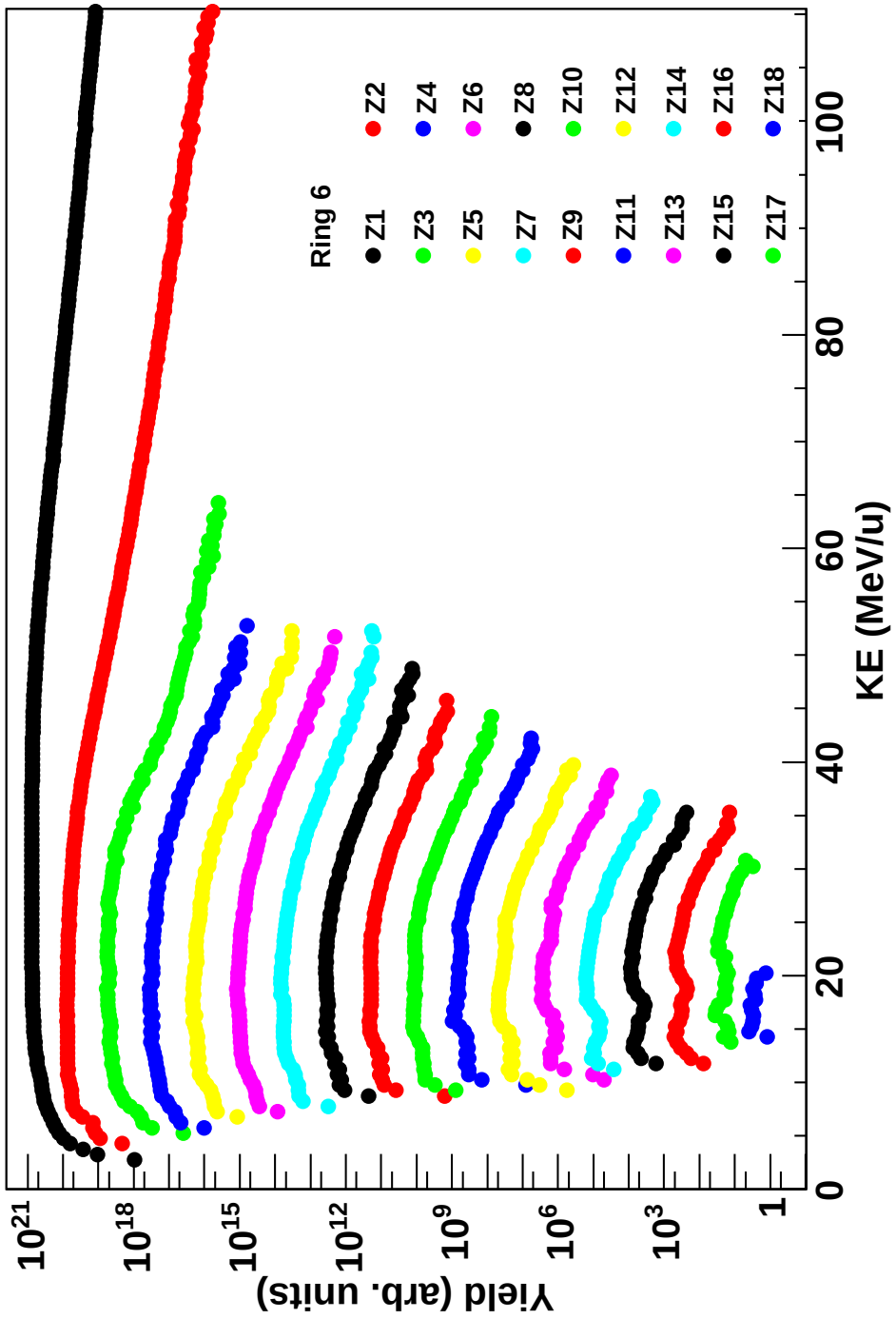

FIG. 137. Ring 6 energy spectra for the 35 MeV/u ^{64}Ni+^{64}Ni system.

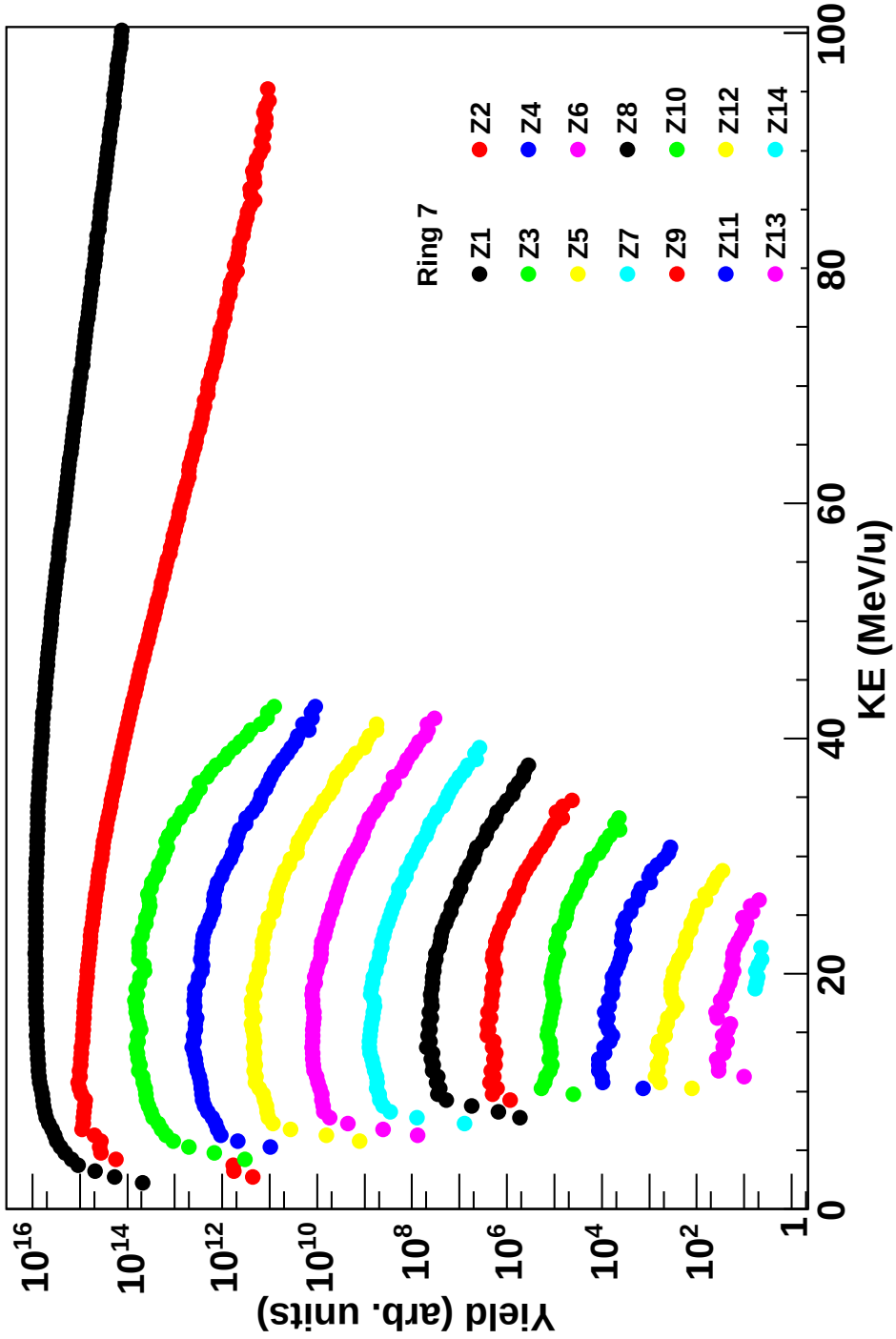

FIG. 138. Ring 7 energy spectra for the 35 MeV/u ^{64}Ni+^{64}Ni system.

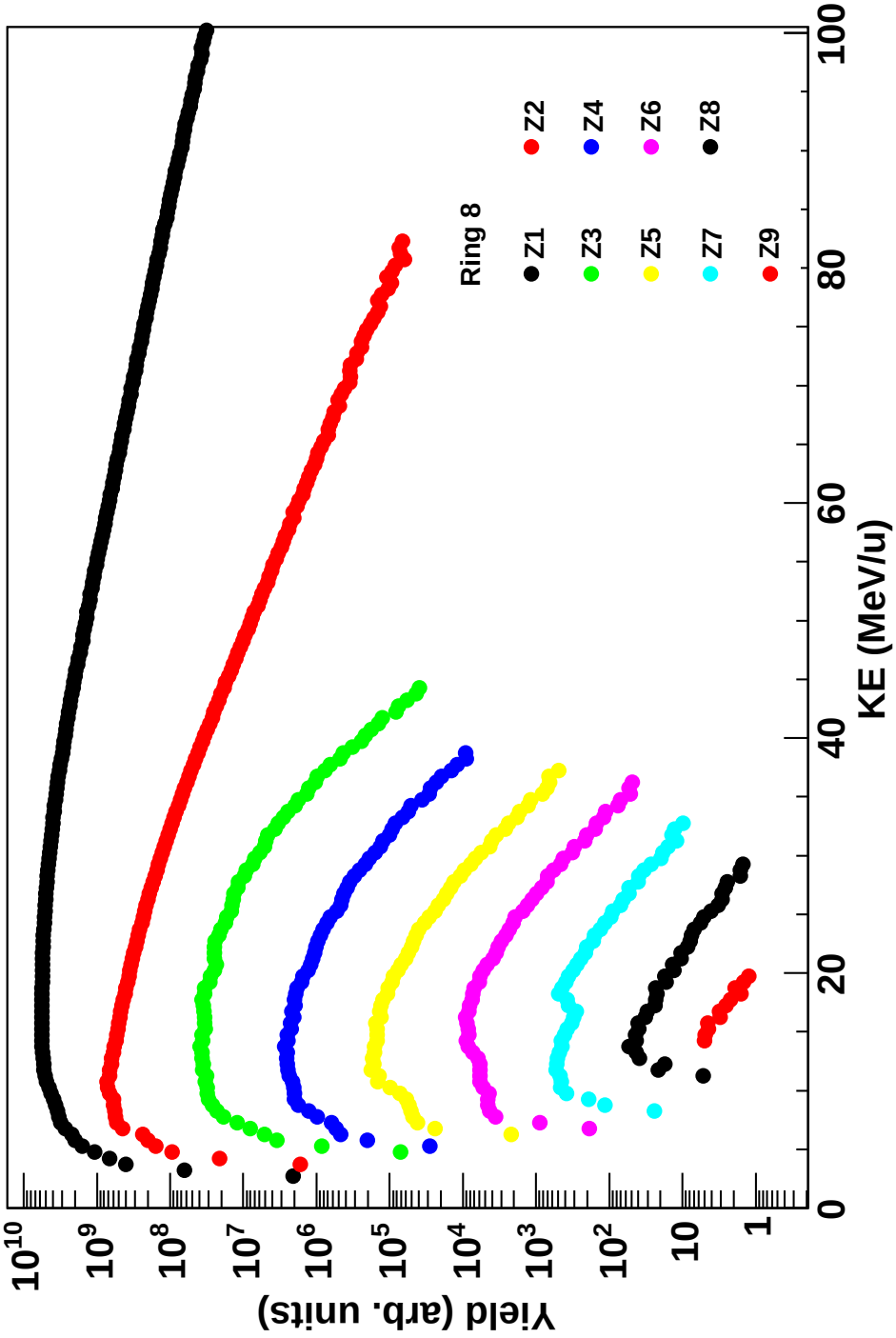

FIG. 139. Ring 8 energy spectra for the 35 MeV/u ^{64}Ni+^{64}Ni system.

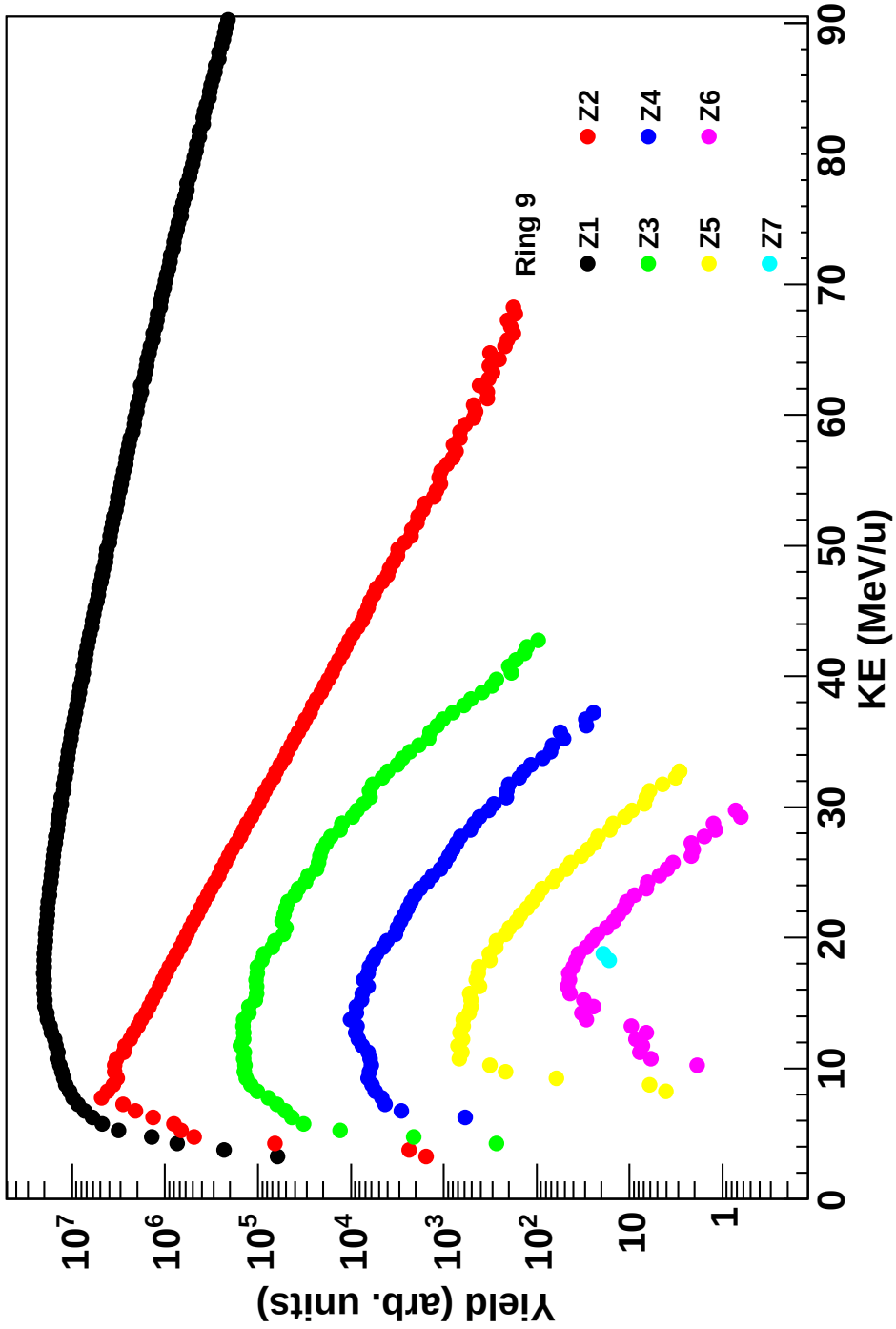

FIG. 140. Ring 9 energy spectra for the 35 MeV/u ^{64}Ni+^{64}Ni system.

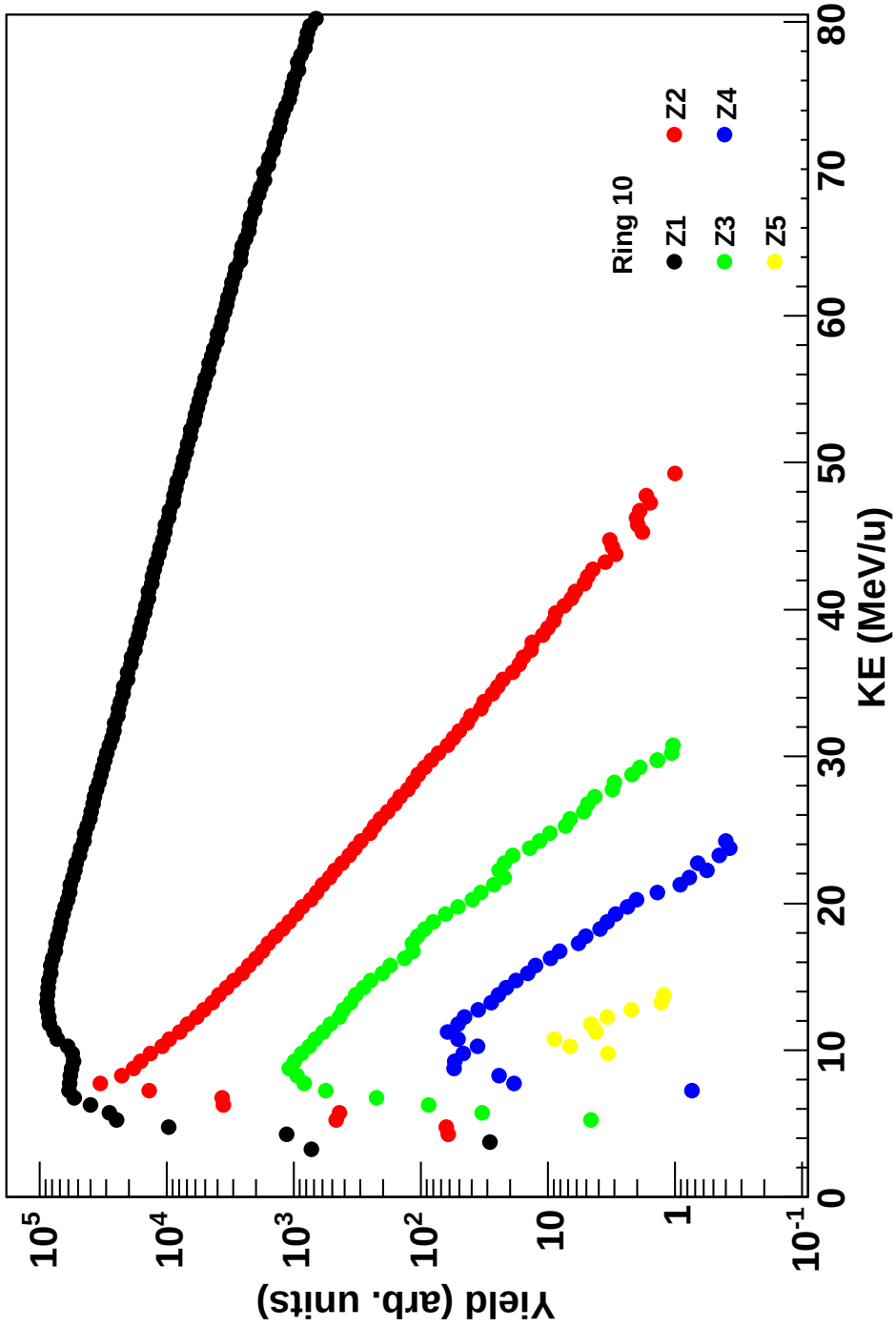

FIG. 141. Ring 10 energy spectra for the 35 MeV/u ^{64}Ni+^{64}Ni system.

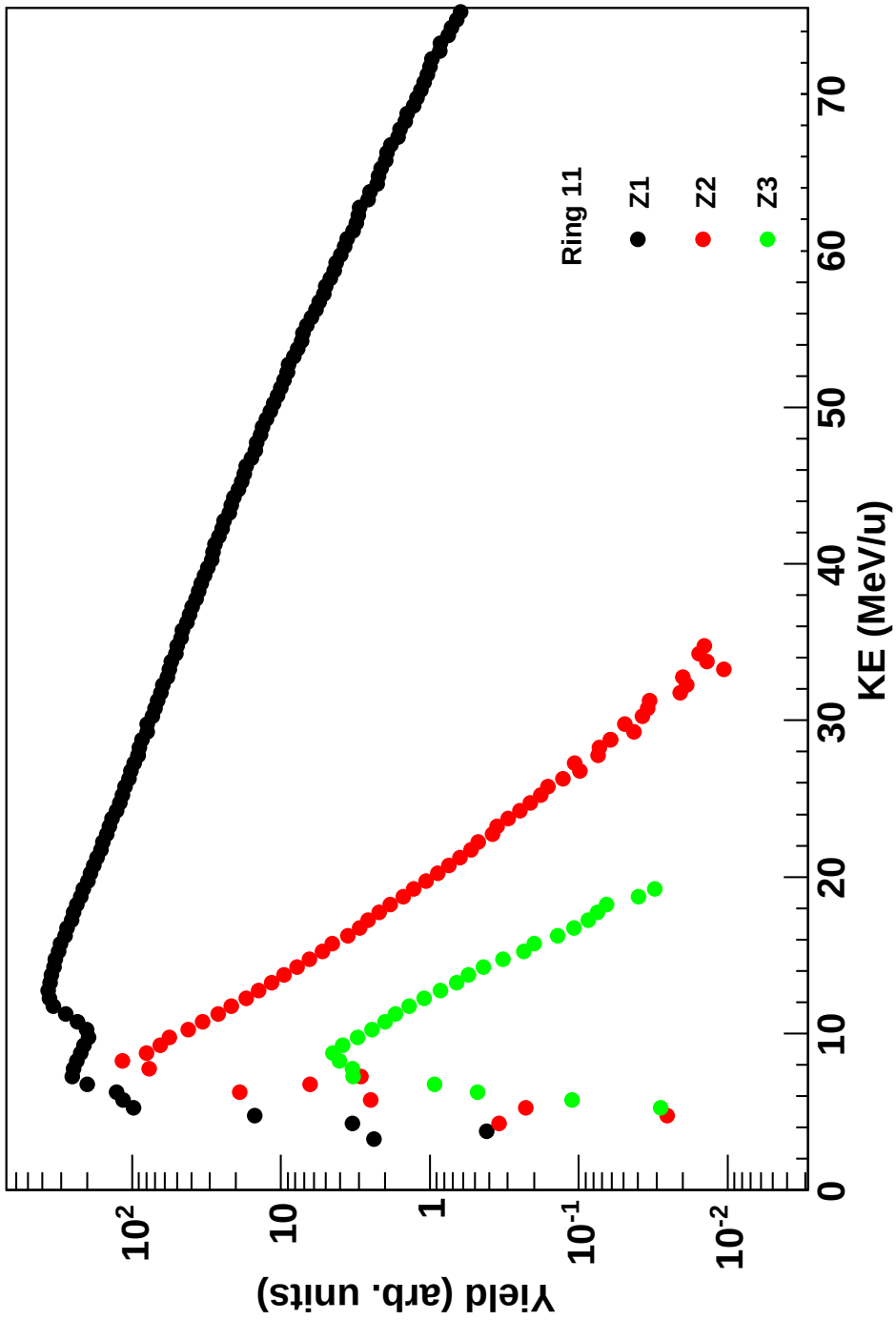

FIG. 142. Ring 11 energy spectra for the 35 MeV/u ^{64}Ni+^{64}Ni system.

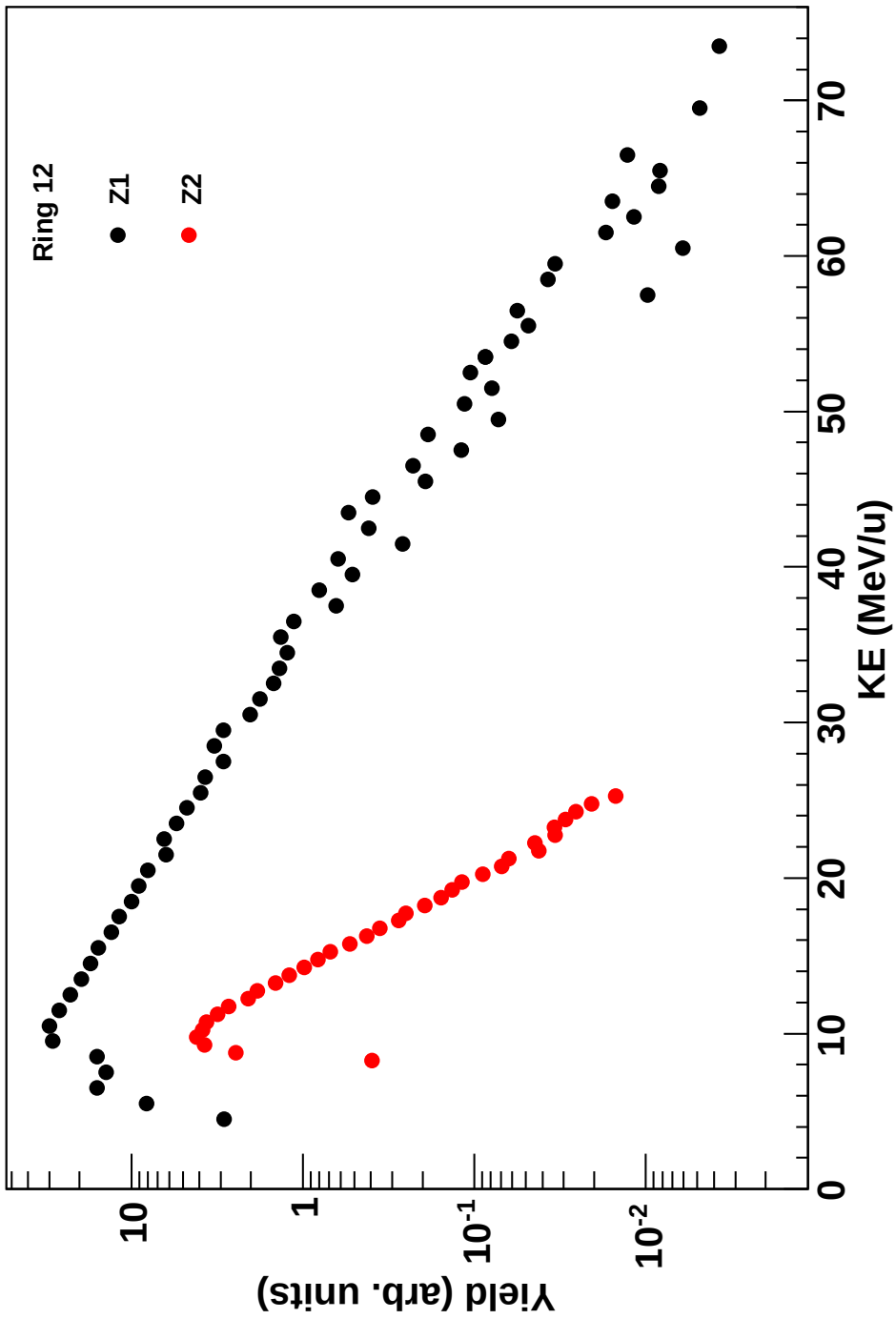

FIG. 143. Ring 12 energy spectra for the 35 MeV/u ^{64}Ni+^{64}Ni system.

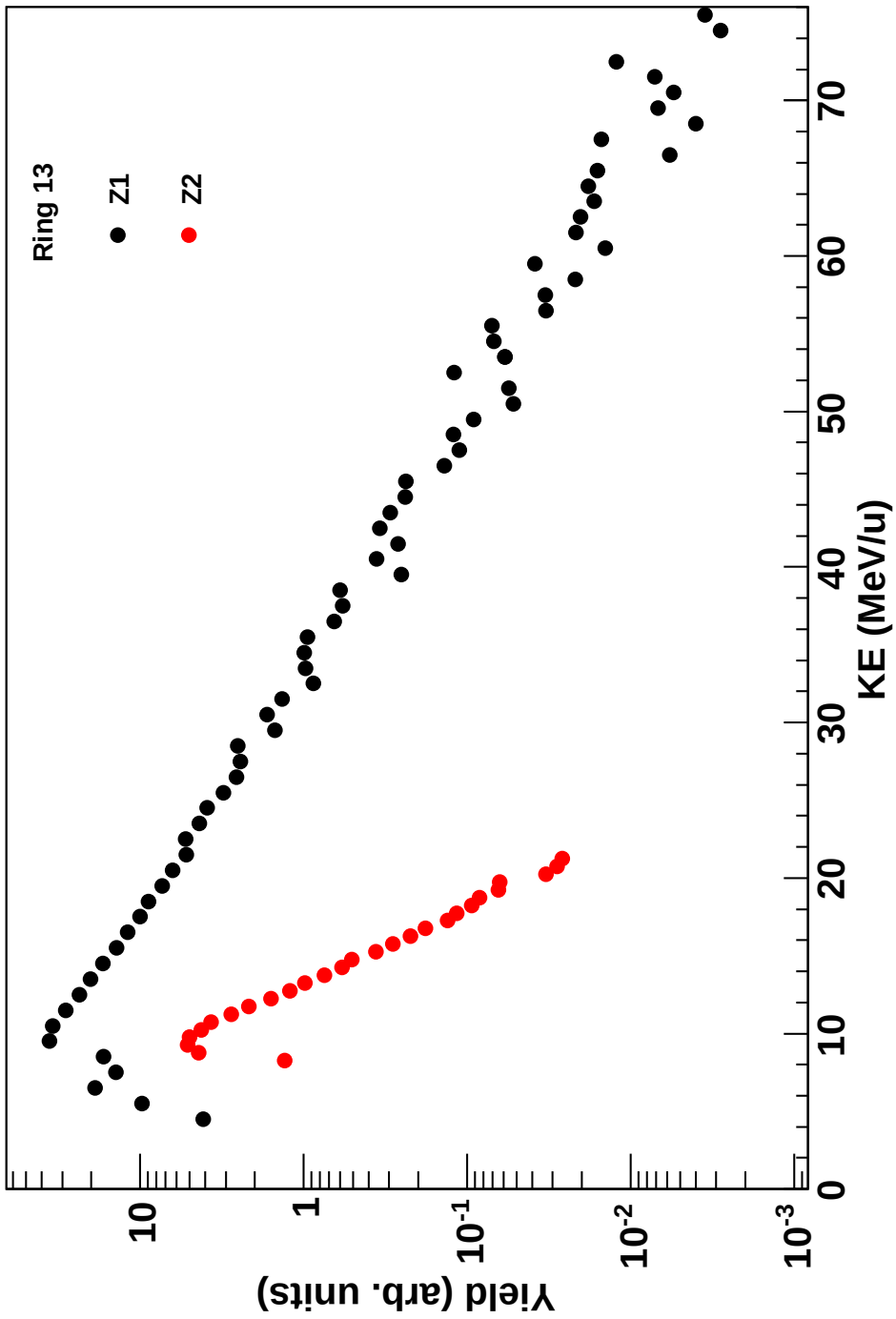

FIG. 144. Ring 13 energy spectra for the 35 MeV/u ^{64}Ni+^{64}Ni system.

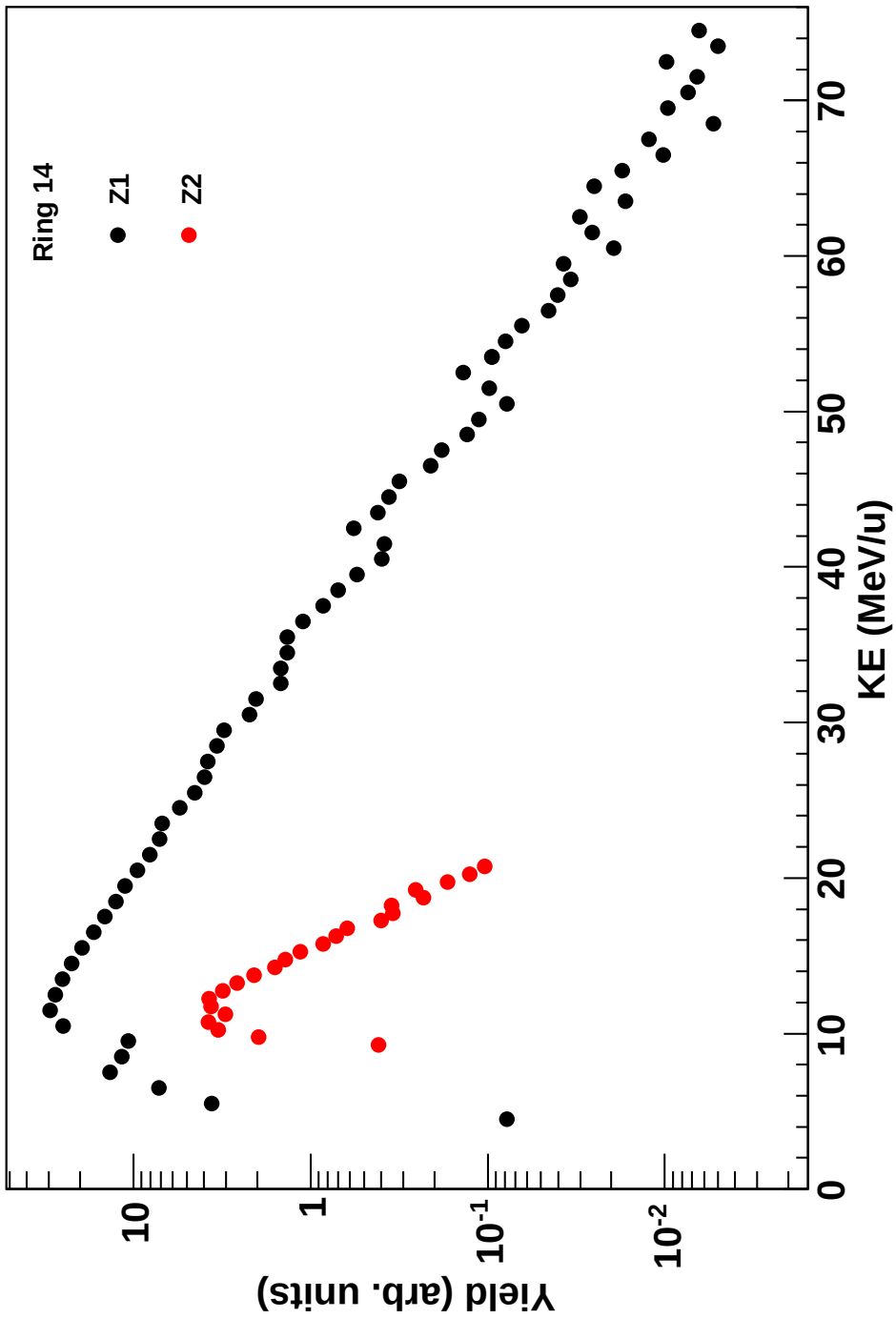

FIG. 145. Ring 14 energy spectra for the 35 MeV/u ^{64}Ni+^{64}Ni system.

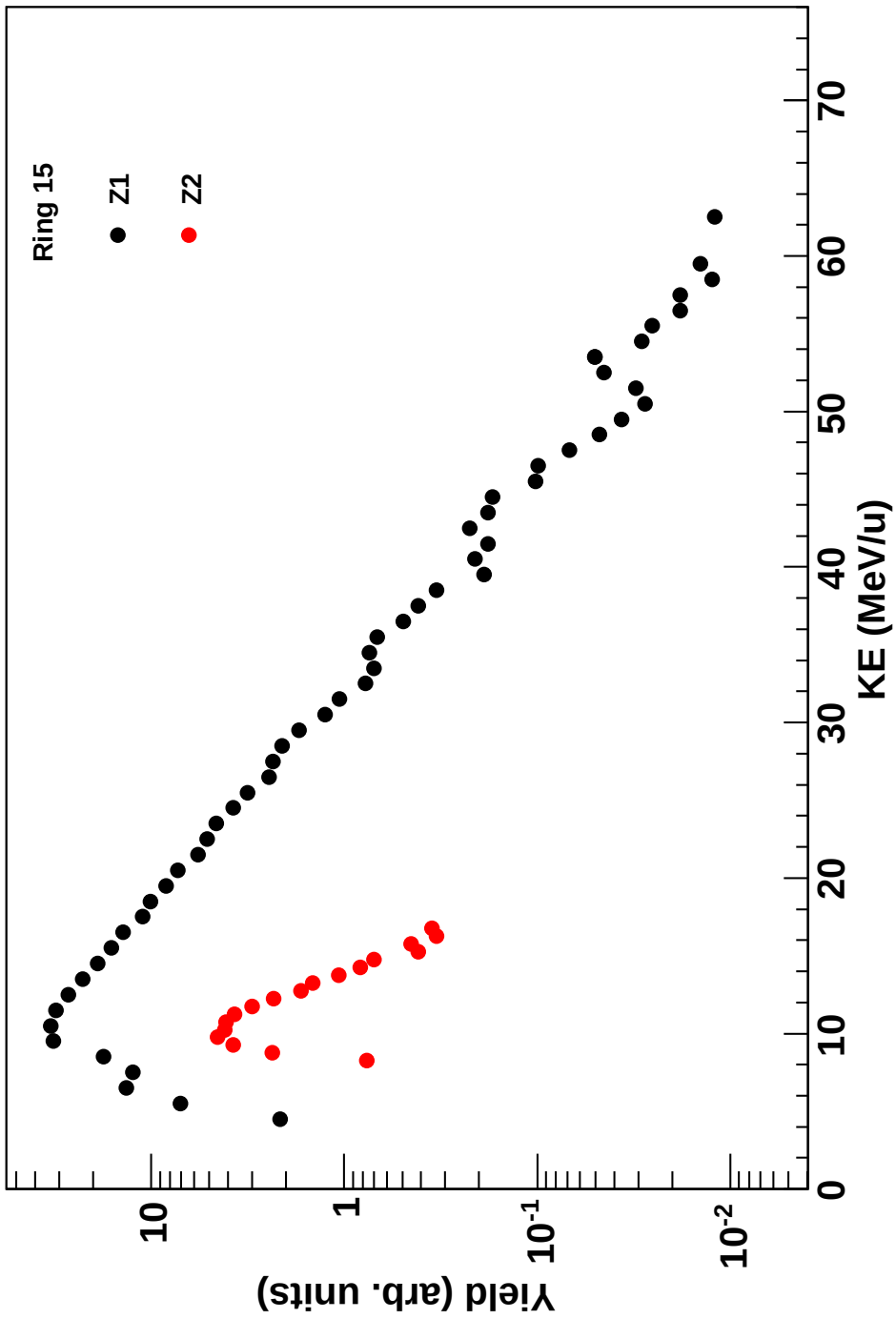

FIG. 146. Ring 15 energy spectra for the 35 MeV/u ^{64}Ni+^{64}Ni system.

APPENDIX C

C++ EXAMPLE MODULE FOR ACCESSING EXPERIMENTAL DATA

Shown below is the TestModule.cxx which provides an example C++ module for accessing the experimental data. This file can be obtained at /home/sjygroup/zkohley/070208/src/TestModule.cxx on the TAMU Cyclotron Institute Computer Cluster.

```
1  //       $Id: TestModule.cxx,v 1.1 2009/04/02 20:02:10 zkohley Exp
       $
2  //
3  //////
4  #include "TestModule.h"
5
6  #include "PhysEvent.h"
7  #include "SimEvent.h"
8  #include "TString.h"
9
10 ClassImp(TestModule)
11
12 TestModule::TestModule(){
13 }
14 //----------------------------------------
15
16 TestModule::TestModule(const Char_t *name, const Char_t *title) :
       CycModule(name, title)
17 {
18 }
19 //-----------------------------------------------
20
21 TestModule::~TestModule() {
22 }
23 //----------------------------------------
24
25 void TestModule::Init() {
26   SetState(kInit);
27
28   //These values are set in the ConfigTestModule.C file
29   //Default is max 20% contam and 1.5 MaxPSigma
```

```
30    printf("A-Identification: MaxContamination=%f  MaxPercentSigma
          :%f\n",fMaxContam,fMaxPSigma);
31  }
32
33  //-----------------------------------------
34
35  void TestModule::DefineHistograms(){
36    printf("inside of defining histograms\n");
37    TString title;
38
39    TDirectory *savdir = gDirectory;
40
41    //creating directories in the output TFile
42    TDirectory *EventDir        = gDirectory->mkdir("Event");
43
44    EventDir->cd();
45    //Initializing new histograms
46    hZDist = new TH1F("hZDist","hZDist",100,-0.5,99.5);
47    hADist = new TH1F("hADist","hADist",100,-0.5,99.5);
48
49
50
51    printf("End of DefineHistograms\n");
52    gDirectory = savdir;
53    savdir->cd();
54  }
55
56  //-----------------------------------------------------
57  void TestModule::Begin() {
58    SetState(kBegin);
59
60    printf("end of Begin method\n");
61  }
62  //---------------------------------
63
64  void TestModule::End() {
65    //End of job
66    SetState(kEnd);
67
68  }
69  //-----------------------------------------
70
71  void TestModule::Finish() {
72    SetState(kFinish);
73  }
```

```
74
75 //------------------------------------------------
76
77 void TestModule::Clear() {
78 }
79 //------------------------------------------------
80 void TestModule::Event(CycEvent* evin, CycEvent *evout) {
81
82   //Declaring CycEvent as a PhysEvent (PhysEvent.h)
83   //aka experimental data
84   PhysEvent *physev = (PhysEvent*)evin;
85
86   //Also can check to see if it is inherting
87   //from SimEvent class (SimEvent.h)
88   //such as AMD or CoMD results.
89   TString evClass = evin->IsA()->GetName();
90   SimEvent *simev = 0;
91   if(evClass.Contains("SimEvent")){
92     simev = (SimEvent*)evin;
93   }
94
95   //For example we will focus on using the PhysEvent
96   //and PhysParticle.
97   //Ignoring the SimEvent class.
98
99   //Loop over event multiplicity
100  for(int i=0; i<physev->GetMult(); i++){
101
102    //Get ith particle
103    PhysParticle *part = physev->GetParticleAt(i);
104
105    //check if it is filter accpeted (this is only
106    //needed when dealing with simulations) since
107    //all experimental particles are accepted
108    if(part->IsFilterAccepted()){
109
110      //This is an important chunk of code!!!
111      //Here the isotopic identification requirements are
112      //checked.  If they are not met then the A of the particle
113      //is set to 0 and only the GuessA is then valid.
114      if(part->GetA()!=0 && (part->GetPSigma()>fMaxPSigma || part
             ->GetContam()>fMaxContam) ){
115        part->SetGuessA(part->GetA());
116        part->SetA(0);
117      }
```

```
118
119         //Now we can fill our histograms
120         //However we may want to just look at fragments
121         //that did not have a "bad" energy spectra
122         if(part->GetEnergyFlag()!=PhysEvent::kBad){
123
124           //fill Z-distribution
125           hZDist->Fill(part->GetZ());
126
127           //for A-distribution only want
128           //isotopically id fragments so...
129           if(part->GetA()>0) hADist->Fill(part->GetA());
130
131         }
132
133       }//filtered accpeted if statement
134     }//for-loop over mult
135
136   }
```

Shown below is the header file (TestModule.h) which is associated with the example module (TestModule.cxx) shown above.

```
1  // -*- mode: c++ -*-
2  //
3  // $Id: TestModule.h,v 1.1 2009/04/02 20:02:11 zkohley Exp $
4
5  #ifndef E070208_TestModule
6  #define E070208_TestModule
7
8  #ifndef CYC_CycModule
9  #include "CycModule.h"
10 #endif
11
12 #ifndef ROOT_TH1
13 #include "TH1.h"
14 #endif
15
16 //Necesarry classes
17 class PhysEvent;
18 class SimEvent;
19 class SimParticle;
20 class PhysParticle;
21
22 class TestModule : public CycModule {
23 public:
24
25 private:
26   //Event information
27
28   Double_t fMaxContam;
29   Double_t fMaxPSigma;
30   TString fDataType;
31   TString fSysName;
32
33   //Declare the histograms
34   TH1F *hZDist;
35   TH1F *hADist;
36
37 public:
38   TestModule();
39   TestModule(const Char_t *name, const Char_t *title);
40   virtual ~TestModule();
41
```

```
42    //Basic CycApps structure for a module
43    virtual void    Init();    // Called once per job
44    virtual void    Begin();   // Called once per run
45    virtual void    Event(CycEvent* inev, CycEvent *outev=0);
46    virtual void    End();     // Called once per run
47    virtual void    Finish(); // Called once per job
48    virtual void    DefineHistograms();
49    virtual void    Clear();
50
51    //Setters from the ConfigTestModule.C
52    void SetMaxContam(Double_t m)     {fMaxContam = m;}
53    void SetMaxPSigma(Double_t p)     {fMaxPSigma = p;}
54    void SetDataType(TString s)       {fDataType = s;}
55    void SetSysNameType(TString s)     {fSysName = s;}
56
57    ClassDef(TestModule,0)  // BRAHMS Module definitions
58  };
59
60  #endif
```

Shown below is the Config file (ConfigTestModule.C) which is used to run the TestModule object inside the CycMain Module. This code is in /home/sjygroup/zkohley/070208/dTestModule/ and is run by typing

CycMain ConfigTestModule.C -T phys -S zn70

into the terminal, which would analyze the 35 MeV ^{70}Zn+^{70}Zn data set.

```
1  #ifndef __CINT__
2  hello()
3  #endif
4  {
5  #include <iostream>
6
7     //Load the appropriate library.
8     //For my data this is the lib070208 library
9     //Named after the date the run started on.
10    gSystem->Load("lib070208.so");
11
12    BrAppOptionManager* optionManager = BrAppOptionManager::
          Instance();
13    optionManager->SetVersion(1,0, "A test configuration script");
14    optionManager->SetHelp("\nFirst argument is the configuration
          script");
15
16
17    //These are CycApps option objects that allow for the different
18    //parameters to be input when running the job.
19    //For example, the first one is the max % contamination, which
20    //is set to the default value of 20%
21    BrAppFloatOption* contamOption =
22      new BrAppFloatOption('C',"contaimination","maxContam",0.20);
23    BrAppFloatOption* psigmaOption =
24      new BrAppFloatOption('P',"% sigma","psigma",2.5);
25    BrAppStringOption* systemOption =
26      new BrAppStringOption('S', "choose system", "zn70,zn64,ni64",
            "zn70");
27    BrAppStringOption* typeOption =
28      new BrAppStringOption('T', "choose event type", "phys,amd,
            comd,bgbd", "phys");
29    BrAppStringOption* dirOption =
30      new BrAppStringOption('D', "input-directory", "Input
            directory", "/data/sjygroup/sjy9/zach/070208/dTestModule/
```

```
        condorqued");
31    BrAppStringOption* inputOption =
32      new BrAppStringOption('i', "input", "Input file", "reduce.
          root");
33    BrAppStringOption* outputOption =
34      new BrAppStringOption('o', "output", "Output file", "test.
          root");
35    BrAppIntOption* runOption =
36      new BrAppIntOption('r',"run-number","run number",0);
37    BrAppIntOption* eventOption =
38      new BrAppIntOption('e', "events", "Max events", 500000000);
39    BrAppIntOption* verboseOption =
40      new BrAppIntOption('v', "verbose", "Verbosity level", 0);
41    BrAppIntOption* debugOption =
42      new BrAppIntOption('d', "debug", "Debug level", 0);
43   BrAppStringOption* addonOption =
44      new BrAppStringOption('A', "add notes on end of outputfile",
          "tstring", "");
45
46
47    if (!optionManager->ProcessCommandLine())
48      return;
49
50    optionManager->ShowVersion();
51    if (optionManager->ShowHelp())
52      return;
53
54    TObject::SetObjectStat(kFALSE);
55
56
57    //The PathManager, CycMainDb, CycRunInfoManager, and
          CycCalibrationManager
58    //are important for correclty accessing the experimental data.
59    PathManager *pathMan = PathManager::Instance();
60    printf("data dir = %s\n",pathMan->GetDataDir());
61    CycMainDb *mainDb = CycMainDb::Instance();
62    mainDb->ConnectToRun(Form("%s/rundb/ACQRunDb.txt",pathMan->
          GetDataDir()));
63    mainDb->ConnectToFileCatalog(Form("..//test_file_catalog/
          FileCatalog.root")); //,pathMan->GetDataDir()));
64    mainDb->ConnectToCalib(Form("%s/caldb/CalDb.root",pathMan->
          GetDataDir()));
65
66    //Set the run number to get from the run db.
67    CycRunInfoManager *runDb = CycRunInfoManager::Instance();
```

```
68
69    //Calibration db manager
70    CycCalibrationManager *calMan = CycCalibrationManager::Instance
          ();
71    calMan->Init();
72
73    //
          ------------------------------------------------------------------

74
75    //This is the MAIN MODULE for running the code
76    //The TestModule Object will run inside of the CycMain Module
77    CycMainModule* mainModule = new CycMainModule("Hello",
78                                                  "Hello test",
79                                                  "Me", 1, 0, 0);
80
81    mainModule->SetMaxEvents(eventOption->GetValue());
82
83    //--Setup Info for Everything-------
84    TString type = typeOption->GetValue();
85    TString sys = systemOption->GetValue();
86    TString dir = dirOption->GetValue();
87    TString input = inputOption->GetValue();
88    TString addon = addonOption->GetValue();
89    TString histFilename, inFile;
90    //if you are reading in a physevent....
91    if(type.Contains("phys")){
92      //No input file because use runNo info
93      histFilename = Form("%s/phys_%s.root",dir.Data(),sys.Data());
94      //if(ZOption->GetValue()>0)  histFilename = Form("%s/phys_%
              s_Z%02.0f.root",dir.Data(),sys.Data(),ZOption->GetValue()
              *100);
95      if(!addon.IsNull())  histFilename = Form("%s/phys_%s_%s.root"
              ,dir.Data(),sys.Data(),addon.Data());
96    }
97
98    //Histograms Object that will automatically write out the
99    //histograms created in TestModule.h
100   CycHistIOModule* histModule = new CycHistIOModule("histograms",
          "Histograms");
101   histModule->AddFile(histFilename);
102   mainModule->AddModule(histModule);
103   mainModule->SetHistOn();
104   printf("Added %s to HistIOModule\n",histFilename.Data());
105
```

```
106   //Need this to make file catalog work
107   CycDbUpdateModule *dbUpdate = new CycDbUpdateModule("DB","DB");
108   mainModule->AddModule(dbUpdate);
109
110   //Here we initialize our new object
111   //and set the setters
112   TestModule *ana = new TestModule("phys","phys");
113   ana->StudyFlow::SetMaxContam(contamOption->GetValue());
114   ana->StudyFlow::SetMaxPSigma(psigmaOption->GetValue());
115   ana->StudyFlow::SetDataType(input);
116   ana->StudyFlow::SetSysNameType(sys);
117
118   //add the object to the CycMain Module
119   mainModule->AddModule(ana);
120
121   //Add Input files to Main Module
122   Int_t runNumbers[2]={0,0};
123   Int_t runNum_NimFilter = 0;
124   if(runOption->GetValue(0)!=0) {runNumbers[0]=runOption->
          GetValue(0); runNumbers[1]=runOption->GetValue(1);
          runNum_NimFilter = runNumbers[0];}
125   else if(sys.Contains("zn64")){runNumbers[0]=13; runNumbers
          [1]=91; runNum_NimFilter = 66;}
126   else if(sys.Contains("zn70")){runNumbers[0]=94; runNumbers
          [1]=201; runNum_NimFilter = 175;}
127   else if(sys.Contains("ni64")){runNumbers[0]=234; runNumbers
          [1]=297; runNum_NimFilter = 285;}
128
129   //As shown the zn64 is runs 13-91
130   //              zn70 is runs 94-201
131   //              ni64 is runs 234-297
132
133
134   //Add all of the runs to the Main Module
135   //for analysis with the TestModule object.
136   if(type.Contains("phys")){
137     Int_t count = 0;
138     while(1){
139       Int_t runNo;
140       if(runNumbers[0]>runNumbers[1]) runNo = runNumbers[0] -
              count;
141       else{ runNo = runNumbers[0] + count; }
142       printf("RunNo:%d\n",runNo);
143       runDb->Register(runNo);
144       mainModule->AddRun(runNo,"phys-event");
```

```
145         if(runNo == runNumbers[1]) break;
146         count++;
147       }
148     }
149
150     runDb->Init();
151
152     printf("Finished with config\n");
153   }
```

APPENDIX D

FLOW PLOTS FOR Z=1-3 ISOTOPES

The typical "flow" plots, <Px/A> vs. Y_r, are presented below for the Z=1-4 isotopes. The reaction plane was calculated using the azimuthal correlations method and a SumZ $> 40\%$ Z_{sys} event selection was imposed. The flow was extracted for the Z=1-2 LCPs as the slope of a linear fit from $-0.35 \leq Y_r \leq 0.35$, shown as a solid line. For the heavier fragments (IMFs) the reaction plane re-orientation method was used as discussed in Chapter IV. Therefore, the flow was extracted from the Z=3-4 plots by calculating the $\overline{\langle Px/A \rangle}$ between $0.0 \leq Y_r \leq 0.45$ after correcting the offset. The results are presented for three different centrality cuts.

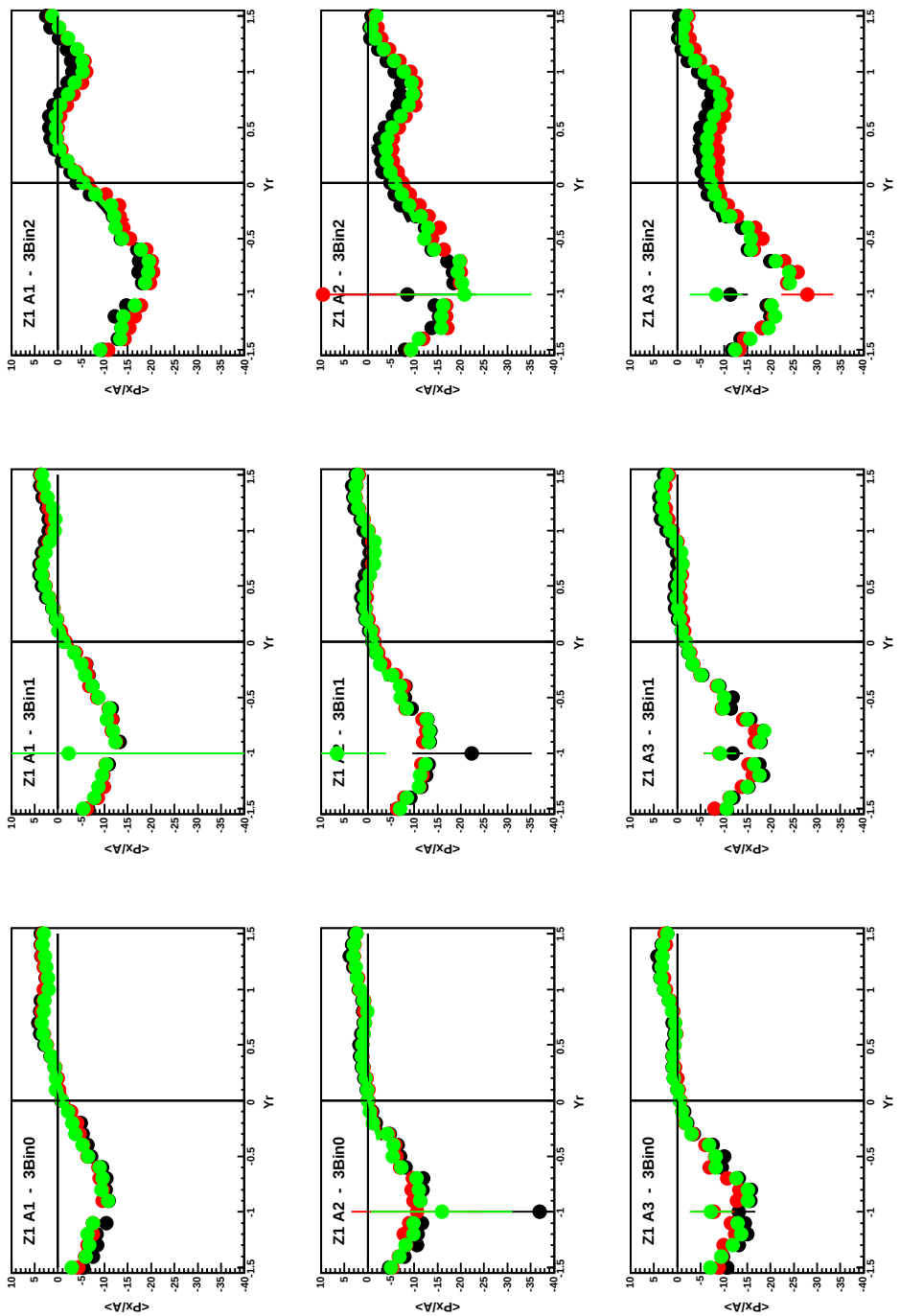

FIG. 147. The <Px/A> is shown as a function of the reduced rapidity, Yr, for the Z=1 isotopes in three different centrality bins, as labeled in the top left of each panel. The results from the 35 MeV/u ^{64}Ni (black), ^{64}Zn (red), and ^{70}Zn (green) systems are presented.

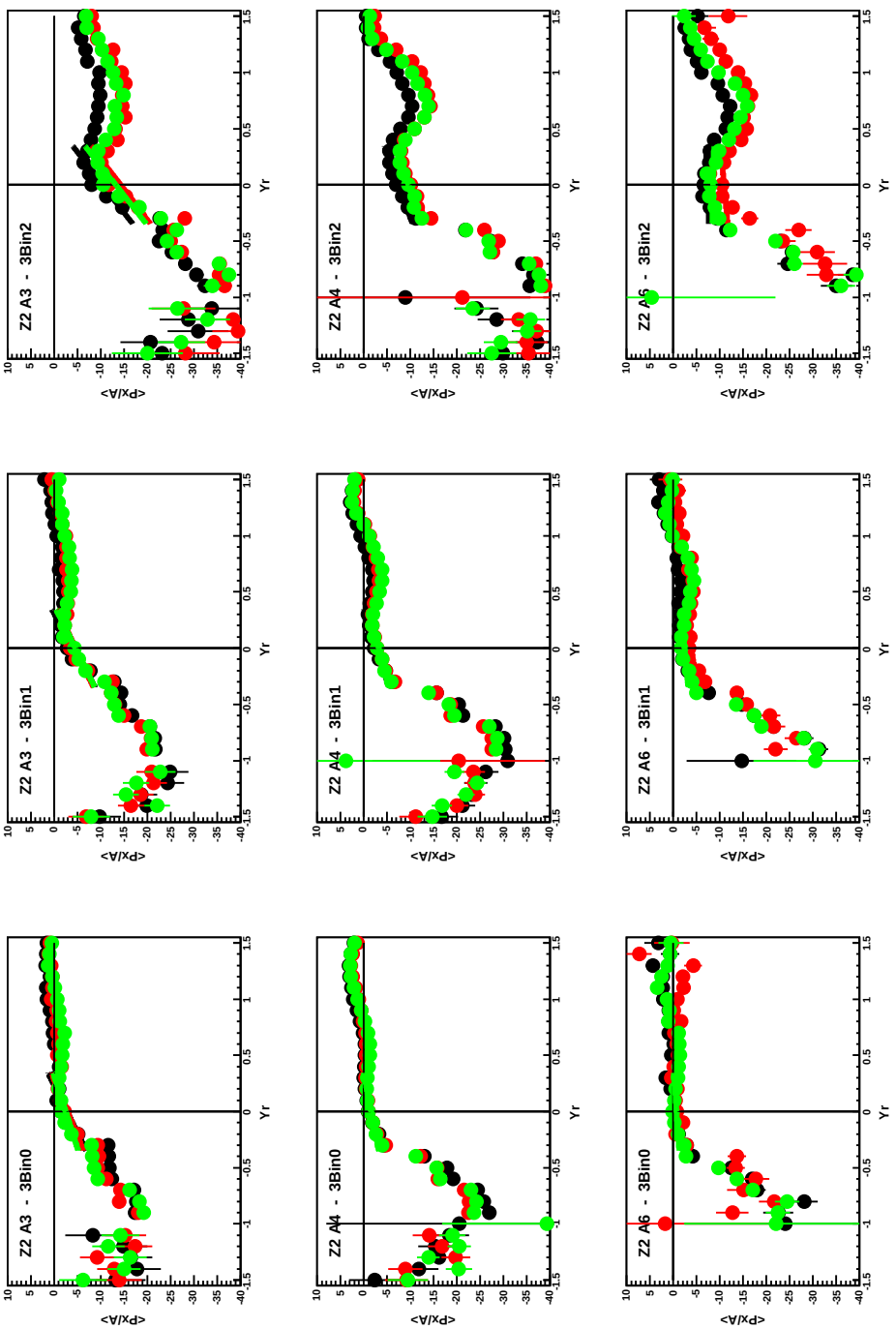

FIG. 148. The <Px/A> is shown as a function of the reduced rapidity, Yr, for the Z=2 isotopes in three different centrality bins, as labeled in the top left of each panel. The results from the 35 MeV/u ^{64}Ni (black), ^{64}Zn (red), and ^{70}Zn (green) systems are presented.

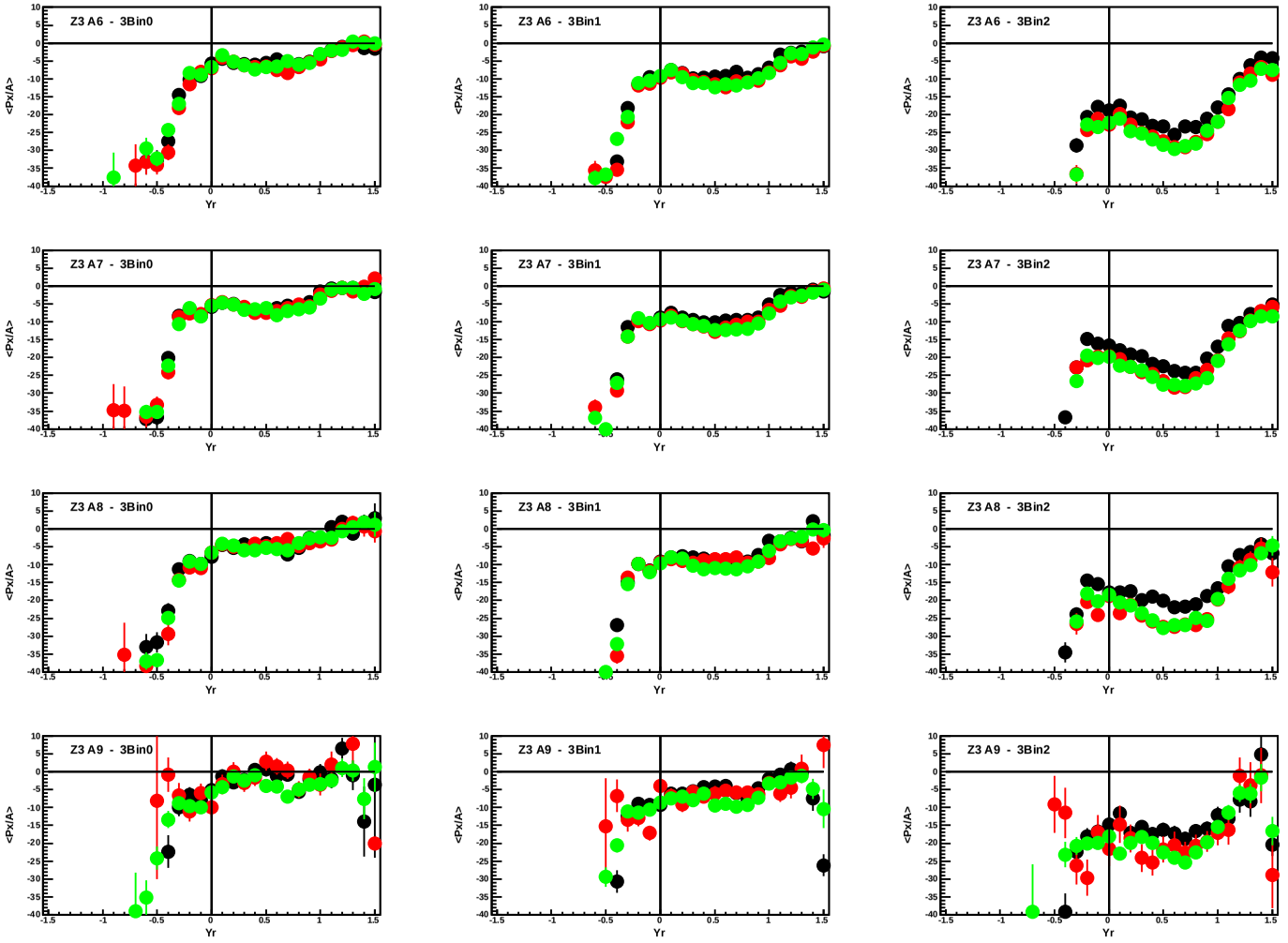

FIG. 149. The <Px/A> is shown as a function of the reduced rapidity, Yr, for the Z=3 isotopes in three different centrality bins, as labeled in the top left of each panel. The results from the 35 MeV/u ^{64}Ni (black), ^{64}Zn (red), and ^{70}Zn (green) systems are presented.

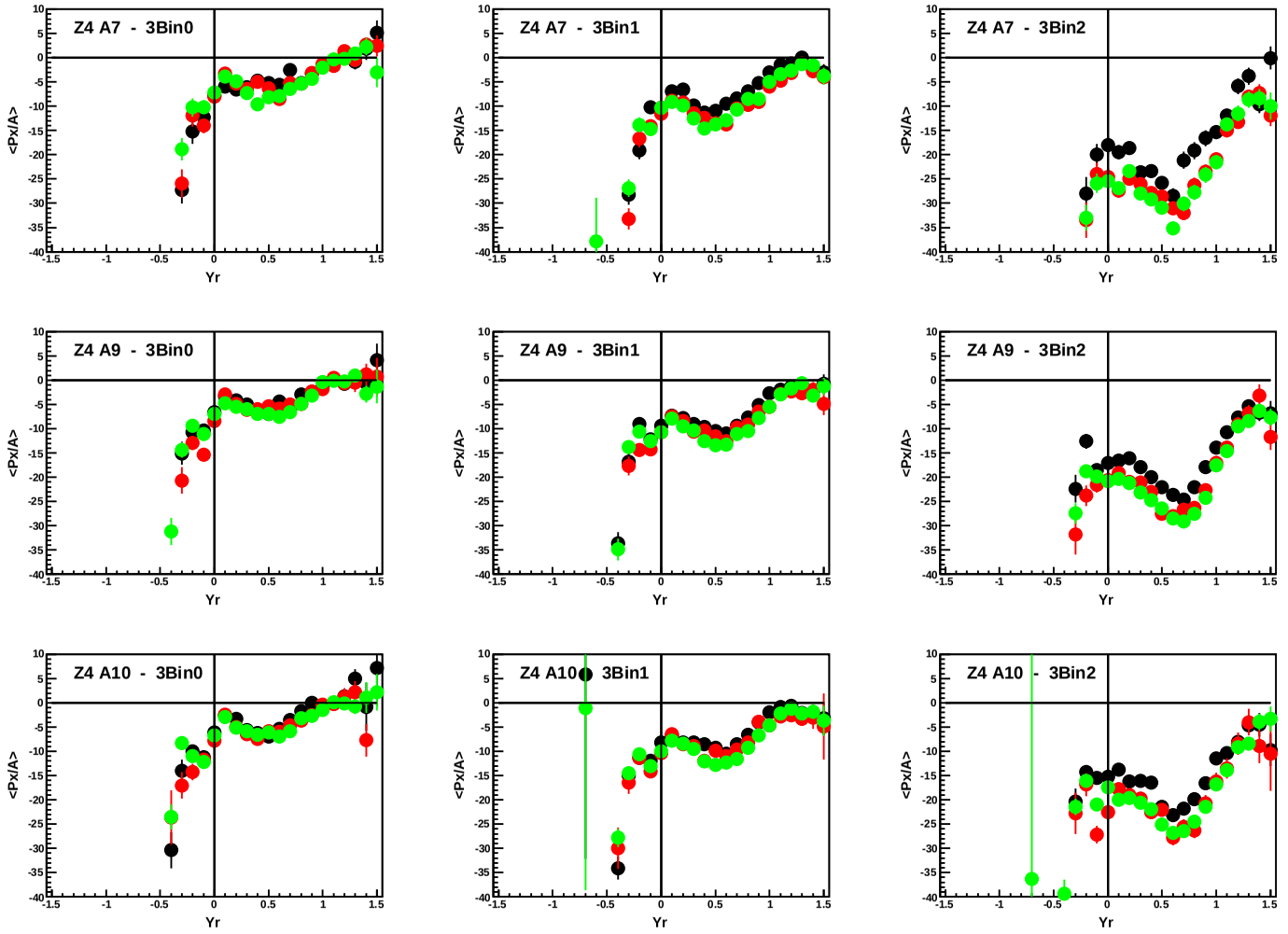

FIG. 150. The <Px/A> is shown as a function of the reduced rapidity, Yr, for the Z=4 isotopes in three different centrality bins, as labeled in the top left of each panel. The results from the 35 MeV/u ^{64}Ni (black), ^{64}Zn (red), and ^{70}Zn (green) systems are presented.

APPENDIX E

LCP KINETIC ENERGY SPECTRA COMPARISON WITH AMD AND COMD SIMULATIONS

The area of each kinetic energy distribution shown in the appendix has been normalized to 1.

The kinetic energy spectra from the AMD model are compared with the experimental data in Figures 151-155 for the mid-peripheral (3Bin1) 35 MeV/u ^{64}Zn+^{64}Zn collisions. The AMD results are shown with and without applying the Gemini statistical decay code after 300 fm/c.

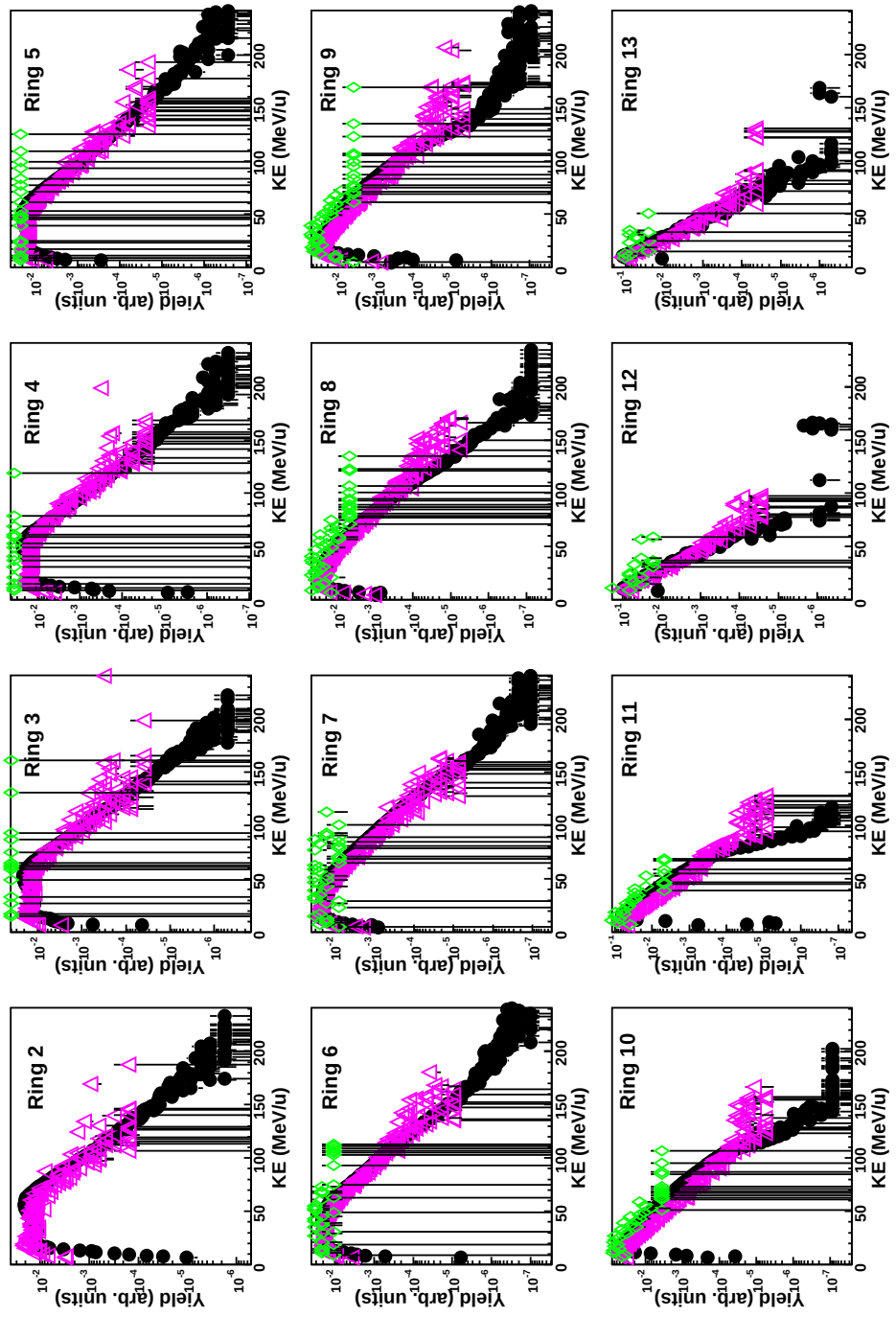

FIG. 151. Kinetic energy distribution of protons for Rings 2-13 from the experimental data (solid black circles) compared with the AMD results at 300 fm/c with (pink open diamonds and without (green open triangles) applying the Gemini decay.

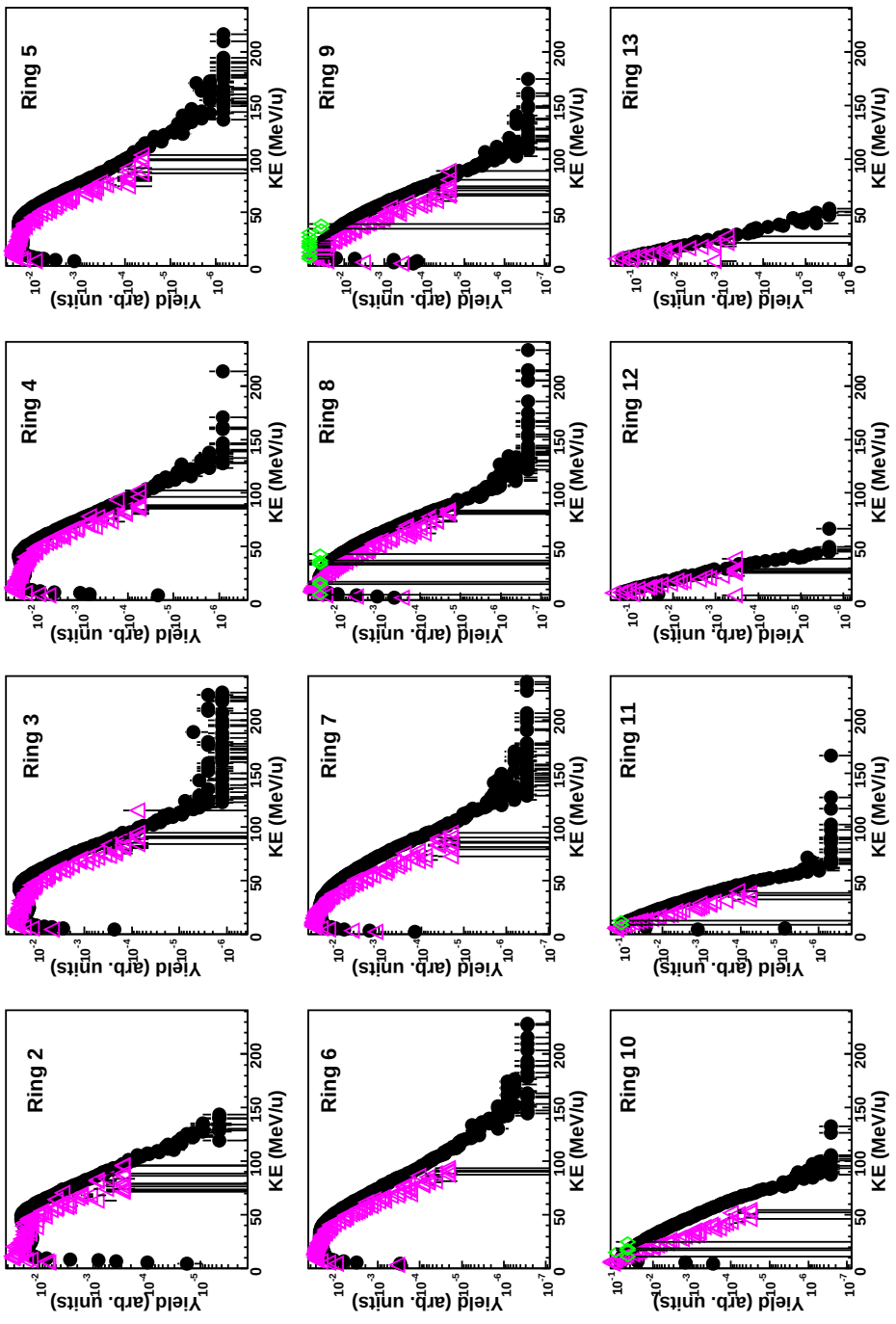

FIG. 152. Kinetic energy distribution of deuterons for Rings 2-13 from the experimental data (solid black circles) compared with the AMD results at 300 fm/c with (pink open diamonds and without (green open triangles) applying the Gemini decay.

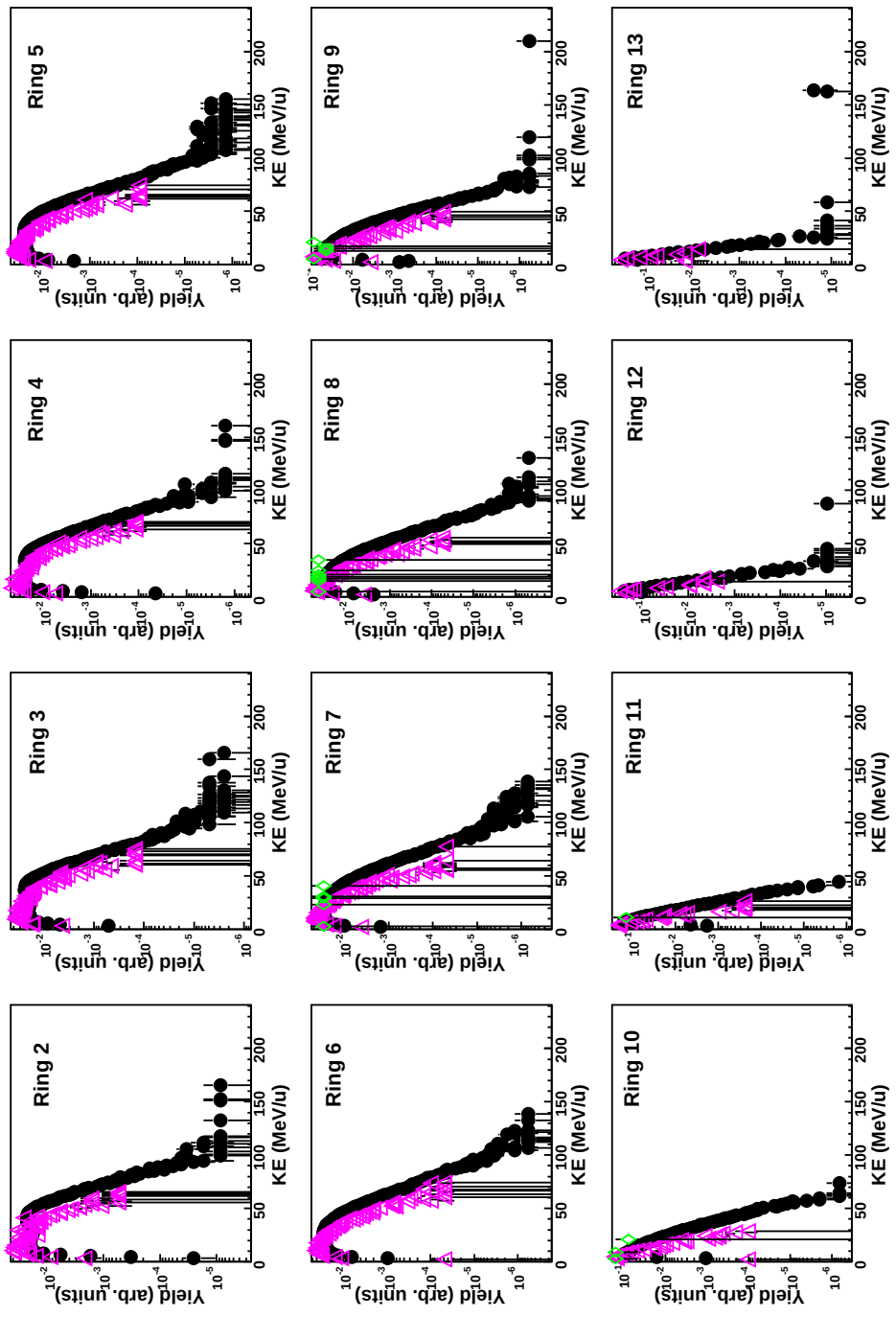

FIG. 153. Kinetic energy distribution of tritons for Rings 2-13 from the experimental data (solid black circles) compared with the AMD results at 300 fm/c with (pink open diamonds and without (green open triangles) applying the Gemini decay.

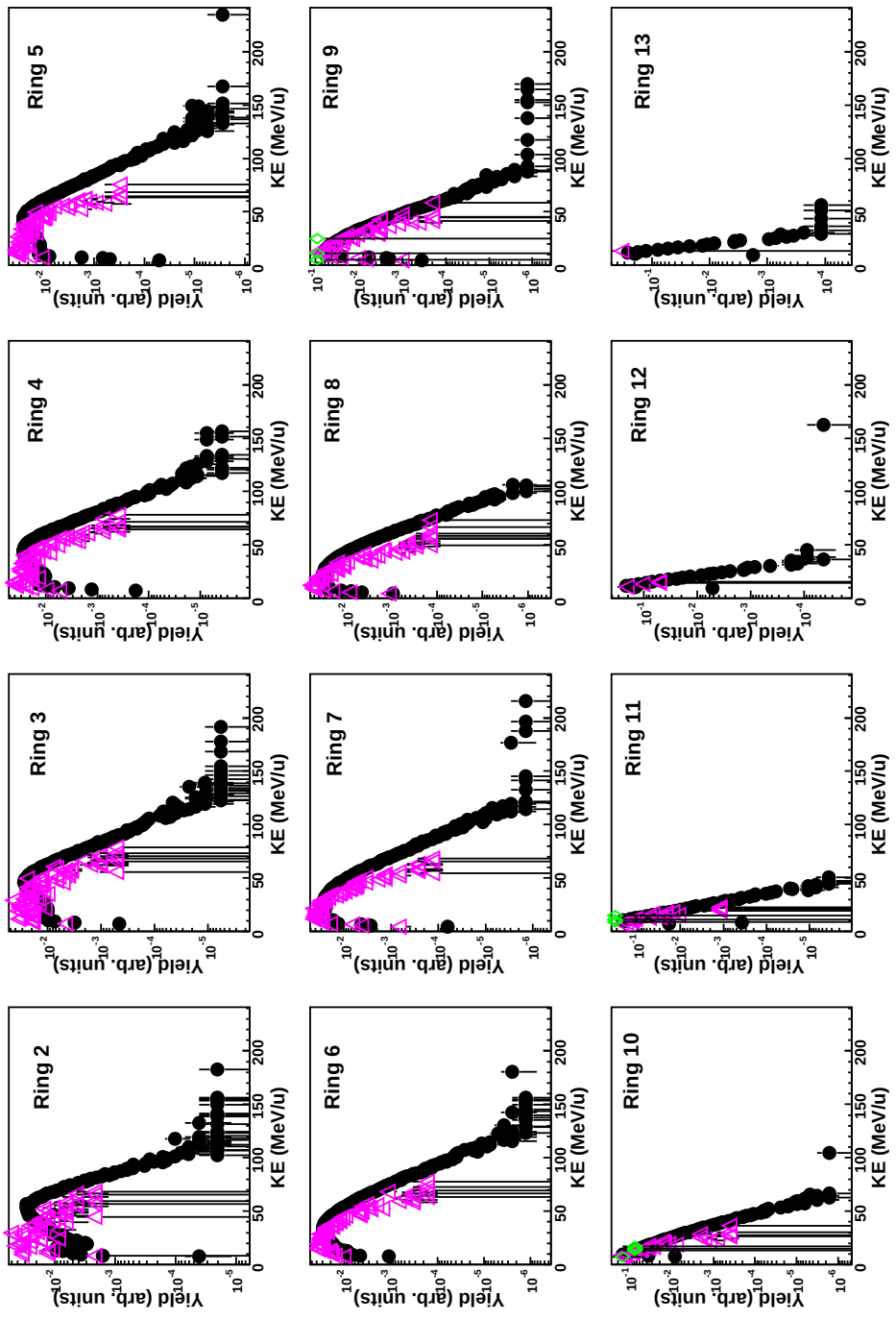

FIG. 154. Kinetic energy distribution of helium-3 for Rings 2-13 from the experimental data (solid black circles) compared with the AMD results at 300 fm/c with (pink open diamonds and without (green open triangles) applying the Gemini decay.

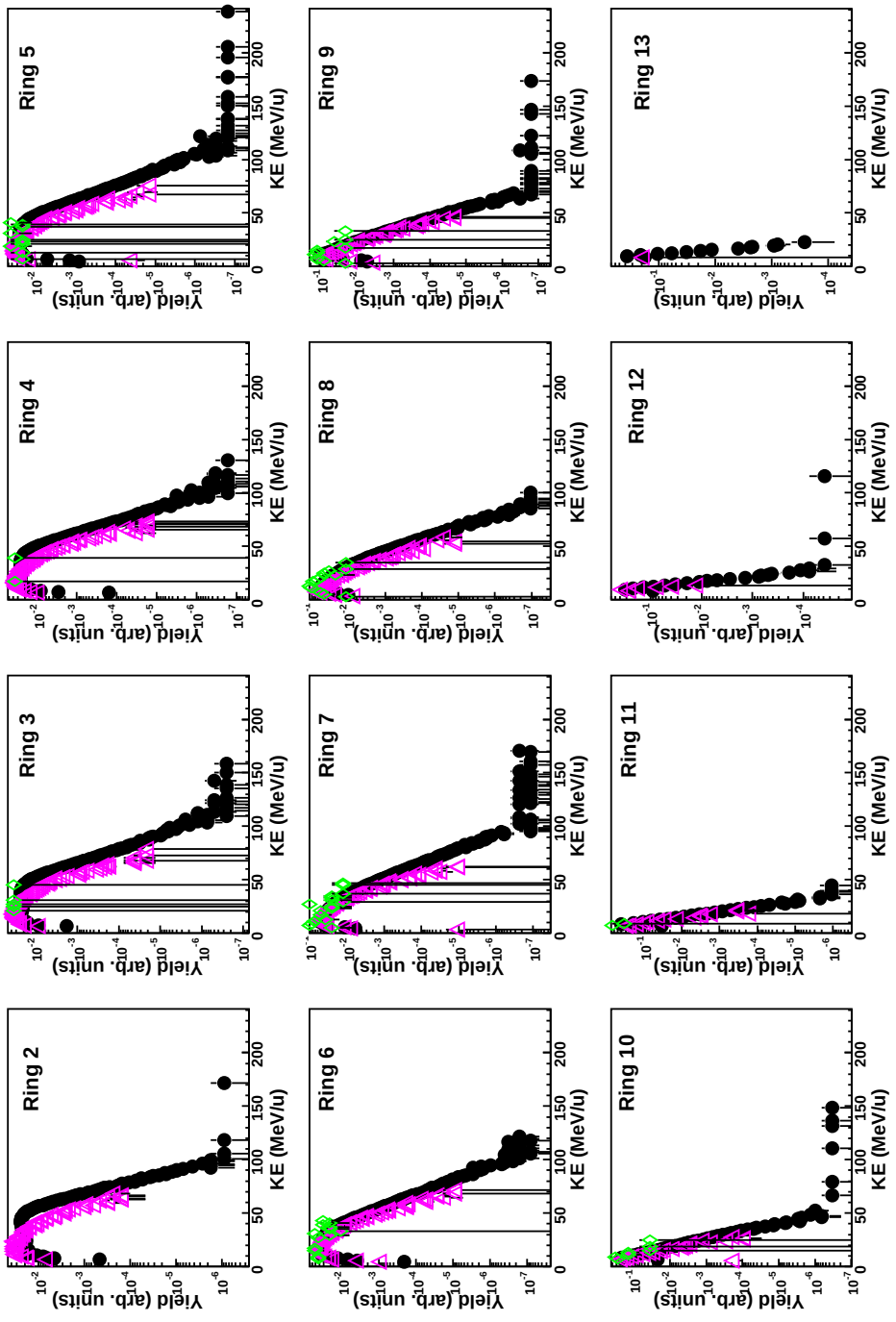

FIG. 155. Kinetic energy distribution of alpha particles for Rings 2-13 from the experimental data (solid black circles) compared with the AMD results at 300 fm/c with (pink open diamonds and without (green open triangles) applying the Gemini decay.

The kinetic energy spectra from the CoMD model are compared with the experimental data in Figures 156-160 for the mid-peripheral (3Bin1) 35 MeV/u ^{64}Zn+^{64}Zn collisions. The CoMD results are shown with and without the application of the Gemini code after 600 fm/c. The results show that the 600 fm/c energy distributions are not significantly changed with the Gemini de-excitation.

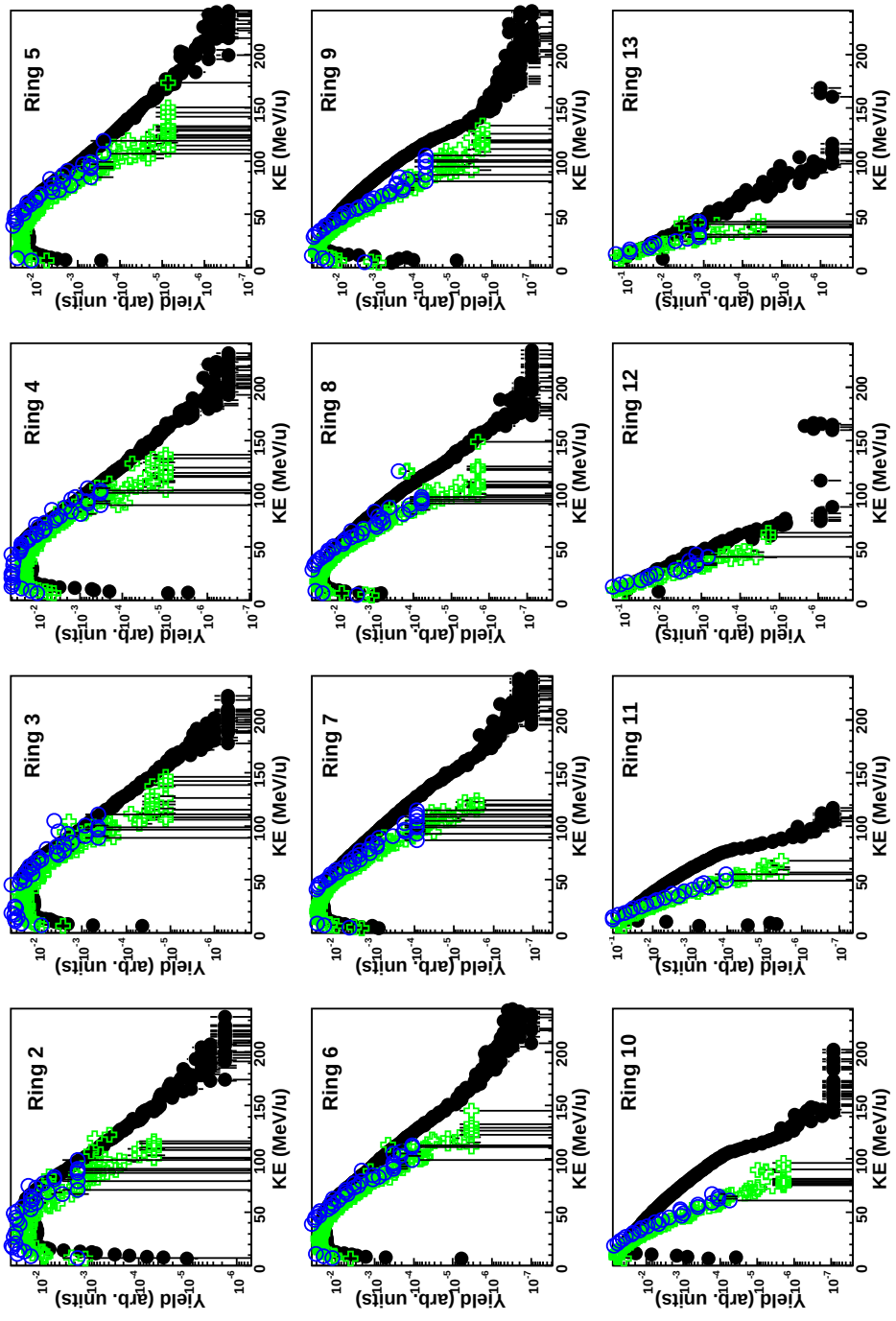

FIG. 156. Kinetic energy distribution of protons for Rings 2-13 from the experimental data (solid black circles) compared the 600 fm/c CoMD calculation with (open green crosses) and without (open blue circles) the Gemini de-excitation.

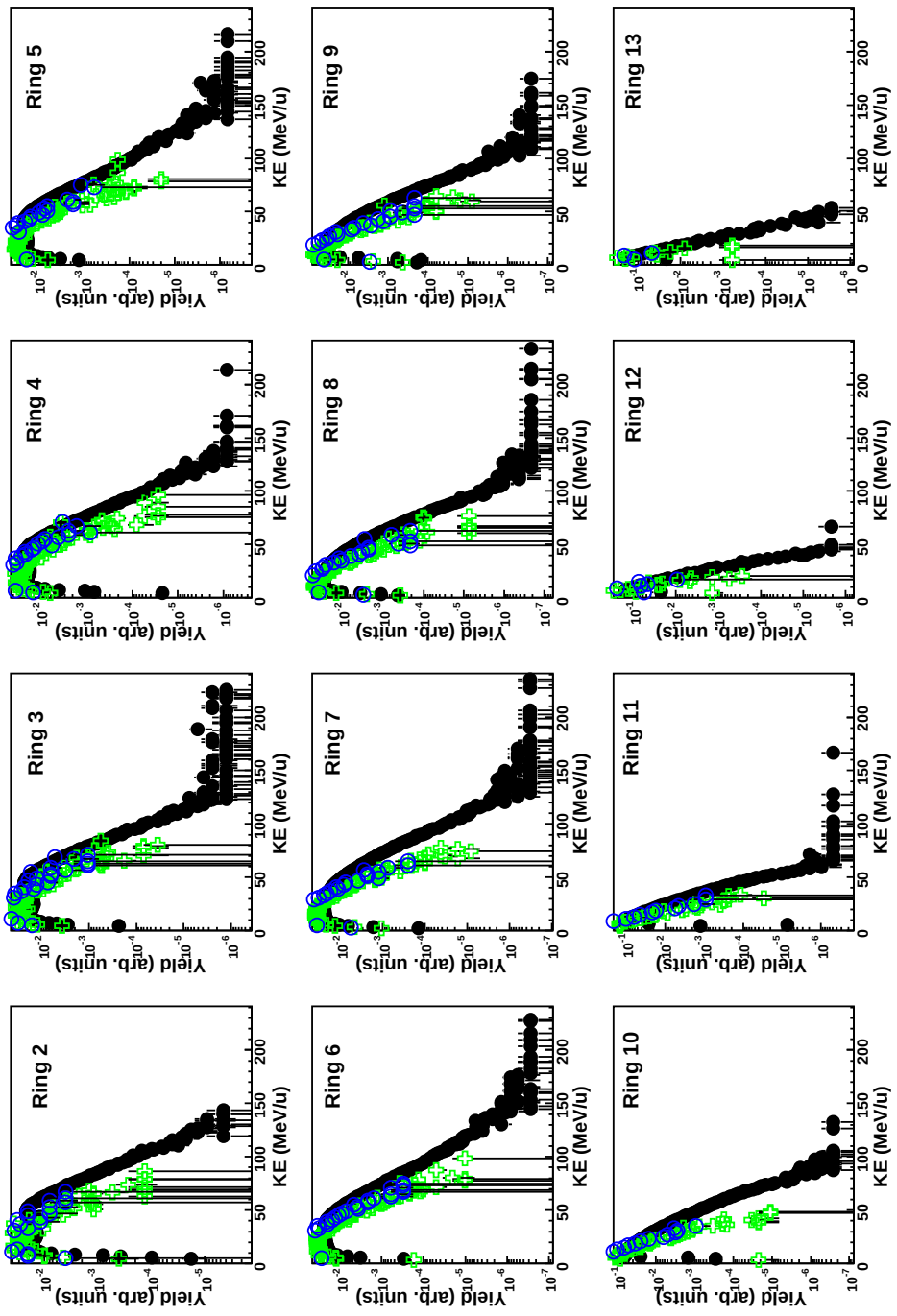

FIG. 157. Kinetic energy distribution of deuterons for Rings 2-13 from the experimental data (solid black circles) compared the 600 fm/c CoMD calculation with (open green crosses) and without (open blue circles) the Gemini de-excitation.

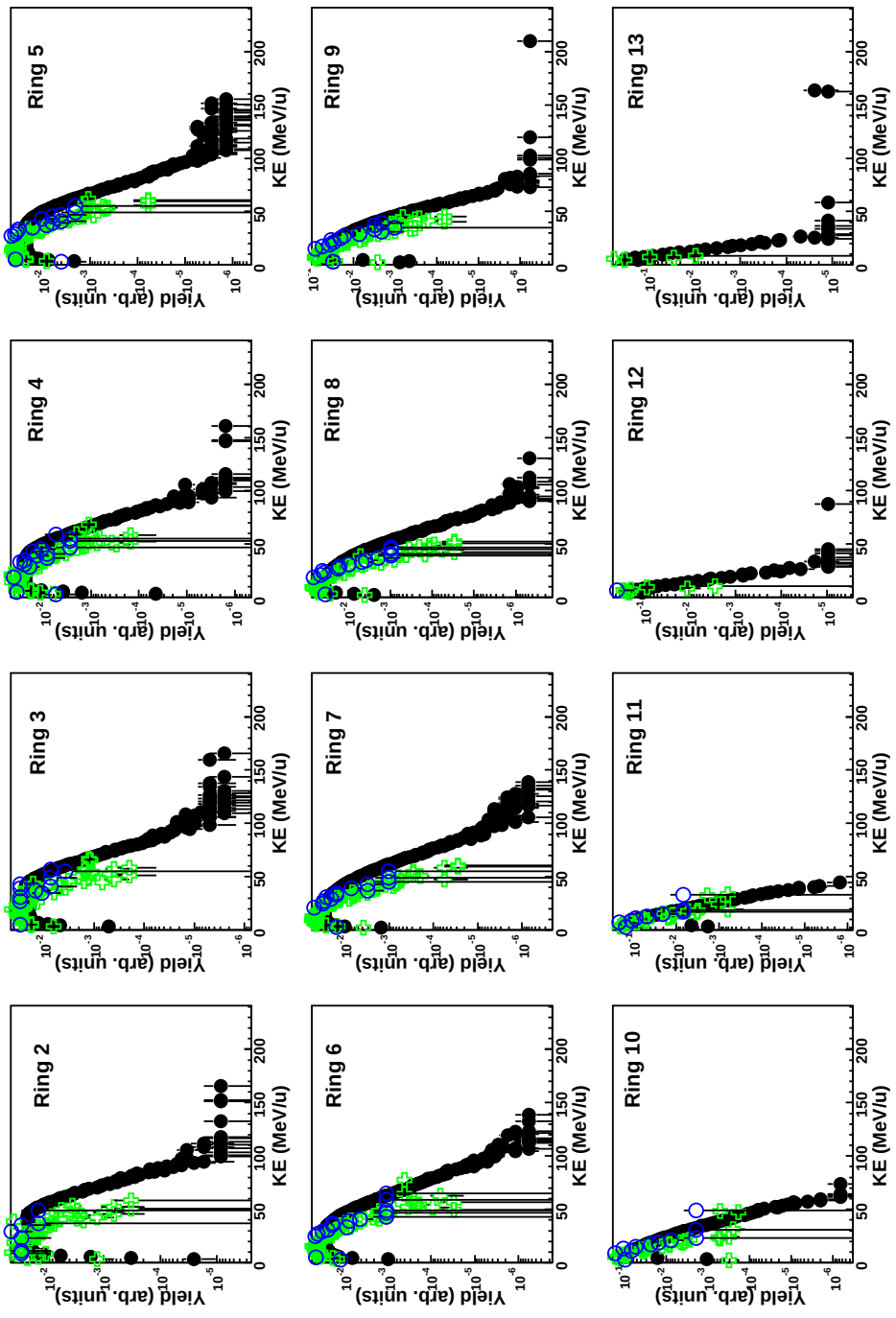

FIG. 158. Kinetic energy distribution of tritons for Rings 2-13 from the experimental data (solid black circles) compared the 600 fm/c CoMD calculation with (open green crosses) and without (open blue circles) the Gemini de-excitation.

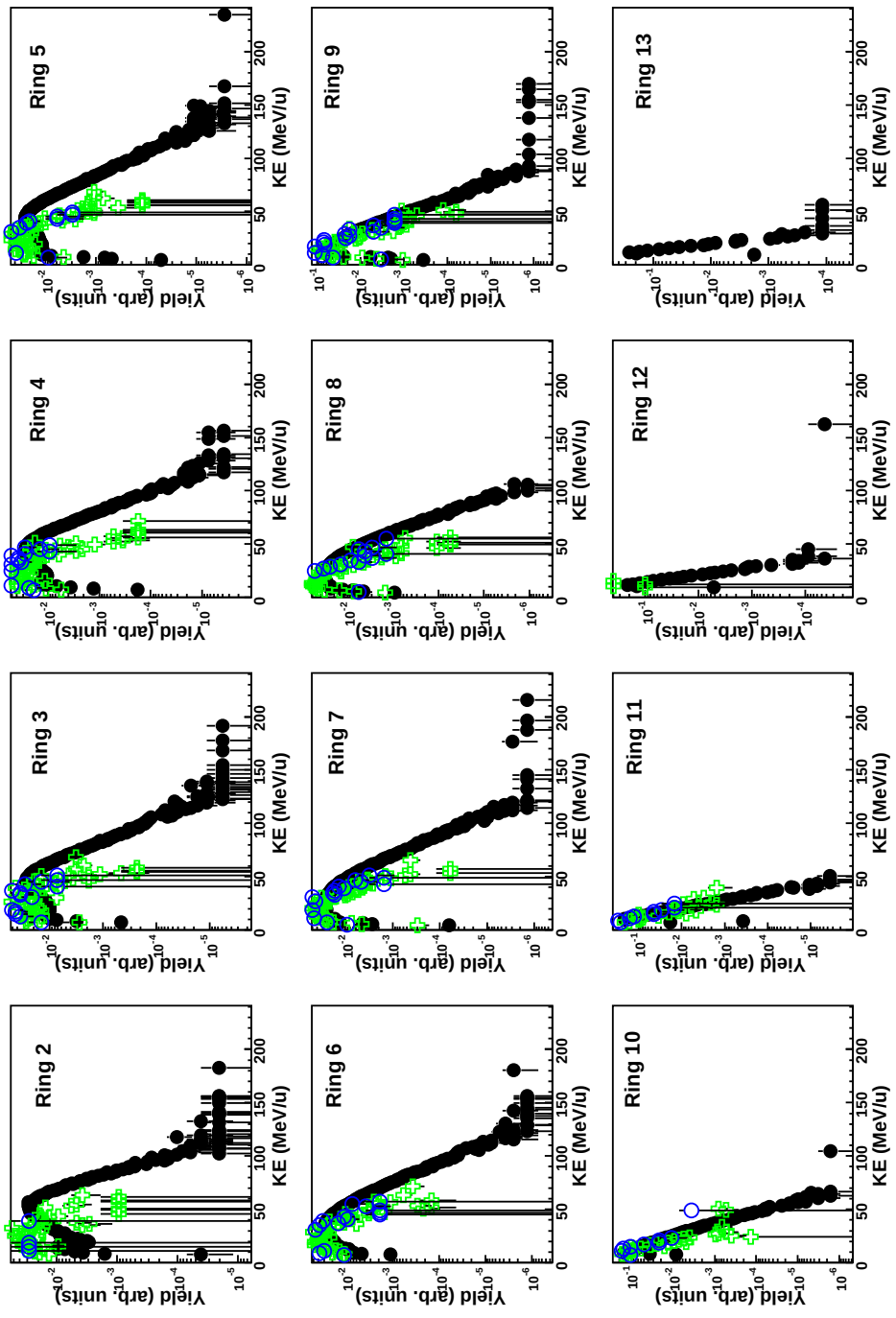

FIG. 159. Kinetic energy distribution of helium-3 for Rings 2-13 from the experimental data (solid black circles) compared the 600 fm/c CoMD calculation with (open green crosses) and without (open blue circles) the Gemini de-excitation.

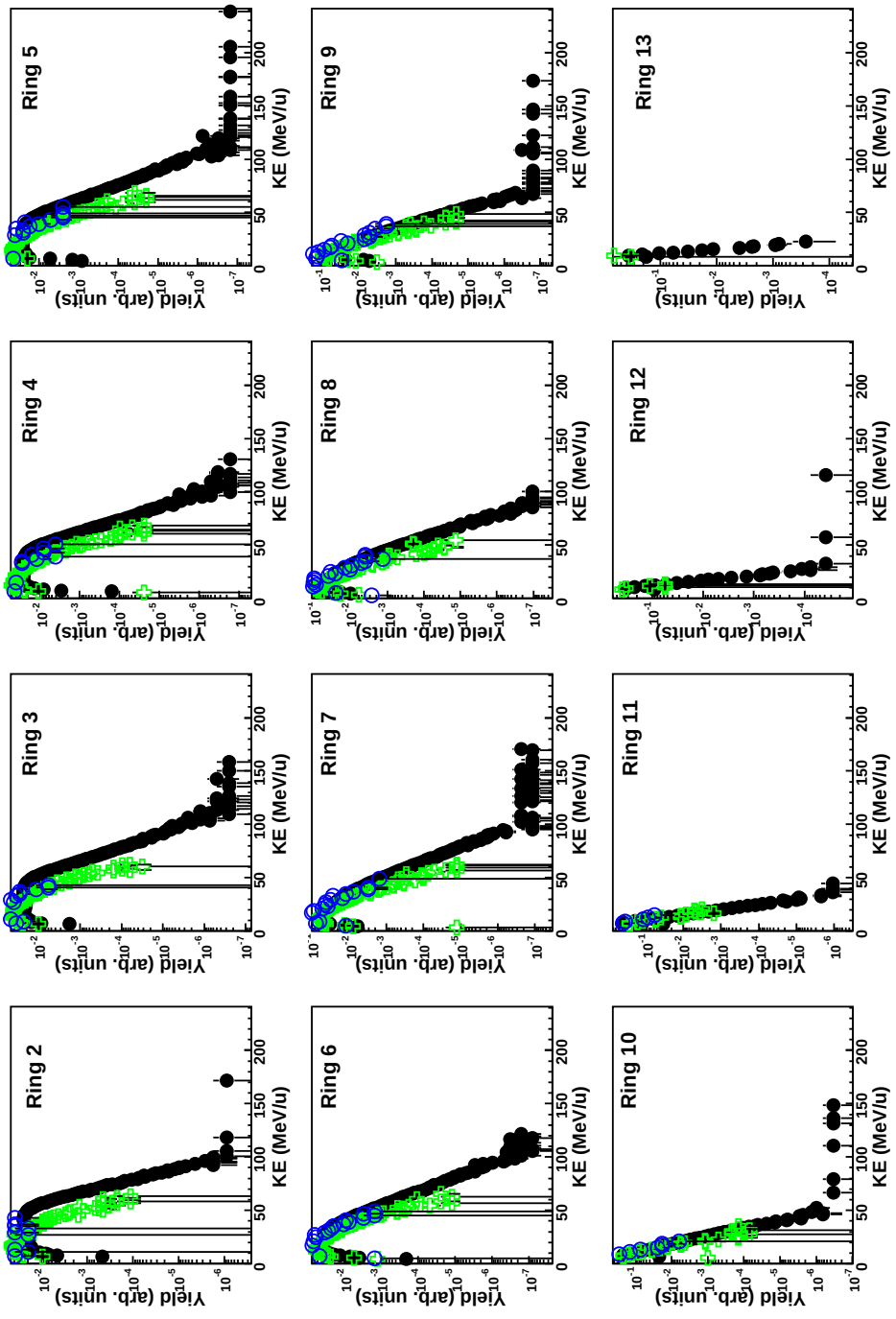

FIG. 160. Kinetic energy distribution of alpha particles for Rings 2-13 from the experimental data (solid black circles) compared the 600 fm/c CoMD calculation with (open green crosses) and without (open blue circles) the Gemini de-excitation.

In Figures 161-165, the CoMD results are shown with the application of the Gemini code after 3000 fm/c and 600 fm/c. In general both the statistical Gemini de-excitation, which has a larger affect at 600 fm/c, and the CoMD dynamical decay, represented by the 3000 fm/c results, produce the similar distributions.

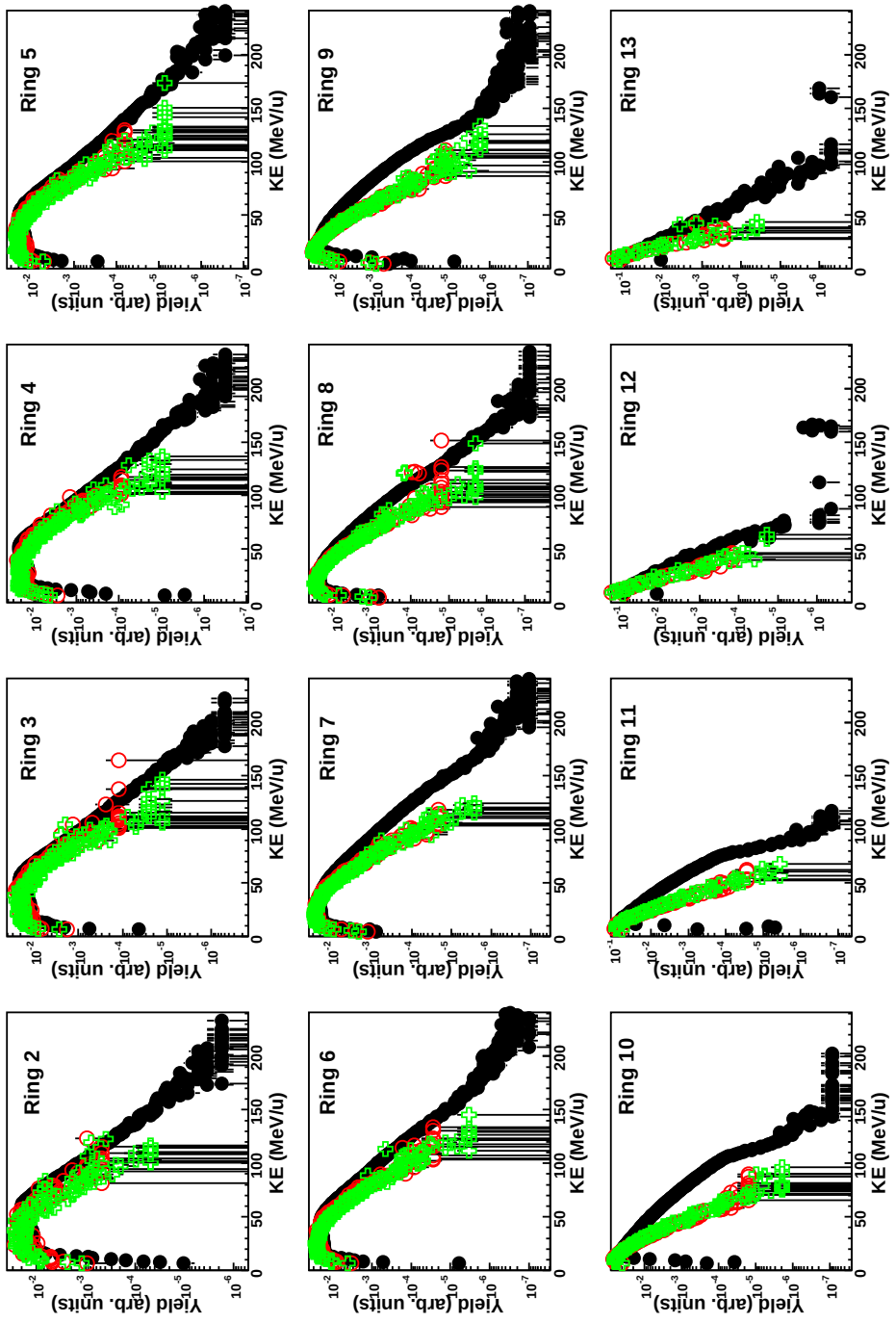

FIG. 161. Kinetic energy distribution of protons for Rings 2-13 from the experimental data (solid black circles) compared with the 3000 fm/c + Gemini (open red circles) and 600 fm/c + Gemini (open green crosses) CoMD simulation.

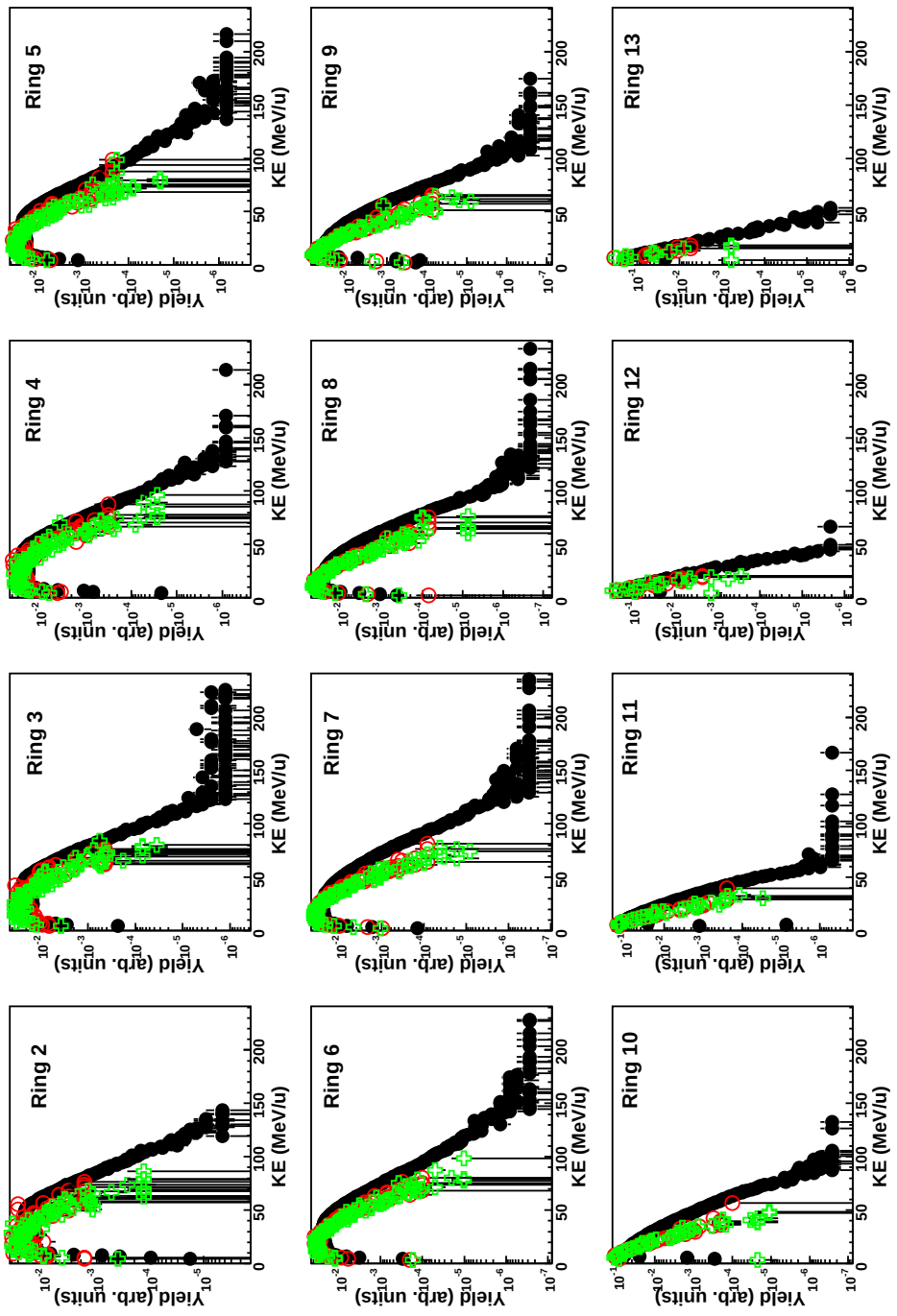

FIG. 162. Kinetic energy distribution of deuterons for Rings 2-13 from the experimental data (solid black circles) compared with the 3000 fm/c + Gemini (open red circles) and 600 fm/c + Gemini (open green crosses) CoMD simulation.

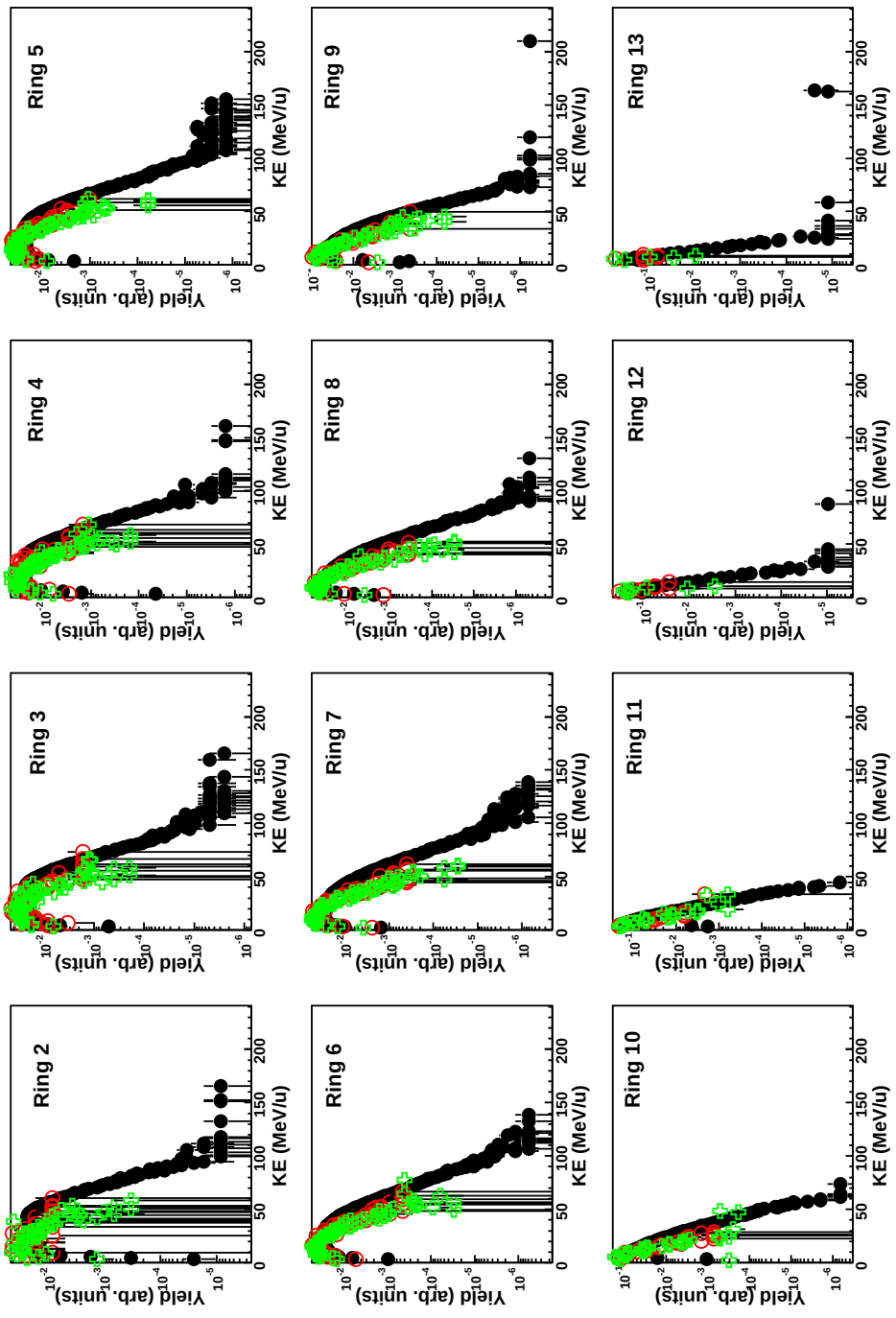

FIG. 163. Kinetic energy distribution of tritons for Rings 2-13 from the experimental data (solid black circles) compared with the 3000 fm/c + Gemini (open red circles) and 600 fm/c + Gemini (open green crosses) CoMD simulation.

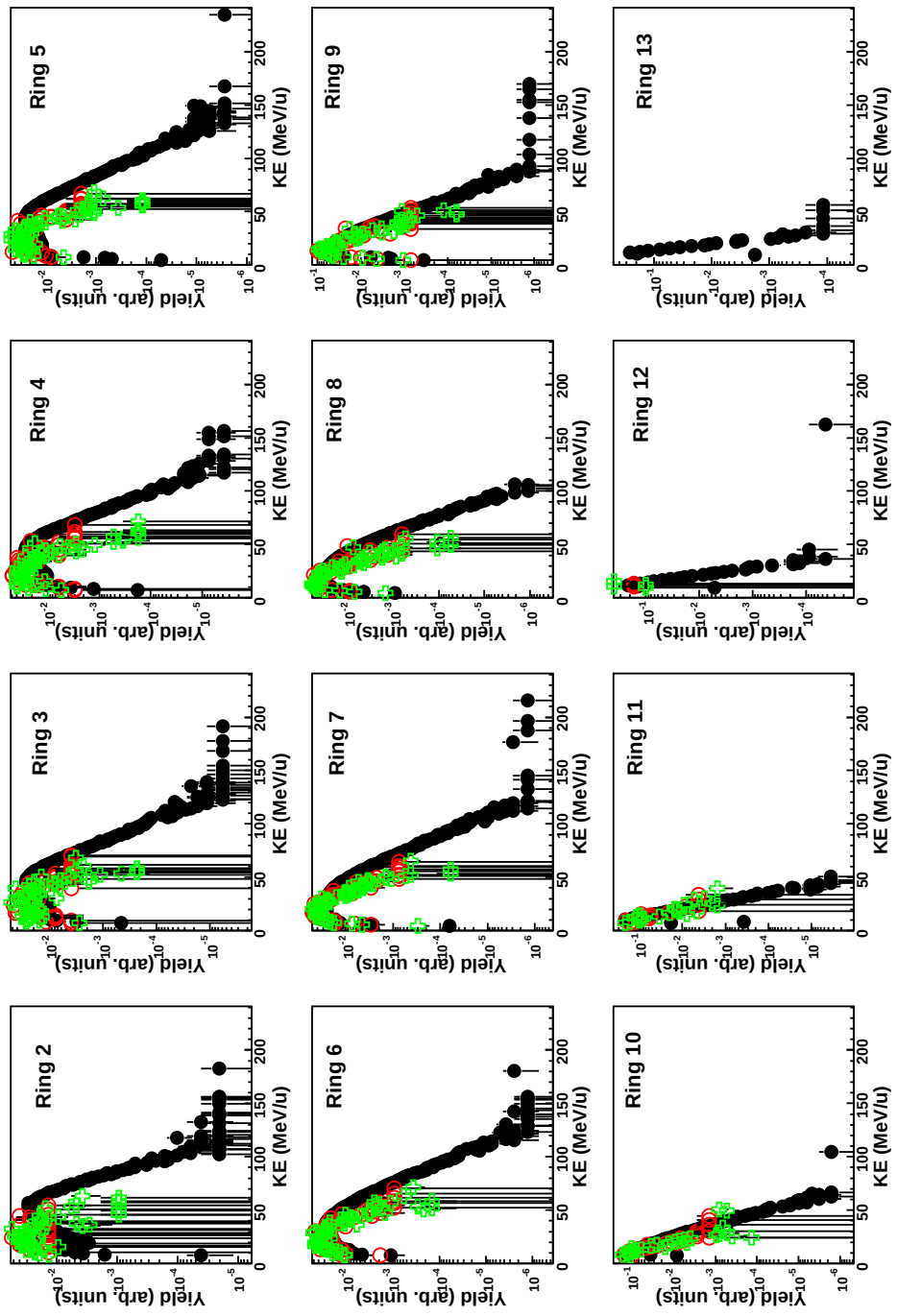

FIG. 164. Kinetic energy distribution of helium-3 for Rings 2-13 from the experimental data (solid black circles) compared with the 3000 fm/c + Gemini (open red circles) and 600 fm/c + Gemini (open green crosses) CoMD simulation.

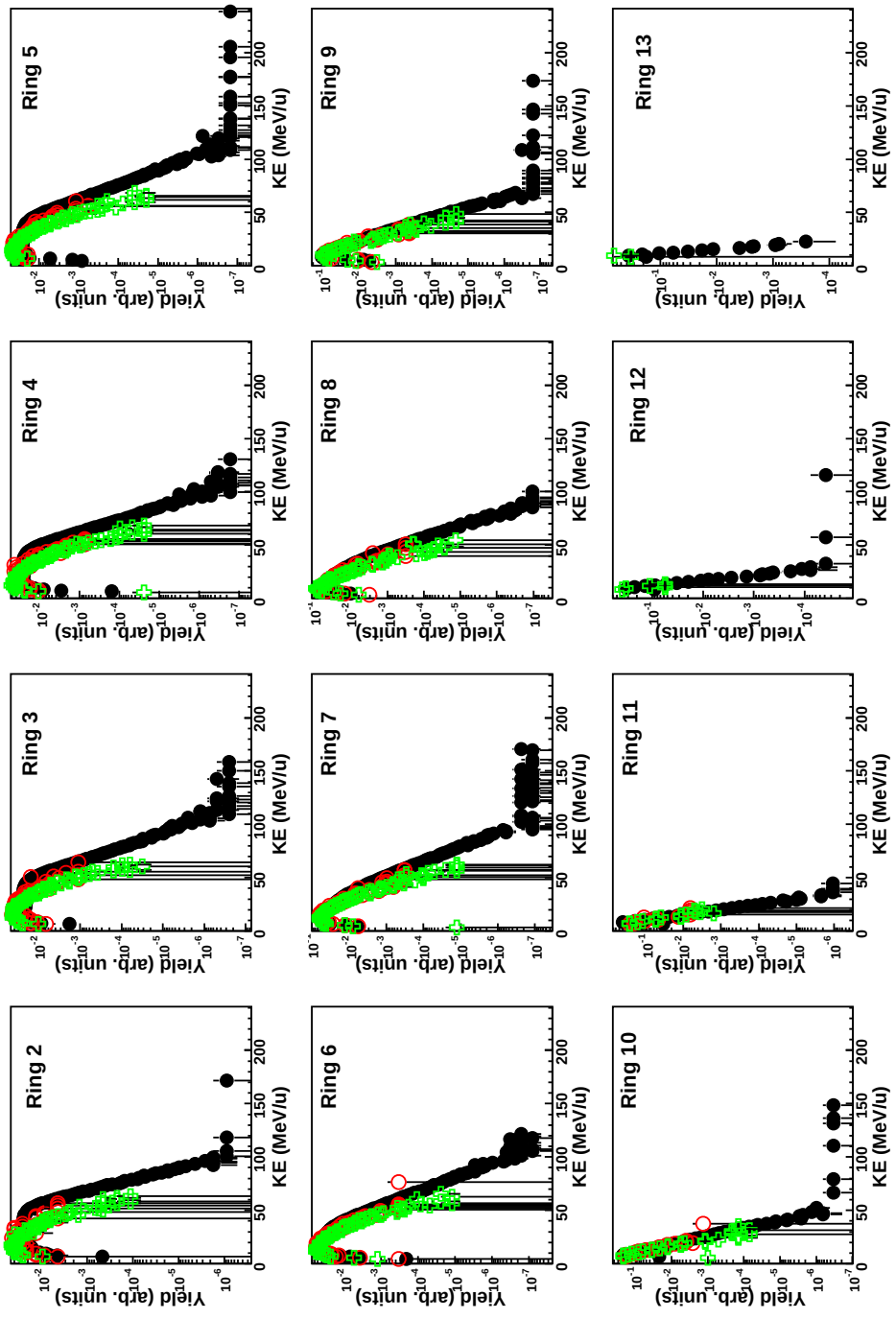

FIG. 165. Kinetic energy distribution of alpha particles for Rings 2-13 from the experimental data (solid black circles) compared with the 3000 fm/c + Gemini (open red circles) and 600 fm/c + Gemini (open green crosses) CoMD simulation.

VITA

Zachary Wayne Kohley

Email: zkohley@gmail.com
Address: MS #3366 Cyclotron Institute
College Station, TX 77843

EDUCATION

Ph.D Nuclear Chemistry, August 2010.
Texas A&M University, College Station, TX
4.00/4.00 GPR

B.S. Chemistry (ACS certified), May 2006
Hillsdale College, Hillsdale, MI
Summa Cum Laude
3.86/4.00 GPR Overall

RESEARCH EXPERIENCE

Research Assistant: July 2006 – present
Advisor: Dr. Sherry Yennello
Topic: Heavy Ion Collisions in Fermi Energy Range
Cyclotron Institute, Texas A&M University, College Station, TX

- Assembly, testing, and calibrations of the large-scale 4π array (NIMROD-ISiS).
- Development and management of an upgrade to the NIMROD-ISiS array.
- Experience with VME, NIM, and CAMAC electronics.
- Programming experience with C++, the ROOT Analysis framework, and Fortran.
- Developed software for the particle identification, energy calibrations and analysis of the experimental data from the NIMROD-ISiS array.

Selected Presentations, Publications, and Honors

Investigation of Transverse Collective Flow of Intermediate Mass Fragments. Z. Kohley, L.W. May, S. Wuenschel, A. Bonasera, K. Hagel, R. Tripathi, R. Wada, G.A. Souliotis, D.V. Shetty, S. Galanopoulos, M. Mehlman, W. B. Smith, S.N. Soisson, B.C. Stein, and S.J. Yennello. *(Submitted to PRL.)*

Transverse Collective Flow of Isotopically Identified Light Charged Particles and the Sensitivity to the Density Dependence of the Symmetry Energy. Z. Kohley, L.W. May, S. Wuenschel, M. Di Toro, M. Colonna, M. Zielinska-Pfabe, K. Hagel, R. Tripathi, A. Bonasera, G.A. Souliotis, D.V. Shetty, S. Galanopoulos, M. Mehlman, W.B. Smith, S.N. Soisson, B.C. Stein, and S.J. Yennello. *(Submitted to PRC)).*

Impact Parameter Characterization, Reaction Plane Determination, and Flow Analysis of 35 MeV/u ^{70}*Zn+*^{70}*Zn,* ^{64}*Zn+*^{64}*Zn,* ^{64}*Ni+*^{64}*Ni.* Z. Kohley, L. May, S. Wuenschel, B.C. Stein, R. Tripathi, S.N. Soisson, G.A. Souliotis, and S.J. Yennello (NIMROD Collaboration). American Physics Meeting, Washington D.C.: 2010.

Selected for the National Nuclear Physics Summer School: 2009
Michigan State University, Lansing, MI.